ROYAUME DU MAROC
Université Mohammed V - RABAT -
جامعة محمد الخامس – الرباط –
Faculté des sciences
كلية العلوم

VRIJE UNIVERSITEIT BRUSSEL

CENTRE D'ÉTUDES DOCTORALES - SCIENCES ET TECHNOLOGIES

N° d'ordre : 3857

THÈSE

En vue de l'obtention du : **DOCTORAT**

Centre de recherche : Centre des Sciences des Matériaux
Structure de Recherche : Laboratoire des Matériaux, Nanotechnologies et Environnement

Discipline : Chimie
Spécialité : Science des Matériaux et Chimie Computationnelle

Présentée et soutenue le :21/10/2023 par :

Ali MOUSSADIK

Nanotechnology and Photocatalysis for the Treatment of Organic Pollutants in Wastewater

JURY

Abderrahman NOUNAH	PES, Université Mohammed V, Ecole Supérieure de Technologie de Salé	Président
Mouloud EL MOUDANE	PH, Université Mohammed V, Faculté des Sciences de Rabat	Rapporteur/Examinateur
Abdellah AADDANE	PES, Université Hassan II, Faculté des Sciences et Techniques de Mohammedia	Rapporteur/Examinateur
Monica CALATAYUD	PES, Sorbonne Université, Université Pierre et Marie Curie, Paris – France	Rapportrice/Examinatrice
Marc ELSKENS	PES, Vrije Universiteit Brussel, Faculté des Sciences et des Sciences de Bio-ingénierie – Belgique	Examinateur
Frank DE PROFT	PES, Vrije Universiteit Brussel, Faculté des Sciences et des Sciences de Bio-ingénierie – Belgique	Invité
Mohamed KACIMI	PES, Université Mohammed V, Faculté des Sciences de Rabat	Invité
Abdellah BENZAOUAK	PA, Université Mohammed V, École Nationale supérieure d'Arts et Métiers	Invité
Adnane EL HAMIDI	PH, Université Mohammed V, Faculté des Sciences de Rabat	Co-Directeur de Thèse
Frederik TIELENS	PES, Vrije Universiteit Brussel, Faculté des Sciences et des Sciences de Bio-ingénierie – Belgique	Directeur de Thèse
Mohammed HALIM	PES, Université Mohammed V, Faculté des Sciences de Rabat	Directeur de Thèse

Année Universitaire : 2023-2024

VRIJE UNIVERSITEIT BRUSSEL

ROYAUME DU MAROC
Université Mohammed V - RABAT -
جامعة محمد الخامس – الرباط –
Faculté des sciences
كلية العلوم

Faculty of Science & Bio-Engineering Sciences
Research Group of General Chemistry

Nanotechnology and Photocatalysis for the Treatment of Organic Pollutants in Wastewater

Ali MOUSSADIK

Thesis submitted in partial fulfilment of the requirements for the academic degree of Doctor in Sciences

Academic Year 2023-2024

PROMOTORS

Prof. Frederik TIELENS
Faculty of Science & Bio-Engineering Sciences, Vrije Universiteit Brussel – Belgium

Prof. Mohammed HALIM
Faculty of Sciences, Mohammed V University in Rabat – Morocco

Prof. Adnane EL HAMIDI
Faculty of Sciences, Mohammed V University in Rabat – Morocco

MEMBERS OF THE JURY

Prof. Abderrahman NOUNAH
Higher School of Technology of Salé, Mohammed V University in Rabat – Morocco

Prof. Marc ELSKENS
Faculty of Science & Bio-Engineering Sciences, Vrije Universiteit Brussel – Belgium

Prof. Frank DE PROFT
Faculty of Science & Bio-Engineering Sciences, Vrije Universiteit Brussel – Belgium

Prof. Monica CALATAYUD
Pierre and Marie Curie University, Sorbonne University – France

Prof. Mouloud EL MOUDANE
Faculty of Sciences, Mohammed V University in Rabat – Morocco

Prof. Abdellah AADDANE
Faculty of Sciences and Technologies, University Hassan II Casablanca – Morocco

Prof. Mohamed KACIMI
Faculty of Sciences, Mohammed V University in Rabat – Morocco

Prof. Abdellah BENZAOUAK
National School of Arts and Crafts, Mohammed V University in Rabat – Morocco

October 2023

Dedication

*I would like to dedicate this thesis to my **Mother**, who gave the little she had to ensure I would have the opportunity of an education, who has been a source of inspiration and gave me strength when I thought of giving up, and who continually provides her moral, spiritual, and emotional support.*

*To all my family, especially my **Aunts,** my **Cousins**, and my **Brothers**, and to all of my **Friends**, for their faith, love, patience, support, and encouragement throughout my research.*

*And lastly, I dedicate this thesis to the memory of my beloved late **Father**, **El Abed Moussadik**. My dear father was a major reason for me to pursue such a career. Thank you very much for showing me that the key to success is hard work. A Son Never Forgets.*

Ali Moussadik

Acknowledgements

This thesis is the outcome of several years of research conducted in cotutelle between the Mohammed V University in Rabat (UM5R), Morocco, and the Vrije Universiteit Brussel (VUB), Belgium, in the frame of an international partnership agreement.

First and foremost, praise and thanks go to Allah, the Almighty, for giving me the strength, knowledge, and opportunity to undertake this research work and to persevere and complete it satisfactorily. Without his unlimited and countless blessings, this achievement would not have been possible.

On this page, I would like to express my immense appreciation, profound gratitude, and heartfelt thanks to my supervisor, **Mr. Mohammed HALIM**, Professor of Higher Education at the Mohammed V University, Faculty of Sciences of Rabat, for his support and guidance and for making it possible for me to continue working at the Laboratory of Materials, Nanotechnologies, and Environment (LMNE).

I would like to sincerely express my deepest gratitude to my co-supervisor, **Mr. Adnane EL HAMIDI**, Associate Professor at the Mohammed V University, Faculty of Sciences of Rabat, for his helpful guidance, continuous encouragement, support and patience during my studies. I value his wisdom, and dedication. He always had time to respond to my inquiries and patiently provided the motivation, vision, and advice necessary for me to move forward in my project.

My deepest thanks go, of course, to my supervisor, **Mr. Frederik TIELENS**, Full Professor at the Vrije Universiteit Brussel, Faculty of Science & Bio-Engineering Sciences, for his guidance, motivation and encouragement, I would like to thank him for giving me the chance to learn from his valuable expertise and engage in productive discussions with him. His extensive knowledge in theoretical modeling was essential to the progress of this work.

I would also like to thank my former supervisor, **Mr. Said ARSALANE**, Professor of Higher Education at the Mohammed V University, Faculty of Sciences of Rabat, for being an inspirational force during my bachelor's, master's, and first years of my PhD.

Besides my supervisors, I would like to offer my thanks to the thesis committee for their willingness to evaluate this PhD thesis, for their time and extreme patience, and for their intellectual contributions to my development as a scientist.

I would like first to express my sincere thanks, deep gratitude, and very great appreciation to **Mr. Abderrahman NOUNAH**, Professor of Higher Education at the Mohammed V University, and Director of the Higher School of Technology of Salé, for accepting being the Chairman over the defense of my thesis.

I would like to offer my thanks to **Mr. Mouloud EL MOUDANE**, Associate Professor at the Mohammed V University, Faculty of Sciences of Rabat, for reporting and reviewing this thesis.

I would like to express my thanks to **Mr. Abdellah AADDANE**, Professor of Higher Education at the University Hassan II, Faculty of Sciences and Technologies of Mohammedia, for reporting and reviewing this thesis.

I would like to extend my thanks to **Mrs. Monica CALATAYUD**, Full Professor at Sorbonne University, Pierre and Marie Curie University in Paris, for reporting and evaluating my thesis.

I would also like to offer my thanks to **Mr. Marc ELSKENS**, Full Professor at the Vrije Universiteit Brussel, Faculty of Science & Bio-Engineering Sciences, for examining and evaluating my thesis.

I would also like to extend my sincere thanks, deep gratitude, and very great appreciation to **Mr. Frank DE PROFT**, Full Professor at the Vrije Universiteit Brussel, Faculty of Science & Bio-Engineering Sciences, and Head of the General Chemistry Group, for accepting being a jury guest during this PhD thesis.

I would like to offer my thanks to **Mr. Mohamed KACIMI**, Professor of Higher Education at the Mohammed V University, Faculty of Sciences of Rabat, and former Head of our Catalysis Laboratory, for accepting being a jury guest during this PhD thesis.

I would like to extend my thanks to **Mr. Abdellah BENZAOUAK**, Associate Professor at the Mohammed V University, National School of Arts and Crafts of Rabat, for accepting being a jury guest during this PhD thesis.

I would also like to express my special thanks to all my colleagues from the UM5R and the VUB, especially **Dr. Abdeladim OULGUIDOUM**, for their valuable suggestions and help in scientific discussions.

Sincere thanks to all Professors and PhD students at the Laboratory of Spectroscopy, Molecular Modeling, Materials, Nanomaterials, Water, and Environment in ENSAM for their help and kindness.

Abstract

Wastewater pollution by different types of contaminants has become one of the most pressing challenges that threaten our modern society. Among various anthropogenic contaminants, organic pollutants present a serious problem. The goal of this research is to develop a multifunctional silver (Ag)-based material that can effectively eliminate a variety of organic pollutants from wastewater. In the first part of this thesis, we prepared self-supported Ag nanoparticles (NPs) on the surface of $AgM_2(PO_4)_3$ NASICON-type materials. The successful growth of Ag NPs on the NASICON matrix has been confirmed through different techniques. The crystalline nature, purity, dispersity, and morphology of the Ag-nanocomposites were revealed by XRD, EDX, and SEM analyses. The investigated applications of the supported Ag NPs include the reduction of methylene blue, methyl orange, and 4-nitrophenol water pollutants. The results showed that Ag NPs can effectively catalyze the conversion of organic dyes and nitrophenol. Detailed kinetic studies have also been conducted, and possible reaction mechanisms have been proposed. Additionally, we demonstrated that the catalysts have long-term stability and can be recycled for multiple times. In the second part of this dissertation, we studied the photocatalytic performance of $AgM_2(PO_4)_3$ for the decomposition of organic dyes under visible-light. The optical and electronic properties of the Ag-based photocatalysts have been examined by combining experimental and density functional theory (DFT) studies. The optical band gaps were determined using UV-Vis DRS. We used the DFT+U method to investigate the electronic band structure. Next, we self-supported Ag_2O NPs on $AgM_2(PO_4)_3$. The successful synthesis of the Ag-nanocomposite was verified by XRD, EDX, and SEM techniques. The visible-light photocatalytic activity was then studied for the decomposition of organic dyes. It was observed that all synthesized Ag-photocatalysts could effectively degrade aqueous dyes under visible-light. Finally, the stability and recyclability of photocatalysts were investigated, and possible photocatalytic mechanisms were proposed.

Keywords: Wastewater treatment; Nanotechnology; Photocatalysis; Organic pollutants degradation; DFT; NASION-type materials; Silver nanoparticles; Ag-based semiconductors.

Samenvatting

Afvalwatervervuiling door verschillende soorten vervuilende stoffen is een van de meest urgente uitdagingen geworden die onze moderne samenleving bedreigen. Onder de verschillende antropogene verontreinigingen vormen organische verontreinigingen een ernstig probleem. Het doel van dit onderzoek is om een multifunctioneel materiaal op basis van zilver (Ag) te ontwikkelen dat effectief verschillende organische verontreinigingen uit afvalwater kan verwijderen. In het eerste deel van dit proefschrift bereidden we zelfondersteunde Ag nanodeeltjes (NP's) op het oppervlak van $AgM_2(PO_4)_3$ NASICON-type materialen. De succesvolle groei van Ag NP's op de NASICON matrix is bevestigd door verschillende technieken. De kristallijne aard, zuiverheid, dispersie en morfologie van de Ag-nanocomposieten werden onthuld door XRD-, EDX- en SEM-analyses. De onderzochte toepassingen van de ondersteunde Ag NP's omvatten de reductie van methyleenblauw, methyloranje en 4-nitrofenol waterverontreinigende stoffen. De resultaten toonden aan dat Ag NP's de omzetting van organische kleurstoffen en nitrofenol effectief kunnen katalyseren. Er zijn ook gedetailleerde kinetische studies uitgevoerd en mogelijke reactiemechanismen voorgesteld. Bovendien toonden we aan dat de katalysatoren langdurig stabiel zijn en meerdere cycli kunnen worden gerecycled. In het tweede deel van dit proefschrift bestudeerden we de fotokatalytische prestaties van $AgM_2(PO_4)_3$ voor de afbraak van organische kleurstoffen onder zichtbaar licht. De optische en elektronische eigenschappen van de Ag-gebaseerde fotokatalysatoren zijn onderzocht door experimentele en density functional theory (DFT) studies te combineren. De optische bandkloven werden bepaald met UV-Vis DRS. We gebruikten de DFT+U methode om de elektronische bandstructuur te onderzoeken. Vervolgens hebben we Ag_2O NP's zelfondersteund op $AgM_2(PO_4)_3$. De succesvolle synthese van het Ag-nanocomposiet werd geverifieerd met XRD-, EDX- en SEM-technieken. De fotokatalytische activiteit bij zichtbaar licht werd vervolgens bestudeerd voor de afbraak van organische kleurstoffen. Er werd waargenomen dat alle gesynthetiseerde Ag-fotokatalysatoren effectief waterige kleurstoffen konden afbreken onder zichtbaar licht. Tot slot werden de stabiliteit en recyclebaarheid van fotokatalysatoren onderzocht en werden mogelijke fotokatalytische mechanismen voorgesteld.

Trefwoorden: Afvalwaterbehandeling; Nanotechnologie; Fotokatalyse; Afbraak van organische verontreinigende stoffen; DFT; NASION-type materialen; Zilveren nanodeeltjes; Ag-gebaseerde halfgeleiders.

Résumé

La pollution des eaux usées par différents types de contaminants est devenue l'un des défis les plus pressants qui menacent notre société moderne. Parmi les divers contaminants anthropogéniques, les polluants organiques posent un grave problème. L'objectif de cette recherche est de développer un matériau multifonctionnel à base d'argent (Ag) capable d'éliminer efficacement une variété de polluants organiques des eaux usées. Dans la première partie de cette thèse, nous avons préparé des nanoparticules (NPs) d'argent autoportées sur la surface de matériaux de type NASICON $AgM_2(PO_4)_3$. La croissance réussie des NPs d'Ag sur la matrice NASICON a été confirmée par différentes techniques. La nature cristalline, la pureté, la dispersion, et la morphologie des nano-composites Ag ont été révélées par les analyses XRD, EDX et SEM. Les applications étudiées des nanoparticules d'Ag autoportées comprennent la réduction des polluants bleu de méthylène, orange de méthyle et 4-nitrophénol. Les résultats ont montré que les nanoparticules d'Ag peuvent catalyser efficacement la conversion des colorants organiques et du nitrophénol. Des études cinétiques détaillées ont également été menées et les mécanismes de réaction possibles ont été proposés. En outre, nous avons démontré que les catalyseurs ont une stabilité à long terme et peuvent être recyclés pour des cycles multiples. Dans la deuxième partie de cette thèse, nous avons étudié la performance photo-catalytique des matériaux $AgM_2(PO_4)_3$ pour la décomposition de colorants organiques sous lumière visible. Les propriétés optiques et électroniques des photo-catalyseurs à base d'Ag ont été examinées en combinant des études expérimentales et de théorie de la fonctionnelle de la densité (DFT). Les bandes interdites optiques ont été déterminées à l'aide de la DRS UV-Vis. Nous avons utilisé la méthode DFT+U pour étudier la structure des bandes électroniques. Ensuite, nous avons auto-porté des NPs Ag_2O sur $AgM_2(PO_4)_3$. La synthèse réussie du nano-composite Ag a été vérifiée par les techniques XRD, EDX et SEM. L'activité photo-catalytique sous la lumière visible a ensuite été étudiée pour la décomposition des colorants organiques. Il a été observé que tous les photo-catalyseurs Ag synthétisés pouvaient dégrader efficacement les colorants aqueux sous lumière visible. Enfin, la stabilité et la recyclabilité des photo-catalyseurs ont été étudiées et les mécanismes photo-catalytiques possibles ont été proposés.

Mots-clés : Traitement des eaux usées ; nanotechnologie ; photocatalyse ; dégradation des polluants organiques ; DFT ; matériaux de type NASION ; nanoparticules d'argent ; semi-conducteurs à base d'Ag.

List of Figures

List of Tables

Table of Contents

General Introduction

Today, the cry of "environmental pollution" is heard from all corners of the world.[1] Water pollution, in particular, has now become a distinct threat to the very existence of mankind on this earth. It is now considered one of the biggest environmental issues of the 21st century.[2] The explosive growth of the population, rapid urbanization, and the intensification of industrial and agricultural activities are the principal factors contributing to the increased levels of water pollution.[3] These factors have resulted in stretching the use of our natural water resources to the maximum, while concurrently, the generation of huge amounts of different wastewater presents a risk to the quality of these resources.[4–6] Nowadays, it is approximated that 80% of industrial and municipal wastewaters are disposed into the environment without treatment, with detrimental effects on human health and ecosystems.[7] In the global context, water pollution with synthetic organic substances produced mainly by chemical industries is recognized as the most dangerous threat to the aquatic environment.[8] Organic pollutants, such as organic dyes, nitroaromatic compounds, heterocyclic compounds, phenolic substances, etc., with high toxicity, are impervious to degradation by natural processes and therefore have been noticed to persist in the environment.

Synthetic dyes, among all, constitute the larger group of organic pollutants released into wastewaters from various industries.[9] Scientific reports revealed that, of the 0.7 million metric tons of 10,000 different synthetic dyes fabricated globally each year, around 10 to 15% are directly discharged into the waterways during manufacturing processes.[10] This massive influx of undesirable effluent not only introduces aesthetic concerns but far more, it blocks sunlight entering the water and decreases oxygen exchange of aquatic organisms, which adversely affects the photosynthesis process. Furthermore, many of these hazardous substances are suspected or established mutagens or carcinogens, which pose a serious risk to human health.[11] Another important class of organic pollutants generated by industrial wastes are nitrophenolic compounds (NPCs).[12] These hazardous water-soluble compounds are non-biodegradable and are emitted into the aquatic ecosystem through the effluents of agrochemical, pharmaceutical, dyestuff, and military industries.[13] The existence of NPCs in water poses a significant concern to public health, as they often exhibit toxicity, mutagenicity, or potential carcinogenicity to humans, animals, and marine life. Even at very low concentrations, many NPCs are considered harmful and dangerous.[14] However, conventional wastewater treatments currently in use today may not be very effective in removing organic pollutants as they can be slow- or non-destructive to some or most of these pollutants.[15] This makes the development of advanced and innovative approaches necessary to prevent any further discharge of contaminated waste into the environment.

In this respect, nanotechnology, specifically the use of metallic nanoparticles (NPs), has shown potential in addressing several environmental problems, including the remediation of wastewater pollution.[16]

Numerous research have been reported in which metal NPs with a dimension smaller than 100 nm have been applied to eliminate various toxic contaminants from water bodies.[17] Owing to their small size, metal NPs show an array of unique properties that are very distinctive from their bulk counterparts. Hence, they can be employed as nanocatalysts for the reduction, decomposition, or degradation of organic pollutants in complex wastewater with small dosages and in large scale applications. Among different metal NPs, silver nanoparticles (Ag NPs) have particularly attracted significant interest by virtue of their catalytic activity, optical response, low toxicity, environmental friendliness, and relative abundance. In the laboratory-scale, Ag NPs showed pretty significant results in treating multiple aqueous pollutants, including organic dyes and NPCs.[18] However, despite their excellent performance, "naked" Ag NPs present strong tendencies for aggregation during operations, which leads to major changes in their physicochemical properties and thus compromises their outstanding catalytic activities. To address these problems, many scientists have focused to the use of immobilized Ag NPs on suitable support materials to improve stability, permit good accessibility, enable easy recovery, and favor nanocatalyst recycling.[19] Nonetheless, there are still other important challenges that need to be overcome in the current situation. The foremost concern is the deactivation and loss of catalytic performance during recycling experiments, which mainly results from the poisoning of supported Ag NPs by intermediate products and/or inorganic ions adhering to their surfaces more strongly than the target reactants themselves. Deactivation is a major problem for practical applications of catalysts in wastewater treatment techniques. Therefore, finding a suitable and simple regeneration strategy to recover the initial catalytic activity of deactivated Ag NPs is a serious challenge to be faced.

Besides nanotechnology, heterogenous photocatalysis using semiconductor materials is another popular approach that has been gaining widespread popularity for treating organic pollutants in wastewater.[20] This technique involves irradiating a semiconductor photocatalyst with ultraviolet (UV), visible or near-infrared light, based on its band gap energy, to generate conduction band electrons (e^-) and valence band holes (h^+). These produced pairs of charge carriers (e^- and h^+) can then separate and move to the semiconductor surface, where they initiate redox reactions. On the semiconductor, the photogenerated e^-/h^+ pairs scan the surface and visit different locations to reduce adsorbed electron acceptors and oxidize adsorbed electron donors.[21] In wastewater treatment, dissolved O_2 often acts as the electron acceptor, while HO^- and H_2O are present as the donors of electron to produce the powerful $\bullet O_2^-$ and •OH species. These highly reactive oxygen radicals have a strong oxidizing ability and can non-selectively degrade/mineralize all organic pollutants in wastewater, eventually converting them into H_2O and CO_2.[22] The role of photoexcited semiconductor materials, then, is to serve as electron and hole pools in a series of multi-electron transfer processes to facilitate the elimination of recalcitrant organic compounds that fail to be removed by conventional wastewater treatments. However, industrial commercialization of this technique has been significantly hindered due to the fact that traditional semiconductors, like titanium dioxide (TiO_2) and zinc oxide (ZnO) possess wide band gaps and can only

be activated by UV light,[23] which constitutes merely about 4% of the entire solar spectrum. In contrast, visible light makes up about 43% of the sunlight spectrum and is also the main component of indoor artificial lighting. Therefore, it is crucial to investigate and create new visible light-active semiconductors with narrow band gaps that can exploit economical and safe energy sources to tackle water pollution.

The first part of this PhD thesis will focus on investigating the catalytic performances of self-supported Ag NPs on Ag-based materials with NASICON (Na super-ionic conductor)-type structure for the chemical reduction of organic dyes and NPC pollutants, along with the application of different regeneration methods to address the inevitable Ag nanocatalyst deactivation. Earlier works from our research group[24–26] have demonstrated that Ag-containing NASICON materials with the chemical formula $AgM_2(PO_4)_3$, can be promising self-support materials for highly active Ag NPs in various catalytic reactions. Furthermore, the supported Ag NPs can be re-oxidized under heat treatment and reversibly return back into the NASICON structure, regenerating the starting material composition. These interesting structural features, catalytic properties, and regeneration abilities of such materials inspired us to study the application of Ag-NASICON materials for the removal of toxic organic contaminants from water.

The second part of this PhD project will be devoted to studying the ability of Ag-NASICONs to act as visible-light photocatalysts for the photochemical treatment of organic dyes in wastewater. Very recently, several Ag-containing photocatalysts, including Ag_3PO_4,[27] Ag_2O,[28] Ag_3VO_4,[29] $AgSbO_3$,[30] Ag_2CrO_4,[31] AgX (where X = Cl, Br, I),[32] etc., have shown remarkable photocatalytic activity when exposed to visible light or sunlight illumination. This is because of their unique crystal and electronic structures. In addition, it is believed that an *in situ* photoreduction of Ag NPs from Ag-based compounds under light illumination can improve the optical response of these materials and boost the photocatalytic activity due to the localized surface plasmon resonance (LSPR) effect. Metal/semiconductor junctions can be formed to promote the transfer of charges between Ag NPs and Ag-based compounds, which can assist in the remediation of a variety of efficiency challenges. Nevertheless, it is argued that excess Ag NPs may serve as new recombination centers, reducing the effectiveness of charge separation and thus decreasing the photoactivity of organic decomposition. Therefore, to surmount this limitation, our goal is to develop a new strategy to periodically regenerate the catalytic performance of Ag-based photocatalysts, in order to make them recyclable and cost-effective.

Thesis aim and objectives

The general aim of this PhD dissertation is to discuss the application of nanotechnology and photocatalysis to address wastewater pollution issues. The synthesis and characterization of various metal NPs and photocatalysts forms one key aspect of such applications. The use of metal NPs and photocatalysts in environmental remediation processes is a current challenge. Hence, this work project

is centered on the development of efficient, reusable, and regenerable Ag-based nanocatalysts and Ag-based photocatalysts and their testing in a laboratory scale for the treatment of toxic organic contaminants in wastewater. Two Ag-based materials are studied, namely $AgTi_2(PO_4)_3$ and $AgZr_2(PO_4)_3$ NASICON-type materials. The thesis's major objectives can be segmented into two parts:

Part 1: Investigation of self-grown Ag NPs on $AgM_2(PO_4)_3$ ($M = Ti^{4+}$ or Zr^{4+}) as nanocomposite catalysts for aqueous organic pollutants reduction, with the aim of exploring several regeneration processes of deactivated surface Ag NPs at the end of the catalytic experiment.

The specific sub-objectives of this first part include:

i. Synthesis of self-supported Ag NPs on $AgM_2(PO_4)_3$ surface using cost-effective strategy that can be facilely scaled-up for large-scale practical applications.

ii. Characterization of the synthesized Ag NPs/$AgM_2(PO_4)_3$ nanocomposites using different physical and chemical techniques.

iii. Investigating the new prepared Ag nanocomposites for highly efficient environmental remediation of toxic organic pollutants.

iv. Exploring the ability to eliminate various model pollutants from industrial wastewater, so as to extend the applicability to real wastewater conditions.

v. Development of efficient and easy-to-use regeneration processes for our Ag-based catalysts, which can reduce the cost of the treatment processes.

Part 2: The use of Ag-based semiconductors as visible-light photocatalysts is a relatively new area of research. The main purpose of this second part is to study the photocatalytic performance of $AgM_2(PO_4)_3$ ($M = Ti^{4+}$ or Zr^{4+}) nanocomposites in the photo-discoloration of organic dyes. This will be done by combining experimental methods with density functional theory (DFT) studies to better understand the electronic and photocatalytic properties of these materials.

The main specific sub-objectives of this second part are:

i. Examining the photocatalytic performance of $AgTi_2(PO_4)_3$ NASICON-type material for the decomposition of organic dyes under visible light illumination, which represents 43% of the solar spectrum.

ii. Synthesis of self-supported Ag_2O catalysts on the surface of $AgZr_2(PO_4)_3$ to widen the light absorption response to the visible light region and evaluating the photocatalytic activities of the newly synthesized nanocomposite for the photochemical decomposition of organic contaminants in aqueous solution.

iii. Probing the mechanism to unveil the real reactive species in the heterogeneous photochemical process and identifying the responsible active radicals for organic pollutants degradation via quenching experiments.

iv. Exploring the stability of these materials upon exposure to prolonged light illumination and their regeneration by simple treatment processes.

Thesis structure

The thesis is divided into six chapters. Aside from the introduction, literature review, experimental and computational methods, and conclusion sections, this thesis comprises four major chapters that cover the key aspects of the study as well as important findings and discussions. These four chapters are presented based on four research articles and form the core of the project. Three of these research papers have been published in scholarly journals, while the fourth has been submitted for publication. The structure of the thesis, along with the related academic contributions, are outlined below.

Chapter I

This chapter will first present a literature survey on the global water situation and the wastewater pollution crisis, in particular the occurrence of synthetic organic pollutants in wastewater and their adverse effects. Then, a brief review on the limitations of current wastewater treatment techniques in eliminating organic contaminants is presented. Subsequently, the applicability of nanotechnology and photocatalysis for the removal of toxic organics is presented. The discussion on nanotechnology centers around Ag NPs and their role as nanocatalysts, while the discussion on photocatalysis emphasizes Ag-containing semiconductors serving as photocatalysts. This chapter also discusses the various methods used for the synthesis of Ag NPs and their applications in the treatment of organic pollutants. Furthermore, the fundamentals of photocatalysis, the parameters influencing the photocatalytic performance of Ag-based semiconductors, and different factors that enhance their photocatalytic efficiencies, such as the plasmonic properties of Ag NPs, are also presented. Finally, a brief literature background on NASICON materials, their structural properties, synthesis methods, and previous applications of Ag-based NASICON materials as catalysts is reported.

Chapter II

This chapter gives an overview of the materials, experimental techniques, and computational methods employed in this thesis. It starts with the materials and protocols for the preparation of the samples utilized in this project. Subsequently, characterization techniques performed to analyze the samples are presented. The theoretical tools for the calculations of electronic structures and the computational approaches utilized are also described. Lastly, the specific procedures of catalytic reduction and photocatalytic oxidation experiments are given, together with the kinetic models adopted.

Chapter III

This chapter deals with the self-supported Ag NPs on $AgTi_2(PO_4)_3$. Firstly, the preparation and characterization of Ag NPs/$AgTi_2(PO_4)_3$ are described. Subsequently, the catalytic performance of the

Ag NPs/$AgTi_2(PO_4)_3$ composite is evaluated toward the reductive conversion of methylene blue (MB) and methyl orange (MO) as reference organic dyes in wastewater. Afterwards, the kinetics and catalytic mechanism underlying the conversion of MB and MO by means of Ag NPs/$AgTi_2(PO_4)_3$ are studied. Finally, the regeneration of the original $AgTi_2(PO_4)_3$ compound using heat treatment and the reusability of a newly generated Ag NPs/$AgTi_2(PO_4)_3$ for the conversion of MB and MO are investigated.

Contributions

- *Published paper*

A. Moussadik, F. S. Brigiano, F. Tielens, M. Halim, M. Kacimi, A. El Hamidi, Self-supported Ag nanoparticles on $AgTi_2(PO_4)_3$ for hazardous dyes reduction in industrial wastewater. Journal of Environmental Chemical Engineering, 2022. https://doi.org/10.1016/j.jece.2021.106939.

- *Conference presentation*

A. Moussadik, M. Halim, A. E. Hamidi: In situ generated Ag NPs on titanium phosphates surfaces for efficient catalytic reduction of methylene blue and methyl orange in water. International Congress on Pure and Applied Sciences (ICPAS), 23th-25th June 2021, Moulay Ismail University, FS, Meknes, Morocco.

Chapter IV

This chapter is devoted to the synthesis, characterization, and applications of the Ag NPs/$AgZr_2(PO_4)_3$ nanocomposite. After describing the preparation and characterization of the nanocomposite, the reductive conversion of 4-nitrophenol (4-NP) as a reference nitrophenolic compound over the nanocomposite is studied. Then, the kinetics and the mechanism of 4-NP conversion by means of the nanocomposite are analyzed. Finally, yet importantly, the regeneration of the starting $AgZr_2(PO_4)_3$ phase using nitric acid (HNO_3) treatment and the reusability of a newly formed Ag NPs/$AgZr_2(PO_4)_3$ nanocomposite for the reductive treatment of 4-NP are examined.

Contributions

- *Published paper*

A. Moussadik, M. Halim, S. Arsalane, F. Tielens, M. Kacimi, A. El Hamidi, In situ synthesis of self-supported Ag NPs on $AgZr_2(PO_4)_3$ NASICON type phosphate: Application in catalytic reduction of 4-nitrophenol, Mater Res Bull, 2022. https://doi.org/10.1016/J.MATERRESBULL.2022.111764

- *Conference presentation*

A. Moussadik, M. Halim, S. Arsalane, A. E. Hamidi, Removal of 4-nitrophenol from the aqueous medium by catalytic reduction in the presence of silver nanoparticles, National PhD Students Days

CERNE2D on Water-Energy-Environment, 12th-14th June 2019, Mohammed V University, FSR, Rabat, Morocco.

A. Moussadik, S. Arsalane, M. Halim, A. E. Hamidi, New Ag nanoparticles catalysts using NASICON $AgZr_2P_3O_{12}$ type phosphate for environmental catalysis applications: Synthesis and characterization. International Congress, Applied Materials for the Environment (CIMAE), 5th-7th December 2018, Ibn Zohr University, FS, Agadir, Morocco.

Chapter V

This chapter outlines the project regarding the visible light photodecomposition of rhodamine B (RhB) as a reference dye contaminants in water using the $AgTi_2(PO_4)_3$ material. The catalyst's electronic properties are studied using DFT method supplemented with a Hubbard correction term U. The photocatalytic performance, reaction kinetics, and stability of the as-prepared Ag-based NASICON material upon RhB photodecomposition under visible light are presented. Finally, the mechanism of photocatalytic processes over $AgTi_2(PO_4)_3$ is discussed in detail.

Contributions

- *Published paper*

A. Moussadik, N. Lazar, D. Mazkad, F. S. Brigiano, K. Baert, T. Hauffman, A. Benzaouak, Y. Abrouki, M. Kacimi, F. Tielens, M. Halim, A. El Hamidi, Investigation of electronic and photocatalytic properties of $AgTi_2(PO_4)_3$ NASICON-type phosphate: combining experimental data and DFT calculations, Journal of Photochemistry and Photobiology A: Chemistry, 2022.
https://doi.org/10.1016/j.jphotochem.2022.114289

Chapter VI

In this chapter a novel heterogeneous multi-phase Ag_2O NPs/$AgZr_2(PO_4)_3$ nanocomposite is proposed, characterized, and studied as a visible-light active photocatalyst for the decomposition of MO pollutant. The relevant kinetics and detailed photocatalytic mechanism for MO decomposition are explored and interpreted. Then, the regeneration of the initial $AgZr_2(PO_4)_3$ NASICON phase using hydrogen peroxide (H_2O_2) and reusability of a newly prepared nanocomposite are examined.

Contributions

- *Submitted paper*

A. Moussadik, D. Mazkad, N. Lazar, A. Benzaouak, Y. Abrouki, M. Kacimi, M. Halim, F. Tielens, A. El Hamidi, Self-grown Ag_2O nanoparticles on Ag-NASICON material for visible-light degradation of dyes in wastewater (submitted).

- *Conference presentation*

A. Moussadik, D. Mazkad, N. Lazar, F. S. Brigiano, A. Benzaouak, M. Kacimi, M. Halim, A. El Hamidi and F. Tielens. First Principles and Experimental Investigations of $Ag_2O/AgZr_2(PO_4)_3$ Nanocomposite for Visible Light Photocatalysis. DFT 2022, 28 August - 2 September 2022, Vrije Universiteit Brussel, Brussels, Belgium.

A. Moussadik, N. Lazar, D. Mazkad, F. S. Brigiano, K. Baert, T. Hauffman, A. Benzaouak, Y. Abrouki, M. Kacimi, F. Tielens, M. Halim, A. El Hamidi, Photocatalytic activity of self-supported Ag_2O on $AgZr_2(PO_4)_3$ for azo dye degradation: a combined experimental and DFT study, The 3rd International Congress of Process Engineering for Sustainable Development 2022, (3rd ICPESD22), 29th June 2022, Hassan Premier University, FST, Settat, Morocco.

Finally, the general conclusion section summarizes the research presented in this PhD dissertation and highlights the contributions to the academic field and the novelties of this thesis.

Chapter I: Literature review

I.1 Water resources and the global water crisis

Water is essential for all living beings on Earth, and it ranks among the world's most critical resources. It makes up approximately 70% of the planet's surface, with an estimated volume of 1.386 billion km^3.[33] Of all the water on Earth, 97.5% is saltwater found in the oceans and marginal seas. Only 2.5% is freshwater, which is found in ice caps, groundwater, lakes, and rivers. This freshwater is what humans, animals, and plants rely on for their needs. However, of the 2.5% of the Earth's freshwater, 68.7% is locked up in glaciers, permanent snow covers of both poles, mountainous regions, and Greenland, while 30.1% is found underground, most of it situated in deep aquifers that are difficult to access.[34] Only 1.2% of the planet's freshwater is contained in ground ice and permafrost, river systems, lakes, shallow groundwater, and reservoirs, which is the water we are most familiar with and the most accessible sources of water to satisfy human needs in our daily lives.[33,34] Fig. I.1 illustrates the global distribution of water on Earth.

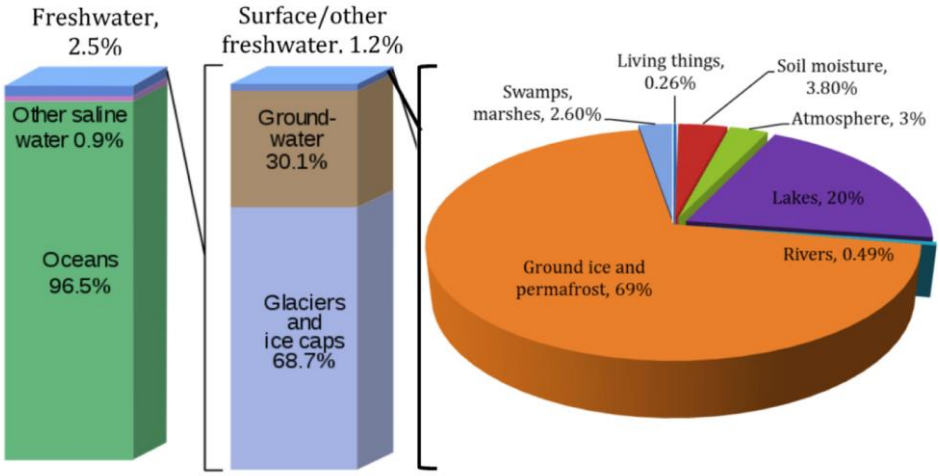

Figure I. 1. Distribution of available global water.[35]

However, despite the fact that water circulates in a closed hydrologic cycle, water scarcity increases across the globe because of its uneven distribution.[36] With a global population of 8 billion people today, the availability of clean water has become a major issue.[3] This concern has been referred to as the "global water crisis" and has been a subject of debate for many years. The overuse of conventional freshwater supplies worldwide is mainly driven by population expansion and economic development. This has led to a situation of water scarcity. Moreover, the pressure on the global water system is expected to increase by 2050 when the world population is projected to grow between 9.4 and 10.2 billion, representing a rise of 22 to 34%.[3] At present, about 3.6 billion people or roughly 47% of the global population, reside in region that suffer from water scarcity for at least one month annually.[37] By 2050, it is projected that over half of the world's population (57%), spread across 44 countries, will likely experience water scarcity for at least one month yearly. Of those affected, 95% will be in

developing countries.[37] Most of the countries that will suffer water scarcity are located in North Africa and Asia.[36] These include Morocco, Tunisia, Libya, Bahrain, Kuwait, Jordan, Saudi Arabia, Qatar, Yemen, and the United Arab Emirates. (Fig. I.2).

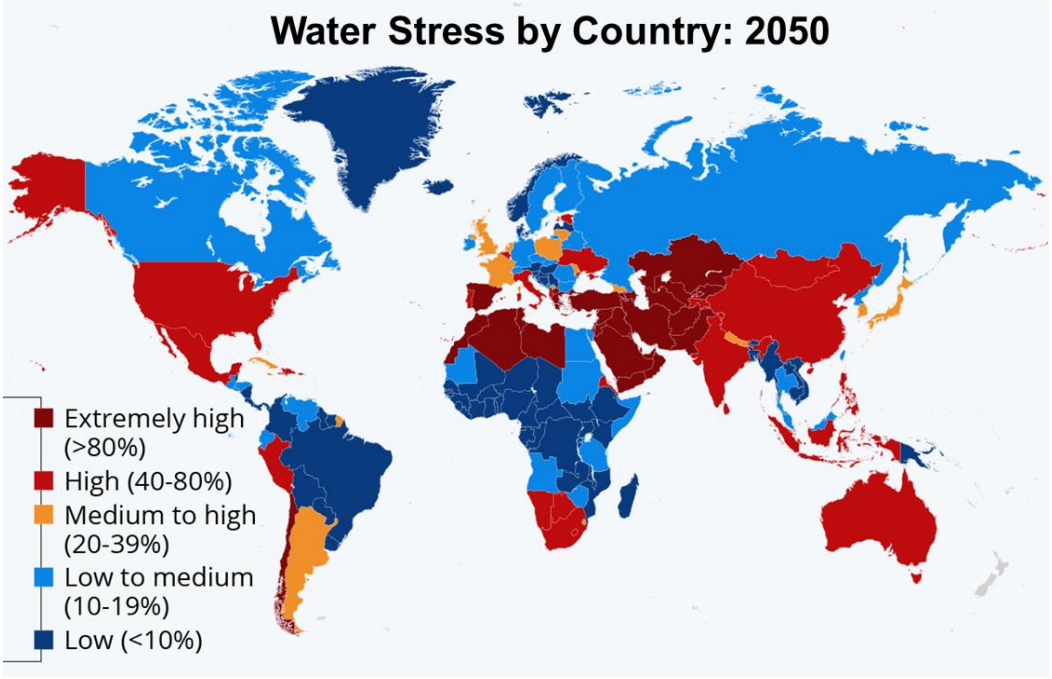

Figure I. 2. Projected global water stress by 2050.[36]

The shortage of water is predicted to worsen as the fast growth of urban areas puts significant strain on adjacent water sources. At present, about 4 billion people (representing 55% of the global population) reside in urban areas.[38] Urban centers are expected to experience a substantial influx of people moving from rural areas and the majority of population growth in the coming years.[39] As a result, this percentage is projected to rise to 68%, with 6.3 billion people residing in urban regions by 2050.[38] The majority of this growth (around 90%) is likely to take place in the world's two most poorest regions, South Asia and Sub-Saharan Africa, where access to fresh and clean water is already a significant problem. Adding to that, global warming and climate change are predicted to exacerbate the already complex relationship between global development and water demand, putting water resources at even greater risk. As per the 2007 Fourth Assessment Report (AR4) released by the United Nations Intergovernmental Panel on Climate Change (IPCC),[40] climate change could result in a 10-30% decrease in water availability. The report also estimates that if global temperatures rise by 2 °C, an additional 1 to 2 billion individuals might face a significant risk of not having access to water for their basic needs.

Besides all the aforementioned factors, water pollution from waste produced by industries, agriculture, households, and municipalities is worsening the situation and adding more pressure on the available freshwater supplies.[41] Water pollution is becoming a serious challenge in many regions around the globe, negatively impacting both the quality and quantity of water required for human consumption and

ecosystem preservation. According to the 2017 United Nations World Water Development Report (UN WWDR),[7] over 80% of used water in the world, and over 95% in some underdeveloped countries, is not collected or treated prior to discharge, polluting rivers, lakes, and coastal areas and therefore compromising freshwater sources. Thus, in order to save natural freshwater resources as well as limit the environmental consequences of hazardous wastewater effluent, the development of advanced, efficient, and affordable wastewater treatment technologies is a must.

I.2 Wastewater pollution

Water pollution occurs when water undergoes changes in its chemical, physical, or biological characteristics that render it unsuitable for its intended purpose.[42] The importance of water in sustaining human lives cannot be overemphasized. Therefore, its continued contamination can have serious consequences. The human body consists of approximately 45-75% water, and the possibility of life existing without it is unlikely.[43] However, the biggest challenge that society faces when it comes to using water is the almost inevitable pollution of this scarce and finite resource. When the term "water pollution" is mentioned, it is used to refer to any alteration in the chemical, physical, or biological composition of water in a way that it becomes unhealthy and unsafe for utilization by humans or other living organisms.[42] Water pollution can affect different types of water bodies, such as groundwater, rivers, lakes, oceans, and aquifers. It can also have negative impacts on ecosystems, biodiversity, climate, and socio-economic development.

Water pollution can originate from two types of sources: point sources, which can be traced to a specific location, and non-point sources, which are more diffuse in nature.[42,44]

- **Point sources** correspond to a specific location where the pollution resulted from human population and human activities. For instance, it can originate from solid waste disposal, wastewater treatment plant effluents, and industrial wastewater outlets.[45,46] The pollutants are discharged to a waterway through discrete conveyances such as sewer channels and outlet pipes, and the effect on the water body will depend on the pollutant load and the water body's capacity to dilute the discharge. The point source of pollution can be traced, and the polluting material can be collected and treated.

- **Non-point sources** correspond to diffuse or multiple-point pollution sources that cannot be linked to a single discharge point. Instances of such diffuse pollution include agricultural and urban run-off, which enter surface water and infiltrate groundwater.[47] The management of non-point sources of pollution is complex and can only be controlled by prevention.

The main types of water pollution are chemical substances rather than biological agents. These chemical components exist in both inorganic and organic forms. The agricultural and industrial sectors are the primary contributors to chemical pollution in water.[42] The most prevalent chemical contaminants in wastewater are heavy metals, inorganic acids, and organic compounds (e.g., herbicides, pesticides,

pharmaceuticals, personal care products, dyes, and other organic chemicals).[48] These substances can show persistent, biocumulative, and synergetic effects on the health and functioning of ecosystems, food production, human health and well-being. Many researches have indicated that conventional methods of wastewater treatment are not always effective at completely removing or degrading a wide range of contaminants. Additionally, large amounts of pollutants are introduced into water bodies from agricultural runoff and industrial discharge without any treatment. In a cycle like the one depicted in Fig. I.3, recalcitrant organic pollutants can bypass barriers, such as conventional wastewater treatment plants (WWTPs) and underground passages, contaminating water sources used for drinking and harming aquatic ecosystems.[49,50]

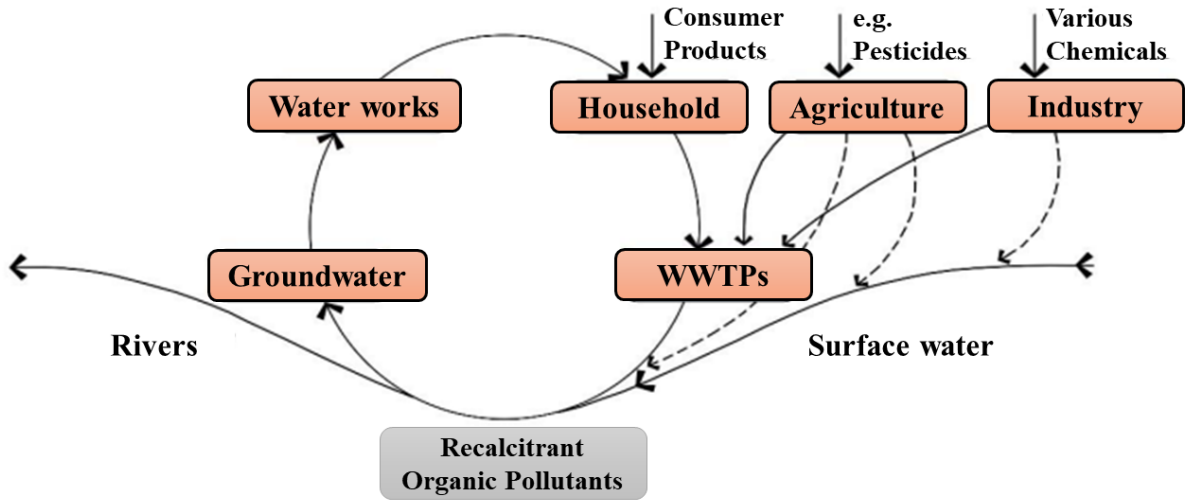

Figure I. 3. Wastewater pollutants pathway.

I.2.1 Organic pollutants

During the last decades, the detection of organic pollutants in wastewater, surface water, and groundwater has increased. These pollutants originate from sources such as agricultural landfills, contaminated soil, industrial waste, and leaks from storage of hazardous compounds.[51] The existence of organic substances in water poses a significant threat to public health, as many of them are toxic to humans, animals, and aquatic life. Two important classes of recalcitrant organic pollutants that are frequently encountered in the environment owing to their widespread use in industry are synthetic dyes and nitrophenolic compounds (NPCs).

I.2.1.1 Synthetic organic dyes

An organic dye is a colored substance that can be applied to a material. Dyes can be derived from natural origins or produced in laboratories. The first synthetic organic dye is Mauveine, which was discovered by chance in 1856 by the English scientist William Henry Perkin.[52] Since that time, the dyestuff industry has evolved remarkably. Almost all synthetic dyes are made from aromatic organic substances. A substrate is defined as the material that a dye is applied to, using various methods like dyeing, surface coating, printing, etc. The substrates can include materials such as textile fibers, leather, polymers,

drugs, oils, foodstuffs, and so on.[53] However, not all colored materials qualifies as a dyestuff, because a colored substance may lack a suitable application on a substrate. For instance, copper sulfate is a colored compound but it cannot be used as a dye because it does not adhere to a substrate. Fig. I.4 displays structures of some organic dyes.

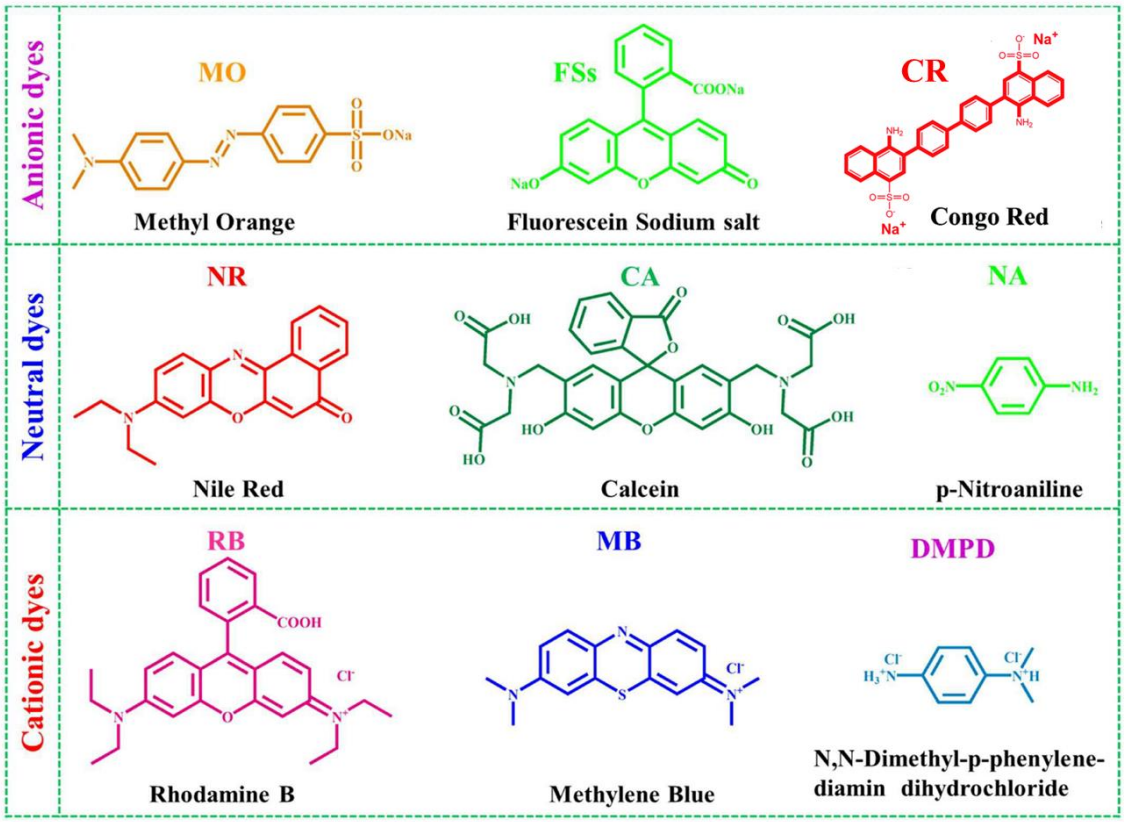

Figure I. 4. Structures of some organic dyes.[54]

Synthetic organic dye effluents can be introduced into the environment from their own manufacturing processes; however, the major sources come from their use in subsequent industrial sectors, such as textiles, leather tanning, pulp and paper, paint, printing, cosmetics, pharmaceuticals, plastics, and the food industry. There are over than 100,000 dyes commercially available, with around 10,000 being produced on an industrial scale. This results in more than 0.7 million tons of dyes being produced annually.[10] The textile market is estimated to use two-thirds of all dyes.[55] During the dyeing process, wastewater containing dyes is produced, and a significant amount of dyes are lost. On average, 10-15% of textile dyes end up in the wastewater stream.[56] However, this percentage can vary based on the specific dye used, with certain basic dyes, it can be 5%, while with certain reactive dyes, it can reach 50%.[9] Estimating the exact amount of dye each country releases into the environment presents a challenge. However, globally, the textile industry discharges approximately 200 billion liters of colored wastewater and around 280,000 metric tons of colorants into ecosystems every year. This means that unbelievable quantities of dyes are being directly discharged into water sources.[57] Fig. I.5 shows the effects of chemical dyes on waterways.

Figure I. 5. The effects of chemical dyes on waterways.[58]

The presence of dyes in aquatic basins blocks the entrance of sunlight into water, creating disturbances in the photosynthetic activity of aquatic flora.[59] This adversely alters the level of dissolved oxygen in water sources, resulting in a deterioration in the water quality. Similarly, the dark color of dyes easily shows its presence even at small concentrations, reducing the aesthetic value of water resources. Dumping of dye-containing wastewater in open land fields causes the leaching of harmful chemicals into the soil, resulting in soil and groundwater pollution.[59] Contamination due to dyes also poses a significant threat to aquatic life and marine ecology. For instance, when fish and other aquatic organisms ingest dyes, their bodies can metabolize the dyes into toxic intermediates, which can harm not only the fish and the aquatic organisms themselves but also their predators.[11]

In humans, the dye toxicity is known to cause multiple health diseases, ranging from skin inflammation to central nervous system disorders.[11] It can cause chronic illnesses like skin and eye allergies, burning of the respiratory tract, vomiting, and gastrointestinal infections. The refractory nature of some dyes, like azo dyes, allows them to get retained in systems for a longer period in our eco-life cycle.[60,61] These dyes can lead to skin irritation, allergic reactions, autoimmune diseases, neurobehavioral disorders, and other health problems like nausea and paralysis. They can also lead to severe damages to the reproductive system, liver, kidney, and the brain. For instance, the microflora in the human gut can convert azo dyes into harmful amino acids, which can negatively affect different tissues in the body. Furthermore, some organic synthetic dyes have been reported to induce carcinogenicity on exposure to a higher lethal dose. Therefore, considering the lethal impacts of synthetic dyes on the environment, aquatic ecology, and the human life cycle, it is imperative to design a proper treatment technique for the complete elimination of these contaminants from our ecosystem.

I.2.1.2 Nitrophenolic compounds

The presence of NPCs in wastewater effluents is another problem attracting global concern. A NPC contains at least one nitro group (-NO_2), a hydroxyl group (-OH) and a benzene ring in its chemical structure.[12] Some chemical structures of NPCs are presented in Fig. I.6. NPCs are used as intermediates in the manufacturing of pesticides, insecticides, fungicides, herbicides, pharmaceuticals, and dyes to darken leather.[13] They are also extensively used in explosives.[62] NPCs are constantly released into the environment owing to their diverse applications, via means such as agricultural runoff, industrial waste, and improper wastewaters disposal practices. When these chemicals enter the water, they can undergo transformations into other substances that might be even more detrimental than the original compounds.[63] This transformation can occur due to their interaction with physical, chemical, biological, or microbial elements in the water. NPCs possess more weight than water, causing them to sediment at the bottom of rivers. They also have a low dilution rate and remain toxic even after being diluted.

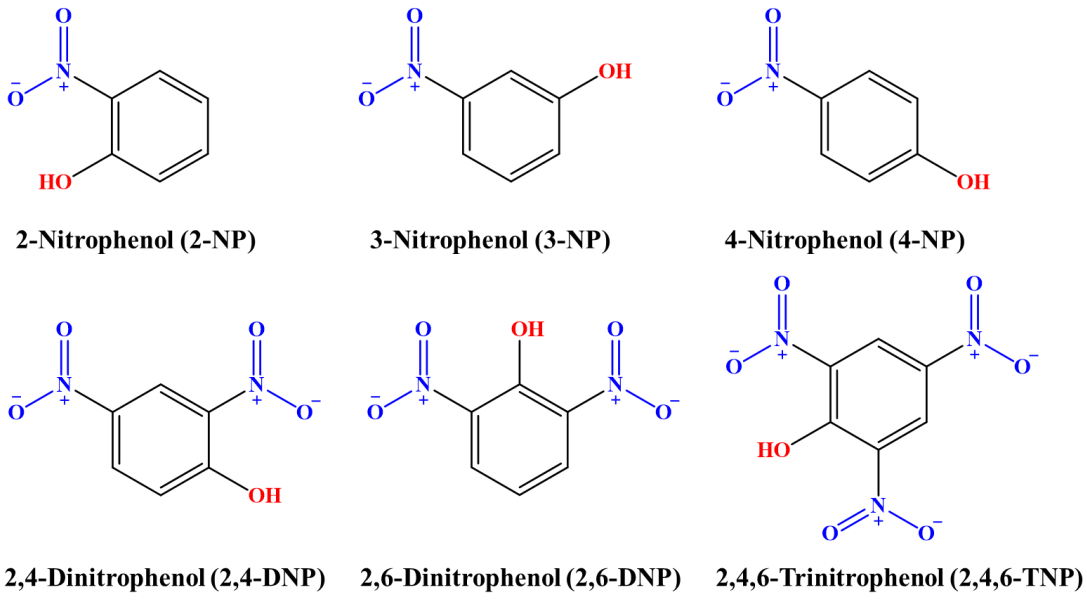

Figure I. 6. Chemical structure of different NPCs.

Numerous studies have shown that NPCs can have harmful impacts on human beings. The immediate effects of NPCs can include eye irritation, skin inflammation, drowsiness, nausea, headaches, cyanosis, and cataracts.[64] Negative effects on the nervous system can cause abdominal pain, diarrhea, weakness, vomiting, convulsions, and even death. Continuous exposures to NPCs can cause coughing, difficulty of breathing, and bronchitis. Researches have also shown that NPCs can reduce ATP production, lead to mutations, and cause renal failure.[64] NPCs can react with hemoglobin in the blood to produce methemoglobin, leading to blood disorders and a decrease in the capacity of red blood cells to transport oxygen to various tissues and organs. Among various NPCs, 2-nitrophenol (2-NP), 4-nitrophenol (4-NP), and 2,4-dinitrophenol (2,4-DNP) have been classified by the United States Environmental Protection Agency (US EPA) as “priority pollutants” because of their toxicity and hazardous diseases

like cancer.[65] In light of growing concerns about the potential harm and adverse impact on the environmental caused by 4-NP, Loos et al.[66] conducted an analysis of some polar organic persistent and toxic contaminants in 122 water samples from 27 rivers in Europe. Their findings revealed that 4-NP is the most widespread river pollutant, present in 97% of water samples at a concentration level of 3471 ng/L (Fig. I.7). Although, the European Commission's Environmental Quality Standards Directive in 2006 set the maximum limit concentration for 4-NP in nearby industrial and urban surface water to be less than 10 ng/L.

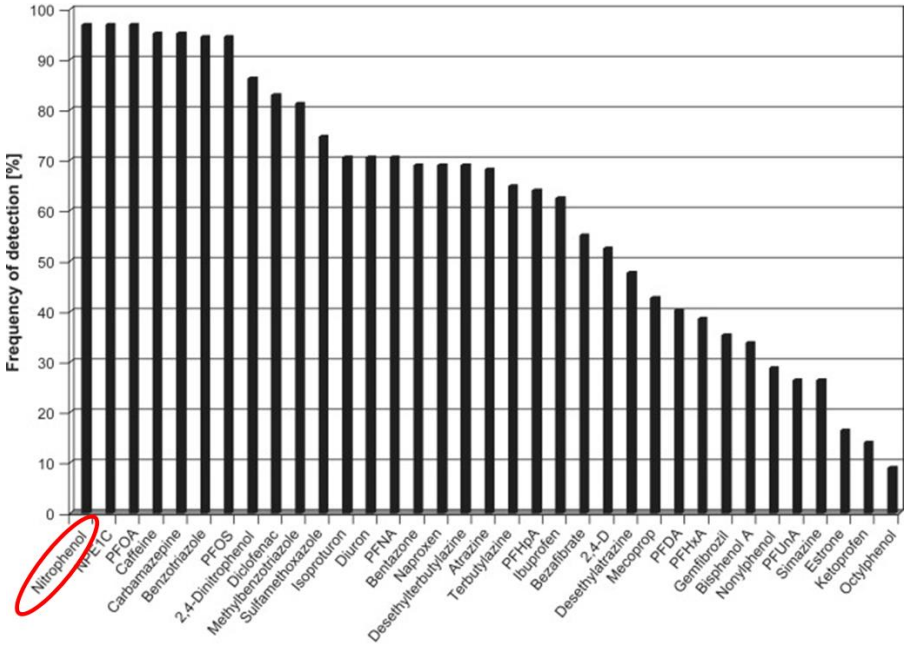

Figure I. 7. Frequency of detection of 4-nitrophenol in natural waters.[66]

Hence, strict regulations governing the discharge of wastewater into the water system have already been imposed by the governments of many countries in order to reduce environmental pollution. However, at present, manufacturers and government officials are seeking innovative solutions to reduce the problem in an efficient way. Therefore, research concerning the possibility of treating wastewater containing organic pollutants is crucial.

I.3 Limitations of current wastewater treatments

Over the past few years, numerous methods have been developed to seek an economical and efficient way for treating wastewater containing refractory organic pollutants, including physicochemical, biological and chemical treatment processes. Physicochemical treatment methodologies comprise filtration, sedimentation, coagulation-flocculation, adsorption, and membrane separation.[67] Whereas biological methodologies include aerobic-anaerobic digestion, activated sludge treatment, aerated lagoon, and pond stabilization.[68] Chemical procedures include pH treatment, and conventional oxidation and reduction methods.[69] Apart from these processes, some advanced oxidation methods like ozonation, UV/ozone catalysis, photo-Fenton, UV/ozone/hydrogen peroxide assisted oxidation,

electrochemical oxidation, etc.[67,70] are also commonly used for the remediation of wastewater containing organic contaminants. Fig. I.8 below shows a pictorial representation of these methods used for wastewater treatment.

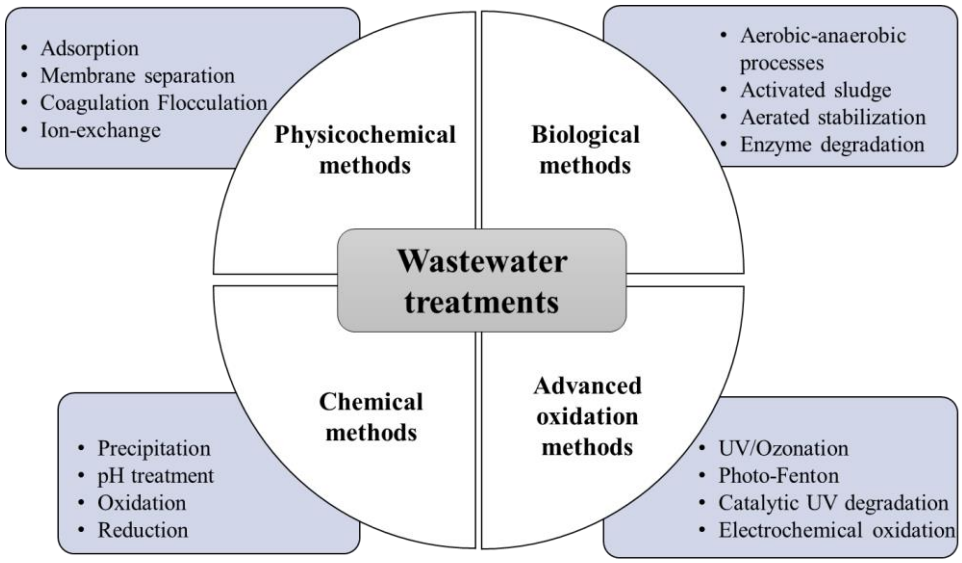

Figure I. 8. Various treatment methods for wastewater.[15]

It is important to comprehend the limitations of the above-mentioned methods to gain insight into why there is a necessity for the use of new techniques such as nanotechnology and photocatalysis for wastewater treatment. Some of the drawbacks of these methods include low removal efficiency, the generation of toxic sludge, high energy consumption, the inability to neutralize recalcitrant organic contaminants, and so on.

I.3.1 Physicochemical methods

Adsorption

Adsorption is the accumulation of substances on a solid surface as a result of Van der Waals forces. This is a physical process, whereas when the same thing occurs due to a chemical bond, it is called chemisorption. The efficiency of organic pollutants removal through adsorption is influenced by numerous factors including pH level, pollutants concentration, temperature, the size of adsorbent particles, time of contact, and characteristics of both the adsorbents and pollutants. Activated carbon is the most extensively applied adsorbent for removing organic pollutant, with its performance depending on the type of carbon and wastewater characteristics.[70] Due to its powdered nature, activated carbon has a high surface area, thereby exhibiting excellent adsorption capacity. Still, the operating cost of activated carbon is too high and its granular form can only retain its adsorption capacity for a limited time before the adsorption sites are filled with pollutants.[70] In addition, once activated carbon has been used to its full capacity, it must either be regenerated or incinerated to transform the pollutants that has been adsorbed into harmless substances. Nevertheless, during the process of chemical regeneration,

compounds that were previously adsorbed by activated carbon are released into the regenerating medium and ultimately end up being disposed of into the environment. Alternatively, incineration releases carbon dioxide into the air, which can contribute to global warming and have an adverse effects on the environment.

Membrane separation

Membrane separation processes are becoming more popular for treating both municipal and industrial waste due to their flexibility and adaptability. Membrane processes can be classified into four distinct categories based on the size of the membrane's pores: microfiltration (MF), ultrafiltration (UF), nanofiltration (NF), and reverse osmosis (RO).[70] MF employs a membrane with pores ranging in size from 0.1 to 10 μm, while separations above 10 μm are considered conventional filtration using filters. Separation is facilitated by two primary transfer mechanisms: sieving and adsorption. MF membranes can only clarify larger solid particles. UF employs a permeable membrane with pores ranging in size from 0.01 to 0.1 μm to separate suspended solids and macromolecules from contaminated solutions. NF whose aperture is only about 0.1-10 nm, can remove macromolecules and particles, but it cannot completely remove pollutants such as organic dyes and NPCs. The RO process uses a semi-permeable membrane to remove contaminants while allowing purified fluid to pass through under pressure. RO membranes can retain at least 90% of most organic compounds and produce a high-quality permeate. RO can be utilized to remove colorants and chemical pollutants, such as those found in dye-containing wastewater. However, the major drawback of membrane processes is their susceptibility to fouling, which requires frequent cleaning with chemicals or aeration. This can result in high energy consumption and no energy output. Therefore, in membrane separation, the cost of periodic replacement must be taken into account when evaluating its economic viability.

I.3.2 Biological methods

Biological treatment methods are based on the capacity of microorganisms to transform organic molecules into a source of energy, carbon, and other minerals that are essential for their growth. They can be divided into three classifications, namely aerobic, anaerobic, and combined anaerobic/aerobic treatments.[68] For the aerobic treatment, free dissolved oxygen in the wastewater is used by microorganisms to decompose organic constituents, whereas in the anaerobic treatment, organic pollutants are converted to methane and carbon dioxide. When a combined anaerobic/aerobic treatment is used, highly concentrated waste can pass through anaerobic digestion (thereby producing energy in the form of biogas) and further through aerobic treatment for a better reduction of chemical oxygen demand (COD). For instance, in the remediation of dye-containing wastewater, the anaerobic component is responsible for eliminating the dyes (e.g., azo dyes) through reductive cleavage, while the aerobic treatment proceeds with the degradation of dye residual products such as aromatic amines. However, the utilization of biological treatments is frequently limited by technical constraints. These

treatments often require large land areas and are sensitive to diurnal variations and the toxicity of certain organic pollutants to the microorganisms used. They also show less flexibility in terms of design and operation.[70] In addition, conventional biodegradation processes are incapable of achieving complete organic elimination.[70] Although some organic pollutants can be degraded by such processes, many others are resistant to biodegradation because of their synthetic origin and complex chemical structure. Another major limitation of biological treatments is their slow degradation rate.

I.3.3 Conventional chemical methods

pH treatment, oxidation, and reduction are the major conventional chemical treatment methods used to treat organic pollutants in wastewater effluent.[69,71,72] Neutralization of the highly acidic or basic pH of the effluent with opposite counter ions causes charge neutralization or precipitation of effluent moieties, which can be further removed using a simple filtration operation. Oxidation using common chemical oxidants such as chlorine (Cl_2), hydrogen peroxide (H_2O_2), potassium permanganate ($KMnO_4$), peracetic acid (CH_3CO_3H), and oxygen (O_2) causes chemical degradation of dyes and NPCs in wastewater, resulting in a decrease in its chemical oxygen demand (COD) and biological oxygen demand (BOD). Nevertheless, the oxidation potential of these chemicals is limited, resulting in incomplete oxidation of pollutants. Further treatment is necessary to meet discharge standards and protect the environment. A few reducing agents like ferrous sulfate ($FeSO_4$), sodium hydrosulfite ($Na_2S_2O_4$), and sodium bisulfite ($NaHSO_3$) also cause dye degradation via precipitation of effluent components. Nevertheless, the degradation rates of these processes are too slow, and they are unable to degrade most of the recalcitrant organic pollutants.

I.3.4 Advanced oxidation processes

Advanced oxidation processes (AOPs) are water-based oxidation methods that use highly reactive and very short-lived oxygen-containing radicals like hydroxyl radicals (•OH), hydroperoxyl radicals (HOO•), and superoxide ions ($•O_2^-$) to destroy target organic pollutants through a series of oxidation reactions. Among these oxygen-containing species, •OH is the most reactive and powerful one, with a high reduction potential of 2.80 volts in acidic conditions. This allows •OH to oxidize almost all organic contaminants in wastewater. The goal of AOPs is to completely mineralize the target pollutants, converting them into CO_2 and H_2O, although it is often sufficient to degrade them into biodegradable intermediates. The hydroxyl radical (•OH) is useful due to its low selectivity and high power, which allow it to destroy even pollutants that are resistant to biological treatments. The most frequently used AOPs for treating wastewater are shown in Fig. I.9.

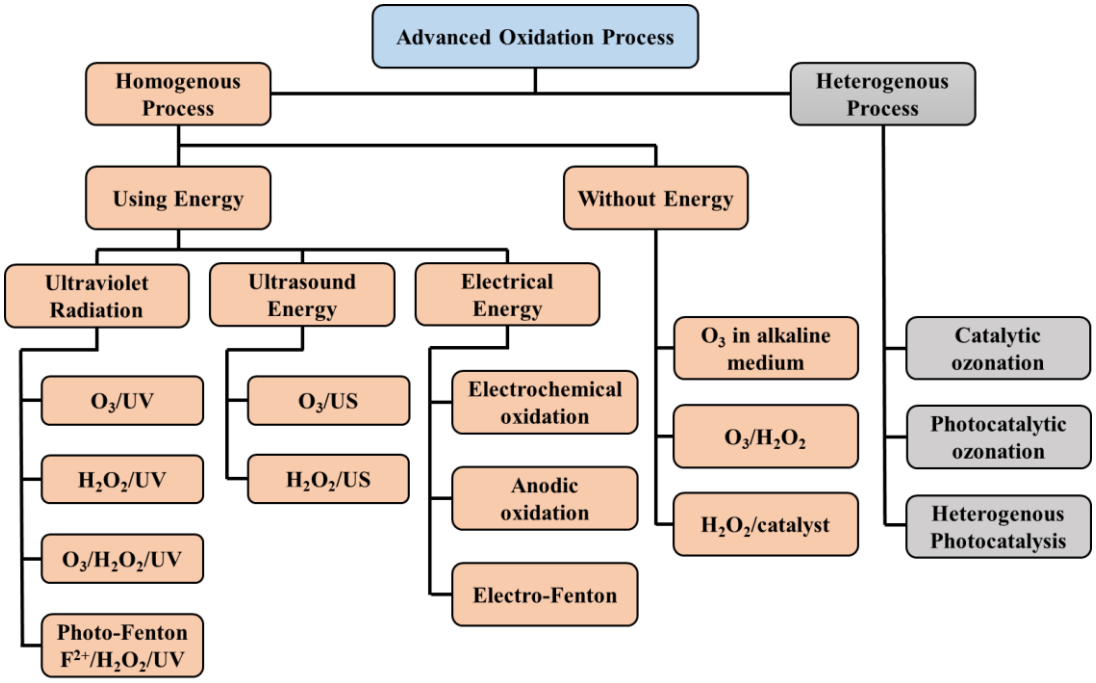

Figure I. 9. Classification of Advanced Oxidation Processes (AOPs).[73]

AOPs can be categorized into two main types: (1) homogeneous AOPs and (2) heterogeneous AOPs. Homogeneous processes can be further divided into two other types: those that necessitate energy input and those that do not need energy input. Most of these processes often involve a mix of ozone (O_3), hydrogen peroxide (H_2O_2), ultraviolet (UV) light, Fenton's reagent (H_2O_2 solution and ferrous iron as a catalyst), ultrasound, or electrolysis. Photocatalysis, where semiconductor photocatalysts are used in conjunction with UV-light to generate the highly reactive oxygen-containing radicals for oxidizing organic pollutants, is also a common method. Despite their advantages, AOPs have several limitations.[74] For instance, the primary disadvantages of the O_3/UV system include the low solubility of O_3 in water, the production of dangerous by-products, such as bromate (BrO_3^-), and high energy consumption. In H_2O_2/UV processes, using corrosive fuels like H_2O_2 may be harmful to humans and aquatic life. While in photo-Fenton oxidation, the main practical restrictions are that the process occurs in an acid medium, at a pH value of about 3, and necessitates the removal of iron. The UV light used in this process adds to the overall cost. On the other hand, using electrochemical oxidation in wastewater treatment is not cost-effective owing to its high energy demand. In addition, the electrochemical performance can be significantly reduced and energy consumption increased due to anode passivation and sludge deposition on the electrodes. Among all AOP technologies, photocatalysis is the most particularly attractive because of its ability to generate powerful reactive radicals using photon energy without the need for additional chemicals. The mild operation conditions and use of inexpensive and chemically stable semiconductor photocatalysts make it an attractive option for complete mineralization of organic pollutants. However, the widespread adoption of this technology is challenging due to the low photonic yield and low efficiency of currently used photocatalysts under visible light. Therefore, there is a pressing need to develop efficient and cost-effective strategies for the total elimination of

organic pollutants from wastewater. This might also be accomplished by improving or adapting current technologies.

I.4 Nanotechnology-based wastewater treatment

Nanotechnology, a field that manipulates tools and devices within the size range of 1 and 100 nm, has emerged as a key technology in the 21st century.[75] The term “nano” is derived from the Greek word νᾶνος or the Latin word *nannus*, both of which mean "dwarf" (extremely small). Nanotechnology offers unique opportunities in surface-based science because of the significantly enhanced surface-to-volume ratio of nanoscale materials. These materials possess various novel properties, including higher chemical reactivity, higher specificity, higher capacity, and higher affinity, making them suitable for improving existing wastewater treatment technologies and developing new ones.[76] Nanomaterials are regarded as new functional materials in the environmental science and engineering field, capable of efficiently removing organic pollutants from various wastewaters in large-scale applications using small dosages.[77] Furthermore, many researchers believe that nanotechnology can provide cost-effective solutions for eliminating organic pollutants.

I.4.1 Nanomaterials

Nanoscale materials are defined as substances that possess at least one dimension measuring less than 100 nm. At this scale, they exhibit novel properties such as optical, electrical, magnetic, catalytic, and others.[78] These emerging features of nanomaterials have the potential for significant impacts on various aspects of our lives. While materials at the micrometer scale show similar physicochemical properties to those of their bulk counterparts, materials at the nanometer scale may show physicochemical properties that are very different. The change in behavior of materials at the nanoscale is primarily attributed to two factors: the increase in relative surface area and the prevalence of quantum effects.[79] These later are crucial in defining the characteristics and properties of materials at this scale.

Nanomaterials can be classified based on their dimensionality, state, chemical composition and morphology.[80] The classification based on nanomaterials dimensionality and shape divides them into 4 categories:

- **Zero-dimensional (0D) nanomaterials:** all of the nanomaterials dimensions are at the nanoscale, measuring less than 100 nm. Examples are quantum dots, fullerenes, nanoparticles, and core-shell.[81]
- **One-dimensional (1D) nanomaterials:** two of the nanomaterials dimensions are at the nanoscale, while one dimension is not at the nanoscale. 1D nanomaterials includes nanotubes, nanorods, nanofibers, and nanowires.[82]

- **Two-dimensional (2D) nanomaterials:** only one dimension of the nanomaterials falls within the nanoscale while the other two are not. Examples are nanosheets, nanofilms, nanolayers, and nanoplates.[83]
- **Three-dimensional (3D) nanomaterials:** contain diverse dimensions beyond 100 nm. This class combines multiple nanocrystals arranged in different orientations. 3D nanomaterials includes nanoballs, nanopillars, nanocones, and nanoflowers.[84]

Fig. I.10 displays a selection of nanomaterials for each dimension.

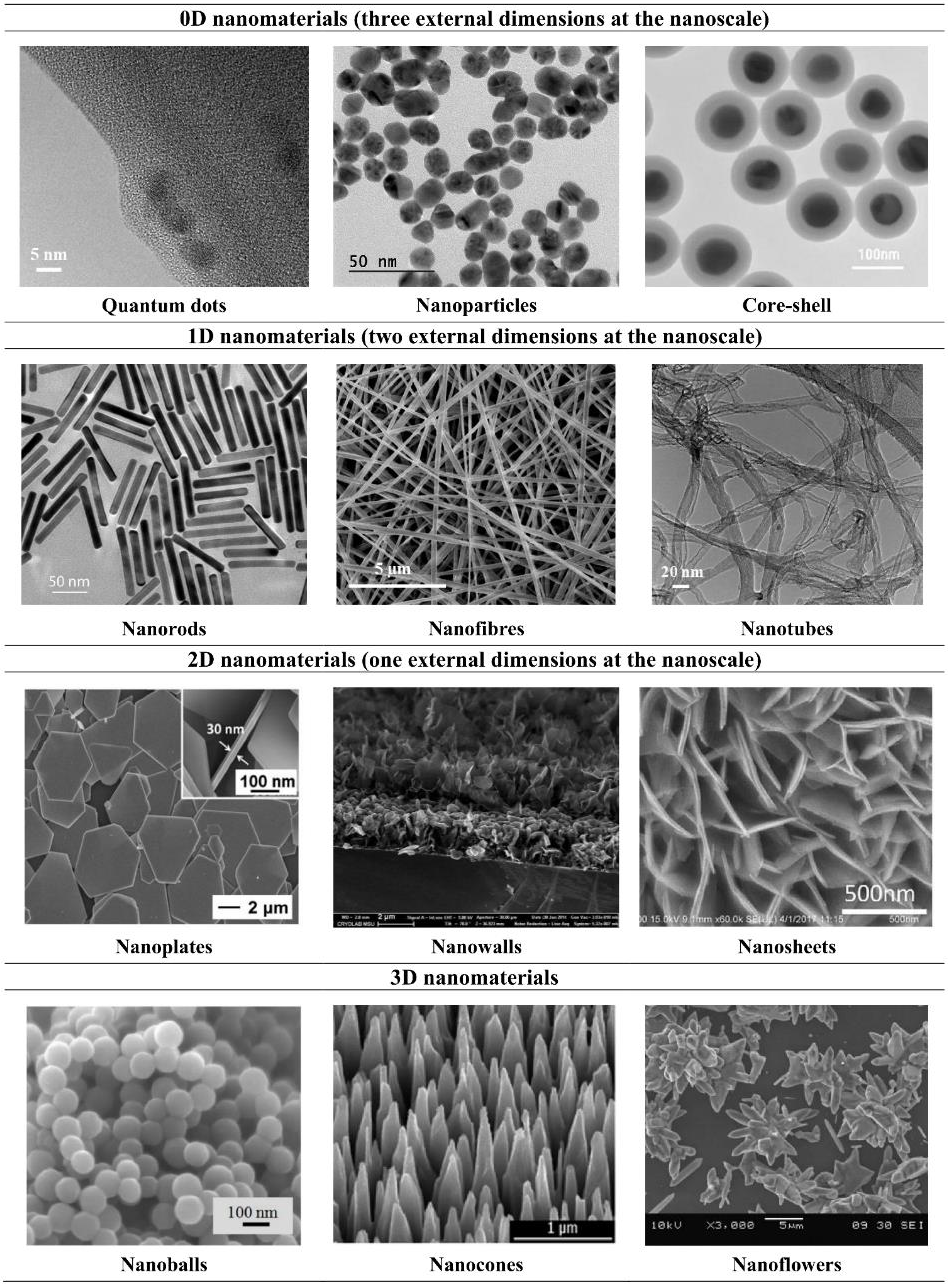

Figure I. 10. Nanomaterials classification based on dimension. 0D: Quantum dots[85], nanoparticles[86], core-shell[87]. 1D: Nanorods[88], nanofibers[89], nanotubes[90], 2D: Nanoplates[91], nanowalls[92], nanosheet[93]. 3D: Nanoballs[94], nanocones[95], nanoflowers[96].

I.4.2 Metal nanoparticles

Metal nanoparticles (NPs) have gained increasing popularity in the field of wastewater treatment due to their exceptional ability to remove various pollutants in a cost-effective manner. Metal NPs are zero-dimensional (0D) nanomaterials that are purely made of metal precursors and have distinct properties. Various types of metal NPs, including gold (Au), silver (Ag), copper (Cu), platinum (Pt), cobalt (Co), nickel (Ni), and others, have been employed as nanocatalysts to improve the quality of the effluents.[97] Metal NPs can be highly effective in treating wastewater because they do not require significant infrastructure, are generally affordable (except for Au) and are easy to operate. Metal NPs for water treatment have been used in laboratory-scale tests with great success.[98] Metal NPs can catalyze the elimination of toxic organic contaminants in various wastewaters, that are otherwise difficult to eliminate.[99] Their distinctive properties, including their diminutive size, high surface area, and reactivity, provide them with this advantage. The substantial surface-area-to-volume ratio of metal NPs is a crucial factor because it provides more active sites for catalysis. Additionally, some metal NPs can be used multiple times, which is a significant sustainability advantage.[99] Among all metal NPs, Ag NPs are the most thoroughly researched because of their significant technical applications.[19,100] Ag NPs exhibit properties commonly associated with their noble metal characters, such as high conductivity, robust chemical activity and stability, along with other properties that can be tailored by controlling the shape, size, and size distribution of the Ag NPs at a reasonable formation cost.[101,102] As a result, there is a growing interest in developing innovative methods to produce tailored Ag NPs.

I.4.3 Properties of metal nanoparticles

Metal NPs have attracted exceptional scientific attention as they exhibit many distinctive properties that differ from their bulk counterparts. As a the size of a material is decreased from the micrometer scale down to the nanometer scale, its physicochemical properties undergo dramatic changes due to the size-induced metal-insulator transition, also known as the quantum confinement effect.[103] The decrease in size results in a greater percentage of atoms on the material's surface, leading to a notable increase in its surface area. This substantially improves the material’s surface-related properties, particularly in terms of catalytic, optical, electronic, and magnetic properties.[104]

The changes in chemical reactivity and properties of metal NPs owing to their size can be explained via several interconnected mechanisms:

- **Reduction of size**: as the dimensions of NPs reduces, the proportion of atoms on or near the surface rises considerably, resulting in a more reactive surface.
- **Changes in the surface free energy**: the augmentation in the surface reactivity causes a change in the surface free energy relative to particle size, which impacts the chemical reactivity of NPs.

- **Variation of atomic structure**: when the NPs size gets smaller and smaller, defects in the form of changes in vacancies, bond length and angle occur on and near the surface, causing atomic structure variation.
- **Changes in the electronic structure**: as the size of NPs diminish, the electronic structure becomes more distinct and begins to resemble the energy states of small molecules.

I.4.3.1 Quantum size effect

The quantum confinement effect explains the size-dependent properties of metal NPs. This phenomenon can be seen in quantum wells, quantum wires, and quantum dots, which are intermediates structures between bulk semiconductors and individual atoms or molecules.[105] The electrons in these structures are confined in one-, two-, or three-dimensional spaces, respectively. The strength of electron confinement increases with electron energy and follows the order of 1D > 2D > 3D, with quantum wells having the weakest confinement. Unlike bulk semiconductor materials, which have continuous electron energy levels, quantum dots have discrete energy levels. This means that electrons can only occupy certain energy states. Fig. I.11 shows how the electron confinement changes from continuous to discrete, which makes the band gap larger and restricts the mobility of electrons. This is because the transition from a three-dimensional system to a zero-dimensional (e.g., metal NPs) system continuously reduces the density of states and increases the electron confinement strength. Therefore, as the size of metal NPs decreases, their energy band gap increases, leading to a higher energy emission from electron-hole recombination. In practical terms, a metal NPs contains hundreds or thousands of atoms and its trapped electrons have discrete energy levels that replace the quasi-continuous density of states. Changes in electrochemical properties can shed light on how the number of atoms in a lattice influences chemical properties. For example, when the lattice of silver contains a large number of atoms, it reaches the "bulk" potential of 0.799 IV. However, when the atoms number decreases, their potential drops dramatically. The electrochemical potential of a single Ag atom is determined to be −1.8 IV.[106] For the size range between bulk and atom, the potential is somewhere in between. The reduction potential values for gold and copper also show similar changes, and this pattern is expected for other elements as well.

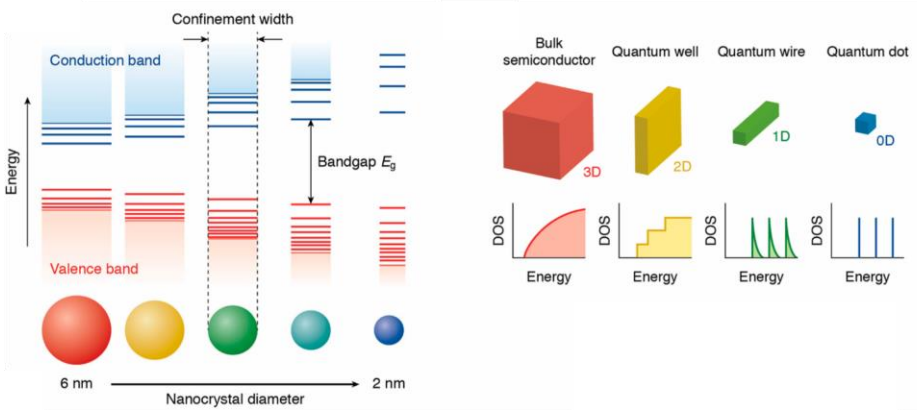

Figure I. 11. Schematic representation of quantum confinement effects.[105]

I.4.3.2 Localized surface plasmon resonance effect

Gustav Mie[107] provided a significant contribution to the theoretical understanding of metal NPs properties. He studied how metal NPs interact with electromagnetic light and attributed the resulting scattering to the collective resonance of conduction electrons in the NPs. This phenomenon is called Surface Plasmon Resonance (SPR) and Mie showed that it is determined by the metal's nature and environment, using Maxwell's classical electromagnetic theory. Mie's theory states that the SPR is a resonant oscillation of charges at the boundary between a metal and a dielectric layer. This occurs when the frequency of the photons matches the inherent frequency of the metal surface electrons oscillating against their positive nuclei's restoring force. Jones and co-workers[108] proposed a simpler explication of the SPR effect by comparing it to a mechanical oscillator. In this comparison, the displacement of a simple harmonic oscillator away from its stable position leads to a constant sinusoidal motion. When an external periodic force with the same frequency is applied to the system, it meets the resonance conditions and can amplify the amplitude of the harmonic oscillator. Correspondingly, when plasmonic materials are exposed to electromagnetic light, the light enhances the displacement of the electron cloud (delocalized electrons) in the conduction band. This creates strong attraction forces between the delocalized electrons and the nuclei of the plasmonic material that are opposed to this displacement. Plasmon resonance occurs when the balance between these two opposing phenomena results in the collective oscillation of the delocalized electron cloud.

For a metal NP that is significantly smaller than the wavelength of light, its electrons collective oscillation is known as the localized surface plasmon resonance (LSPR). The frequency of this oscillation depends mainly on the characteristics of the electrons, such as their effective mass and density, as well as on the NP's shape, size, and charge distribution.[109,110] Fig. I.12 illustrates the process of the electron cloud displacement.

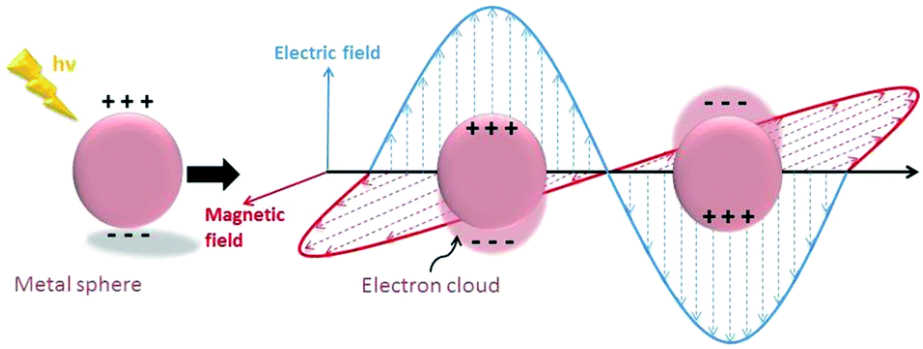

Figure I. 12. Localized Surface Plasmon Resonance effect of metal NPs.[111]

LSPR of metal NPs is influenced by factors such as the metal's dielectric properties, the dispersing medium, the degree of NPs agglomeration, and the shape and size of NPs. While LSPR in most metal NPs occurs in the UV domain of the electromagnetic spectrum, it shifts towards the visible region in a few metals such Au, Ag, and Cu.[112] For example, spherical Au NPs exhibit LSPR between 520 and

550 nm, corresponding to a violet color in the visible domain. Spherical Ag NPs have LSPR at around 380-420 nm, corresponding to a yellow color in the visible region. While, for spherical Cu NPs, the LSPR appears at around 575-600 nm, corresponding to a red wine color in the visible light spectrum. The absorption spectra of colloidal solutions of gold, silver, and copper, depicting the LSPR peak of small-sized and spherical NPs, are illustrated in Fig. I.13.

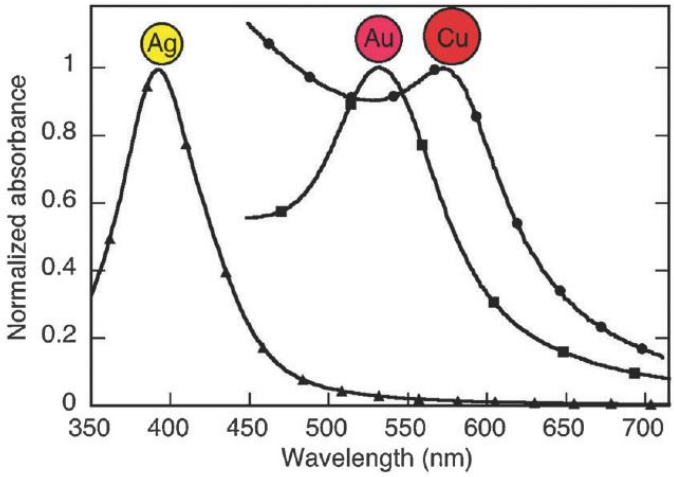

Figure I. 13. Localized surface plasmon absorption bands for Au, Ag and Cu NPs.[112]

Furthermore, according to Mie's theory,[107] ultrasmall spherical metal NPs can show only one LSPR band, while anisotropic NPs can show two or three LSPR bands, depending on their shape. When the size of colloidal metal NPs are larger, their absorption spectra can show wide or extra LSPR bands in the UV-Vis domain because of the plasma resonances, quadrupoles, or higher multipole plasmon excitation.

An overview of the LSPR effect is highlighted below.

(i) When electromagnetic light interacts with the electron cloud in metal NPs, it involves absorption and scattering processes. Absorption is more significant for smaller particles, while scattering becomes dominant for larger particles.

(ii) When small metal particles interact with electromagnetic light, the electron cloud is displaced to create a dipole charge distribution. As the particle size increases, there is a non-uniformity that results in a higher multipolar charge distribution.

(iii) The interaction of electromagnetic light with metal NPs leads to two types of electronic transitions. Inter-band transitions arise from the filled to the vacant bulk bands. The energy necessary for this transition typically lies within the UV zone of the electromagnetic spectrum. Intra-band transitions take place owing to an electronic transition at the Fermi level in partially occupied bands or when an energy overlap occurs between an occupied band and an empty one. The energy needed for this transition typically lies within the visible and near-infrared spectrums. This means that intra-band transitions result in the creation of free electrons.

(iv) At ambient temperature, the average distance traveled by free electrons is typically in the order of a few nanometers. This indicates that in very small nanoparticles, a free electron can easily travel from the particle bulk to its surface. As a result, electrons are effectively be dispersed across the surface of metal NPs.

I.4.4 Synthesis methods of metal nanoparticles

The preparation of metal NPs can be achieved through two main approaches (Fig. I.14). These two approaches are 'Top-down' and 'Bottom-up'.[113] The former method involves breaking down a solid into smaller particles, while the latter essentially refers to building metal NPs starting from atoms in gas or liquid form based on molecular condensations or atomic transformations.

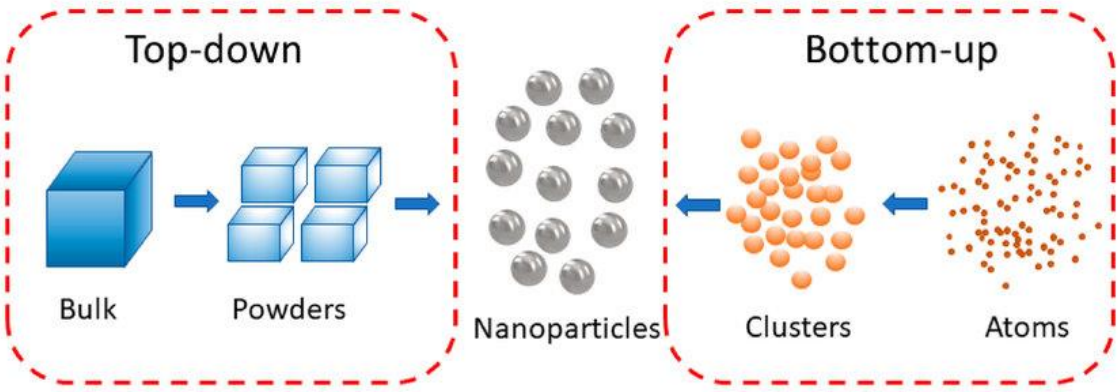

Figure I. 14. Formation of NPs using top-down and bottom-up methods.[114]

Numerous methods for the preparation of metal NPs have been developed over the last few years. In order for a method to be considered successful, it must meet certain criteria, including control over size, shape, and crystal structure. Additionally, it should permit a low aggregation rate, minimize impurities, as well as allow for cost-effective scaling up and reproducibility. In a top-down approach, bulk materials are fragmented into ultrasmall and nanosized particles through various physical and chemical processes. This includes techniques such as thermal decomposition, mechanical techniques (e.g., milling), and laser ablation (Fig. I.15). While top-down techniques are relatively simple to execute, they are not suitable for the synthesis of particles with irregular shapes or extremely small sizes. One major issue with these methods is that they can alter the surface chemistry and physicochemical properties of the metal NPs. In contrast, the bottom-up approach can be divided into two classes: gaseous phase and liquid phase methods (Fig. I.15). Gaseous phase methods have the advantage of producing particles with fewer organic impurities than liquid phase methods. However, they demand complex equipment that can be costly and result in lower yields. On the other hand, liquid phase methods are the most common way to produce metal NPs, and there are many different techniques available (Fig. I.15).

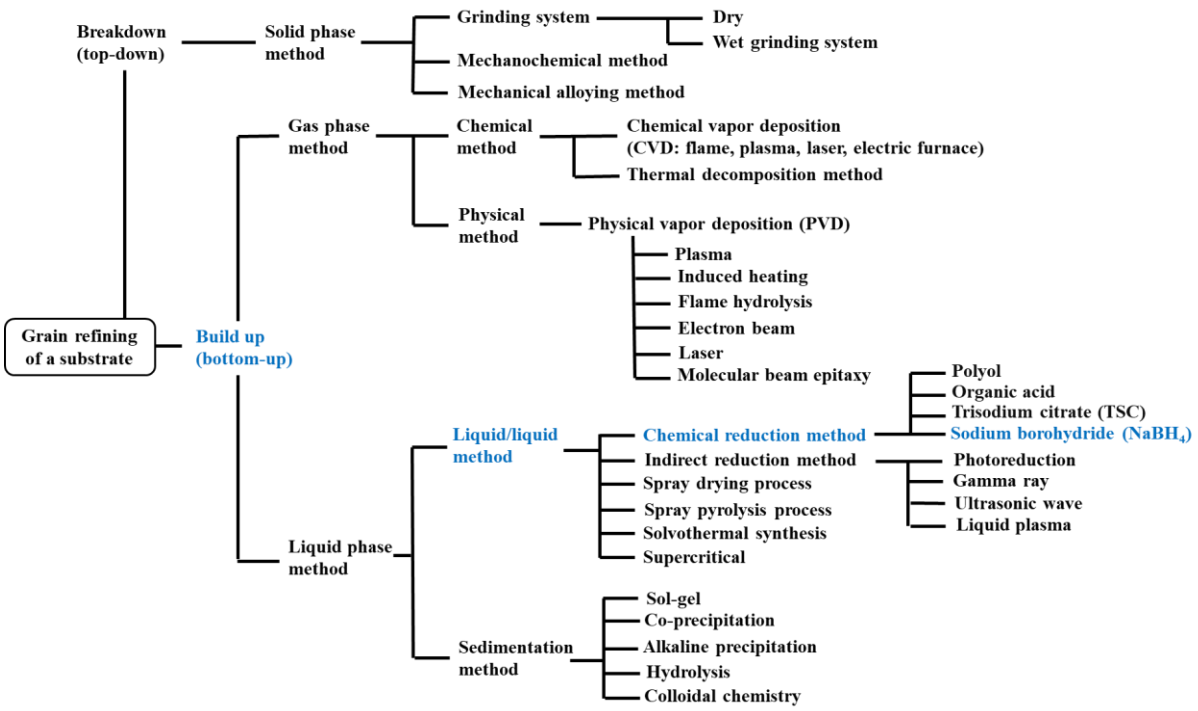

Figure I. 15. Different methods for the preparation of metal NPs.[113]

Synthesizing metal NPs using bottom-up approaches offers several advantages over top-down approaches. These methods have the potential to optimize the synthesis process of metal NPs, making it faster, more cost-effective, and environmentally friendly. Given these benefits, this thesis work focused on bottom-up techniques for synthesizing metal NPs in liquid phases, specifically using the wet chemical reduction method to synthesize Ag NPs. This method is the most commonly applied synthetic procedure for metal NPs in liquid phases.

I.4.4.1 Synthesis of Ag nanoparticles via chemical reduction

Recently, Ag-based NPs catalysts have garnered interest in wastewater treatments, especially in organic pollutants remediation. The use of Ag NPs catalysts has tremendous potential for practical applications owing to their numerous benefits, including ease of preparation, affordability, less toxicity, high chemical reactivity, and good stability.[115,116] As we know, the morphology and size of metal NPs are critical factors in determining their catalytic activity. Therefore, it is essential to carefully control the shape and size of Ag NPs to tailor their catalytic performance.

The most common approach for synthesizing metal NPs in liquid phase involves chemical reduction of metal precursors, typically metal salts that serve as sources of metal ions. This process involves using a reducing agent to convert the metal precursor in solution. Because of the relatively high potential of reduction of Ag^+ to Ag^0 in water (E_0 = +0.799 V)[98] a variety of reductants can be employed, including sodium citrate (E_0 = −0.180 V),[117] sodium borohydride (E_0 = −0.481 V),[98] hydroquinone (E_0 = −0.699 V),[118] hydrazine (E_0 = −0.230 V),[98] ascorbic acid (E_0 = +0.19 V),[98] etc. Sometimes a capping agent such polyvinylpyrrolidone (PVP)[119] is used with the reducing agent to stabilize the formed Ag NPs.

Furthermore, the stability of Ag NPs in dispersion can be assessed by analyzing their LSPR absorbance band. It's well recognized that the UV-Vis absorption band can provide information on the degree of dispersion of metal NPs.[120] Reduction methods offer the ability to control the shape and size of formed metal NPs, which are important characteristics for their catalytic properties. The chemical reduction route offers several advantages, including the ability to easily produce NPs with a wide range of shapes and composition, low levels of impurities, and high yield. Additionally, this approach has the potential for cost-effective large-scale synthesis of NPs, which contributes to its popularity.

(i) Synthesis of Ag NPs using trisodium citrate (TSC)

The first described and one of the most used synthesis route for producing Ag NPs was proposed by Lee and Meisel,[121] which was a modification of Turkevich's recipe for the synthesis of Au NPs.[122] The Türkevich method involves reducing an aqueous solution of Au^{3+} ions ($HAuCl_4$ or $KAuCl_4$) using trisodium citrate ($C_6H_5O_7Na_3$). The citrate anion serves a dual purpose as both a reducing agent and a stabilizing agent. Citrate reduces Au^{3+} to Au^0 and simultaneously stabilize the resulting Au NPs. Since citrate is a relatively weak reducing agent ($E_0 = -0.180$ V), solutions containing Au^{3+} ions are usually heated and often boiled (at around 90 °C). Lee and Meisel,[121] prepared Ag NP in water using the described method. Reduction of Ag ions by trisodium citrate is shown below (Eq. I.1):

$$\mathbf{4Ag^+ + C_6H_5O_7Na_3 + 2H_2O \rightarrow 4Ag^0 + C_6H_5O_7H_3 + 3Na^+ + H^+ + O_2 \uparrow} \qquad (\mathbf{I.1})$$

During the citrate reduction reaction, two very important formation processes are taken into account: the formation of Ag NPs through nucleation and their subsequent growth. In the nucleation stage, a high activation energy is needed for the aggregation of the Ag atoms. This phase involves the reduction of Ag^+ to zero-valent Ag, and the subsequent clustering of Ag^0 atoms to form $(Ag^0)_n$ clusters. This can occur via the reduction mechanism: $nAg^+ \rightarrow nAg^0 \rightarrow (Ag^0)_n$, or through the step-by-step reactions: $Ag^+ \rightarrow Ag^0 \rightarrow Ag^{2+} \rightarrow Ag^{4+} \rightarrow \cdots \rightarrow (Ag^0)_n$. Once the critical size is achieved, the nuclei of NPs will begin to grow.[123] In the growth stage, a low energy of activation is needed for the ordering of newly created Ag NPs. By understanding each reaction step, better control can be accomplished over the shape, size, and size distribution of the prepared NPs. The reduction of Ag^+ ions can be initiated by simply mixing the reactants (Ag ion precursors and TSC) in a round-bottom flask or a beaker. The color of the solution will slowly turns into grayish yellow, indicating that reduction of the Ag^+ ions has started. Parameters such as reactant concentrations, order of reactant additions, reaction time, temperature, pH, surface tension, and viscosity of the solution can be controlled. When the reaction products become supersaturated, spontaneous nucleation occurs and is followed by the growth mechanism.

Pillai and Kamat,[124] stated that due to the slow rate of reduction of the citrate ions, this reactant results in the production of larger-sized Ag NPs with high polydispersity, i.e., once the initial Ag particles are created, the remaining citrate ions bind to the surface of Ag, decreasing the concentration of citrate ions available to further reduce additional Ag^+ ions. This results in fewer new Ag particles being produced,

and the initially formed Ag particles start to grow through a process called Ostwald ripening, where the growth of larger particles occurs at the cost of smaller ones. As a consequence, this reduction method often takes longer time to complete. The whole process is represented in Fig. I.16.

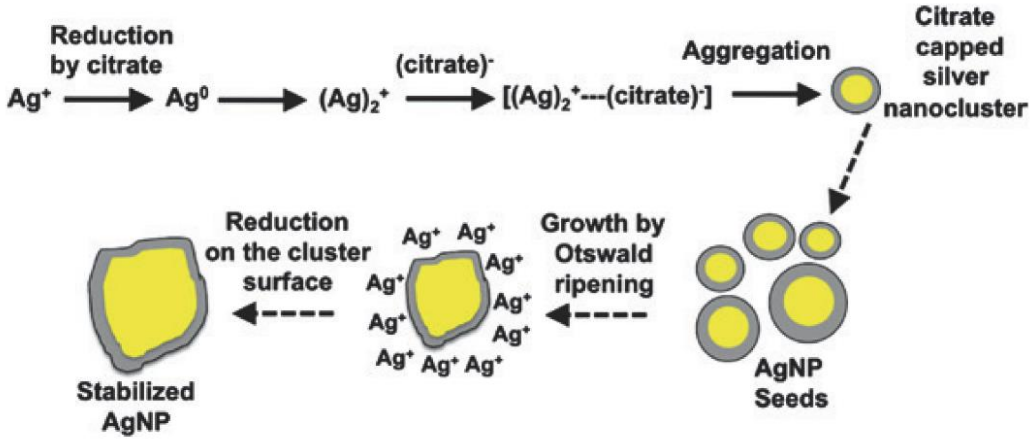

Figure I. 16. Ag NP nucleation and growth mechanisms upon reduction by citrate.[123]

The citrate ions serve as surfactants owing to the presence of a carboxylic moiety in the citrate molecule. They also serve as stabilizing agents, preventing the aggregation of Ag NPs by creating an electrostatic repulsion between the citrate-capped Ag NPs. However, the use of a surfactant can decrease the reactivity of the precursors and slow down the rate of the reduction process. Therefore, alternative reducing agents have been employed instead of TSC, including ascorbic acid,[125] sodium borohydride,[126] hydrogen,[127] hydroquinone,[128] hydrazine hydrate,[129] N,N-Dimethylformamide (DMF),[130] polyethylene glycol,[131] etc. Nevertheless, despite the numerous methods available for synthesizing Ag NPs, only a few provide the ability to control their shapes and sizes. The main limitation to producing monodisperse Ag NPs is the formation of secondary products with different sizes or undesirable shapes. As a result, it is critical to control and set reaction conditions that enable the reproducible production of small-sized Ag NPs with narrow size distributions.

(ii) Synthesis of Ag NPs using sodium borohydride ($NaBH_4$)

The ability of $NaBH_4$ to produce a high concentration of small-sized metal NPs in a very short period of time, which is due to its reduction potential, has garnered significant interest.[126] $NaBH_4$ is a strong reducing agent (E_0 = −0.481 V), thus may offer better control on nucleation and growth of Ag NPs. Small-sized Ag NPs are typically produced through a rapid process in the presence of $NaBH_4$ as reductant and the resulting NPs are generally uniform in size and shape. The first reaction step in the formation of Ag NPs upon reaction with $NaBH_4$ is shown in the following (Eq. I.2):

$$\mathbf{Ag^{+} + BH_4^{-} + 3H_2O \rightarrow Ag^{0} + B(OH)_3 + 3.5H_2} \qquad (\mathbf{I.2})$$

Edwards and his co-workers,[132] used Raman spectroscopy to demonstrate that boric acid $B(OH)_3$ does not act as Brønsted acid in aqueous medium. Instead, it acts as Lewis acid leading to the production of the tetrahydroxyborate anion (Eq. I.3):

$$\mathbf{B(OH)_3 + H_2O \rightarrow B(OH)_4^- + H^+} \qquad (\mathbf{I.3})$$

Then, the overall reaction equation can be expressed as follow (Eq. I.4):

$$\mathbf{Ag^+ + BH_4^- + 4H_2O \rightarrow Ag^0 + B(OH)_4^- + 3.5H_2 + H^+} \qquad (\mathbf{I.4})$$

Shekhar et al.[133] prepared Ag NPs with sizes varying from 25 to 60 nm by mixing different ratios of sodium borohydride and trisodium citrate as reductants. $NaBH_4$ was used to promote rapid nucleation while TSC was used to maintain steady growth. This method allowed the formation of Ag NPs with uniform size and shape. Polte et al.[134] proposed a mechanism for the synthesis of Ag NPs through the reduction of silver perchlorate ($AgClO_4$) by $NaBH_4$, with and without the presence of PVP as stabilizing agent. In the absence of PVP, it was noticed that within the first 100 ms, Ag NPs of about 1 nm were formed and after 400 ms there was a rapid increase in the number of Ag NPs of this size. Over the following 2 s, the size of the Ag particles gradually increased up to 4.6 nm while the number of 1 nm particles decreased. This suggests that smaller particles were merging to form larger particles, resulting in a reduction in the total number of Ag particles in the solution. Similar results were observed in the sample that contained PVP. However, in this reduction process, the 1 nm particles were stabilized for up to 80 min before merging. The formation process for both systems is illustrated in Fig. I.17.

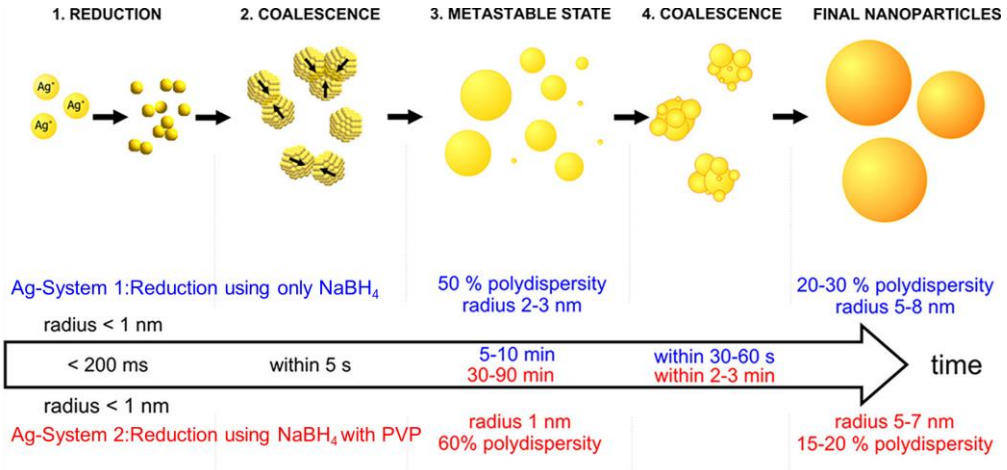

Figure I. 17. Formation mechanism of Ag NPs using $NaBH_4$.[134]

Polte et al.[134] stated that the addition of PVP as a steric stabilizer (Ag-System 2) does not fundamentally change the mechanism of growth. Instead, it just alters the length of each stage. Therefore, the fundamental principle of NPs growth is that the chemical reduction that supplies the monomer must be faster than the actual growth, coalescence (merging), and aggregation of Ag NPs.

Solomon and his colleagues[135] suggested a mechanism for the preparation of Ag NPs based on the reduction and stabilization by $NaBH_4$ without the use of any other agents. The small-sized Ag particles

formation relies on their temporary stabilization via an excess of BH_4^- species. Fig. I.18 shows the stabilized Ag nanoparticles surrounded with a shell of excess borohydride anion. These results indicate that $NaBH_4$ functions not only as a reducing agent but also as an electrostatic stabilizer, delaying the aggregation of Ag NPs.

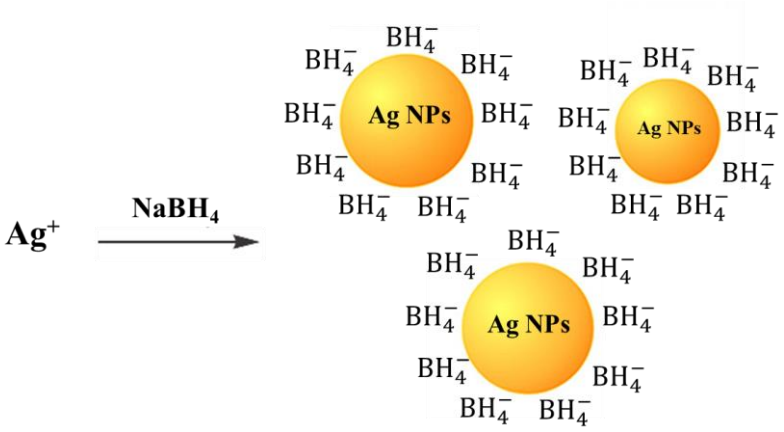

Figure I. 18. Repulsive electrostatic forces of the adsorbed borohydride layer separate Ag NPs.[135]

The adsorption of BH_4^- anion is crucial in stabilizing the growth of Ag NPs by providing a surface charge to these Ag particles (Fig. I.18). As the reaction progresses, there must be sufficient BH_4^- species to keep the Ag NPs stable. However, over time, the protective layer surrounding the Ag NPs breaks down, causing their aggregation. This is mostly due to the degradation of the borohydride anions accompanied by the release of hydrogen gas, as shown in Eq. I.5:

$$\mathbf{BH_4^- + 4H_2O \rightarrow B(OH)_4^- + 4H_2} \qquad (\mathbf{I.5})$$

Even though the adsorbed borohydride creates repulsive electrostatic forces that keep the Ag NPs in suspension, the possibility of "naked" Ag NPs aggregation later in the reaction is inevitable. Fig. I.19 show the change in color of suspended Ag NPs as a function of time. The colloidal Ag solution (A), becomes darker yellow (B), then violet (C), and finally grayish (D). The aggregation tendency of Ag NPs owing to their high surface energy, which subsequently affects their catalytic activity, presents a major issue.

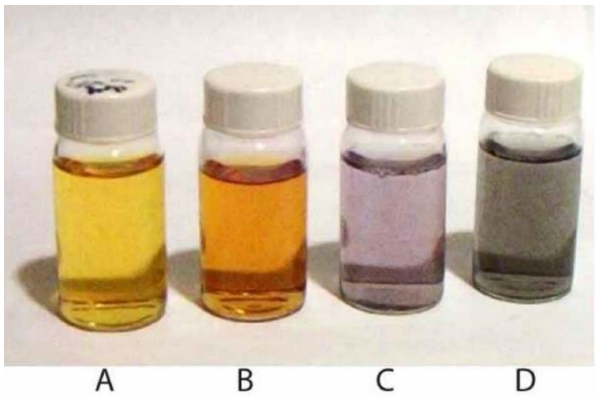

Figure I. 19. Colloidal Ag particles in various stages of aggregation.[135]

Therefore, the most crucial factor to consider when synthesizing Ag NPs in the liquid phase is their stabilization. Stabilizing Ag NPs is essential for their subsequent use in a range of catalytic applications, such as wastewater treatment, and will affect how they interact in the environment. Commonly, the immobilization of Ag NPs on solid supports permits their stabilization. Moreover, supported nanoparticles exhibit higher catalytic activity and selectivity compared to unsupported ones, mainly through synergistic interactions with the support.

I.4.5 Preparation of supported Ag nanoparticles

Nanosized Ag catalysts with large surface areas are used to improve the catalytic performance since the reactions occur on the surface of the particles. However, colloidal "naked" Ag NPs in solution tend to aggregate owing to their high surface energy and strong interactions, which affects their stability and leads to a rapid decline in the activity of the Ag nanocatalyst and poor durability.[136] To surmount this drawback, Ag NPs, are usually supported onto a solid material, which keeps the active Ag nanocatalyst stabilized and dispersed in the reaction medium. This is significant because it enables more efficient and cost-effective use of the valuable Ag catalysts. It also makes it easier to recover and recycle the catalysts and offers greater resistance to poisoning compared to bulk systems. The support material can either work together with the Ag NPs to promote reactions that are mutually and simultaneously beneficial, or can be inert and only serve as a stabilizer to inhibit the aggregation of the immobilized Ag NPs. Thus, choosing the appropriate support material is crucial. However, the solid support usually does not exhibit any catalytic activity on its own. The most commonly used carriers are polymer materials,[137] carbon materials,[138] zeolites,[139] and oxide metal (e.g., alumina (Al_2O_3), silica (SiO_2), titania (TiO_2))[97] to mention a few. Some conventional approaches typically employed for the preparation of supported metal NPs are described in this section.

(i) Impregnation method

Impregnation is one of the earliest techniques utilized to immobilize metal NPs on support materials. In this method, a solution of a metal precursor (e.g., $AgNO_3$, $AgClO_4$, etc.) is mixed with a solid support to obtain a nanocomposite material. Impregnation can be performed using various routes, including incipient wetness impregnation,[140] impregnation by soaking,[141] dry impregnation,[142] co-impregnation,[143] and successive impregnation.[144] Diverse processes take place throughout these procedures at varying rates, including ion exchange between the solvent and the charged surface, selective adsorption of species by van der Waals or Coulomb forces, and others. For instance, incipient wetness impregnation involves "wetting" the solid carrier material with a solution that contains a specific quantity of the metal precursor. The metal is dissolved in a solvent volume that is equal to the support's total pore volume (known as the incipient wetness point), resulting in the formation of a thick paste. The solvent is then evaporated, leaving behind an impregnated support material that can be acquired in an oxidized form or, if needed, can be exposed to a reductant such as sodium borohydride,

sodium citrate or hydrogen gas. Lastly, to activate the surface, the impregnated composite is heated at a high temperature. However, this method has a fundamental drawback as it produces large particles that are not catalytically active due to the presence of inorganic anions on the surface of the solid, which causes sintering upon the thermal activation.[145] Thus, controlling the morphology of the metal NPs using this method is challenging. The supported metal NPs size depends on three key factors: the quantity of metal loaded, the surface area of the support material, and the annealing environment. Smaller particles with better dispersion are produced when there is a low metal loading and a large support surface area. In order to remove unwanted residues, high-heat treatments may be necessary. Nevertheless, this can lead to a significant degree of particle agglomeration, particularly in the case of catalysts with higher metal loadings. The process is demonstrated using a representative example (Fig. I.20).

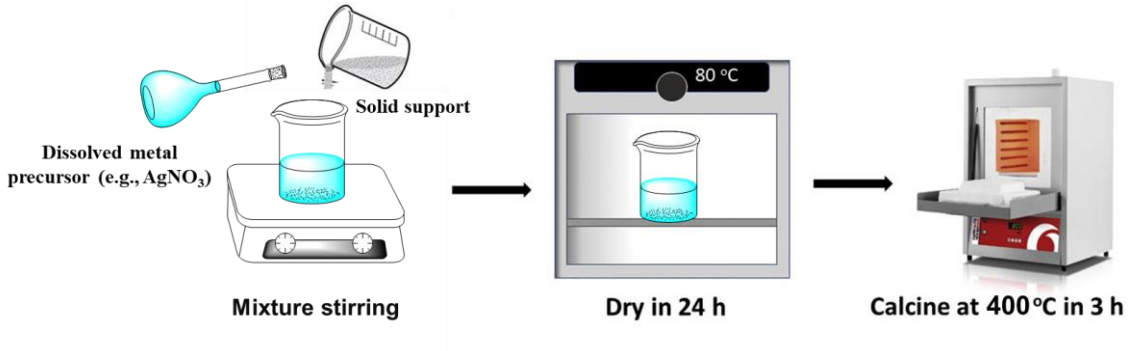

Figure I. 20. Schematic of the impregnation method for synthetizing supported Ag NPs.

(ii) Co-precipitation method

In the co-precipitation process, salts of the active metal and support are dissolved and then mixed together *in situ* to create a combined solid precursor of both materials in a one step.[146] This method can achieve very high amounts of metal loading, even up to 70 wt.% or more, while still keeping particle sizes small. This makes it the most convenient method for forming catalysts with a high ratio of metal weight to volume. By inducing a high degree of supersaturation, this method can generate very small particles even at high loadings, as all components nucleate rapidly and concurrently. Typically, this is accomplished by mixing two concentrated solutions that give rise to an insoluble material. Reagents such as hydroxides (NaOH) or alkali carbonates (e.g., Na_2CO_3 or K_2CO_3) can be used to mix metal chlorides, nitrates, or sulfides, resulting in the production of metal hydroxides or metal carbonates. Because these compounds have low solubility, most of the precursors will precipitate. However, during co-precipitation, it is crucial to avoid local fluctuations caused by factors such as temperature gradients, concentration gradients, or insufficient mixing, as these can lead to additional nucleation processes or different growth patterns resulting in inhomogeneous products. Residual nitrates, sodium, or potassium on the surface must be removed after precipitation and aging because they can cause particle sintering and aggregation during subsequent thermal treatment, which can reduce the surface area of the obtained composite material. Generally, the co-precipitation method provides a strong interaction between the

support material and the metal. Fig. I.21 illustrates a representative example of the co-precipitation method.

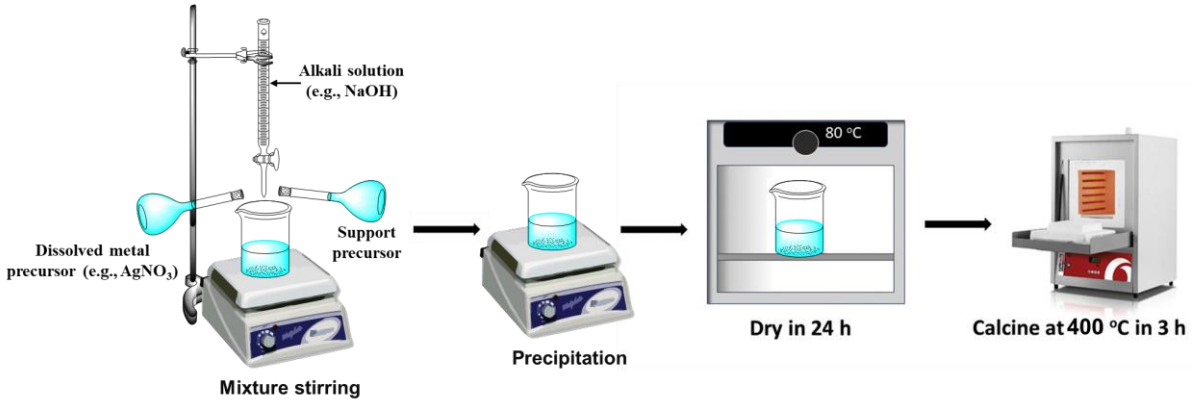

Figure I. 21. Schematic of the co-precipitation route for preparing supported Ag NPs.

(iii) Deposition-precipitation method

Deposition precipitation is similar to co-precipitation because it involves depositing a metal from a precursor solution by changing the pH, temperature, or by evaporation to form a metal compound with low solubility, often in the form of a metal hydroxide.[147] However, in the deposition-precipitation method, the support material already exists and the concentration of the composite is gradually increased to avoid the formation of bulk phases in the solution. Adding a solid support to the solution can result in preferential precipitation on its surface. This is because the support can either decrease the surface free energy of small nuclei or stabilize the precipitate, thus reducing the energy barrier for nucleation. In deposition-precipitation method, the support surface serves as a seed for nucleation and nucleation only takes place on the support material, not in the bulk solution. Changes in pH are usually what prompt metal species nucleation, which leads to the formation of compounds with low solubility. To prevent the precipitation of the bulk compounds, it is crucial to avoid exceeding critical supersaturation levels when introducing the precipitant agent, i.e., the alkaline solution. Therefore, homogeneous deposition-precipitation processes are often favored because they allow for uniform precipitation throughout the reaction vessel. The advantage of deposition-precipitation method over others is that all of the active component stays on the support's surface and none is buried inside the support. This method also results in a narrower particle size distribution. Fig. I.22 shows a representative example for the deposition-precipitation method.

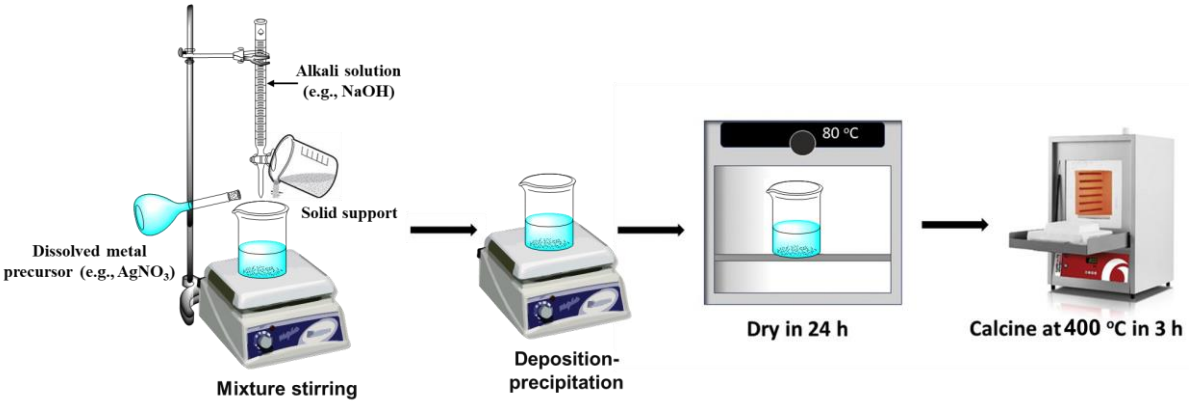

Figure I. 22. Schematic of the deposition-precipitation method for preparing supported Ag NPs.

In the current thesis, we will use a protocol similar to deposition-precipitation. Although we will present a new approach to generate supported Ag NPs. The preparation of self-grown Ag NPs on the surfaces of $AgM_2(PO_4)_3$ (M = Ti or Zr) NASICON phosphates by chemical reduction at room temperature using $NaBH_4$ will be reported for the first time. Our Ag-containing NASICON-type phosphates will act as an Ag-solid precursor. The surface of the NASICON matrix will serve as a nucleating agent, which will permit the synthesis of Ag NPs in a one-pot straightforward self-precipitation/adhesion process in the liquid phase without any further treatment.

I.4.6 Typical examples of Ag-based nanocatalysts used for wastewater treatment

The application of Ag NPs as nanocatalysts for wastewater remediation has been extensively reported due to its remarkable properties and significant catalytic potential. Many recent studies have indicated the catalytic potential of Ag NPs for environmental remediation, such as the reduction of organic dyes and NPCs. $NaBH_4$ is one of the most efficient reducing agents for the catalytic reduction of different kinds of organic contaminants. However, $NaBH_4$ has a lower ability to reduce the target organic species because of the kinetic barrier arising from the difference of potential between the donor (BH_4^-) and the acceptor (organic species). When considering the redox potentials of most dyes and NPCs, and $NaBH_4$, reduction reactions are thermodynamically feasible but kinetically restricted.[148,149] Therefore, it has been shown that the addition of Ag NPs can enhance the reducing ability of BH_4^- by facilitating the electrons transfer from the reductant to the target organic molecule. Since the potential of Ag NPs lays between the redox potentials of BH_4^- anions and the organic molecules, owing to the quantum size effect (see section I.4.3.1), they can serve as an electron relay system.

(i) Silver decorated silica nanoparticles (Ag/SiO_2)

Hu et al.[150] synthesized several spherical-shaped SiO_2 with rough surface by varying the time of formation of silica, from 6, 12, 24, to 48 h. Ag NPs were then added to the surface of the different SiO_2 spheres using a wet-impregnation process. The resulting Ag/SiO_2 composites were employed as catalyst to eliminate organic dyes from contaminated water. The catalytic performance was evaluated by observing the reductive conversion of methylene blue (MB) in the presence of an excess of BH_4^-. The

findings revealed that the Ag/SiO_2-(24h) material had the highest catalytic activity for the MB reduction. According to Hu et al.[150] MB dye was eliminated within 3 min to less than 1% of the starting concentration and the reaction rate constant reached 2.128 min^{-1}. The authors stated that the as-prepared Ag/SiO_2-(24h) nanocomposite can be utilized in different environment with a wide range of pH, and has very good reusability for at least four catalytic reduction cycles.

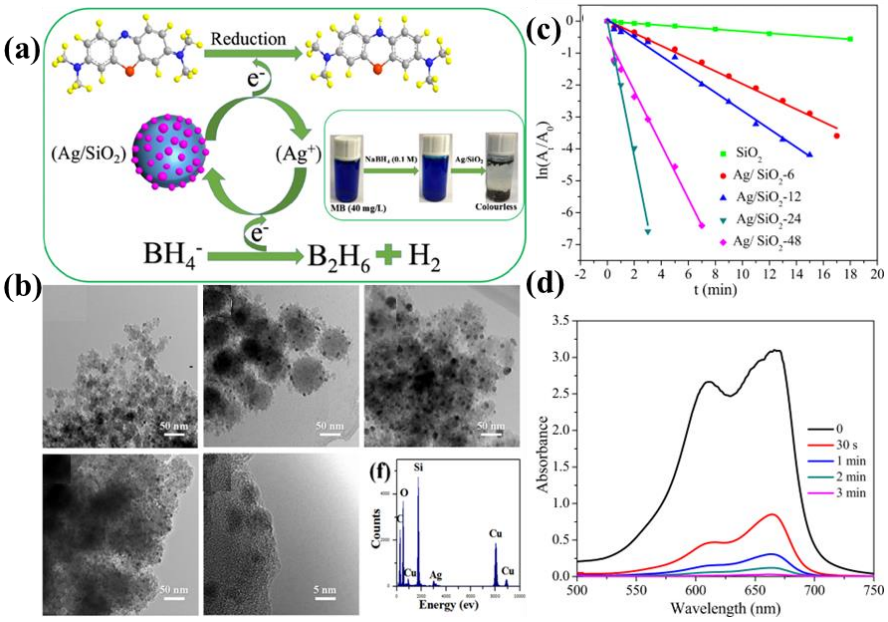

Figure I. 23. (a) Scheme of MB reduction using Ag/SiO_2, (b) morphological images of different synthesized Ag/SiO_2, and elemental analysis of Ag/SiO_2-(48h), (c) ln(C/Co) plot of MB conversion in the presence of Ag/SiO_2 samples, and (d) UV-Vis spectra for MB conversion using Ag/SiO_2-(24h).[150]

(ii) Ag-CeO_2 supported SBA-15

Taratayko et al.[151] prepared silver- and ceria-containing nanocatalysts by impregnating an uncalcined Pluronic P123@SBA-15 hybrid network with solutions of $Ce(NO_3)_3 \cdot 6H_2O$ and $AgNO_3$. Citric acid was added to stabilize the Ag NPs. The resulting nanocomposite had a large surface area and pore sizes with narrow distribution. The SBA-15's uniform porous structure functioned as a nanoreactor, while the properties of the tri-block co-polymer and citric acid helped to stabilize the CeO_2 and Ag particles, which were less than 5 nm in size and highly dispersed. As the active components were jointly loaded, the nanoparticles dispersion increased. The Ag-CeO_2@SBA-15 hybrid system's catalytic properties were evaluated in the reductive transformation of 4-nitrophenol (4-NP) to 4-aminophenol (4-AP) using a solution of $NaBH_4$ as a reductant at ambient temperature (25°C). The synergistic effect, which is due to the creation of the Ag-CeO_2 interface and the cooperation of the active sites of the nanocatalysts, was given special attention. The influence of the interaction and state of the active species on catalytic performance were assessed during the reduction of 4-NP to 4-AP. The prepared nanocomposite catalyst demonstrated excellent activity in reducing 4-NP, with a conversion time of 3 minutes and 27 seconds.

Analysis using gas chromatography indicated that the conversion of 4-NP was complete and that the selectivity towards 4-AP 100%.

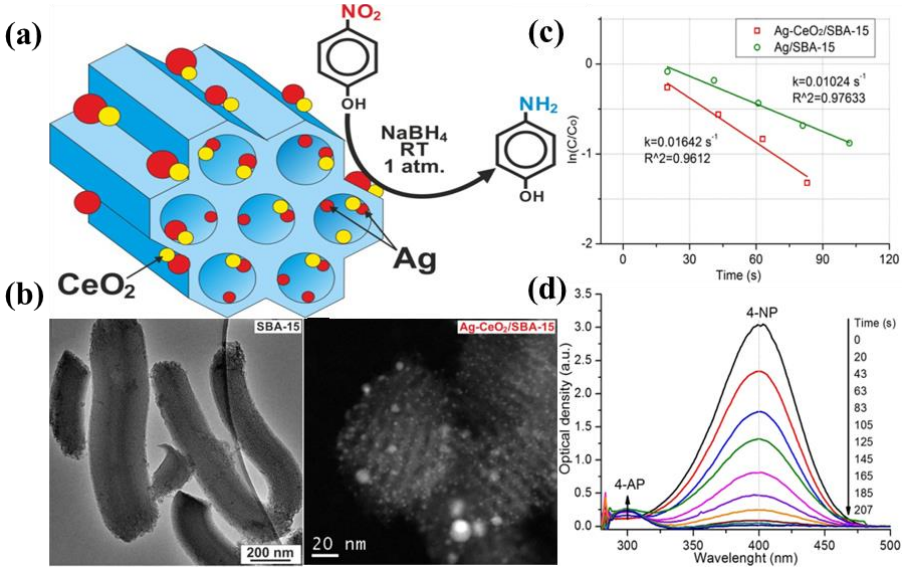

Figure I. 24. (a) Mechanism of 4-NP reduction over Ag-CeO_2/SBA-15, (b) microscope images for SBA-15 and Ag-CeO_2/SBA-15, (c) ln(C/Co) plot of 4-NP reduction as a function of time, and (d) evolution of 4-NP adsorption spectra upon reduction using Ag-CeO_2/SBA-15.[151]

(iii) Ag supported reduced graphene oxide (Ag/rGO)

Dat and his co-workers[152] reported the successful synthesis of Ag supported on reduced graphene oxide (Ag/rGO) by employing a co-precipitation process. They used as precursors $AgNO_3$ and graphene oxide (GO), with ascorbic acid serving as the reductant. The reaction involved two concomitant steps: (i) the homogenous distribution of Ag NPs on the GO sheet surface, (ii) the reduction of GO to its reduced form, resulting in the production of an Ag/rGO nanocomposite. Ag NPs with a size average of 16 ± 3.7 nm were evenly distributed on the surface of rGO, accounting for 67% of the weight of Ag/rGO. The researchers found that Ag/rGO was an effective nanocatalyst for the elimination of MB and methyl orange (MO) aqueous dyes, using $NaBH_4$ as reductant. The reaction efficiency was over 99% for both MB and MO after 30 minutes. However, they noted that the type of dyes may affect the reaction rate and efficiency differently. In their study, the catalytic reduction was faster for the MB compared to the MO. In addition, the Ag/rGO nanocomposite showed very good reusability performance, with a recovery efficiency above 90% even after the fifth recovery during the reduction of MB.

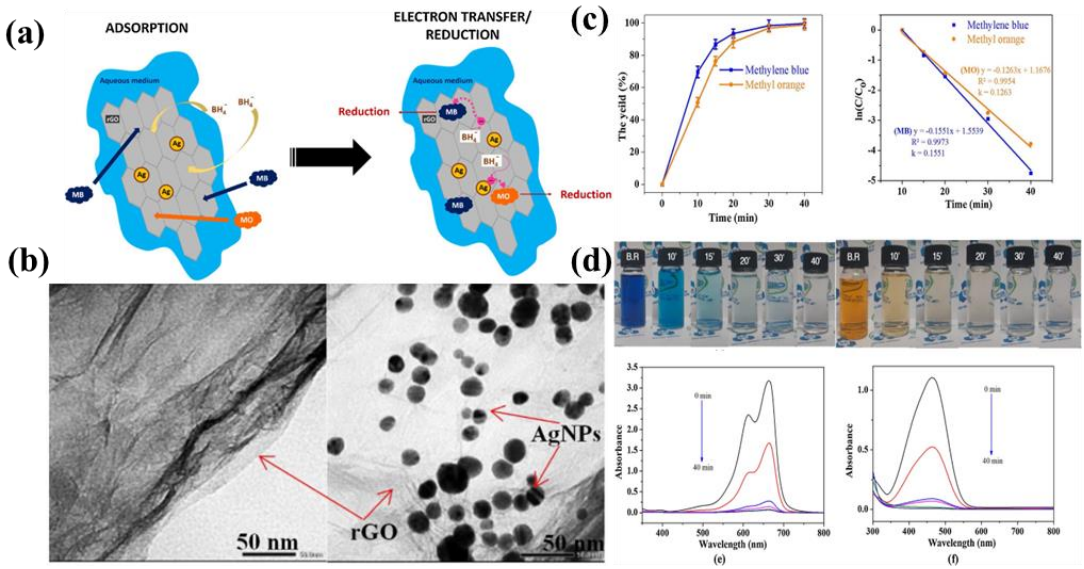

Figure I. 25. (a) Scheme of MB dye reduction over Ag/rGO, (b) micrographs of rGO and Ag/rGO, (c) first-order kinetics plots for the MB and MO reductions, and (d) dye samples color changes as a function of time; UV-Vis spectra of MB and MO reductions as a function of time.[152]

(iv) Ag supported Fe_3O_4@HA magnetic nanocomposites (MNCs)

Amir et al.[153] prepared a new magnetic nanocomposites (MNCs) with the formula Fe_3O_4@HA@Ag by combining the reduction using $NaBH_4$ and the Reflux method. The obtained Fe_3O_4@HA@Ag composites had a spherical shell with a nanostructure size of about 13 nm. Scanning electron microscope (SEM) and transmission electron microscopy (TEM) attested the presence of humic acid (HA) on the surface of Fe_3O_4 with embedded Ag NPs. SEM and TEM micrographs showed that Fe_3O_4@HA@Ag composites were nanosized with had low agglomeration. The main scope of Amir et al.[153] studies, was to investigate the catalytic properties of Fe_3O_4@HA@Ag heterostructure in the decolorization of azo organic compounds such as MB dye. Fe_3O_4@HA@Ag material demonstrated high catalytic performance for the reductive conversion of MB within 20 min in the presence of $NaBH_4$. Moreover, owing to its higher magnetization value of 7.03 emu/g, Fe_3O_4@HA@Ag was utilized as magnetically recoverable catalyst.

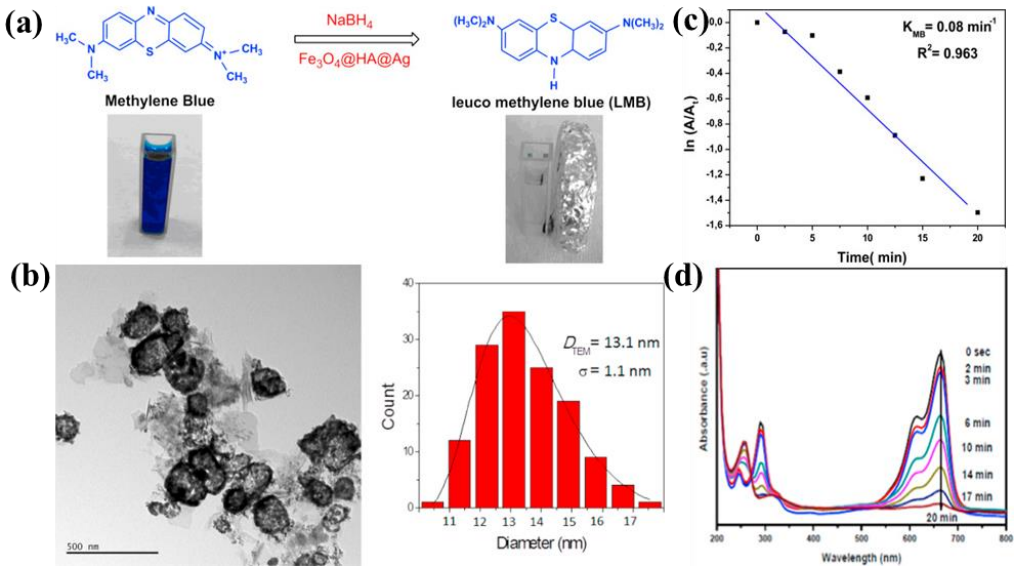

Figure I. 26. (a) Reduction of MB by Fe_3O_4@HA@Ag, (b) micrographs of Fe_3O_4@HA@Ag and nanoparticles size distribution, (c) the pseudo first order kinetic plot of MB vs. time, and (d) UV/vis spectra of MB reduction catalyzed by Fe_3O_4@HA@Ag.[153]

(v) Ag supported ZnO nanorods

Rasaki and his co-workers[154] supported Ag NPs on nanorods of ZnO via a liquid phase precipitation process followed by calcinations. They discovered that the nanorods of ZnO, when used as supports, can effectively inhibit the agglomeration of Ag NPs. The TEM micrographs indicated that the supported Ag NPs were evenly dispersed over the ZnO nanorods' surface. The researchers evaluated the catalytic activity of Ag/ZnO nanocomposite in the transformation of 4-NP into 4-AP at ambient temperature using an excess of sodium borohydride as an electron donor. By adopting the model of Langmuir-Hinshelwood (L-H), they assessed the reaction's kinetics and mechanism and observed that the Ag NPs supported ZnO nanorods exhibited superior catalytic activity in comparison with the free Ag NPs, resulting in a higher conversion rate constant (k_{app}) of $3.97 \times 10^{-3}\ s^{-1}$ of 4-NP. This value was almost double that of free silver NPs ($2.07 \times 10^{-3}\ s^{-1}$). Therefore, they concluded that the strong interaction between Ag NPs and ZnO nanorods significantly improved the rate of electron transfer from $NaBH_4$ to the target organic molecule, leading to the remarkable catalytic activity of the Ag/ZnO nanorods.

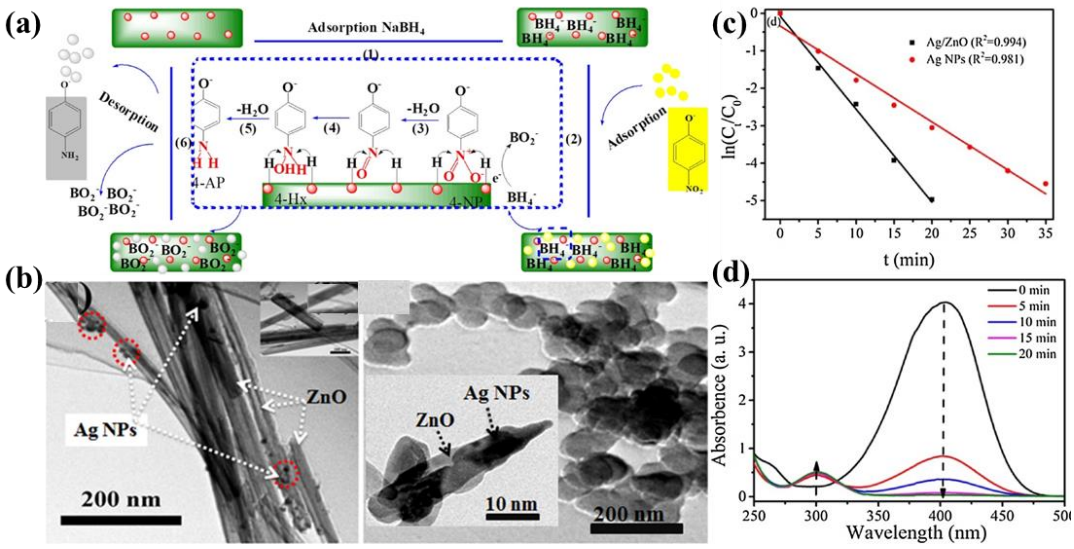

Figure I. 27. (a) Reduction mechanism of 4-NP over Ag/ZnO nanorods, (b) microscope images of Ag supported ZnO nanorods, (c) first order kinetic of 4-NP reduction in the presence of Ag/ZnO, and (d) UV-vis spectra of successive conversion of 4-NP over Ag/ZnO nanorods.[154]

I.5 Photocatalysis-based wastewater treatment

Over the last decades, photocatalysis, an eco-friendly approach based on advanced oxidation processes (AOPs), has gained popularity owing to its potential use in the treatment of environmental pollution.[155] The term "photocatalysis" comes from the Greek words "*phos*" meaning light, and "*katalyo*" meaning to break apart or decompose. In general, photocatalysis refers to a process where light activates a substance known as a photocatalyst, which is often a semiconductor (SC) material, to modify a chemical reaction rate without being consumed in the photocatalytic conversion.[156] The key difference between photocatalytic reactions and conventional catalytic reactions is that light activates the catalyst rather than heat (as is usually the case in thermal catalysis) to reduce the activation energy barrier and facilitate the chemical reactions.[157] In 1972, Fujishima and Honda[158] made the first significant contribution to understanding heterogeneous photocatalytic processes when they discovered that water could be split into hydrogen and oxygen using TiO_2 photoelectrodes. Although their initial focus was on energy-related applications, particularly those involving hydrogen production, their research opened up new frontiers for new possibilities in other areas of photocatalysis. Just four years later, Carey and his colleagues[159] revealed the successful photodecomposition of biphenyl and chloro-biphenyl organic molecules, using TiO_2. Since then, photocatalysis has attracted considerable attention as a means of degrading various chemical pollutants, making it a promising approach for treating wastewater.

This section of the chapter gives an overview of basic principles and current challenges of photocatalysis as well as an introduction to plasmonic Ag NPs and their potential role in plasmonic photocatalysis. These background information are essential for comprehending the research described in this thesis. Subsequently, typical examples of Ag-based photocatalysts used in wastewater treatment are discussed.

I.5.1 Principals of semiconductor photocatalysis

Photocatalysis consists of a series of advanced oxidation processes that are induced by light and involve the generation and reaction of charge carriers (i.e., e^-/h^+ pairs) in a photocatalyst material. A SC, with its specific electronic structure comprising a filled valence band (VB) and an empty conduction band (CB), can serve as a photocatalyst. The energy gap between these two bands is known as the band gap energy (Eg). When exposed to light with energy superior to its band gap, a SC photocatalyst will absorb photons, causing electrons to be excited from the VB to the CB and leaving holes in the VB. Afterwards, these photogenerated e^-/h^+ pairs migrate to the surface, where a significant portion will recombine and release the absorbed energy in the form of heat or light. The remaining e^-/h^+ pairs can participate in chemical reactions, such as reducing oxygen or oxidizing organic compounds.

The perfect process of photocatalysis involves five main stages:

(1) Mass transfer of reactant species from the water to the SC photocatalyst's surface

(2) Adsorption of reactant species onto the SC photocatalyst surface

(3) Activation of the SC via absorption of photons. This stage can be divided into four sub-stages:

(3-i) Photons absorption and excitons generation

(3-ii) Formation of electrons (e^-) in the VB and holes (h^+) in the CB of the SC photocatalyst.

(3-iii) Migration of photogenerated electron-hole pairs to the photocatalyst surface. It have to be noted that at this sub-stage, the e^-/h^+ pairs are likely to undergo recombination, whether in the bulk or on the surface, which is an unfavorable process that hampers the photocatalyst's activity.

(3-iv) Surface oxidations and reductions of adsorbed reactants

(4) Desorption of products and reactants from the SC material surface

(5) Mass transfer from the surface of the SC photocatalyst back into water

In the upcoming discussion, we will take a closer look at step number 3 of the photocatalytic decomposition process. This stage involves the activation of the SC by absorbing a photon with energy equal to or greater than its band gap. This causes the separation of electrons and holes by promoting e^- from the VB to the CB (Eq. I.6).

$$\mathbf{SC + h\upsilon \rightarrow SC(e^-_{CB} + h^+_{VB})} \qquad (\mathbf{I.6})$$

The photogenerated e^-/h^+ pairs participate in oxidations or reductions of adsorbed species at the SC surface (Eq. I.7 to I.10), leading to organic (R) compound decomposition:

$$\mathbf{e^-_{CB} + O_2 \rightarrow O_2^{\bullet -}} \qquad (\mathbf{I.7})$$

$$\mathbf{h^+ + HO^- \rightarrow HO^\bullet} \qquad (\mathbf{I.8})$$

$$R - H + HO^{\bullet} \rightarrow R^{\bullet} + H_2O \qquad \textbf{Photodegration by } HO^{\bullet} \qquad (I.9)$$

$$R + h^{+}_{VB} \rightarrow R^{\bullet+} \rightarrow \textbf{Intermediate(s)/Final products} \qquad \textbf{Photodegration by } h^{+} \qquad (I.10)$$

The protonation of superoxide ions ($\bullet O_2^-$) leads to the generation of hydroperoxyl radicals (HOO•), which can then form hydrogen peroxide (H_2O_2) (Eq. I.11 to I.13). These species serve as electron scavengers, preventing recombination and increasing the reaction rate.

$$O_2^{\bullet-} + H^+ \rightarrow HOO^{\bullet} \qquad (I.11)$$

$$HOO^{\bullet} + e^-_{CB} \rightarrow HOO^- \qquad (I.12)$$

$$HOO^- + H^+ \rightarrow H_2O_2 \qquad (I.13)$$

In heterogeneous photocatalysis, organic compounds are oxidized into intermediate products until they are ultimately converted into H_2O and CO_2. This process can be achieved if certain reaction conditions, such as the choice of photocatalyst, illumination time, light intensity, etc., are carefully selected.[22] Fig. I.28 illustrates some of the mentioned reactions on the surface of a SC photocatalyst.

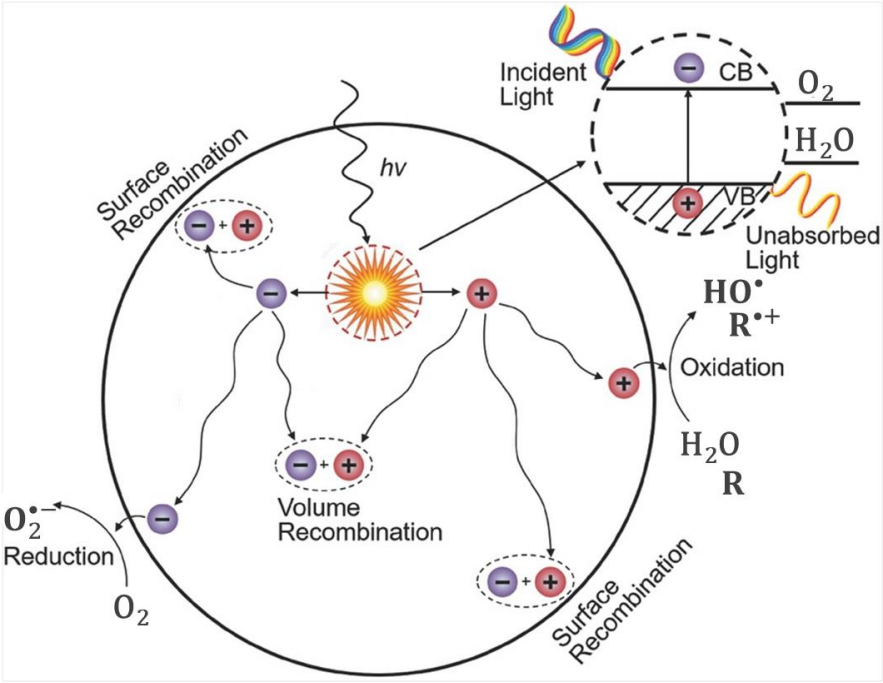

Figure I. 28. The main processes occurring on the surface of a SC photocatalyst.[160]

I.5.2 Challenges facing semiconductor photocatalysts

The main challenges facing photocatalysis processes today is the development of economically viable and industrially available SC photocatalysts. Currently, much research is being conducted on SC materials, including unaltered and altered titanium dioxide (TiO_2),[161] zinc oxide (ZnO),[162] metal sulfides (such as CdS, ZnS, MoS_2, Cu_2S, CoS_2, etc.),[163] composite SCs, etc. Figs. I.29 and I.30 exhibit the band-gap positions of typical p-type and n-type SCs with respect to the energy level of redox reactions in water (voltage vs. NHE at pH = 7).[164] Among them, TiO_2 and ZnO have become the most

studied and applied photocatalysts.[165] These two SC materials are generally used in photocatalysis due to their high oxidation ability, stability, nontoxicity, and low cost. But, they require high energy UV irradiation to activate the production of e^-/h^+ pairs, which are necessary for the subsequent light induced reactions. Nevertheless, the proportion of UV radiation in the whole solar spectrum is less than 4%, while visible radiation accounts for about 43% and is the main component of indoor artificial lighting.[166] As a result, SCs with band gaps greater than 3.1 eV, such as TiO_2 and ZnO, are inefficient at utilizing natural sun light or artificial visible light irradiations. To address this limitation, various alternatives have been proposed to extend the absorption capability of these materials into the visible region. These include coupling with a small band gap SC, doping with metal and non-metal, or the addition of transition metals.[166–168] Developing new photocatalyst materials that can be activated directly by visible light is another important approach to ameliorating the performance under visible light illumination. In addition to modifying traditional photocatalysts, many new materials with lower band gaps have been studied, resulting in significant progress in enhancing photocatalytic activity by improving the absorption of solar light.[169] Recently, numerous studies have shown that Ag-based SCs have narrow band gap energies and exhibit strong visible light absorption, making them potentially advantageous for wastewater remediation.[164,170,171] Furthermore, depositing plasmonic Ag NPs on Ag-based SC surfaces is a promising approach to increasing photocatalytic activity and efficiency.[172,173] Despite advancements, it remains challenging to develop an affordable photocatalytic process that is both highly reactive and selective under moderate conditions. Hence, significant research efforts are being made to surmount these difficulties and enhance the photocatalytic efficiency.

The following sections will discuss plasmonic Ag-based SCs that have improved light absorption ability and great interfacial electron transfer.

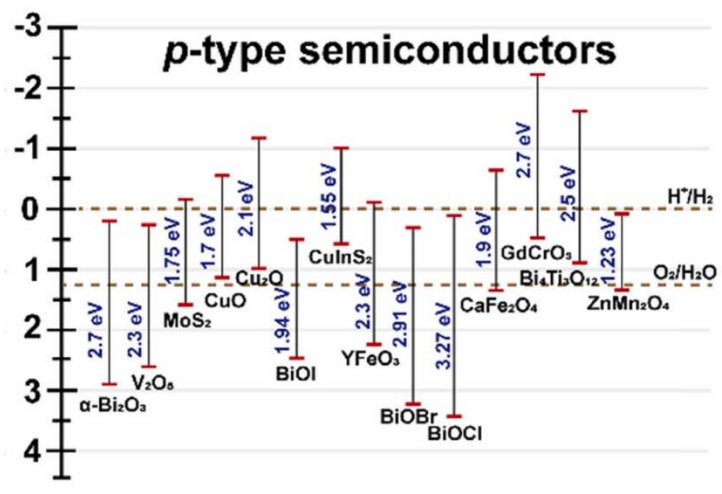

Figure I. 29. Positions of some p-type SC photocatalyst band-gaps.[164]

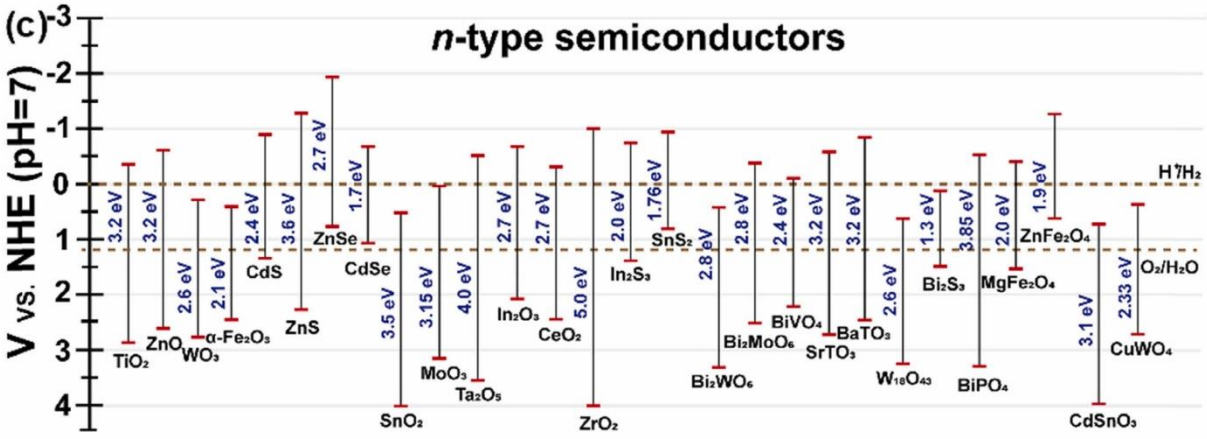

Figure I. 30. Positions of some n-type SC photocatalyst band-gaps.[164]

I.5.3 Ag-based semiconductors used as photocatalysts

Ag-containing SCs have been used in photocatalysis for several decades due to their photosensitivity, which was first discovered in photography. The exceptional properties of Ag-based SCs are due to the distinct filled d-orbitals ($4d^{10}$) of Ag ions that leads to the creation and hybridization of their energy band structures.[174,175] Most Ag-based SCs, including Ag_3PO_4 (E_g = 2.55 eV), Ag_2O (1.3 eV), AgBr (2.57 eV), Ag_2S (1.05 eV), Ag_2CO_3 (2.4 eV), and so on, have narrow band gaps and are responsive to visible light irradiation (see Fig. I.31). However, the photocatalytic efficiency of a SC is influenced not by more than just its band gap; other factors such as its crystal structure, composition, morphology also play an important role. Because of their potential for visible light absorption, significant effort has been made to designing, preparing, and characterizing Ag-based photocatalysts.

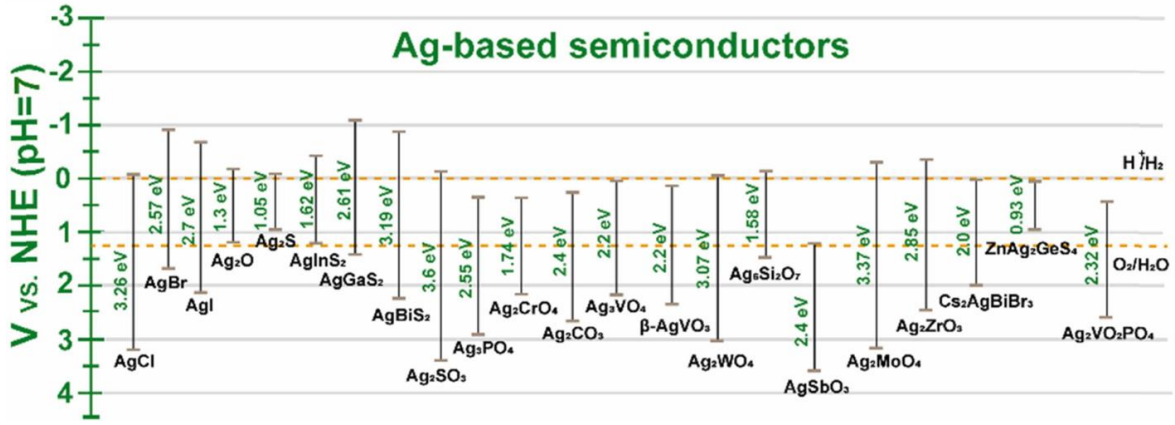

Figure I. 31. Positions of some Ag-based photocatalyst band-gaps.[164]

Ag-containing SCs are a kind of photosensitive materials that tends to decompose when exposed to light irradiation. For instance, when Ag halide (AgX, X = Cl, Br, I) particles absorb a photon, they generate e^-/h^+ pairs. The photogenerated e^- can reduce lattice Ag^+ to metal Ag^0.[176] With continued exposure to light, clusters of Ag^0 get self-deposited on the surface of Ag halide particles. Because of this instability under light illumination, Ag-based SCs were not commonly employed as photocatalysts until recently.[177]

Kakuta and his colleagues[178] reported that $AgBr/SiO_2$ composite can photocatalyze the production of H_2 under UV irradiation. They noticed that zero-valent Ag^0 only photogenerated and self-deposited on the AgBr surface during the initial stages of the catalytic reaction, and that AgBr did not further degrade with additional UV exposure. They proposed that photoinduced electrons from AgBr were trapped by the *in situ* formed metal Ag, which prevented further reduction of Ag^+ and promoted charge carrier separations. This resulted in stable $Ag^0/AgBr/SiO_2$ composite under light illumination because the subsequently generated electrons from AgBr enriched on the surface of the metal Ag instead of being transferred to its lattice, causing reduction. This self-stabilization mechanism, in which metal Ag is produced by the partial photodecomposition of an Ag-containing compound when exposed to light, has been highlighted in many studies. In general, this mechanism applies to most Ag-based photocatalysts. Ag-based compounds are also highly efficient photocatalysts. This is owing to the efficient plasmon resonance of the noble nanosized silver particles, which strongly absorbs sunlight in the visible range through the LSPR effect.[172] This effect of small sized metal Ag has been used to enhance the performance of various SCs and develop new plasmonic photocatalysts. Moreover, the excellent conductivity of the small sized silver particles can facilitate the transfer of electrons, reducing e^-/h^+ recombination and enhancing the interfacial charge transfer. As a result, plasmonic Ag NPs supported on Ag-catalysts are expected to exhibit high efficiencies and stability under visible light.

One aim of the current thesis is to demonstrate the photocatalytic performance of Ag-containing NASICON-type materials through plasmonic photocatalysis and to test the efficacy of photocatalytic degradation of selected model organics in wastewater. In this section, the beneficial aspects of plasmonic Ag NPs properties in photocatalysis, influential surface plasmon parameters, and the Ag NPs/Ag-based SC junction will be overviewed. Subsequently, photocatalytic applications of Ag-based photocatalysts in environmental remediation will be presented.

I.5.4 Plasmonic Ag nanoparticles

Nanosized plasmonic metal particles, specifically Ag NPs, have shown great potential in the degradation of organic pollutants under mild conditions.[179] The deposition of plasmonic Ag NPs on Ag-based SC material could enhance e^-/h^+ recombination and then ameliorate the photocatalytic activity of Ag-based compounds.[172] Compared with traditional SC photocatalysts, plasmonic Ag-photocatalysts possess two distinct features: Localized surface plasmon resonance (LSPR) and metal/SC junction, where each features contribute to photocatalysis in a different way.

The prominent benefits associated with plasmonic material are given as follows:

- **Improved light absorption**: LSPR can extend the absorption of light towards the visible region.
- **Reduced diffusion length:** This matches the 10 nm minority carrier diffusion length, with the strong light absorption due to LSPR, the incident light interacts closer to the NPs surface, reducing the

distance that free radicals must travel to interact with reactive species. This is advantageous for photocatalysts with poor transport of electrons.

- **Enhanced local electric field:** LSPR generates an intense local electric field that promotes the formation of new e^-/h^+ pairs. This local electric field also heats the nearby environment of the plasmonic Ag to boost the rate of redox reactions and polarizes nonpolar molecules for improved adsorption.
- **Decrease electrons and holes recombination:** When e^- and h^+ are generated inside or near the metal/SC junction, they are forced to move in opposite directions, preventing the recombination of photocarriers.

The term "plasmonic" mainly refers to the LSPR and its induced effect (as discussed in section I.4.3.2). Developing plasmonic photocatalysts can provide a solution to the challenges faced by current SC photocatalysts. In our case, the Ag NPs, due to the LSPR effect, activate Ag-based SC toward the visible region, as demonstrated in Fig. I.32(a). The Ag NPs adsorb visible light photons and transfer the generated electrons to the SC's conduction band. Additionally, as depicted in in Fig. I.32(b), the Ag NPs can serve as electron traps, where the illumination source activates the Ag-based SC, and the photogenerated e^- are transferred to the Ag metal, leading to a longer charge-carrier lifetime and thus decreasing the recombination process.

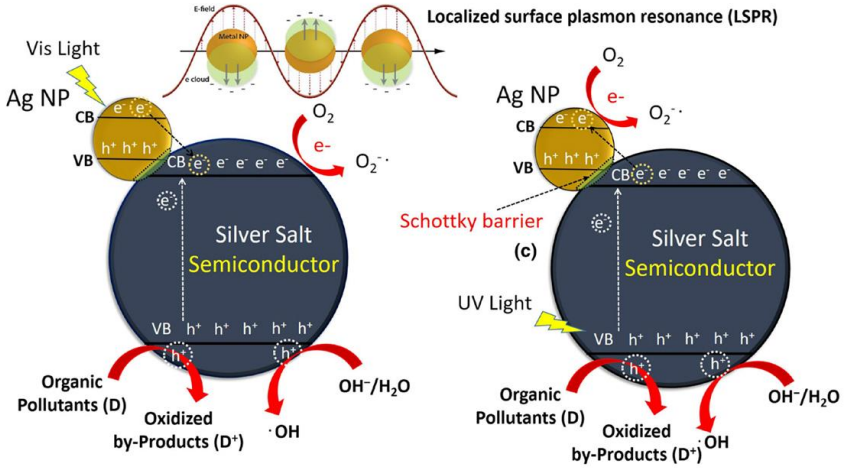

Figure I. 32. The different photogenerated charge carriers transfer paths when Ag NPs are supported on the Ag-based SCs surface.[180]

I.5.4.1 Localized surface plasmon resonance

The photocatalytic process using LSPR effect can be interpreted via four possible mechanisms: i) hot electron injection; ii) amplification of the electric field, also called plasmonic resonance energy transfer (PRET); iii) resonant photons scattering; and iv) plasmonic heating.[181,182] The first two mechanisms represents effects that occur in the near-field and can be controlled by engineering the junction between the Ag NPs and the Ag-based SC material. On the other hand, the third mechanism defines an effect that

occurs in the far-field, which can enhance the photon absorption of SCs by increasing the incident light optical path length. Finally, the fourth mechanism is a photothermal effect that leads to a plasmonic heating and can drive photocatalytic reactions.

1. Hot electron injection mechanism

The mechanism of injecting high-energy (hot) electrons (as shown in Fig. I.33) has an energy level associated with the oscillation energy of the Ag NPs electronic cloud (see Fig. I.12).[182] The electronic cloud oscillation is linked to electrons transfer from the Ag NP to the SC. This oscillation is influenced by the incident electromagnetic field, creating areas around the Ag NPs with a richer electron environment and thus generating hot electrons and holes. Upon absorption of light by Ag NPs, their lowest occupied energy level passes to the excited state. This allows high-energy electrons to be transferred to the SC conduction band through two different pathways: e^- transfer (direct transfer) or h^+ transfer (tunnel effect transfer). It has to be underlined that the hot electrons and holes produced during this process are not the same as the photogenerated electrons and holes of the SC. However, similar to any other excited electron, high-energy electrons can relax to a lower state with low energy if they are available, and then they can be injected into the SC conduction band if it has a lower energy level relative to the plasmonic resonance energy level. In general, noble metal NPs have exceptional electronic mobility and the ability to absorb visible light, which makes them promising materials for this kind of transfer of energy. While the behavior of high-energy electrons in plasmonic NPs has been extensively studied, there is less understanding of the behavior of hot holes. The hot electron transfer has the same principle as that outlined in the metallic band diagram, while the high-energy holes have been suggested to migrate from the SC valence band to the interior of the Ag NPs. This charge transfer takes place when the Ag NPs oscillate and are in close proximity to a SC that has a deficit of positive charge. It is also important to note that the transfer of holes is only a proposed explanation for a potential mechanism to balance the overall generation of high-energy charges within the Ag NPs.

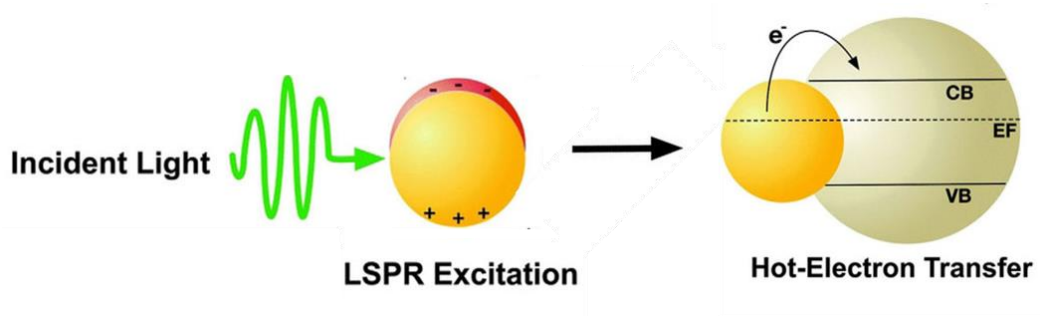

Figure I. 33. The excitation of LSPR and energy transfer to adjacent SC through hot electron.[182]

2. Plasmon resonant energy transfer mechanism

Another explanation for the improved photocatalytic activity of Ag NPs supported on SC materials is the electromagnetic field amplification near the interface between Ag NPs and the SC. This results in an increased rate of generation of e^- and h^+ in the SC.[182] The presence of an intense electric field near

the metallic Ag improves the photocatalytic performance through the plasmonic resonance energy transfer (PRET) mechanism, as shown in Fig. I.34. The PRET mechanism involves incident irradiation creating an intense electric field near the metallic Ag, which promotes the photogeneration of charge carriers nearby the surface of the SC through dipole-dipole interaction between Ag NPs and the SC. This mechanism can intensify the electric field in specific, very small locations called hot spots. According to a fine difference time domain (FDTD) examination conducted by Hou and co-workers,[183] the electric field in a hot spot can be a thousand times stronger than the incident electric field on a SC surface. This results in thousand times more e^-/h^+ photogeneration and photo-absorption in comparison with ordinary incident light excitation of SCs.

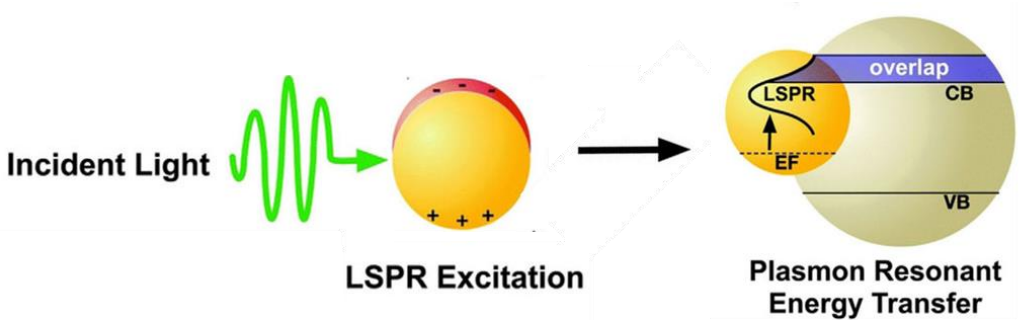

Figure I. 34. The excitation of LSPR and energy transfer to SC through PRET.[182]

3. Far-field scattering mechanism

Plasmonic Ag NPs exhibit exceptional scattering capabilities that stem from their LSPR properties.[182] When plasmonic metallic Ag is exposed to visible light, incident resonant photons can be scattered, making their optical path length longer. The plasmonic Ag NPs function as nano-mirrors in this process, as shown in Fig. I.35. Photons that the SC material does not absorb can be scattered by Ag NPs, allowing them to travel through the SC, which improves the visible light absorption and photocatalytic activity. However, the intensity of light scattering is dependent on the size of the particles, with relatively big Ag NPs producing more intense scattering. Therefore, plasmonic Ag NPs should be large enough to produce significant light scattering. For instance, Christopher and his colleagues[184] observed that cubic-shaped Ag NPs supported on TiO_2 were more efficient at scattering light to TiO_2 and enhancing methylene blue dye photodegradation compared to spherical Ag NPs supported on TiO_2.

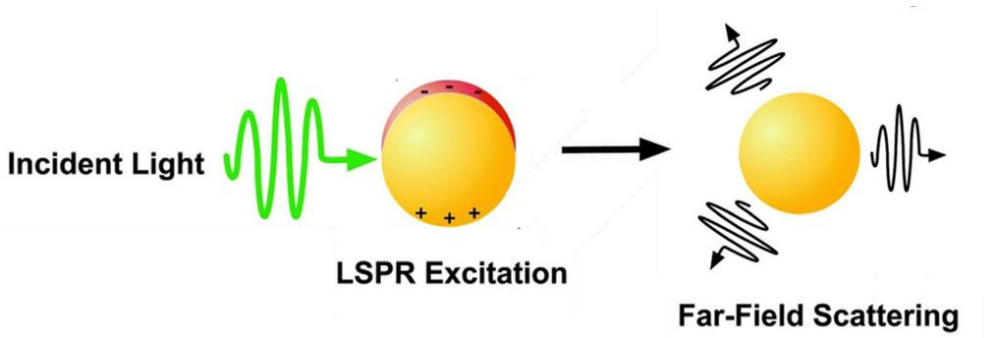

Figure I. 35. The excitation of LSPR and energy transfer to SC through far-field scattering.[182]

4. Plasmonic heating mechanism

When plasmonic Ag NPs are illuminated with light, the photogeneration of LSPR can cause a temperature increase in the nearby medium of Ag NPs.[182] Upon excitation of Ag NPs by visible light, the hot electrons produced may not have sufficient energy to enter the SC and take part in photocatalytic reactions. Instead, they remain in the Ag NPs and undergo relaxation processes, which convert the absorbed light into heat through electron-electron and electron-phonon interactions.[185] The heat generated by this process, referred to as the plasmonic heating effect, is concentrated near the surface of the Ag NPs and leads to photothermal conversion, as shown in Fig. I.36.[186] The distance between particles, determined by the distribution of Ag NPs, has a significant impact on the photothermal performance of Ag NPs because of two distinct effects: thermal superposition and plasmonic coupling. The first effect refers to the increased thermal accumulation that occurs when heat is transferred from adjacent hot Ag NPs, while the second effect refers to the thermal accumulation that results from the plasmonic coupling of adjacent Ag NPs, which enhances the local electromagnetic field and heat production. When the concentration of Ag NPs is low and the average distance between particles is large, these effects become negligible. The impact of plasmonic heating on the photocatalytic performance can be determined by measuring the temperature near the Ag NPs surface. Numerous studies have demonstrated that plasmonic heating of Ag NPs can improve the photocatalytic activity by increasing the reaction rate due to the temperature rise.

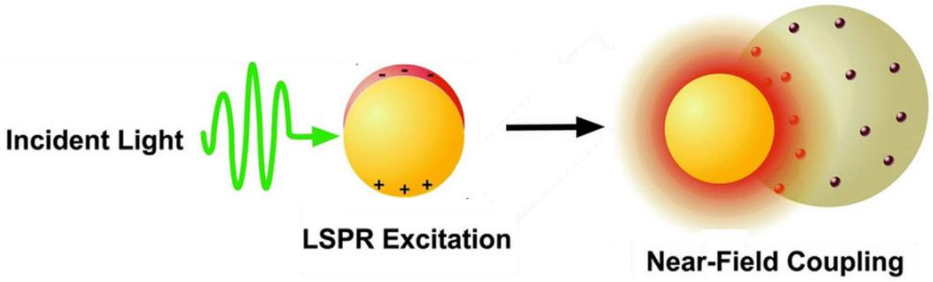

Figure I. 36. The excitation of LSPR and energy transfer to SC through plasmonic heating effect.[182]

I.5.4.2 Ag nanoparticles/semiconductor junction

When Ag NPs and a SC material come into close contact, a metal/SC junction is created. The nature of this junction are determined by the interaction between the Ag NPs and the SC, which is influenced by the work function (**Φ**) of both materials. The work function represents the minimum energy needed to remove an electron from the surface of a particle and move it to a point in the vacuum beyond the surface where it can escape from the particle. It is calculated as the difference between the Fermi level and the vacuum level.[187]

During a metal/SC junction two cases can occurs:

(1) **Schottky junction** occurs when the absolute value of the Ag NPs work function is greater than that of the SC, $|\mathbf{\Phi}_M| > |\mathbf{\Phi}_{SC}|$. After contact, electrons on the interface of the SC have higher energy than those

in Ag NPs, so electrons from the SC will transfer to the Ag NPs until the Fermi energy level of both materials are aligned, i.e., $E_{F,Ag} = E_{F,SC}$.[188]

(2) **Ohmic contact** occurs when the absolute value of the Ag NPs work function is smaller than that of the SC, $|\mathbf{\Phi}_M| < |\mathbf{\Phi}_{SC}|$. After contact, electrons on the interface of Ag NP have higher energy than those of the SC, so electrons from the Ag NPs will transfer to the SC until the Fermi energy alignment is achieved.[188]

A schematic representation of a metal/SC junction is displayed in Fig. I.37. In the case of a Schottky junction (Fig. I.37(a)), upon illumination by light, the generated e^- are transferred from the SC to the adjacent metal with a lower E_F (higher work function) via the Schottky junction. This transfer causes the metal's Fermi level to shift towards the SC's Fermi level. This results in the SC's Fermi level reaching thermodynamic equilibrium with the metal's Fermi level. Once equilibrium is achieved, a double layer forms at the metal/SC interface. The SC becomes positively charged close to its surface while the metal becomes negatively charged due to electrostatic induction. As a consequence, the concentration of free charge carriers nearby the surface of the SC will be depleted in comparison with the SC bulk. This region is referred to as the space charge region, which is also known as the depletion layer. Therefore, the Schottky barrier can trap electrons and prevent them from traveling back to the SC, making the metal a sink for electrons. This helps to extend the lifespan of photogenerated electrons for the photocatalytic reaction, as it prevents e^-/h^+ pair recombination. To enable efficient transfer of electrons across the Schottky barrier, the metal's Fermi level must be lower than the SC's conduction band. This is why Ag NP, which has a high work function of 4.74 eV, is commonly used to form heterojunctions with SCs.[189] On the other hand, in the case of an ohmic contact (Fig. I.37(b)), visible light illumination produces hot electrons in plasmonic metal NPs through LSPR effect. These hot photogenerated electrons are then transferred from the metal to the interior of the SC and accumulate in the space charge region, leaving the metal positively charged and creating holes in the metal. The emerged region between the metal and SC is known as the accumulation layer. The built-in potential between the metal and the SC continuously shifts the energy band edges of the SC. Lastly, the e^- in the CB of the SC and the h^+ remained in the metal take part in reduction and oxidation reactions, respectively.

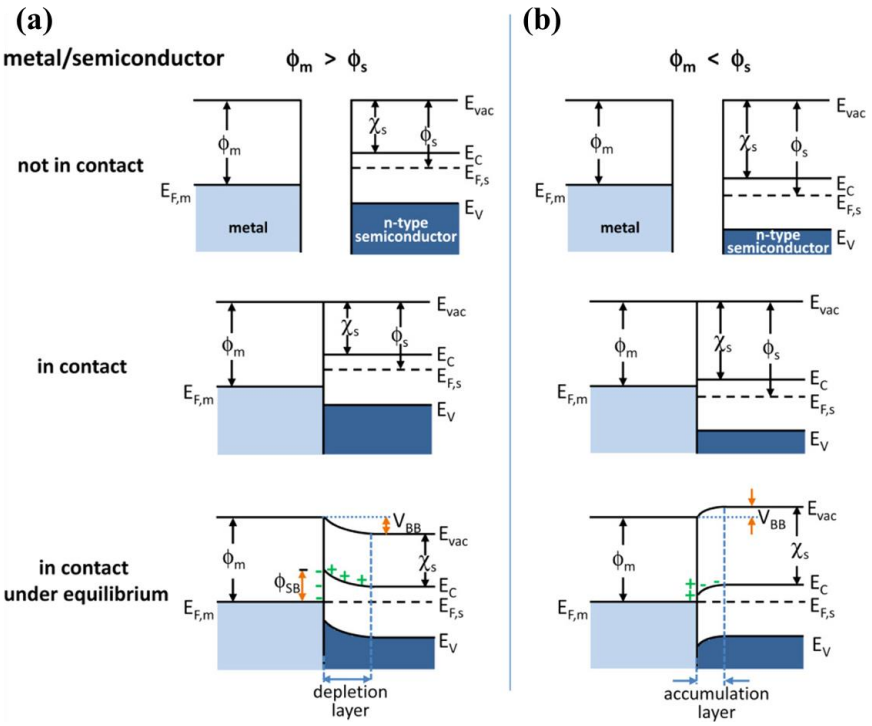

Figure I. 37. Energy band diagrams during contacts of n-type SC and metal. E_v, valence band energy maximum; E_c, conduction band energy minimum; E_{vac}, vacuum energy; $\mathbf{\Phi}_m$, metal work function; $\mathbf{\Phi}_s$, SC work function; χ_s, SC electron affinity.[190]

I.5.5 Typical examples of Ag-based photocatalysts used for wastewater treatment

In recent years, environmental scientists have been dedicated to finding new SC materials with high photocatalytic activity for the decomposition of organic pollutants when exposed to visible light illumination. Ag-based SCs have attracted attention due to their intrinsic electronic structure, suitable band gap energy, and high photocatalytic activity. One example is silver oxide (Ag_2O), which has a narrow band gap and behaves as a p-type SC. Ag_2O has been discovered to be a highly responsive visible light SC photocatalyst because of the hybridization between O2p and Ag4d orbitals, allowing it to absorb visible light efficiently.[191] However, its strong photosensitivity was previously thought to hinder its application as a photocatalyst, as it could cause the material to decompose during the photocatalytic reaction. In 2011, Wang and his colleagues[191] discovered that Ag_2O could be used as an efficient photocatalyst when stimulated by visible light with a good degree of self-stability. The researchers remarked that after 30 min of reaction, a small amount of zero-valent Ag^0 was self-adhered to the Ag_2O surface. This *in situ* formation of metallic Ag beneficially enhanced the photocatalytic efficiency and stability of the Ag-nanocomposite material. The self-stabilization mechanism proposed by Wang and his co-workers[191] has been confirmed by other researchers studying Ag-based photocatalysts.

(i) Ag_2O supported on g-C_3N_4 photocatalysts

Liang et al.[192] used a chemical precipitation route at room temperature to synthesize a range of Ag_2O/g-C_3N_4 photocatalysts with different amounts of Ag_2O content. The results showed that Ag_2O NPs were

evenly distributed on the surface of g-C_3N_4 and that a heterostructure was formed. The supported Ag_2O NPs were between 100-500 nm in size. The synthesized photocatalysts were very effective in degrading organic pollutants such as methylene blue (MB), methyl orange (MO), rhodamine B (RhB), and phenol under visible and near-infrared irradiation. The rate constants for the photodegradation of RhB dye using Ag_2O/g-C_3N_4 (8:1) were 0.05188 min^{-1} and 0.01368 min^{-1} when illuminated with visible and near-infrared light, respectively, which were approximately 26 and 343 times superior to pure g-C_3N_4 and even higher than Ag_2O alone. According to Liang and his colleagues[192] the improved photochemical activity of Ag_2O/g-C_3N_4 was mainly due to the *in situ* formation of plasmonic Ag NPs on Ag_2O surface during the photodegradation process. Upon light excitation, the generated e^- from Ag_2O move to its surface and reduce lattice Ag^+ ions into nanosized Ag metal. Then the produced Ag particles serve as an e^- sink to prevent the charge carriers recombination and also avoid the photo-corrosion of Ag_2O. Furthermore, the photoinduced h^+ in the valence band of Ag_2O directly decompose the target organic pollutants, resulting in enhanced photocatalytic performance. Additionally, the Ag_2O/g-C_3N_4 heterostructure exhibited good stability during recycling experiments.

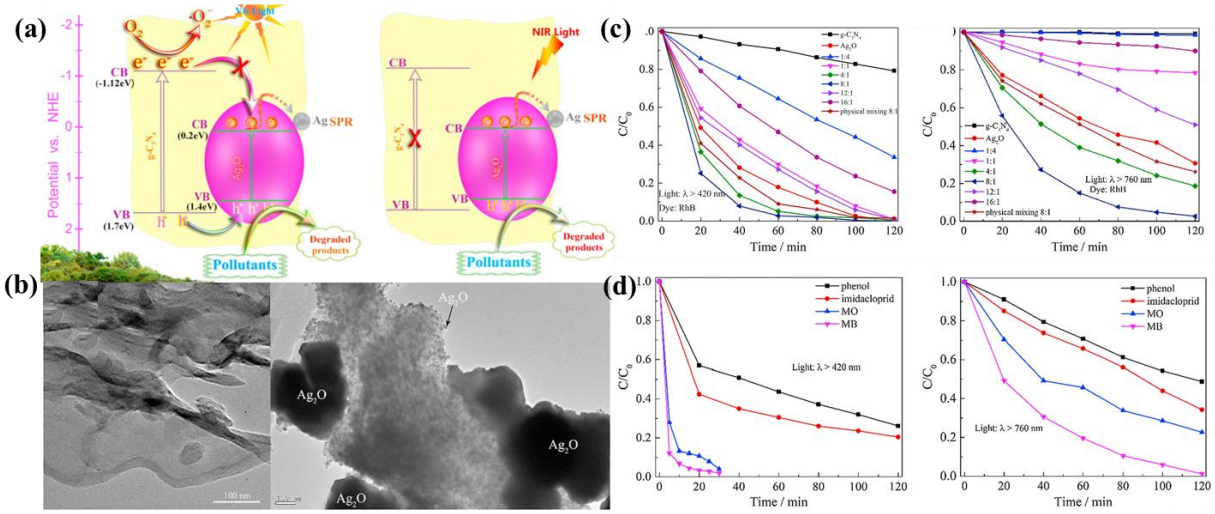

Figure I. 38. (a) Photodegradation mechanism of organic pollutant over Ag_2O/g-C_3N_4, (b) TEM micrographs of pure g-C_3N_4 and Ag_2O/g-C_3N_4, (c) the rate constants of RhB decomposition, and (d) different organics photodegradation over Ag_2O/g-C_3N_4 under visible and near-infrared irradiation.[192]

(ii) Ag supported on Ag_2MoO_4 photocatalysts

Li et al. [193] synthesized Ag/Ag_2MoO_4 composites by treating Ag_2MoO_4 with a solution of $NaBH_4$ at ambient temperature. They found that Ag NPs were self-supported on the surface of Ag_2MoO_4 with a size average of around 80-100 nm. The distribution of the supported Ag NPs on the Ag-based compound was random. They also observed that by increasing the concentration of $NaBH_4$, more Ag NPs can be produced from Ag_2MoO_4 material. The researchers evaluated the performance of the photocatalyst composite by studying its ability to degrade an organic pollutant under visible light illumination. The findings indicated that the Ag/Ag_2MoO_4 composite had significantly improved photocatalytic activity in comparison with untreated Ag_2MoO_4, achieving a photodegradation efficiency of 99.5% in just 60

minutes and exhibiting excellent stability over five consecutive cycles. Li et al.[193] attributed the improved visible light photocatalytic performance to the LSPR effect of self-supported Ag NPs. They also determined that the primary active species involved in the photocatalytic reaction were •OH and h^+.

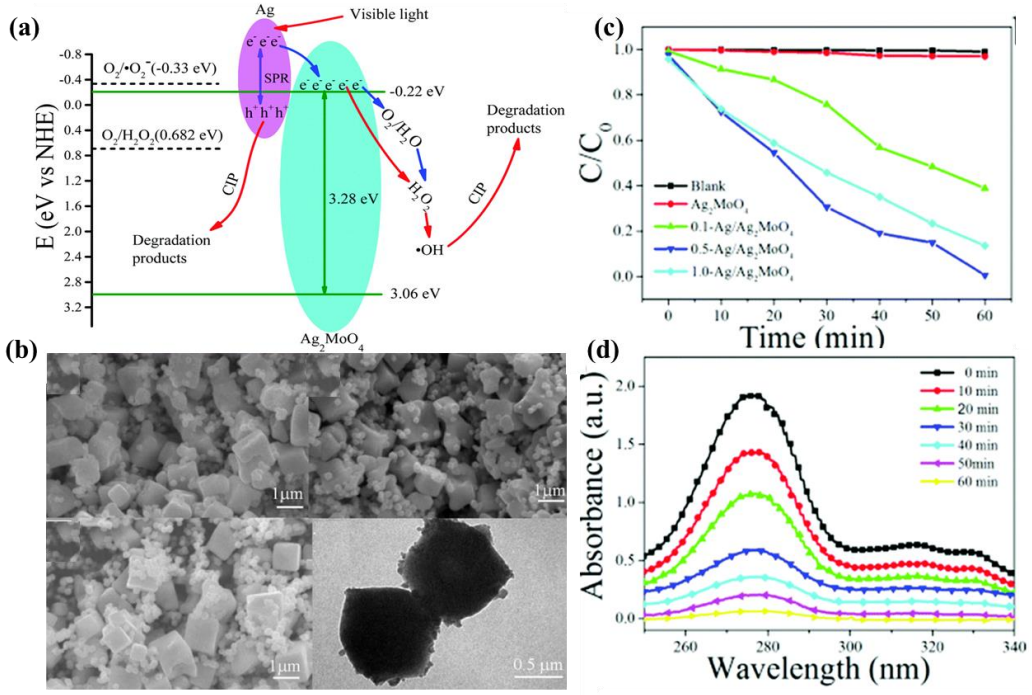

Figure I. 39. (a) Mechanism of the target pollutant degradation over Ag/Ag_2MoO_4, (b) morphological images of Ag/Ag_2MoO_4, (c) visible light degradation of the organic pollutant over the untreated Ag_2MoO_4 and different synthesized Ag/Ag_2MoO_4, and (d) the evolution in the absorption of the target pollutant over the 0.5-Ag/Ag_2MoO_4 at different irradiation times.[193]

(iii) Ag supported on Ag-halides

Ag halides, specifically AgX, where X can be Cl, Br, or I, exhibit a strong response to visible light. However, like Ag_2O, they were believed to possess poor stability due to their photosensitive properties. Kuai and his co-workers[194] synthesized AgBr compound and then produced Ag/AgBr composite after an irradiation by visible light. Based on their finding, they suggested a formation mechanism for Ag particles on AgBr surface similar to that reported for Ag_2O. Upon visible light illumination, nanosized Ag particles were formed *in situ* on the Ag-halide surface through reduction of lattice Ag^+ ions by the photogenerated e^-. The constructed Ag layer on AgBr prevented its decomposition under further light irradiation and improved its stability. Additionally, the subsequently generated electrons from AgBr, were transferred to Ag, then get captured by O_2 in water, resulting in the formation of $•O_2^-$. Meanwhile, the h^+ on the VB of AgBr oxidized Br^- into Br^0. Finally, the powerful oxidation abilities of $•O_2^-$, h^+, and Br^0 decomposed the organic pollutant. According to the researchers, Ag/AgBr composite was able to completely degrade methyl orange dye within 5 minutes of sun exposure and maintained its activity even after five recycling reactions.

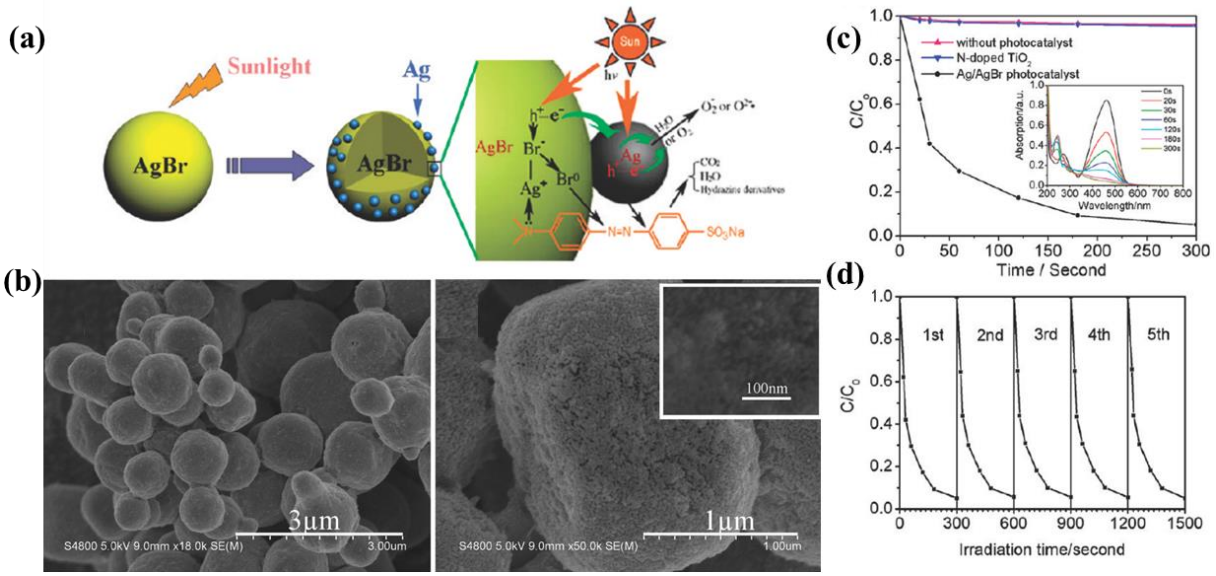

Figure I. 40. (a) Schematic of Ag NPs production on AgBr and the photodecomposition mechanism of MO, (b) micrographs of the Ag/AgBr composite, (c) the photodecomposition curve of MO. The inset depicts the absorption spectra of MO decomposition as a function of time, and (d) cycling photocatalytic experiments over Ag/AgBr composite.[194]

(iv) Ag-based oxoacid photocatalysts

Typical Ag oxoacid photocatalysts include, $AgNbO_3$, $AgGaO_2$, Ag_3AsO_4, $AgAlO_2$, $AgSbO_3$, $AgInO_3$, $AgCrO_4$, $AgGeO_3$, etc. Among them, Ag_3PO_4 is well known for its excellent performance as a SC photocatalyst in degrading various toxic contaminants in water. It has a narrow band gap (Eg = 2.36 - 2.42 eV) and a cubic crystal structure. Its VB oxidation potential of 2.9 eV, making this material very effective in most photocatalytic oxidation processes when exposed to visible light. The lattice Ag^+ ions inside Ag_3PO_4 can combine with photogenerated e^- to form Ag/Ag_3PO_4 composite, which can maintain the stability of Ag_3PO_4 and greatly benefit its overall photocatalytic activity. Bi and his co-workers[195] developed a method for synthesizing Ag/Ag_3PO_4 composites with controllable formation ratios of small sized Ag particles, using glucose as a reductant in a solution of ammonia (NH_4OH). According to Bi et al.[195] Ag NPs were observed to appear on the planes, edges, and the whole surface of Ag_3PO_4 microcubes. Compared to pure Ag_3PO_4 microcubes, Ag/Ag_3PO_4 composites showed superior photocatalytic activity in degrading rhodamine B dye. This was due to the rapid separation rate and fast mobility of photogenerated e^-/h^+ pairs, which were made possible by the good electronic conductivity of Ag NPs. The researchers stated that the supported Ag particles on Ag_3PO_4 can act as electron traps and transport paths, reducing the recombination of e^-/h^+ pairs. Additionally, electrons trapped by Ag nanoparticles show higher transfer abilities compared to Ag_3PO_4. Therefore, the main role of the supported Ag NPs in this system was to accelerate the transfer of photoexcited e^- from the conduction band of Ag_3PO_4 to Ag NPs to dissolved O_2 in water. This will lead to the production of $\bullet O_2^-$ species that

will cause the degradation of organic contaminants. These factors ultimately played a significant role in the outstanding catalytic performance of Ag/Ag_3PO_4 photocatalyst.

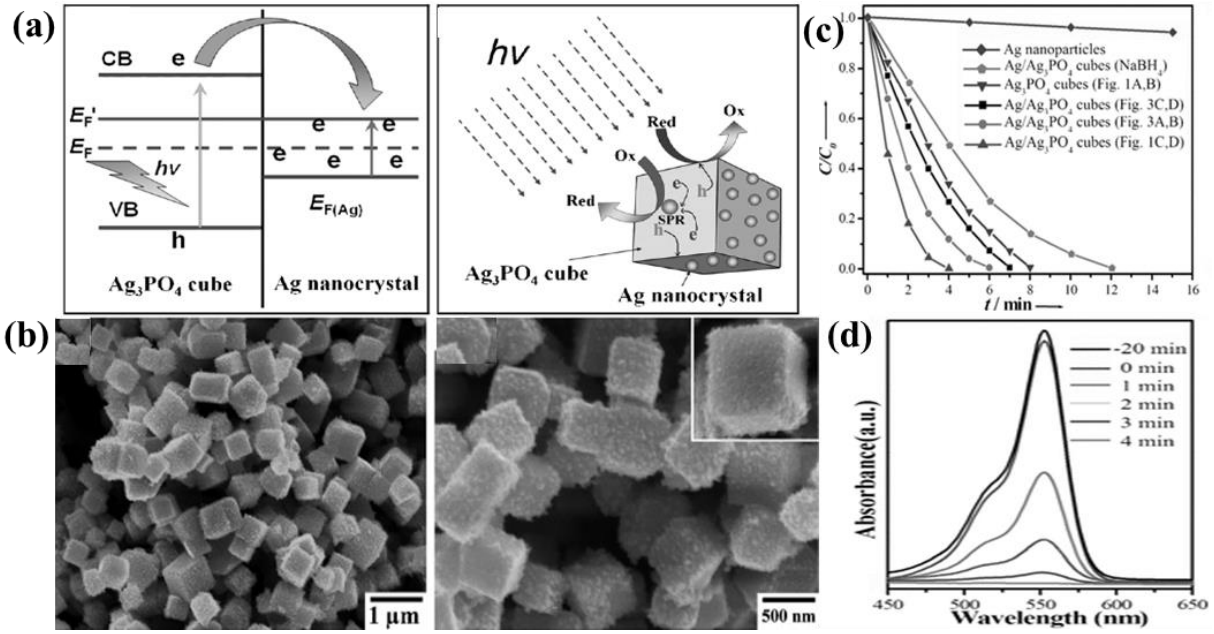

Figure I. 41. (a) Diagrams showing the separation of photoinduced charges in Ag/Ag_3PO_4, (b) morphological images of the Ag/Ag_3PO_4, (c) visible light photocatalytic activities of Ag/Ag_3PO_4, Ag_3PO_4 microcubes, and Ag NPs, and (d) the absorption spectra of RhB decomposition in the presence of Ag/Ag_3PO_4 as a function of irradiation time.[195]

(v) Ag_2O/Ag_2CO_3 composite photocatalyst

Hu et al.[196] reported the synthesis of Ag_2O/Ag_2CO_3 composites through a solid-state method. They found that by adjusting the basicity of the solid-state reaction system, they could control the composition of the resulting products. Increasing the alkalinity of the reaction system can lead to a change in the product from Ag_2CO_3 to Ag_2O/Ag_2CO_3 composite, and finally to Ag_2O. The authors investigated the catalytic performance of the prepared composite materials in the photodegradation of dye molecules under visible light illumination. The Ag_2O/Ag_2CO_3 heterostructure showed better photocatalytic properties compared to pure Ag_2O and Ag_2CO_3. According to the researchers, the visible-light enhancement of the Ag_2O/Ag_2CO_3 heterostructure was due to the *in situ* production of Ag NPs, which acted as a bridge between photogenerated carriers of both components. When the Ag_2O/Ag_2CO_3 composite was exposed to visible light illumination, photogenerated electrons reduced a small amount of lattice Ag^+ in Ag_2CO_3 to Ag^0 particles. Then, e^- on the conduction band of Ag_2CO_3 transferred to the *in situ* formed Ag^0 particles and recombined with h^+ from the valence band of Ag_2O. Throughout the catalytic reaction, the h^+ enriched the valence band of Ag_2CO_3 and participated in the photodegradation process. This caused the photogenerated e^- to accumulate in the conduction band of Ag_2O. This accumulation of e^- leaned the energy band of Ag_2O upward, giving it sufficient reduction capability to

convert O_2 to $\bullet O_2^-$. Finally, the photogenerated $\bullet O_2^-$ and h^+ degrade the organic dyes through redox reactions.

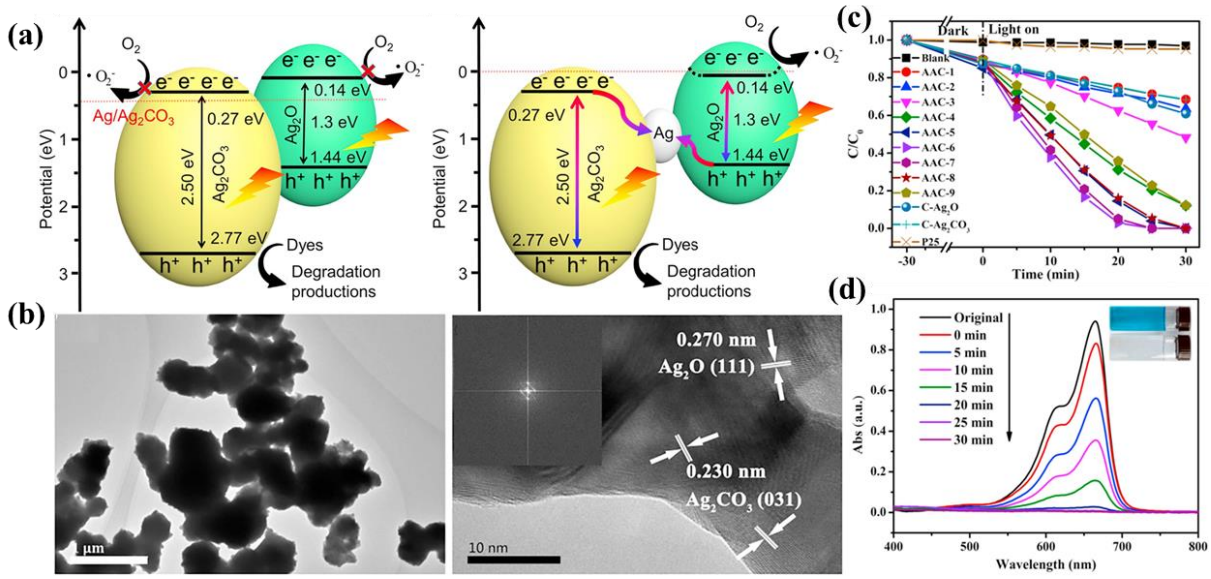

Figure I. 42. (a) Mechanism of the charge transfer process in Ag_2O/Ag_2CO_3 composite when exposed to visible light, (b) micrographs of the prepared Ag_2O/Ag_2CO_3 composite, (c) MB visible light photodegradation over Ag_2O/Ag_2CO_3, and (d) absorption spectra of MB in the presence of Ag_2O/Ag_2CO_3 as a function of illumination time.[196]

I.6 NASICON-type materials

I.6.1 Discovery and compositional diversity

NASICON-type materials constitute a broad group of compounds, structurally isomorphous, with the general formula $A_xM_2(TO_4)_3$ ($0 \leq x \leq 4$). The first NASICON material, $NaZr_2(PO_4)_3$ (abbreviated as NZP), was prepared by Sljukic et al.[197] in 1967, and its crystal structure was solved a year later by Hagman and Kierkegaard.[198] The term NASICON is an acronym from Sodium (Na) Super (S) Ionic (I) Conductor (CON), and it was originally used to describe the solid phase solution $Na_{1+x}Zr_2P_{3-x}Si_xO_{12}$ (where $0 \leq x \leq 3$), after the discovery of its high ionic conductivity by Goodenough and Hong[199] in 1976. Since then, this popular acronym has been used to refer to the entire isostructural NASICON family. The most important facts in NASICON materials are the stability and flexibility of their three-dimensional (3D) crystal structures, $[\mathbf{M_2(TO_4)_3}]^-$, along with the high mobility of the "A" cations situated in the interstitial sites, which generally induce the formation of superstructures, giving rise to a diverse range of NASICON polymorph.

NASICON materials have been prepared with a variety of different chemical compositions[200], wherein:

The A-site can be filled with:

- monovalent cations: Li^+, Na^+, K^+, Rb^+, Cs^+, H^+, NH_4^+, Cu^+, Ag^+;

- divalent cations: Mg^{2+}, Ca^{2+}, Sr^{2+}, Ba^{2+}, Cu^{2+}, Pb^{2+}, Cd^{2+}, Mn^{2+}, Co^{2+}, Ni^{2+}, Zn^{2+};
- trivalent cations: Al^{3+}, Y^{3+}, La^{3+}, Lu^{3+};
- tetravalent cations: Zr^{4+}, Hf^{4+}, Ge^{4+};

The A-site can also be vacant if the M-site is filled with a pentavalent cation.

The M-sites can be filled with:

- divalent cations: Cd^{2+}, Ni^{2+}, Mn^{2+}, Co^{2+}, Zn^{2+}, Mn^{2+};
- trivalent cations: Fe^{3+}, Sc^{3+}, Ti^{3+}, V^{3+}, Cr^{3+}, Al^{3+}, ln^{3+}, Ga^{3+}, Y^{3+}, Lu^{3+};
- tetravalent cations: Ti^{4+}, Zr^{4+}, Hf^{4+}, Sn^{4+}, Si^{4+}, Ge^{4+};
- pentavalent cations: V^{5+}, Nb^{5+}, Ta^{5+}, Sb^{5+}, As^{5+};

In addition the orthophosphate group $(PO_4)^{3-}$ can be partially substituted by $(SO_4)^{2-}$, $(WO_4)^{2-}$, $(MoO_4)^{2-}$, $(AsO_4)^{3-}$, and $(SiO_4)^{4-}$.

I.6.2 General structural of NASICON materials

The basic crystallographic formula of the NASICON family can be written as $(\mathbf{A1})_{\mathbf{0\rightarrow1}}(\mathbf{A2})_{\mathbf{0\rightarrow3}}[\mathbf{M_2(TO_4)_3}]$ in which $[\mathbf{M_2(TO_4)_3}]^{-}$represents the rigid framework, and $(\mathbf{A1})$ and $(\mathbf{A2})$ represent the two distinct interstitial sites inside the framework. Based on the NASICON material's composition, the symmetry may decrease from R-3c to R-3, C2/c, Cc, etc. In the compounds with the highest symmetry R-3c, the crystal structure is made up of a network of $[MO_6]$ octahedra and $[TO_4]$ tetrahedra that share corners, in which the combination of two $[MO_6]$ octahedra joined by three $[TO_4]$ tetrahedra forms the characteristic $M_2(PO_4)_3$ subgroups commonly called "lantern" subunits. The $M_2(TO_4)_3$ subgroups are repeated along the threefold axis, forming columns that are connected in a hexagonal pattern. These lantern subunits form an open 3D structure, in which the A cations can accommodated the two types of interstitial spaces, A(1) and A(2) (see Fig. I.43). The A(1) site is the most stable one and is located in a six-fold oxygen coordination with a distorted octahedral position between the lower and upper $[MO_6]$ octahedra of neighboring lanterns, which form infinite ribbons of $[O3A_{(1)}O3MO3A_{(1)}O3]$ along the c-axis of the hexagonal crystal structure (Fig. I.43(b)). The A(2) site is situated in an eight-fold oxygen coordination between the infinite ribbons along the c-direction of the unit cell and is connected to the A(1) site, forming the 3D array of migration pathways that allow the mobility of cations within the NASICON skeleton (Fig. I.43(c and d)). In our case, $AgM_2(PO_4)_3$ (M = Zr or Ti) NASICON-type structures contains only one Ag^+ cation per formula unit, and thus, only the A(1) site is filled, while the interstitial A(2) position remain vacant.

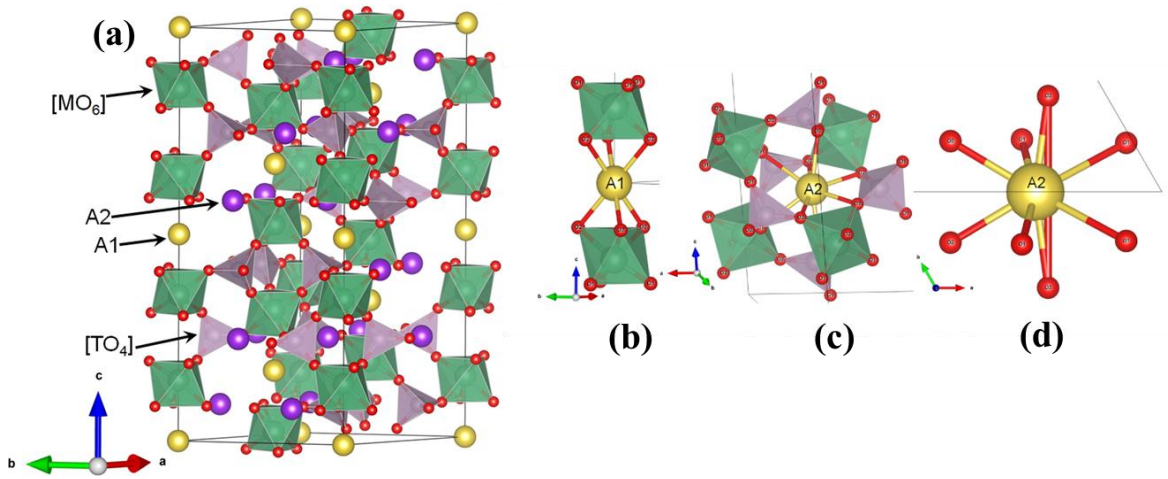

Figure I. 43. (a) General view of the $A_xM_2(TO_4)_3$ structure, (a) the A1-site coordination environment of 6b(0, 0, 0), (b) the A2-site coordination environment of 18e(x, 0, 1/4), and (c) the shortest possible distance between A2 and O atoms.[201]

I.6.3 Migration pathways in NASICON materials

The mobility of the monovalent ions (A) inside the NASICON crystalline framework is due to the phenomenon of diffusion through lattice defects, known as Frenkel-like (interstitial) defects[202]. The Frenkel defects produce vacant sites in the crystal structure, allowing any nearby ions to jump into these vacant sites. This jump makes the ion's previous location vacant, which in turn could be hosted by another ion. These processes can result in ions transferring across the entire solid material. In the case of $(\mathbf{A1})_{\mathbf{0\rightarrow1}}(\mathbf{A2})_{\mathbf{0\rightarrow3}}[\mathbf{M_2(TO_4)_3}]$ NASICON compounds the diffusion phenomenon occurs in the form of hopping in migration pathways through oxygen triangles T1 and T2, which are referred to as "bottlenecks", as shown in Fig. I.44(a).[201] In the rhombohedral $R\bar{3}c$ NASICON structures, three distinct migration pathways (the hop path of monovalent ions in the interstitial site) were proposed. The first pathway was between neighboring A(1) and A(2) sites, while the second connects between A(2) and A(2) sites, as illustrated in Fig. I.44(b). The third route was most likely from A(1) to A(1).[203,204] The first path was the shortest path and was the most preferred path in NASICON's materials. However, it appeared that the A(1) to A(1) path did not exist.

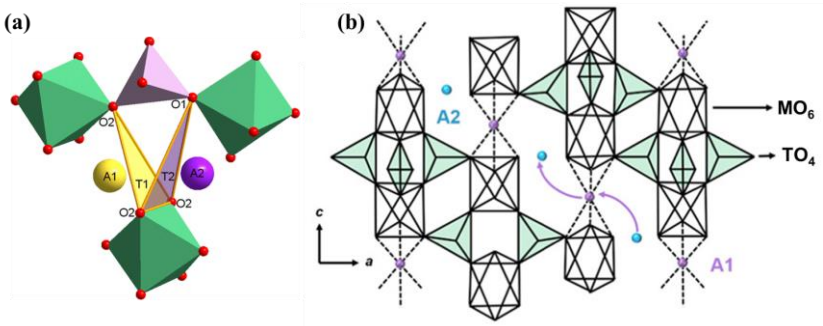

Figure I. 44. (a) Schematic of T1 and T2 bottlenecks between A1 and A2 sites,[201] and (b) the NASICON structure showing A sites (type 1) and A sites (type 2).[205]

I.6.4 Synthesis of Ag-containing NASICON materials

$AgM_2(PO_4)_3$ (M = Zr or Ti) NASICON-type phosphates have been prepared using various approaches, which can be broadly categorized as solid-state reactions and wet-chemical methods.[206] This latter includes co-precipitation, sol-gel, and hydrothermal methods. Fig. I.45 summarizes the systematic steps involved in each preparation method used to synthesis NASICON-based materials.

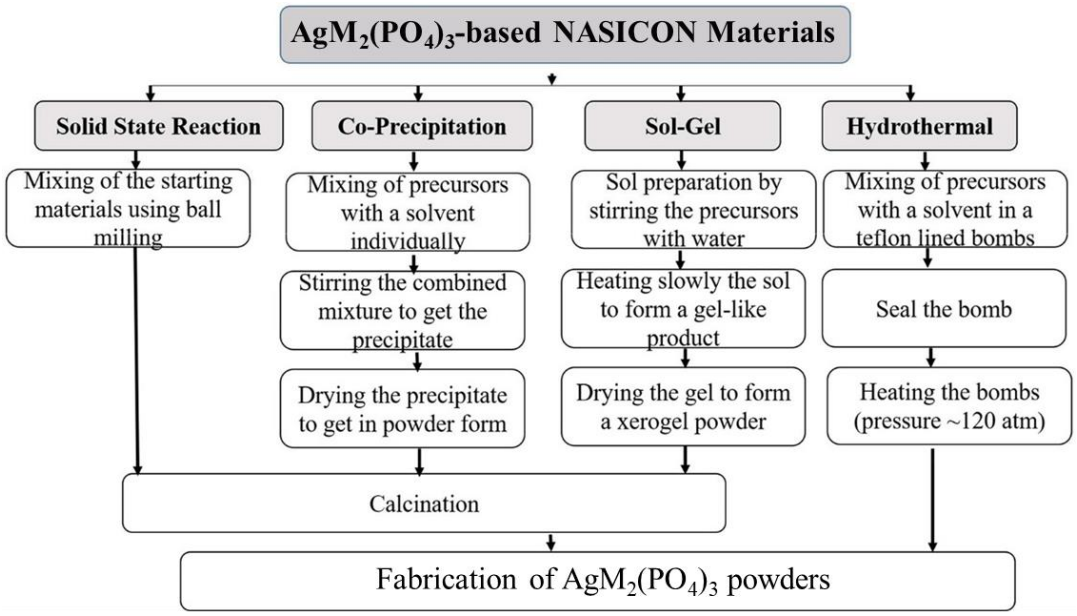

Figure I. 45. The different steps involved in the synthesis methods of silver-based NASICON materials.[206]

One of the biggest challenges in synthesizing silver-containing NASICONs is producing pure crystalline structure without any impurity phases such as zirconium oxide (ZrO_2) and zirconium pyrophosphate (ZrP_2O_7) for $AgZr_2(PO_4)_3$ or titanium oxide (TiO_2) and titanium pyrophosphate (TiP_2O_7) for $AgTi_2(PO_4)_3$. Usually, ZrO_2 (or TiO_2) acts as a barrier restricting the mobility of monovalent Ag ions located at the A1 site and reduce the overall Ag ions transport.[207,208] Moreover, ZrP_2O_7 (or TiP_2O_7) can alters the nominal composition of the silver-containing NASICONs, resulting in lower ionic conductivity and structure stability.[209] Therefore, controlling the synthesis and calcination processes is crucial to prevent the formation of detrimental phases.

In this thesis, the $AgM_2(PO_4)_3$ (M = Zr or Ti) NASICON-type materials powder were synthesized through solid-state reaction and co-precipitation method.

(i) Solid-state reaction

Solid-state reaction is a traditional route for preparing inorganic materials such as $AgM_2(PO_4)_3$ (where M = Zr or Ti). In this approach, chemical precursors are mixed through grinding, followed by the solid-state reaction and densification via heating processes, which typically necessitate high temperatures of around 700-1000 ºC and a long dwell time of up to 12 h. The very high temperatures are necessary to

complete the solid-state reaction and attain optimal densification, which will minimize the grain boundary resistance. The resulting products usually possess a highly ordered crystalline structure, large grains with few grain boundaries, and excellent ionic transport. In the solid-state method, the thermal processing parameters like the annealing temperature and the heat treatment duration affect the phase purity, cell volume, and ionic transport of the end product. Wei et al.[210] reported the synthesis of $AgTi_2(PO_4)_3$ by a solid-state process. The starting materials were $AgNO_3$, TiO_2, and $NH_4H_2PO_4$. It is worth mentioning that metal oxides such as TiO_2, ZrO_2, HfO_2, etc., silver nitrate ($AgNO_3$), and ammonium phosphate, including $NH_4H_2PO_4$, $(NH_4)_2HPO_4$, and $(NH_4)_3PO_4$, are commonly employed precursors for the traditional solid-state synthesis of silver-containing NASICONs. In Wei et al.[210] work, the reactants were mixed in stoichiometric quantities, thoroughly grinded, and then treated in two stages at 450 °C for 5 h followed by 900 °C for 24 h. They found that the $AgTi_2(PO_4)_3$ produced consisted of irregular block-shaped particles with different sizes ranging between 100 and 500 nm. Average grain sizes obtained by this method are generally less than one micron, but their distribution is wide. Furthermore, by applying a controlled solid-state synthesis, Wei et al.[210] described the prepared Ag-based NASICON material as having a single-phase composition with no impurities detected and a high degree of crystallinity.

(ii) Co-precipitation method

Co-precipitation synthesis offers an efficient synthetic path for crystalline $AgM_2(PO_4)_3$ (M = Zr or Ti) solids, which has been demonstrated in many reports.[24–26,211,212] The typical co-precipitation procedure implies dissolving a salt precursor in a solvent, followed by precipitation and the formation of a gel network, and then heat treatment for crystallization. The co-precipitation approach is a valuable means of producing pure and highly ordered crystalline materials. In addition to its simplicity, chemical co-precipitation allows for atomic-level mixing of the components, resulting in a final product with near-ideal stoichiometry, consistent particle size distribution, and a smaller particle average size. Furthermore, the co-precipitation method also enables a large-scale synthesis of $AgM_2(PO_4)_3$ (M = Zr or Ti) solids. Arsalane et al.[24] first show that it is possible to synthesize $AgZr_2(PO_4)_3$ NASICON phosphates by the co-precipitation method. The starting products, $ZrOCl_2.8H_2O$ and $AgNO_3$, were dissolved in water and mixed with $(NH_4)_2HPO_4$. Generally, silver acetate ($AgC_2H_3O_2$) or silver oxide (Ag_2O) cannot be used as the starting materials, probably because of the pre-formation of silver phosphate. The obtained gelatinous precipitate was heated in an oven until the evaporation of water. The recovered solid was then grinded and subjected to sequences of heating to 500 °C. The final pure product was formed after successive heat treatments between 500 and 900 °C for 48h. Beyond this, no impurities such as ZrO_2 and ZrP_2O_7 were observed. Similarly, Ziyad et al.[25] described the preparation of silver-thorium phosphate $AgTh_2(PO_4)_3$ via the co-precipitation method. This was done by mixing stoichiometric amounts of $Th(NO_3)_4.5H_2O$, $AgNO_3$, and $(NH_4)_2HPO_4$ that were dissolved in small volumes of water. The obtained amorphous precipitate was heated slowly in an oven until complete

water evaporation. The solid recovered was gradually heated to 550°C and subjected to repeated cycles of grinding. The final product was then calcined at 850°C in an air atmosphere for two days. Its composition was verified through chemical analysis and was found to be in perfect agreement with $AgTh_2(PO_4)_3$. Brik et al.[26] prepared the pure $AgHf_2(PO_4)_3$ phase from hafnium chloride ($HfCl_4$) and silver nitrate ($AgNO_3$). The two reagents were dissolved in water, and a solution of $(NH_4)_2HPO_4$ was added drop by drop to the mixture under vigorous stirring to form the precipitate. Usually, during the synthesis of Ag-based NASICON material, an excess of $AgNO_3$ is used to avoid the formation of ZrP_2O_7. The mixture was then dried at 120°C to remove the solvent. The powder is calcined at 500°C with intermittent grinding and then treated at 900°C for only 24 h. To produce a pure phase and a high-crystallin NASICON phase, it is necessary to carefully control the synthetic parameters such as the precursors, solvents, and temperatures used.

I.6.5 Why Ag-containing NASICON-type materials?

Ag-based NASICONs have gained interest because of their structural flexibility, ionic mobility, thermal and chemical stability, and catalytic activities, which make them useful in a variety of applications. Previous studies by our research group have shown that Ag-based NASICON phosphates with the general formula $AgM_2(PO_4)_3$, (where M = Zr^{4+}, Th^{4+}, or Hf^{4+}), are promising self-support materials for creating highly active Ag NPs catalysts. Our group findings indicate that the mobile Ag^+ ions situated in the 3D NASICON crystal can be partially reduced under a high-temperature reductive atmosphere, such as hydrogen gas, producing nano-sized Ag particles, and simultaneously exchanged with protons (H^+), yielding self-supported Ag NPs on a new formed $Ag_{1-x}H_xM_2(PO_4)_3$ NASICON matrix, and without the collapse of the parent compound's skeleton. Afterwards, the *in situ* formed Ag NPs can serve as nanocatalysts for various organic reactions. Furthermore, the supported Ag NPs can be re-oxidized under heat treatment and can diffuse back into the NASICON structure in a reversible way, regenerating the starting material.

For example, Arsalane and his colleagues[24] studied the use of $AgZr_2(PO_4)_3$ as a precursor for Ag NPs in the catalytic oxidation of butan-2-ol. Their results showed that the Ag^+ cations situated in the 3D tunnels of the NASICON skeleton were very mobile and could be partially reduced under a flux of H_2 gas at 350 °C to form nanosilver particles with sizes ranging from 10 to 30 nm. The Ag ions were also exchanged with protons without collapsing the NASICON crystal integrity. The *in situ* generated Ag NPs on the surface of the NASICON support acted as active catalysts in the oxidative dehydrogenation of butan-2-ol to butene and methyl ethyl ketone. According to Arsalane and his co-workers[24], the involved reactions proceed via the following mechanism (Eq. I.14):

$$\mathbf{AgZr_2(PO_4)_3 + C_4H_9OH \xrightarrow{H_2\ /\ 350\,^{\circ}C} Ag_{1-x}H_xZr_2(PO_4)_3 + xAg^0 + C_4H_8O + C_4H_{10} + CO_2} \quad \mathbf{(I.14)}$$

Furthermore, under an oxygen atmosphere at 640 °C, the metallic silver can be re-oxidized and reversibly diffused back into the NASICON structure, regenerating the initial material composition, $AgZr_2(PO_4)_3$, without any alteration of the NASOCON skeleton. The reversible reaction occurs via the following mechanism (Eq. I.15):

$$x\mathbf{Ag^0} + \mathbf{Ag_{1-x}H_xZr_2(PO_4)_3} + x\mathbf{O_2} \xrightarrow{640\,^{\circ}\mathrm{C}} \mathbf{AgZr_2(PO_4)_3} + \frac{x}{2}\mathbf{H_2O} \qquad (\mathbf{I.15})$$

Similarly, Ziyad et al.[25] and Brik et al.[26] have investigated the oxidative dehydrogenation of alcohol in the presence of $AgTh_2(PO_4)_3$ and $AgHf_2(PO_4)_3$, respectively, by using a similar reduction method. They showed that the Ag^+ embedded in the NASICON structure can be reduced during the course of the catalytic reaction by butan-2-ol or H_2 and migrate via the pathways of the 3D crystal network to form metallic nanoparticles on the surface, followed by a protonation of the NASICON phosphate. Afterwards, the *in situ* formed Ag NPs can serve as active catalysts in the alcohol conversion process. Analogous to Arsalane's work, the self-supported metallic NPs can be re-oxidized under heat treatment and reversibly return back into the NASICON material, restoring the initial composition.

These interesting structural features, catalytic properties, and regeneration ability of such materials inspired this PhD thesis to investigate the catalytic performance of self-supported Ag NPs on Ag-based NASICON materials for the remediation of organic pollutants in wastewater, along with the application of different regeneration methods to address the inevitable Ag nanocatalyst deactivation during reactions. Furthermore, Ag-based compounds are well known as excellent SC photocatalysts for degrading organic pollutants under visible light. Hence, we also investigated the electronic properties and explored the photocatalytic activity of $AgM_2(PO_4)_3$ (M = Ti or Zr) for the treatment of wastewater under visible light. According to what we covered in the previous sections, Ag ions in Ag-based compounds can combine with photogenerated electrons to form Ag NPs. The junction between Ag NPs and Ag-based materials can maintain a continuous flow of electrons consumption, which significantly improves the stability of Ag-based compounds as well as their photocatalytic efficiency

Chapter II: Experimental and computational methods

II.1. Material synthesis

II.1.1. Chemicals

The list of chemicals utilized in this thesis are provided in Table II.1. The double distilled water (DDW) was employed for the preparation and treatment of Ag-based catalysts and for the catalytic reductions and oxidations of the model organic pollutants.

Table II. 1. Specification of chemicals used in this thesis.

Chemical	Purchase	Purity	Purpose
Silver nitrate | $AgNO_3$	Sigma-Aldrich	≥99.0%	Catalyst preparation
Titanium dioxide | TiO_2	Sigma-Aldrich	≥99.0%	Catalyst preparation
Titanium tetrachloride | $TiCl_4$	Sigma-Aldrich	≥99.0%	Catalyst preparation
Zirconium (IV) oxychloride octahydrate | $ZrOCl_2.8H_2O$	Sigma-Aldrich	≥99.5%	Catalyst preparation
Di-ammonium phosphate | $(NH_4)_2HPO_4$	Riedel-de Haën	≥99.0%	Catalyst preparation
Sodium hydroxide | NaOH	Sigma-Aldrich	≥98.0%	Catalyst treatment
Nitric acid | HNO_3	Merck Millipore	65%	Catalyst treatment
Hydrogen peroxide | H_2O_2	Merck Millipore	30%	Catalyst treatment
Sodium borohydride | $NaBH_4$	Sigma-Aldrich	≥96.0%	Catalytic reaction
Methylene blue | $C_{16}H_{18}ClN_3S$	Sigma-Aldrich	≥98.0%	Catalytic reaction
Methyl orange | $C_{14}H_{14}N_3NaO_3S$	Sigma-Aldrich	≥98.0%	Catalytic reaction
4-Nitrophenol | $C_6H_5NO_3$	Sigma-Aldrich	≥99.0%	Catalytic reaction
Rhodamine B | $C_{28}H_{31}ClN_2O_3$	Sigma-Aldrich	≥95.0%	Catalytic reaction

II.1.2. Preparation of $AgTi_2(PO_4)_3$

(i) Solid-state method

$AgTi_2(PO_4)_3$ fine powder was prepared through a simple solid-state approach as reported in earlier literature[210]. In brief, silver nitrate $AgNO_3$, titanium dioxide TiO_2, and di-ammonium phosphate $(NH_4)_2HPO_4$ were mixed in stoichiometric quantities and ground together for one hour. The mixture was then placed in a ceramic crucible and heated at 450 °C for 4 h in a muffle furnace. Afterward, the sample was ground again and heated at 600, 800, and 900 °C for 48 h in an air atmosphere to produce the final Ag-based NASICON phase.

(ii) Co-precipitation method

$AgTi_2(PO_4)_3$ was also prepared using a straightforward method that involved co-precipitation followed by calcination. The starting precursors were $AgNO_3$, $TiCl_4$ solution and $(NH_4)_2HPO_4$. In a typical procedure, a solution of $TiCl_4$ was softly mixed with an aqueous solution of $AgNO_3$ while stirring moderately in an ice bath, Then, an aqueous solution of $(NH_4)_2HPO_4$ was added to the above mixture drop-wise. After mixing for 2 h, an amorphous precipitate was produced. The obtained solid precipitate was then dried overnight at 80 °C and after grinding in an agate mortar, it was progressively heated, with intercepted grinding, up to 800 °C for 24 h in an air atmosphere. Finally, it was annealed to 900 °C for 12 h.

II.1.3. In situ self-growth of Ag nanoparticles on $AgTi_2(PO_4)_3$

Ag NPs were self-grown on the surface of $AgTi_2(PO_4)_3$ through an *in situ* reduction process at ambient temperature (25 °C) in the presence of $NaBH_4$. A mass of 0.2 g of $AgTi_2(PO_4)_3$ sample was added to 100 mL of double distilled water (DDW) and dispersed by ultrasonic treatment for 5 min, followed by stirring for another 5 min. Then, 100 mL of $NaBH_4$ (C = 6.14 mM) was added to the above heterogenous suspension while continuously stirring. The ratio of concentration between $NaBH_4$ and the Ag^+ contained in the NASICON-type material was 1.5 : 1. After reaction for 10 min, Ag NPs were self-supported on the surface of $AgTi_2(PO_4)_3$ as shown in Fig. II.1. Finally, the formed Ag-nanocomposite was centrifuged, washed several times by DDW, and dried overnight at 60 °C.

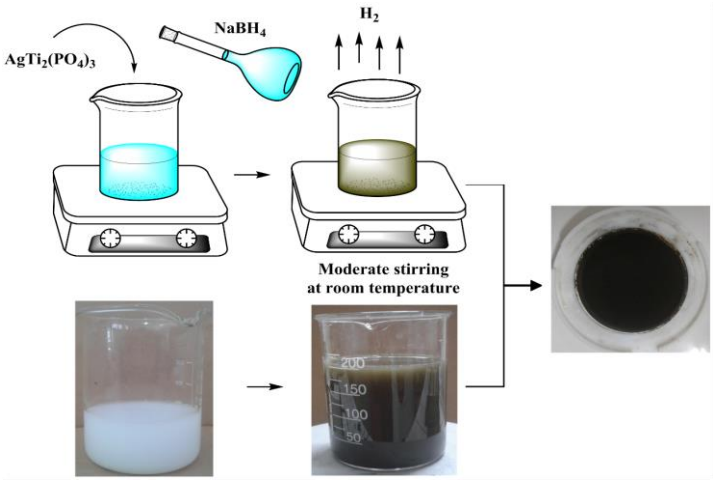

Figure II. 1. In situ formation of Ag NPs on $AgTi_2(PO_4)_3$ surfaces.

II.1.4. Preparation of $AgZr_2(PO_4)_3$

$AgZr_2(PO_4)_3$ NASICON-type material was prepared according to the previous report.[24] First, stoichiometric quantities of $AgNO_3$, $ZrOCl_2.8H_2O$, and $(NH_4)_2HPO_4$ were separately dissolved in a minimal amount of DDW. The zirconium solution was then smoothly mixed with the silver solution while stirring, followed by the drop-wise addition of the phosphate solution. Immediately a gelatinous white precipitate occurred which became more consistent after 2 h of stirring. Subsequently, the solid

precipitate was dried overnight at 80 °C, and after being grinded thoroughly in an agate mortar, it was calcined for 12 h in a muffle furnace at several different temperatures (400, 600, and 800 °C), with intermediate grinding between each temperature stage. The $AgZr_2(PO_4)_3$ NASICON phase formation began at 800 °C and was fully achieved at 900 °C for 48 h.

II.1.5. In situ self-growth of Ag nanoparticles on $AgZr_2(PO_4)_3$

The production of Ag NPs from $AgZr_2(PO_4)_3$ was accomplished through a wet chemical reduction at room temperature with varying amounts of $NaBH_4$ concentrations. Firstly, five masses of $AgZr_2(PO_4)_3$ sample (m_i = 200 mg) were separately suspended in 100 mL of cooled DDW. Then, different volumes (V_x = 8, 14, 20, 30, and 100 mL) were taken from a freshly made solution of $NaBH_4$ (Ci = 17.38 mM) and diluted to 100 mL with cooled DDW. Next, Each of the sodium borohydride solutions ($V_{1\rightarrow5}$) was softly added to the $AgZr_2(PO_4)_3$ heterogeneous solutions while stirring continuously. The ratio of concentration between $NaBH_4$ and $AgZr_2(PO_4)_3$ were 0.4 : 1 (Solution referred to as $S_{0.4}$), 0.7 : 1 ($S_{0.7}$), 1 : 1 (S_1), 1.5 : 1 ($S_{1.5}$) and 5 : 1 (S_5). As the $NaBH_4$ solutions were mixed with the Ag precursor solutions, the color of the mixtures changed from white ($AgZr_2(PO_4)_3$ suspension) to yellow-brown for $S_{0.4}$, $S_{0.7}$, and S_1 and to yellow-green for S_4 and S_5. This indicated the formation of Ag NPs as shown in Fig. II.2(a) to (f). After 2 hours of stirring, the resulting products were centrifuged for 40 min, rinsed with DDW, and then dried at 60 °C overnight (see Fig. II.2(b') to (f')). The filtrates from solutions $S_{0.4}$ to S_5 (Fig. II.2(b'') to (f'')) were analyzed chemically to determine the amount Ag NPs that were not supported and had leaked into the solutions.

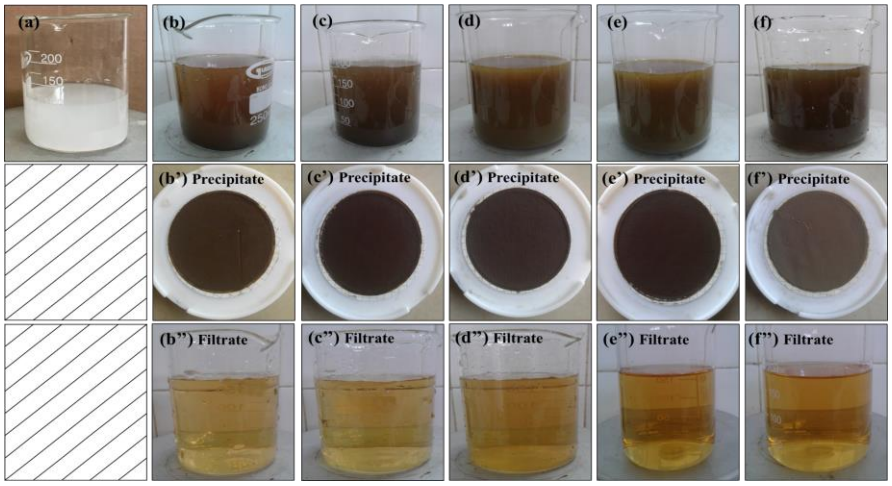

Figure II. 2. Colors solutions of $AgZr_2(PO_4)_3$ (a) as-synthesized, and after reduction by $NaBH_4$ at the molar ratio (b, b' and b'') $\frac{[BH_4^-]}{[AgZrP]}$ = 0.4, (c, c' and c'') $\frac{[BH_4^-]}{[AgZrP]}$ = 0.7, (d, d' and d'') $\frac{[BH_4^-]}{[AgZrP]}$ = 1, (e, e' and e'') $\frac{[BH_4^-]}{[AgZrP]}$ = 1.5, and (f, f' and f'') $\frac{[BH_4^-]}{AgZrP}$ = 5.

II.1.6. In situ self-growth of Ag_2O nanoparticles on $AgZr_2(PO_4)_3$

The $Ag_2O/AgZr_2(PO_4)_3$ nanocomposite material was prepared by the facile *in situ* self-formation of Ag_2O particles on $AgZr_2(PO_4)_3$ surface at room temperature using sodium hydroxide, NaOH, as a

precipitation agent. The preparation procedure of the $Ag_2O/AgZr_2(PO_4)_3$ sample was as follows: 0.4 g of $AgZr_2(PO_4)_3$ powder was dispersed into 100 mL of DDW followed by ultrasound treatment for 20 min. Then, 100 mL of aqueous NaOH (50 mM) was added to the above suspension, and the mixture was stirred for 30 min in the dark at room temperature. Finally, the obtained brown product was recovered by filtration, washed several times, and dried in an oven overnight.

II.2. Characterization techniques

This section outlines the characterization techniques utilized in the current study to determine crystallographic information, identify functional groups, capture characteristic micrographs, analyze morphology and surface structure, and examine surface and bulk elemental composition. The experimental and theoretical methods being mostly applied in this thesis are reported in this section.

II.2.1. X-ray diffraction (XRD) analysis

X-ray diffraction is a valuable analytical method for identifying unknown crystalline phases as well as for the qualitative and quantitative analysis of described crystalline phases.[214] Crystalline solids can be considered as a periodic arrangement of identical lattice points linked in space by three vectors forming a crystal lattice. X-ray diffraction experiments can determine the unit cell and the positions of atoms within the crystallographic cell. In an X-ray diffractometer, a metal target (usually Cu or Mo) is bombarded with high-energy electrons to produce X-rays. A filter is used to absorb undesirable components and obtain a monochromatic X-ray with a strong characteristic Kα line for diffraction. Phase identification is achieved when a beam of the monochromatic X-ray hits a set of parallel lattice planes (identified by the Miller index, hkl) at an angle of θ. Each atom within the planes elastically scatters the incident radiation in all directions without any change in energy. Constructive interference (diffraction) occurs only when Bragg's Law is obeyed, Eq. II.1.

$$n\lambda = 2d\,sin\theta \qquad (\mathbf{II.1})$$

Here, n is an integer that represents the order of diffraction, λ is the X-rays wavelength, d is the distance between atomic planes of a specific (hkl) crystal lattice, and θ is the angle between the incoming X-rays and the diffraction plane. By keeping the wavelength of the X-rays constant and measuring the angle θ, we can find out the distance d between various planes in a crystal. The direction of diffraction is determined by the size and shape of the crystallographic cell, while the intensity of a diffracted beam is related to the positions of atoms within the unit cell. Fig. II.3 shows the principal of XRD.[215]

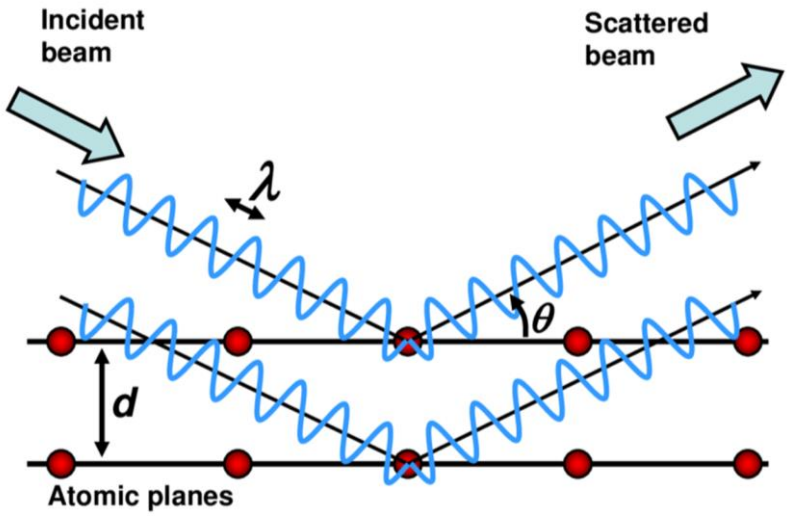

Figure II. 3. Scheme of the diffraction geometry. 2dsinθ represents the path length between crystal plane.

The average size of crystals in powder form can be estimated using the Scherrer equation,[216] which is applied to the most intense peaks in the X-ray diffraction pattern. In Scherrer's formula, the line width of a specific X-ray diffraction peak is inversely related to the crystallite particle size Eq. II.2.

$$\boldsymbol{D = \frac{K\lambda}{\beta cos\theta}} \qquad (\mathbf{II.2})$$

where *D(nm)* represents the average size of the crystallite particles. *K* is a factor that accounts for the shape of the particles. For roughly spherical crystals, the shape factor is usually around 0.9. λ represents the wavelength of the X-rays (which is 0.154 nm for Cu(Kα)). β is the full width at half maximum (FWHM) of the selected diffraction line (in radians). θ is Bragg's diffraction angle for the chosen peak.

Instrument specification:

In the current study, we used a Shimadzu 6100 diffractometer with Cu(Kα) radiation, operating at a current of 30 mA and an accelerating voltage of 40 kV, to perform XRD measurements at room temperature. We scanned the diffraction angle (2θ) from 10 to 70° with a step size of 0.02° and a scan speed of 1.2°/min, and recorded the diffraction intensity versus 2θ. Finally, to identify the crystalline phases we matched the diffraction peaks with the International Centre for Diffraction Data (ICDD) database.

II.2.1.1. Rietveld method

The characterization of a crystal structure can only be considered complete when the crystallographic parameters are refined using the experimentally obtained diffraction data. In this context, the Rietveld refinement represents a useful technique for obtaining structural information and the quantitative analysis of phases from an X-ray diffraction pattern.[217] The software performs a series of cyclic calculations of the user-selected parameters (including lattice parameters, atomic positions, site

occupancies, preferred orientation, and both shape and peak width, etc.) to reduce the difference between the experimental data and a diffraction pattern derived from a given structure model. The Rietveld method consists of an approximation of a calculated line profile to the experimentally obtained X-ray pattern using a non-linear least squares fit of a structural model and a non-structural model (profile, parameter, instrumental and spectral), which depends on the angular variation of the linewidths and the peak shape.[218,219] This least-squares refinement leads to a minimal residual quantity Sy expressed as, Eq. II.3:

$$\boldsymbol{S_y = \sum_i w_i (y_{o,i} - y_{c,i})^2} \qquad \textbf{(II. 3)}$$

where w_i is the weight factor, defined as $w_i = \frac{1}{y_{o,i}}$, $y_{o,i}$ is the intensity observed at each step i (2θ) and $y_{c,i}$ is the intensity calculated at each step i.

There are four different categories which contribute to the intensities of the experimentally obtained X-ray diffraction patterns and these are: (i) Instrumental factors: diffractometer efficiency, X-ray intensity from the source, etc.; (ii) Structural factors: atomic dispersion factors, structure factor, polarization, multiplicity and temperature; (iii) Sample factors: absorption, size, crystallization and orientation of the crystallites; and (iv) Measurement factors: includes the method for the measurement of the peaks area, the method for the obtention of the background, peaks produced by the K(2α) radiation and smoothness.

Therefore, the intensity $y_{c,i}$ at each position i is calculated as, Eq. II.4:

$$\boldsymbol{y_{c,i} = y_{b,i} + \sum_{\varphi} S_{\varphi} \sum_{K} L_{\varphi,K} |F_{\varphi,K}|^2 \Phi(2\theta_i - 2\theta_{\varphi,K}) P_{\varphi,K} A_{\varphi,K}} \qquad \textbf{(II. 4)}$$

where $y_{b,i}$ represents the background intensity. The subscript "φ" denotes the various crystalline phases, while the subscript "K" denotes the hkl Miller indexes of the Bragg diffractions. S_{φ} is the Rietveld scale factor of the phase φ. The term $L_{\varphi,K}$ includes the multiplicity and Lorentz-polarization factors. $F_{\varphi,K}$ represents the structure factor. Φ is the reflection profile function that models both instrumental and sample effects. $P_{\varphi,K}$ is the preferred orientation function. $A_{\varphi,K}$ is the absorption correction. The summation is over all phases.

The exhaustive information obtained from the Rietveld analysis allows for the following applications:

i) Crystal structure refinement: this method allows to refine cell parameters, atomic positions, thermic factors and atoms occupancy.

ii) Microstructural characterization of the different phases: determination of the crystallite size, micro-deformations found in the crystal network and preferred orientations.

iii) Quantitative analysis of multi-phase materials: determination of the proportions of the different phases in the sample by means of their corresponding scale factors (S).

The Rietveld refinement not only requires a profile function to model the diffraction peaks but also functions that model the FWHM, the asymmetry, the preferred orientation, the background, etc.

- Profile Functions:

The peak description is usually described by three parameters: the peak position, the intensity and the width of the function which is represented by the FWHM. The most used symmetric profile functions are defined by the following Eq. **II.**5, to II.7:

$$\boldsymbol{Gaussian\ (G) = \frac{C_0^{1/2}}{H_i \pi^{1/2}} exp\left[-\frac{C_0(2\theta_i - 2\theta_k)^2}{H_i^2}\right]} \qquad \textbf{(II. 5)}$$

$$\boldsymbol{Lorentzian\ (L) = \frac{\sqrt{C_1}}{H_i \pi} exp\left[\frac{1}{1 + \frac{C_1(2\theta_i - 2\theta_k)^2}{H_i^2}}\right]} \qquad \textbf{(II. 6)}$$

$$\boldsymbol{Pseudo\ Voigt\ (V_p) = \eta Gaussian\ (G) + (1 - \eta) Lorentzian\ (L)} \qquad \textbf{(II. 7)}$$

The Pseudo-Voigt function is a convolution of Gaussian and Lorentzian function, with **η** is a refinable parameter. In this thesis we adopted the Pseudo-Voigt function to model our experimental XRD patterns.

- Full width at half maximum (FWHM):

The FWHM is typically modelled using the following Eq. **II.**8:

$$\boldsymbol{FWHM^2 = H_i = U\ tan^2(\theta_i) + V\ tan\theta_i + W} \qquad \textbf{(II. 8)}$$

where U, V and W are the refined Caglioti parameters.

- Preferred Orientation:

The intensity of the diffraction peaks can be altered by the orientation of the crystallites, which adopt a random orientation or a preferred orientation (tendency of the crystallites to orientate towards a given crystallographic direction). The effects of a preferred orientations are included in the diffraction profile by means of the function $P_{\varphi,K}$, where φ represents the acute angle between the scattering vector and the normal of the crystallites, Eq. II.9:

$$\boldsymbol{P(\varphi) = G_2 + (1 - G_2) e^{-G_1 \varphi^2}} \qquad \textbf{(II. 9)}$$

where G are the refined parameters. G_1 gives information about the degree of preferred orientation for a given direction, while G_2 indicates the proportion of the phases presenting no orientation.

Quality of the fit

The refinement's quality is determined by how well the calculated pattern matches the experimental pattern; therefore, it is crucial to have a numerical measure to assess the quality of the fits and gain insights into how well the fitted model corresponds to the experimental data. Different indicators (also

called residuals) must be minimized during the refinement to determine the quality of the fit and these are:

a) The profile residual (reliability factor, R_p) and the weighted profile residual (R_{wp}), which quantify the degree of reliability of the fit from a peak's shape point of view, Eq. II.10 and II.11:

$$\boldsymbol{R_p = \frac{\sum|y_i(o) - y_i(c)|}{\sum|y_i(o)|}} \qquad (\mathbf{II.10})$$

$$\boldsymbol{R_{wp} = \sqrt{\frac{\sum w_i|y_i(o) - y_i(c)|^2}{\sum w_i(y_i(o))^2}}} \qquad (\mathbf{II.11})$$

b) The Bragg residual (R_B) and the structure residual factor (R_F), which give information about the reliability of the results from the point of view of the unit cell crystallographic data, and are expressed as follows, Eq. II.12:

$$\boldsymbol{R_B = \frac{\sum|I_i(o) - I_i(c)|}{\sum|I_i(o)|}} \;\; ; \;\; \boldsymbol{R_F = \frac{\sum|F_i(o) - F_i(c)|}{\sum|F_i(o)|}} \qquad (\mathbf{II.12})$$

c) The expected profile residual (R_{exp}) provides information about the quality of the fit, and the goodness of fit (χ^2) gives the difference between the theoretical prediction and the observed data (Eq. II.13 and II.14):

$$\boldsymbol{R_{exp} = \sqrt{\frac{N - P_1 - P_2}{\sum w_i y_i(o)}}} \qquad (\mathbf{II.13})$$

$$\boldsymbol{\chi^2 = \sqrt{\frac{\sum|y_i(o) - y_i(c)|^2}{N - P_1 - P_2}} = \frac{R_{wp}}{R_{exp}}} \qquad (\mathbf{II.14})$$

where, N corresponds to the number of structural parameters and P the number of profile parameters. The value of χ^2 should be close to 1 when there are no systematic errors in the fitted model, but in many cases that's not possible. Ideally the value of χ^2 must be slightly smaller than 4 for an optimal refinement.[220]

Quantitative phase analysis

Rietveld quantitative phase analysis is based on the principle that the diffracted peak intensities by a crystalline phase is proportional to the amount of diffracting material. Therefore, the information about quantitative phase analysis can be extracted from the scale factor, S_φ, that is obtained from the last refinement iteration in Eq. II.4. S_φ accounts for the diffracted peak intensities of each crystalline phase and thus expresses the amount of phase in a crystalline sample. If we assume that a sample with multiple phases is fully crystallized, then the sum of the weight fractions w_φ will be equal to unity. Therefore, the relative weight fraction $w_{\varphi,i}$ of phase i in a mixture of multiple phases was expressed by Hill and Howard[221] according to Eq. II.15:

$$w_{\varphi,i} = \left(\frac{S_{\varphi,i} \cdot (ZMV)_{\varphi,i}}{\sum_{\varphi,j=1}^{N} S_{\varphi,j} \cdot (ZMV)_{\varphi,j}} \right) \times 100 \qquad (\mathbf{II.15})$$

where M_φ represents the molecular weight and Z_φ represents the number of atoms in a unit cell of a volume V_φ. The summation is over all phases. We note that the above equation does not take into account possible corrections due to absorption effects; i.e., absorption of the sample is negligible.

Rietveld method set-up:

In this thesis, we modelled the X-ray diffraction data using the FullProf software[222], with the aim of identifying and quantifying the formed phases. The structure models for the refinement of our Ag-based materials were taken from Crystallography Open Database (COD). We fitted the data with a Pseudo-Voigt function and refined the background with 54 points. We refined these parameters one by one and then together: scale factors, background coefficients, instrumental parameters, lattice constants, atomic displacement parameters (Debye-Waller factors), preferential orientations, atomic positions, profile half-width (u, v, w), and site occupancies. We checked the fitting quality by looking at the goodness of fit (χ^2), the profile residual (R_p) and the weighted profile residual (R_{wp}).

II.2.2. Vibrational spectroscopy

Vibrational spectroscopy measures the energy changes of molecules or groups of atoms when they vibrate upon light excitation. These vibrations can affect the dipole moments of molecules (infrared spectroscopy, IR) or the polarizabilities of molecules (Raman spectroscopy). Depending on the type of spectroscopy, the sample is exposed to:

i) Different wavelengths of light (IR) and absorbs some of them when the dipole moment changes.
ii) One wavelength of light (Raman) and scatters some of it when the polarizability changes.

The energies of the absorbed or scattered light are specific and can be analyzed.

II.2.2.1. Attenuated total reflectance Fourier transform infrared (ATR-FTIR) spectroscopy

Fourier transform infrared (FTIR) is a type of absorption spectroscopy that is used to collect infrared spectra and analyze chemical bonding information.[223] This technique is based on the principle that chemical bonds vibrate at specific frequencies that correspond to their energy levels, allowing for the identification of different bond types based on their vibrational frequencies. One of the most commonly used FTIR sampling tools today is attenuated total reflectance (ATR).[224] The ATR-FTIR technique can be applied to both solid and liquid samples. It typically requires little to no sample preparation and enables qualitative or semi-quantitative examination of samples. The key advantages of ATR sampling are its short sampling time and the deep penetration of the infrared (IR) beam into the sample. The ATR dispositive uses a crystal with a high refractive index, called an internal reflecting element (IRE), coupled with an IR beam. When the IR beam hits the internal surface of the IRE, it reflects back and

produces an evanescent wave that projects orthogonally into the sample placed on the ATR crystal. The fundamental principles of the ATR technique are governed by the refractive index of both the crystal and the sample, as illustrated in Fig. II.4.

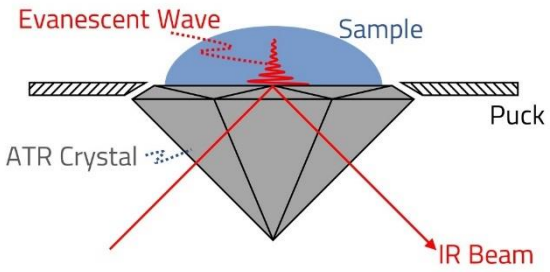

Figure II. 4. Graphical representation of a single bounce ATR.

In the current study, a single-bounce ATR configuration was utilized, where a diamond prism is used to produce a single internal reflection. This ATR configuration is appropriate for analyzing samples with strong absorption and was applied to examine the orthophosphate groups of our Ag-based NASICON powders. Table II.2 lists some of the properties of the diamond employed as the ATR crystal.

Table II. 2. General properties of the ATR crystal.

Material	Wave range (cm^{-1})	Refractive index (at 1000 cm^{-1})	Depth of penetration (μm)	pH range
Diamond	25000-100	2.4	2	1-14

Instrument specification:

In this work, a Jasco FT/IR 4600 spectrometer equipped to an ATR Pro one module (ATR-FTIR) with a single bounce diamond crystal was used to perform FTIR-ATR measurements. The spectra were acquired in the frequency range of 4000-400 cm^{-1} with a resolution scan of 4 cm^{-1}.

II.2.2.2. Raman spectroscopy

Raman spectroscopy is a another useful technique to characterize materials.[225] It involves exciting the molecules or active groups in a sample with incident light and measuring the scattered light. The light that is scattered can be classified into two types; Rayleigh scattering, which is intense and has the same frequency as the incident light, and Raman scattering (or inelastic scattering), which is very weak and has frequencies that differ because of the loss or gain of phonons. The difference of frequency between the incident and scattered light is called the Raman shift, which can be plotted as a Raman spectrum. This Raman shift can identify compounds that scatter light and the peak intensities can reveal information about stoichiometry, stress and crystallinity of the material. Raman spectroscopy is an important and highly sensitive technique for analyzing the electronic transitions and structure of materials.

Fig. II.5 shows three different potential outcomes from Raman spectroscopy. When the incoming and scattered photons have the same energy, the scattering is elastic and referred to as Rayleigh scattering. In Stokes scattering, the photon transfers some of its energy to the target functional group in the sample (in our case the orthophosphate group, PO_4^{3-}, of the Ag-based NASICON-type materials) and excites it to a higher (virtual) energy state. The photon that is emitted has less energy than the incoming photon. This photon involved in this process is referred to as the Raman photon. Stokes scattering occurs when the functional group goes from its ground state (ν_0) to a higher energy level (ν_1). In anti-Stokes scattering, the functional group is already in an excited level (ν_1) and receives more energy from the incoming photon. It then emits a photon with more energy than the incoming photon and returns to a lower ground state (ν_0).

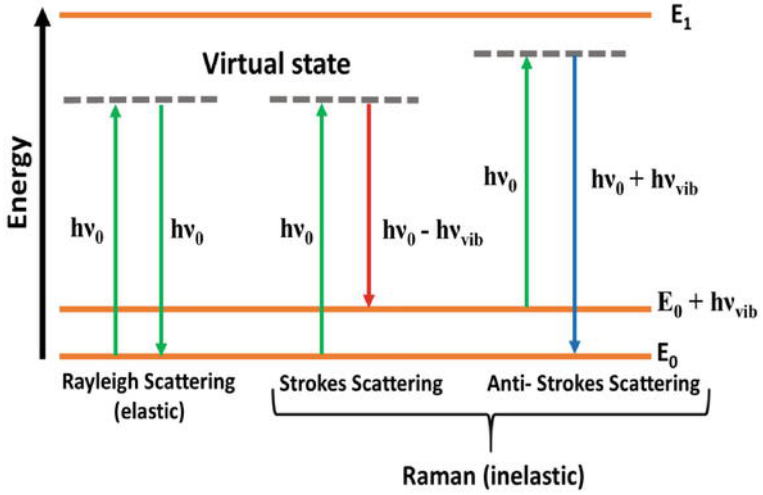

Figure II. 5. Diagram of the energy levels for Rayleigh and Raman scattering.

Instrument specification:

In this thesis, a LabRAM HR Evolution confocal Raman microscope (HORIBA Scientific) with a green laser excitation at 532-nm and a maximum power of 2 mW was used to perform Raman spectroscopy. The spectrum was acquired in the range of 100 and 1700 cm^{-1} with a resolution scan of 2 cm^{-1}.

II.2.3. Scanning electron microscopy (SEM) analysis

Scanning electron microscopy (SEM) is a technique that produces images of a sample's surface by analyzing the interactions between electrons and the sample.[226,227] The SEM works by bombarding the surface of the sample with an electron beam and detecting the particles that are re-emitted. These particles produce a 3D image of the surface. The material's atoms are excited by the incident electrons and emit photons (the de-excitation process). The volume of photon emission is influenced by factors such as the energy of the incident electrons, the atomic number of the material, and the energy level of the ionized state. In the SEM apparatus, a tungsten filament located at the top of the microscope emits an electron beam that hits the sample's surface.[226] A voltage ranging from 1 to 30 kV accelerates electrons emitted from the tungsten filament. The beam is focused and directed by a condenser and

objective lenses in a vacuum, which the electrons pass through. Scanning coils and an aperture let the beam go through them. The beam is moved with high precision by the scanning coils, which act as lenses. When the electrons bombard the sample, they lose energy through various processes. High energy backscattering electrons, secondary electrons from inelastic scattering, and X-ray radiation are produced by this operation. A detector records the secondary electrons from the sample surface and forms the SEM micrographs.[226] The escape of secondary electrons is impeded due to their low energy of approximately 50 eV. This makes the technique highly sensitive to surface features. The morphology of the sample generates image contrast, where surfaces parallel to the beam appear the darkest and surfaces perpendicular to the beam appear the brightest. A 3D image of the sample surface is produced as a result. The image quality is enhanced by high energy backscattered electrons, which are produced by the elastic scattering of the incident electron beam with atoms on the sample surface. The image gets brighter as the nucleus that the beam interacts with has a higher atomic mass (Z number).[226] SEM was used in this work to study the production of Ag NPs on the NASICON material surface. Fig. II.6 exhibits a schematic explanation of how a SEM microscope works.

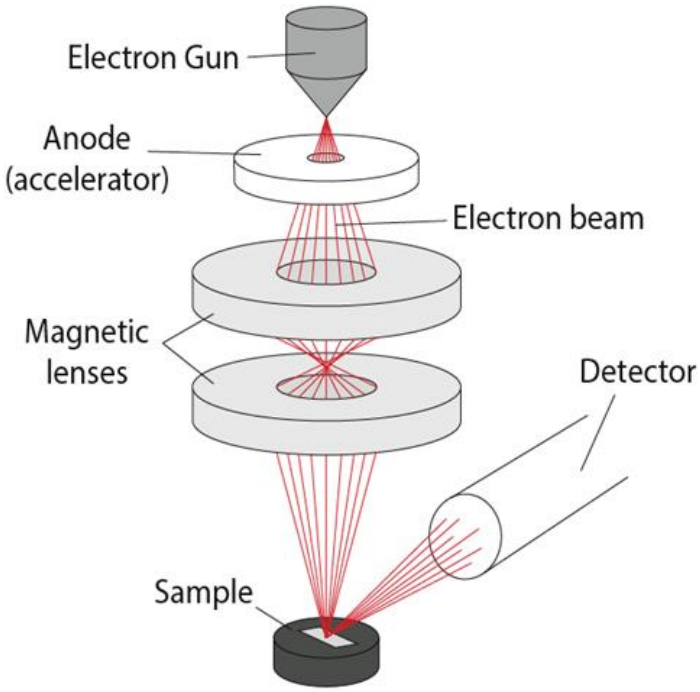

Figure II. 6. Schematic diagram of the scanning electron microscope.

Instrument specification:

In this study, A Thermo Fisher environmental scanning electron microscope with a Schottky field emission gun (Quattro ESEM-FEG) working at voltage of 20 kV and an energy dispersive X-ray spectrometer (EDX) were used to collect scanning electron microscopy (SEM) images. The powdered

samples were attached to stainless steel stubs using carbon tabs and coated with a 2 nm layer of gold, to avoid charge accumulation on the samples surface.

II.2.4. Energy dispersive X-ray (EDX) spectroscopy

Energy dispersive X-ray spectroscopy (EDX) is a characterization method coupled with the SEM technique that allows the determination of the sample's elemental composition. This method fully exploits the fact that each atom has a unique number of electrons that belong to different shells with different energies. Thus, between two shells the energy difference is dependent and characteristic on the atomic number of the element and can be used as a fingerprint of each element, being able to identify the type of elements present in the material.

In the EDX technique, when a beam of primary electrons hits the sample, part of their energy is transferred to the atoms of the sample. As a result, the primary electrons can excite sample electrons off from the inner shells, creating a vacancy site or a hole in the shell. Consequently, the atoms remain in an ionized state. In order to recover its original fundamental state, an electron from a shell with higher energy fills the electron vacancy (which has a positive charge) emitting characteristic X-rays with an energy equal to the energy difference between the two shells. The energy levels of the X-rays that are released rely on and are specific to the elements present in the material. An EDX detector collects the produced characteristic X-rays, which can be used for either qualitative (mapping showing the elemental distribution) or semi-quantitative (atomic concentration of each element of the sample) analysis. The generated data consists of a spectrum containing the peaks of the emitted X-Rays by all the elements in the sample. An additional software permits the auto-identification of the characteristic peaks and the calculation of the atomic percentages of each detected element.

II.2.5. X-ray photoelectron spectroscopy (XPS)

X-ray photoelectron spectroscopy (XPS) is a technique that is sensitive to material surfaces and gives information about elemental composition, elemental composition, and local elemental environment of materials (Fig. II.7(a)).[228] During XPS analysis, the material being examined is subjected to a beam of X-ray photons. The Kα emissions of Al (1486.6 eV) or Mg (1253.6 eV) are usually used.[229] When the X-ray photon beam bombards the sample, it causes a photoelectron to be ejected, leaving behind a core hole (Fig. II.7(b)). The kinetic energy of the ejected electrons can be determined and their binding energy can be calculated following Eq. II.16:

$$E_{kin} = h\nu - E_{BE} - \phi \qquad (\mathbf{II.16})$$

where E_{kin} expresses the kinetic energy of the ejected electron collected by the detector, hν represents the incoming X-ray photon energy, E_{BE} is the electron binding energy, and ϕ is the photoelectric work function. Here, the binding energy is characteristic of the element that emits the electron as well as the orbitals wherein the electron is located. Thus, separation of the kinetics energy by the analyzer and

subsequent plotting of the intensities versus the calculated binding energies enables the identification of the type of atom, oxidation state and quantification of the abundance of the elements present near the surface region. Finally, once the photoelectron is ejected from the core, the atom compensates the charge by emitting an Auger electron or an X-ray photon (Fig. II.7(c)).

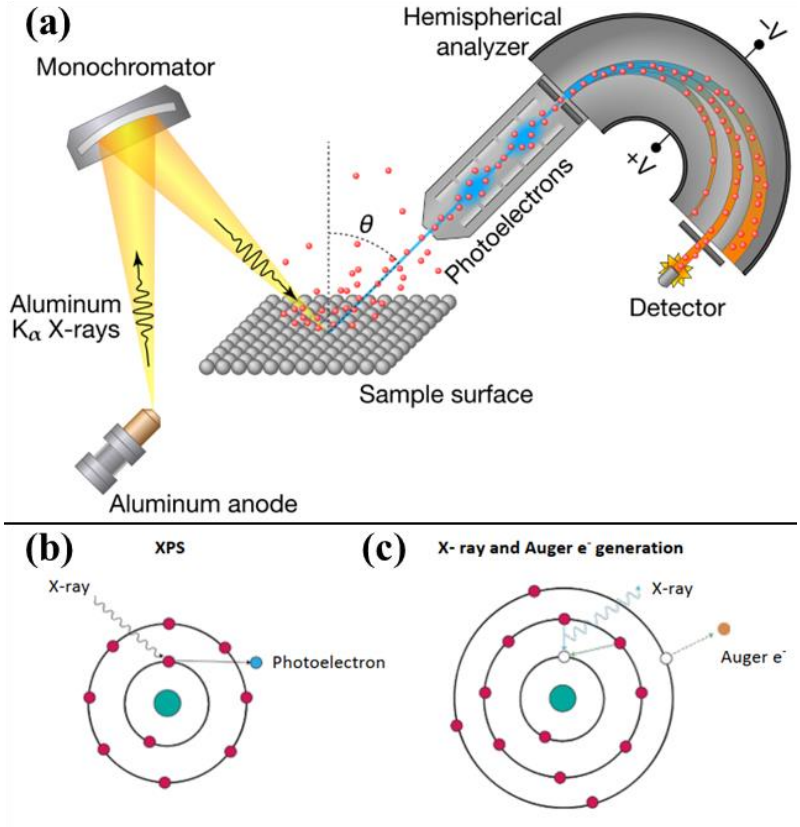

Figure II. 7. Illustration of basic instrumentation for X-ray photoelectron spectroscopy, (b) ejection of photoelectrons in XPS, and (c) relaxation process with generation of an X-ray and/or emission of an Auger electron.

The binding energy can be matched with a list of standard values from the NIST database. This can help identify chemical identity and environment.[230] The orbital of the photoelectron influences the XPS spectrum. When a photoelectron is emitted from an orbital other than the s orbital ($l > 0$), spin coupling interactions occur between the electron spin (s) and the angular momentum (l), resulting in the total angular momentum (j). Since the electron spin can be $\pm 1/2$, two possible values for j exist. s orbitals have no orbital angular momentum ($l = 0$), in this case the XPS spectrum will show singlet peaks. On the other hand, for all remaining orbitals, spin coupling causes XPS peaks to split into a doublet. The ratio of these peaks is $2j+1$. For instance, when observing emission from a 2p orbital, where the angular momentum (l) is equal to 1, its total angular momentum (j) can have two values 3/2 or 1/2.

Instrument specification:

In this thesis, a PHI VersaProbe III photoelectron spectroscope (Physical Electronics) with Al (Kα) (1486.71 eV) as the radiation source was used to perform X-ray photoelectron spectroscopy (XPS). The materials were placed in a vacuum chamber with a base pressure of 5×10^{-9} mbar, and the X-ray beam was focused on a 100-micron spot on the materials surface, defining the area of analysis. Survey spectra and high-resolution spectra were obtained using pass energies of 200 and 5 eV, respectively. The charge of spectra was corrected using the adventitious C1s, which had a binding energy of 284.6 eV.

II.2.6. Ultraviolet-Visible diffuse reflectance spectroscopy (UV-Vis DRS)

Ultraviolet-visible diffuse reflectance spectroscopy (UV-Vis DRS) is a widely used and essential sampling tool for the determination of SCs materials properties. When the incident radiation is absorbed by the sample surface, it can be scattered, transmitted and reflected. Considering that the material contains layers in where the crystallites are randomly oriented, the light beam interacts with the particles of the material and it can be scattered to deeper layers via random reflections and dispersions. Diffuse reflectance occurs when the incident radiation is scattered and returned back to the surface to be re-emitted in any possible angle (Fig. II.8(a)). Before recording the reflectance spectrum of any sample, it is important to first record the reflectance spectrum of a standard reference, such as a spectralon white disk that reflected 100% of light (Fig. II.8(b)).

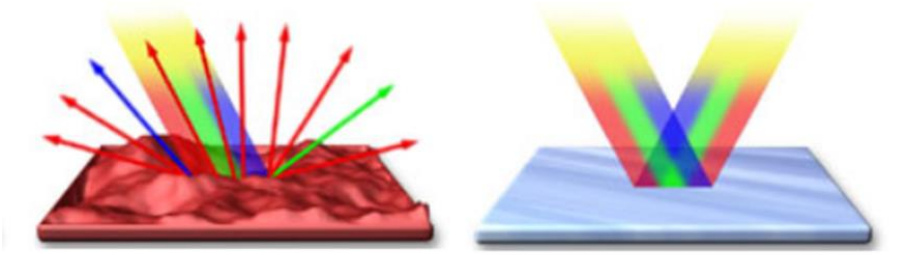

(a) Diffuse reflection **(b) Specular reflection**

Figure II. 8. Illustration of a light beam being reflected on (a) a rough surface (sample), and (b) a smooth surface (reference sample).

UV-Visible DRS uses a spectrophotometer with an integrated sphere. The integrated sphere is an optical arrangement with a cavity that has a uniform coating of highly reflective material like barium sulphate ($BaSO_4$) on the inner surface. The spheres have small aperture that let radiation to pass through the sample, enter the sphere, and be captured by the detector's optics.

Instrument specification:

In this work we used a Perkin Elmer Lambda 900 UV/Vis Spectrometer with an integrating sphere to analyze the optical absorption and band gap energies of NASICON materials. The optical characteristics

of the powders material were measured across the wavelength range of 190-1100 nm using as a reference material a spectralon disk.

II.2.6.1. Optical bandgap calculation

The band gap of a SC material is the difference of energy between the highest energy level in the VB and the lowest energy level in the CB. An electron needs at least this much energy to move from the VB to the CB. The band gap of a SC material can be either direct or indirect. The CB's lowest-energy state and the VB's highest-energy state have a specific crystal momentum (k-vector). In a direct band gap SC, these states have the same k-vector, allowing an electron to directly emit a photon after absorbing light. In an indirect band gap SC, these states have different k-vectors, so an electron has to transfer a phonon to the crystal lattice before emitting a photon. Fig. II.9 shows a diagram of the band gap.

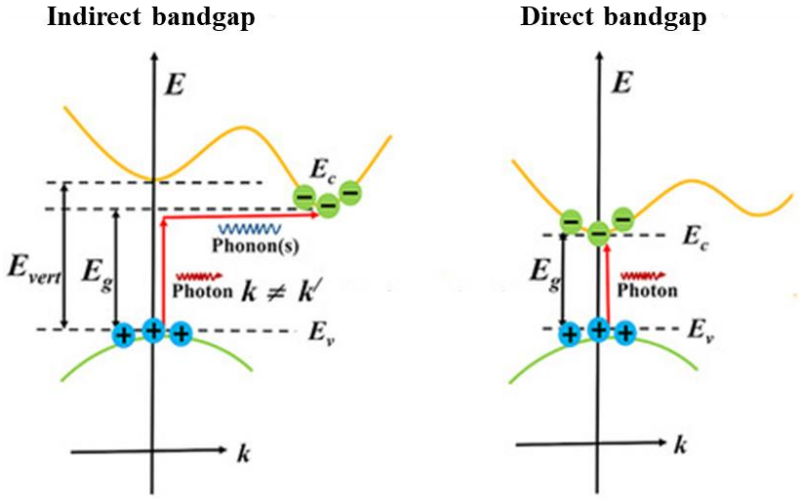

Figure II. 9. Schematic of indirect and direct bandgap energy.

A material's band gap energy can be calculated by plotting optical absorbance data with respect to the energy. For this, the raw diffuse reflectance spectrum is converted to the absorbance spectrum by using the Kubelka-Munk equation,[231] Eq. II.17:

$$\boldsymbol{F(R) = \frac{(1-R)^2}{2R} \approx \alpha} \qquad \textbf{(II. 17)}$$

where R represents the reflectance measured from the UV-Vis DRS in diffuse reflectance mode. Tauc (1966)[232] proposed in his studies about the electronic and optical properties of amorphous germanium the relation, $\omega^2\varepsilon_2 = (h\omega - E_g)^2$, for the determination of the absorption near the edge, which is interpreted as due to indirect transitions (n = 2). Subsequently, Davis and Mott (1970) described a new theoretical model (Eq. II.18) based on the original Tauc relation, where A is a material specific constant.[233] In order to translate the diffuse reflectance spectra into the absorption spectra, the absorption coefficient (α) is replaced on the David and Mott equation by the Kubelka-Munk function,

which is proportional to the absorption coefficient (α). This approach is widely used for the determination of band gaps and the state transition in SCs (Eq. II.19).

$$(\boldsymbol{\alpha h\nu})^{1/n} = \boldsymbol{A}(\boldsymbol{h\nu} - \boldsymbol{E_g}) \qquad (\mathbf{II.18})$$

$$(\boldsymbol{F(R)h\nu})^{1/n} = \boldsymbol{A}(\boldsymbol{h\nu} - \boldsymbol{E_g}) \qquad (\mathbf{II.19})$$

According to the Eq. II.19, h corresponds to the Planck's constant, ν denotes the vibration frequency, A represents a constant of proportionality, and Eg expresses the optical band gap. The value of the exponent n indicates the type of the transition occurring in the sample: (i) for direct allowed transition, n = 1/2, (ii) for indirect allowed transition, n = 2, (iii) for direct forbidden transition, n = 3/2, and (iv) for indirect forbidden transition, n = 3. Tauc plots are built by plotting the quantity $(\alpha h\nu)^{1/n}$ on the ordinate versus the photon energy (hν) on the abscissa and the optical band gap energy (Eg) can be determined from Tauc plots by drawing a tangent line to the band edge.

II.3. Analytical method

II.3.1. Ultraviolet-Visible (UV-Vis) spectroscopy

UV-Vis spectroscopy measures how light in the ultraviolet and visible spectral region (200-800 nm) interacts with matter in terms of absorption or reflectance. Molecules with π-electrons or non-bonding electrons can use the ultraviolet or visible light energy to excite these electrons to higher energy levels. The difference of energy between the initial states and final states determines the wavelength of the light that is absorbed, according to Bohr relation, $\Delta E = \frac{hc}{\lambda}$.

UV-Vis spectroscopy can also measure the concentration of a solute in a given solution based on the Beer-Lambert law.[234] When light passes through a solution placed in a cuvette (Fig. II.10), the transmittance is the fraction of light that goes through the solution (I) compared to the light that hits the solution (I_0).

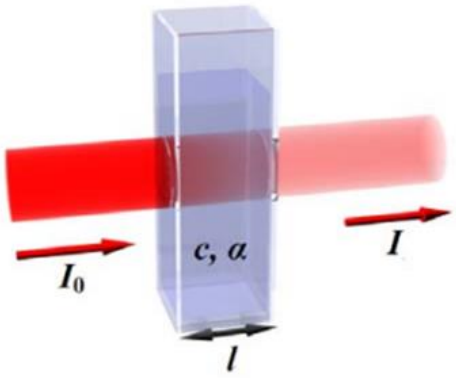

Figure II. 10. Representation of the Beer-Lambert law upon light absorption in liquid media.

The light intensity that passes through a solution, I, depends on the initial light intensity, I_0, the length of the cuvette that contains the solution, l, and the concentration of the solute that absorbs light, C.[235] This relationship is given by Eq. II.20:

$$\boldsymbol{I = I_0\ 10^{-\varepsilon lC}} \qquad (\mathbf{II.20})$$

where ε represents the extinction coefficient (also referred as the molar absorption coefficient) of the solute. The attenuation of the intensity of light due to absorption by the solution in a cuvette is expressed by Eq. II.21:

$$\boldsymbol{A = \log\left(\frac{I}{I_0}\right) = -\log T} \qquad (\mathbf{II.21})$$

The Beer-Lambert law shows that the absorbance of the solution depends linearly on the light-absorbing solute concentration and the solution length following Eq. II.22:

$$\boldsymbol{A = \log\left(\frac{I}{I_0}\right) = \varepsilon lC} \qquad (\mathbf{II.22})$$

UV-Vis spectroscopy analysis measures I and I_0 intensities either at the same time or one after another depending on the type of spectrophotometer (single or double beam). A "blank" is used to measure I_0, which accounts for the light absorbed and/or reflected by the cuvette and the solvent. The solute will absorb different amounts of light at different wavelengths. These values are plotted on a graph called an absorption spectrum, which shows absorbance versus wavelength.

Instrument specification:

In this work, absorption spectra were obtained on an Analytik jena, Specord 210 plus spectrophotometer by scanning the wavelength from 200 to 800 nm using 1 cm quartz cells and distillated water as blank.

II.4. Computational methods

There are many computational tools applied to calculate the properties of materials. Depending on the subject at hand and the accuracy with which certain structural and electronic aspects of the system under examination can be resolved, many different models are available,[236] which can often be usefully used across a wide range of length and time scales. Thus, before embarking on computational calculations, as often the case in research, it is critical to first establish which properties and phenomena we are most interested in as well as what kind of questions one is going to answer. In the current work, since we are interested in the electronic properties of our material, we need to be able to account for quantum mechanics, and for this purpose we have applied density functional theory (DFT) as the most accurate choice. The following section discusses and explains in details the basics of DFT as a powerful quantum mechanical approach for electronic structure calculations in terms of the approximations that are considered.

II.4.1. Quantum mechanical many-body problem

Before going through the DFT more carefully, it would be helpful to take a step back and review some fundamental quantum mechanics. So, in 1925, Erwin Schrödinger [237] , utilized de Broglie's relations to describe the properties of matter at the nanoscale. This led to the formulation of the famous time-dependent Schrödinger equation that bears his name.

$$i\hbar\frac{\partial}{\partial t}\Psi(\vec{r},t) = \hat{H}\Psi(\vec{r},t) \qquad (\mathbf{II.23})$$

where ħ expresses the Planck's constant (h) divided by 2π, $\hat{H}$ is the time dependent Hamiltonian operator, which corresponds to the system total energy, $\Psi(\vec{r}, t)$ represents the time dependent wave function, which tells us the probability of finding a particle in some region in space at a time t, and $\vec{r}$ is the position.

with

$$\hat{H} = \hat{T} + \hat{V} = -\frac{\hbar^2}{2m}\vec{\nabla}^2 + V(\vec{r},t) \qquad (\mathbf{II.24})$$

where $\hat{T}$ denotes the kinetic-energy operator and $\hat{V}$ is the potential energy operator, m is the particle mass, and ∇ is the Laplace operator.

The application of the Hamiltonian to a single particle results in the time-dependent Schrödinger equation:

$$i\hbar\frac{\partial}{\partial t}\Psi(\vec{r},t) = \left[-\frac{\hbar^2}{2m}\vec{\nabla}^2 + V(\vec{r},t)\right]\Psi(\vec{r},t) \qquad (\mathbf{II.25})$$

while for N particles in 3 dimensions, the Schrödinger equation is represented as follows:

$$i\hbar\frac{\partial}{\partial t}\Psi(\vec{r}_1,\vec{r}_2,\ldots,\vec{r}_N,t) = \left[\sum_{i=1}^{N} -\frac{\hbar^2}{2m}\vec{\nabla}^2 + V(\vec{r}_1,\vec{r}_2,\ldots,\vec{r}_N,t)\right]\Psi(\vec{r}_1,\vec{r}_2,\ldots\vec{r}_N,t) \quad (\mathbf{II.26})$$

However, special cases are the solutions of the above equation, where the Hamiltonian itself has no dependence on time, and the solution then describe standing waves, also known as stationary states or orbitals. This also implies a time-independent potential $V(\vec{r}_1,\vec{r}_2,\ldots\vec{r}_N)$. Not only is the time-independent Schrödinger equation simpler to solve, but its solutions also offer valuable understanding for resolving the related time-dependent equation.

The time-independent Schrödinger equation can be treated by separating the spatial and temporal parts of the wave function using the separation of variables approach via:

$$\Psi(\vec{r},t) = \psi(\vec{r})f(t) \qquad (\mathbf{II.27})$$

Introducing this expression into Eq. II.25, and solving the equation by separation of variables yields:

$$f(t) = e^{-iEt/\hbar} \qquad (\mathbf{II.28})$$

and

$$\left[-\frac{\hbar^2}{2m}\vec{\nabla}^2 + V(\vec{r})\right]\psi(\vec{r}) = E\psi(\vec{r}) \qquad \textbf{(II.29)}$$

The second equation above is the single-particle time-independent Schrödinger equation.

while for N particles in 3 dimensions, the equation is represented as follows:

$$\left[\sum_{i=1}^{N} -\frac{\hbar^2}{2m}\vec{\nabla}^2 + V(\vec{r}_1, \vec{r}_2, \ldots, \vec{r}_N)\right]\psi(\vec{r}_1, \vec{r}_2, \ldots \vec{r}_N) = E\psi(\vec{r}_1, \vec{r}_2, \ldots, \vec{r}_N) \qquad \textbf{(II.30)}$$

The electrostatic interaction is the only basic interaction that matters in solid-state physics and chemistry. Therefore, for a system composed of M nuclei A with a mass M_A and a charge Z_A as well as N electrons i, the Schrödinger equation is described by a Hamiltonian of a well-defined form,

$$\hat{H} = \sum_{i=1}^{N} -\frac{\hbar^2}{2m}\vec{\nabla}^2 + V(\vec{r}_1, \vec{r}_2, \ldots, \vec{r}_N) = \hat{T}_{nucl} + \hat{T}_{elec} + \hat{V}_{elec-nucl} + \hat{V}_{elec-elec} + \hat{V}_{nucl-nucl} \quad \textbf{(II.31)}$$

$$\hat{H} = -\sum_{A=1}^{N}\frac{\hbar^2}{2M_A}\vec{\nabla}_A^2 - \sum_{i=1}^{N}\frac{\hbar^2}{2m_e}\vec{\nabla}_i^2 - \sum_{i=1}^{N}\sum_{A=1}^{M}\frac{Z_A e^2}{4\pi\varepsilon_0 r_{iA}} + \sum_{i=1}^{N}\sum_{j>i}^{M}\frac{e^2}{8\pi\varepsilon_0 r_{ij}} + \sum_{A=1}^{M-1}\sum_{B>1}^{M}\frac{Z_A Z_B e^2}{8\pi\varepsilon_0 R_{AB}} \quad \textbf{(II.32)}$$

with $\hat{T}_{nucl}$ is the nuclei kinetic energy, $\hat{T}_{elec}$ is the electrons kinetic energy, $\hat{V}_{nucl-elec}$ the potential energy for the attraction between nuclei and electrons, $\hat{V}_{elec-elec}$ the potential energy for the electron-electron repulsion and $\hat{V}_{nucl-nucl}$ the nuclei-nuclei repulsive potential energy term. r_{iA}, r_{ij} and R_{AB} are respectively the distances from electron i to nucleus A, from electron i to electron j, and from nucleus A to nucleus B.

In principle, this Hamiltonian (Eqs. II.31 and 32) can be used to solve for the energy levels of an interacting system using the time-independent Schrödinger equation, Eq. II.30. However, solving this equation by hand would be too complex and would result in unmanageable calculations for systems with more than one electron. This is due to the strong interactions between electrons, which results in the many-body problem. To avoid such an impasse, a range of physically justified and consistent approximations have been developed.

Born-Oppenheimer approximation

The many-body problem, as mentioned above, was simplified by the Born-Oppenheimer approximation in 1927.[238] This approach separates Schrödinger's equation into nuclear and electronic parts, taking into account that nuclei are significantly heavier and move at a slower rate compared to electrons. Hence, the Born-Oppenheimer approximation assumes that the nuclei are fixed at specific points "frozen", and that the electrons are subject to a potential generated by each fixed nucleus configuration depending on each atom. This means that the term associated with the kinetic energy of the nuclei, $\hat{T}_{nucl}$, can be

ignored, allowing the Hamiltonian to be represented as the sum of an operator that solely depends on the electron coordinates ($\hat{H}_{elec}$) and another term that solely depends on the nuclei coordinates ($\hat{H}_{nucl}$):

$$\hat{\boldsymbol{H}} = \hat{\boldsymbol{H}}_{\boldsymbol{elec}} + \hat{\boldsymbol{H}}_{\boldsymbol{nucl}} \quad (\mathbf{II.33})$$

with

$$\hat{\boldsymbol{H}}_{\boldsymbol{elec}} = \hat{\boldsymbol{T}}_{\boldsymbol{elec}} + \hat{\boldsymbol{V}}_{\boldsymbol{elec-nucl}} + \hat{\boldsymbol{V}}_{\boldsymbol{elec-elec}} \quad (\mathbf{II.34})$$

and

$$\hat{\boldsymbol{H}}_{\boldsymbol{nucl}} = \hat{\boldsymbol{V}}_{\boldsymbol{nucl-nucl}} = \mathbf{constant} \quad (\mathbf{II.35})$$

Now, solving Eq. II.30 just requires solving the electronic part.

$$\hat{\boldsymbol{H}}_{\boldsymbol{elec}}\boldsymbol{\psi}_{\boldsymbol{elec}}(\vec{\boldsymbol{r}}_{\boldsymbol{1}}, \vec{\boldsymbol{r}}_{\boldsymbol{2}}, \dots, \vec{\boldsymbol{r}}_{\boldsymbol{N}}) = \boldsymbol{E}_{\boldsymbol{elec}}\boldsymbol{\psi}_{\boldsymbol{elec}}(\vec{\boldsymbol{r}}_{\boldsymbol{1}}, \vec{\boldsymbol{r}}_{\boldsymbol{2}}, \dots, \vec{\boldsymbol{r}}_{\boldsymbol{N}}) \quad (\mathbf{II.36})$$

with the system total energy is calculated by summing the electronic energy $\boldsymbol{E}_{\boldsymbol{elec}}$ and nuclei-nuclei repulsion energy $\boldsymbol{E}_{\boldsymbol{nucl}}$ that comes from the constant potential energy $\hat{\boldsymbol{V}}_{\boldsymbol{nucl-nucl}}$:

$$\boldsymbol{E} = \boldsymbol{E}_{\boldsymbol{elec}} + \boldsymbol{E}_{\boldsymbol{nucl}} \quad (\mathbf{II.37})$$

The two terms associated with the kinetic energy of electrons and the electron-nuclei interaction, as well as the term that represents the nuclei-nuclei repulsion, can be calculated through analytical methods. However, the presence of the electron-electron repulsion term makes it difficult to solve Eq. II.30 exactly for systems with multiple electrons. As a result, additional approximations are necessary.

Basically, there are two different methods for solving the electronic part of the many-body time-independent Schrödinger equation: (i) a wave function-based method known as Hartree and Hartree-Fock approximations, and (ii) an electronic density-based method known as DFT.

II.4.2. Hartree and Hartree-Fock approaches

Hartree approximation

Despite that the Born-Oppenheimer approximation was proven effective in simplifying the Schrödinger equation, it still not able to successfully solve more complex systems, which are common in reality. To address this issue, Hartree proposed the single electron wavefunction approach in 1928.[239–242] This method treats the electrons as non-interacting particles with each electron having its own individual wavefunction. In other words, the interaction between electrons is handled in a mean-field manner, with each electron experiencing an average non-local potential generated by the rest of the electrons. As a result, the Schrödinger equation (Eq. II.36) can be expressed as a one-electron equation, and the many-electron wave function can be represented as the product of all one-electron wave functions.

$$\boldsymbol{\psi}_{\boldsymbol{elec}}(\vec{\boldsymbol{r}}_{\boldsymbol{1}}, \vec{\boldsymbol{r}}_{\boldsymbol{2}}, \dots, \vec{\boldsymbol{r}}_{\boldsymbol{N}}) = \prod_{\boldsymbol{i=1}}^{\boldsymbol{N}} \boldsymbol{\psi}_{\boldsymbol{elec}}(\vec{\boldsymbol{r}}_{\boldsymbol{i}}) \quad (\mathbf{II.38})$$

Furthermore, taking into account the Rayleigh-Ritz variational principle, which asserts that the expectation value of a Hamiltonian for any "trial" wavefunction $\boldsymbol{\psi_{trial}}$ always produces an energy $\boldsymbol{E(\psi_{trial})}$ that is either equal to or greater than the ground state energy $\boldsymbol{E_0}$:

$$\boldsymbol{E(\psi_{trial}) = \frac{\langle \psi_{trial}|H|\psi_{trial}\rangle}{\langle \psi_{trial}|\psi_{trial}\rangle} \geq E_0} \qquad (\mathbf{II.39})$$

with $\boldsymbol{\psi_{trial}}$ is the ground state wave function when $\boldsymbol{E(\psi_{trial}) = E_0}$.

Utilizing the Rayleigh-Ritz variational principle (Eq. II.39) with the wavefunction in Hartree form (Eq. II.38) and the electronic Hamiltonian (Eq. II.36) leads to the so-called Hartree equation:

$$\boldsymbol{\left[-\frac{\hbar^2}{2m}\vec{\nabla}^2 - V_{ext}(r) + V_H(r)\right]\psi_i(\vec{r}) = \varepsilon_i\psi_i(\vec{r})} \qquad (\mathbf{II.40})$$

Here, $\boldsymbol{\varepsilon_i}$ acted as Lagrange multipliers within the applied variational principle to ensure the normalization of the eigenfunctions $\boldsymbol{\psi_i(\vec{r})}$, $\boldsymbol{V_{ext}(r)}$ represents the electron-nuclei interaction, while $\boldsymbol{V_H(r)}$ represents the Hartree potential that accounts for the Coulomb repulsive interactions between each electron and the average electronic density $\boldsymbol{n(r')}$ of all the other electrons:

$$\boldsymbol{V_H(r) = -\frac{1}{4\pi\varepsilon_0}\int d^3r'\, n(r')\frac{e^2}{|r-r'|} = -\frac{1}{4\pi\varepsilon_0}\sum_{j=1}^{N}\int d^3r'\frac{e^2}{|r-r'|}|\psi_j(r')|^2} \qquad (\mathbf{II.41})$$

with the electron density, $\boldsymbol{n(r')}$ is given by:

$$\boldsymbol{n(r') = \sum_{j=1}^{N}|\psi_j(r')|^2} \qquad (\mathbf{II.42})$$

The Hartree equation, Eq. II.40, resembles the one-particle Schrödinger equation. However, it describes an electron in the electrostatic field of all electrons, including itself, leading to the so-called self-interaction error (SIE) in the Hartree equations. Despite this SIE, the exact solutions, $\boldsymbol{\psi_i(\vec{r})}$, to the Hartree equation are required to solve the one-particle Hamiltonian. This issue can be resolved iteratively: starting with some initial guesses for the wavefunctions that enter the one-particle Hamiltonian, the Hartree equation is solved to obtain a new set of wavefunctions. This new set is used to calculate a new one-particle Hamiltonian and the process is repeated until self-consistency is achieved. A method such as the Hartree approach that includes a self-consistency cycle is called a self-consistent field (SCF) method.

However, in the Hartree approximation, the electron spins and their fermionic nature are not accounted for in Hartree wavefunctions. As a result, the Pauli exclusion principle,[243] which stipulate that the wavefunction of many-electron system must be anti-symmetric upon exchanging any two-electron coordinates, is not satisfied:

$$\boldsymbol{\psi(\vec{r}_1,\vec{r}_2,\ldots,\vec{r}_i,\ldots,\vec{r}_j,\ldots,\vec{r}_N) = -\psi(\vec{r}_1,\vec{r}_2,\ldots,\vec{r}_j,\ldots,\vec{r}_i,\ldots,\vec{r}_N)} \qquad (\mathbf{II.43})$$

Hartree-Fock approximation

To fulfill the Pauli exclusion principle (i.e., ensure the anti-symmetry criterion) and incorporate the fermionic characteristics of electrons into the wavefunction of many-electron system, $\boldsymbol{\psi_i(\vec{r})}$, Fock[244] (1930) assumed that the many-electron wavefunction should be approximated, instead of the product in the Hartree approach (Eq. II.38), by a single Slater determinant,[245] which means, an anti-symmetrized product of N-orthonormal one-electron wavefunctions, $\boldsymbol{\psi_i(\vec{r_i}, s_i)}$, composed of a spatial orbital $\boldsymbol{\phi_i(\vec{r})}$ and a spin function $\boldsymbol{\sigma(s_i)}$, as follows:

$$\boldsymbol{\psi(\vec{r}_1, \vec{r}_2, \ldots, \vec{r}_i, \ldots, \vec{r}_j, \ldots, \vec{r}_N)} \approx \frac{\mathbf{1}}{\sqrt{N!}} \begin{vmatrix} \boldsymbol{\psi_1(\vec{r}_1, s_1)} & \boldsymbol{\psi_2(\vec{r}_1, s_1)} & \ldots & \boldsymbol{\psi_N(\vec{r}_1, s_1)} \\ . & \boldsymbol{\psi_2(\vec{r}_2, s_2)} & \ldots & \boldsymbol{\psi_N(\vec{r}_2, s_2)} \\ . & . & . & . \\ . & . & . & . \\ & & & . \\ \boldsymbol{\psi_1(\vec{r}_N, s_N)} & \boldsymbol{\psi_2(\vec{r}_N, s_N)} & \ldots & \boldsymbol{\psi_N(\vec{r}_N, s_N)} \end{vmatrix} \quad \mathbf{(II.44)}$$

where N represents the total number of electrons, and the coefficient $\frac{\mathbf{1}}{\sqrt{N!}}$ is a normalization factor. In the Slater determinant, each line and each column represent a certain position in space, and a certain one-electron state, respectively. Interchanging the spin and spatial coordinates of two electrons in the Slater determinant leads to the interchange of two lines and columns, thereby changes the determinant sign. This satisfies the conditions of the anti-symmetric principle.

With this anti-symmetrized wavefunctions, the Hartree equation (Eq. II.40) is replaced by the Hartree-Fock (HF) equation:

$$\left[-\frac{\hbar^2}{2m}\vec{\nabla}^2 - V_{ext}(r) + V_H(r) - \frac{\mathbf{1}}{4\pi\varepsilon_0} \sum_{j=1}^{N} \delta_{\sigma_i\sigma_j} \int d^3r' \frac{e^2}{|r - r'|} \psi^*{}_j(r')\psi_i(r') \right] \psi_i(\vec{r}) = \varepsilon_i \psi_i(\vec{r}) \quad \mathbf{(II.45)}$$

This equation, also, derives from the variational approach (Eq. II.39) by searching for the ground-state energy of the many-electron Schrödinger equation with the single Slater determinant. However, it has an extra term in comparisons with the mean field equation of Hartree, the last term in the left hand side, which is called the "exchange" potential operator, referred as $\boldsymbol{V_x^{HF}(r)}$. This term defines the exchange effects between electrons of like spin to avoid each other, except for the case of $\boldsymbol{i = j}$, when the Coulomb and exchange terms cancel each other. This corresponds to the cancellation of the unphysical self-interaction. The solution to the HF equation is quit similar to the iterative SCF method that is mentioned in the Hartree approach.

However, in the HF formulation a single Slater determinant cannot express the exact wavefunction because it does not take into account the explicit electron-electron interaction. In the HF approach, the probability of an electron being in a particular position around an atom is influenced by its distance to the nuclei, rather than its distance to the other electrons. This means that the correlation resulting from the Coulomb interaction among electrons is entirely ignored. While Slater determinants allow for the

complete consideration of correlation among electrons with parallel spins (electron exchange), they do not take into account the correlation between electrons with anti-parallel spins. The energy of a system calculated by the HF method, consequently, must differ from the exact energy by an energy difference that is called the correlation energy:

$$E_{corr} = E_0^{exact} - E_0^{HF} < 0 \qquad (\mathbf{II.46})$$

Therefore, in order to introduce this correlation energy contribution, the DFT has been proposed.

II.4.3. Density functional theory (DFT)

The DFT is a powerful and widely used quantum mechanical methodology that is applied to solve the many-electron problem (Eq. II.36) derived from the Born-Oppenheimer approximation. Instead of using the many-electron wavefunction, this method deals with the total density of electrons, however, without any loss of information. This simplifies the many-electron problem by reducing it from 3N degrees of freedom to just 3 degrees of freedom (Fig. II.11). But more importantly, this method overcomes the principal shortcoming of the HF approach, which ignores the electron correlation. As a result, it can accurately calculate the chemical and physical properties of large systems and provide results that are comparable to experimental data.

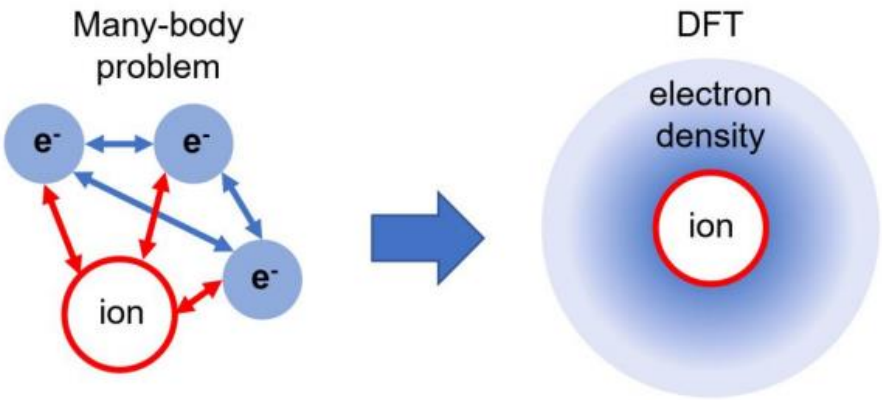

Figure II. 11. Schematic illustration of transforming many-electrons system to electron density.

II.4.3.1. Hohenberg-Kohn theorems

The two central Hohenberg-Kohn theorems[246] (1964) formally established the modern DFT. The first theorem indicates that the electron density of the ground state can replace the many-electron wavefunction in the many-electron problem without losing any information. The second theorem sets up a variational principle for an energy functional that relies on the electron density of the ground state instead of the many-electron wavefunction. This principle bears resemblance to the conventional variational principle in quantum theory.

The following states the two Hohenberg-Kohn theorems:

Theorem I asserts that for any system of interacting particles subjected to an external potential $\boldsymbol{V_{ext}(r)}$, the external potential can be uniquely defined by the ground state particle density $\boldsymbol{n(r)}$, except for an additive constant.

According to the Hohenberg and Kohn, the energy of the ground state can be expressed as follow:

$$\mathbf{E}_{HK}[\boldsymbol{n}] = \int \boldsymbol{V_{ext}n(r)dr} + \boldsymbol{F}[\boldsymbol{n(r)}] \qquad (\mathbf{II.47})$$

where the term $\boldsymbol{V_{ext}(r)}$ is the Coulomb attraction by nuclei. It is crucial to note that the term "*external"* in $\boldsymbol{V_{ext}(r)}$ refers to the fact that, from the viewpoint of electrons, the Coulomb attraction by nuclei is considered external and hence, is system-dependent. The term $\boldsymbol{F[n(r)]}$ is the system-independent internal potential which has a universal functional, i.e., its mathematical form is the same for all systems. However, the explicit formula of this universal functional is unknown.

Theorem (I) can be proved via a proof by contradiction. It is observed that the Hamiltonian $\boldsymbol{\hat{H}}$ of a system and the energy at the ground-state $\boldsymbol{E_0}$, can be solely obtained via the external potential, and they are interconnected by:

$$\boldsymbol{\hat{H} = \hat{F} + \hat{V}_{ext}} \qquad \textbf{and} \qquad \mathbf{E}[\boldsymbol{n(r)}] = \langle \boldsymbol{\psi} | \boldsymbol{\hat{H}} | \boldsymbol{\psi} \rangle \qquad (\mathbf{II.48})$$

In comparison with Eq. II.34, where the external potential defines the electrons-nuclei Coulomb interactions, it can be noticed that the operator $\boldsymbol{\hat{F}}$ represents the kinetic energy operator $\boldsymbol{\hat{T}}$ and the electron-electron interaction operator $\boldsymbol{\hat{V}_{e-e}}$.

$$\boldsymbol{\hat{F} = \hat{T} + \hat{V}_{e-e}} \qquad (\mathbf{II.49})$$

where the ground-state expectation value of the operator $\boldsymbol{\hat{F}}$ is the functional $\boldsymbol{F[n(r)]}$.

Hohenberg and Kohn demonstrated that two different external potentials cannot produce the same ground-state electron density. Therefore, two different external potentials must give rise to two different electron densities. This means that the external potential is solely defined by the electron density. Consequently, all the properties at ground-state, including the energy of the ground-state, its derivatives, and the nuclei positions, are also uniquely defined by the electron density.

Theorem II postulates that for any system of interacting particles, there is a universal energy functional $\boldsymbol{E[n(r)]}$ that is dependent on the density and is applicable for any external potential. Thus, for a specific external potential, the true energy of the ground state $\boldsymbol{E[n_0(r)]}$ of a system represents the lowest minimum value that this universal functional can attain, and the density that minimizes this functional corresponds to the true ground state density $\boldsymbol{n_0(r)}$.

Accordingly, Hohenberg and Kohn utilized the variational principle of Rayleigh-Ritz to derive the minimum properties of the energy functional and defined it as:

$$\boldsymbol{E[n(r)] = min\langle\psi|\hat{H}|\psi\rangle} \qquad (\mathbf{II.50})$$

The Hamiltonian operator expectation value must be minimized in relation to the norm-conserving anti-symmetric wavefunction $\boldsymbol{\psi(r)}$, that reproduces a specified electron-density $\boldsymbol{n(r)}$. The calculation of the ground-state density $\boldsymbol{n_0(r)}$ and the energy of the ground-state $\boldsymbol{E[n_0(r)]}$ is achieved by minimizing the energy functional:

$$\boldsymbol{\delta E[n(r)] = 0} \qquad (\mathbf{II.51})$$

The particle conservation subsidiary condition, $\boldsymbol{\int n(r)dr = N}$, is accounted using a Lagrangian parameter ($\boldsymbol{\mu}$), which guarantees the orthonormality constraint. This results in the minimization of a modified energy functional.

$$\boldsymbol{\delta\left[E[n(r)] - \mu\left(\int n(r)dr - N\right)\right] = 0} \qquad (\mathbf{II.52})$$

This gives rise to the subsequent Euler-Lagrange equation:

$$\left.\frac{\boldsymbol{\delta E[n(r)]}}{\boldsymbol{\delta n(r)dr}}\right|_{\boldsymbol{n_0(r)}} = \boldsymbol{\mu} \qquad (\mathbf{II.53})$$

Nonetheless, since the exact formula of the energy functional is still unknown, it's not possible to derive the aforementioned equation using the approach proposed by Hohenberg and Kohn. Therefore, further approximations are required. This major issue was treated by the ingenious Kohn-Sham (KS) ansatz which will be the subject of the next sections.

II.4.3.2. The Kohn-Sham formulation

Based on the aforementioned Hohenberg and Kohn theorems, Kohn and Sham[247] (1965) proposed a brilliant scheme that substitutes the real muti-electrons system with an auxiliary system of independent-particle. The fundamental assumption of KS approach is that the ground-state densities, $\boldsymbol{n_0(r)}$, of both systems are equal. Within the KS scheme, the real interacting system with a real potential is mapped into an imaginary system of non-interacting particles. In this system, electrons move within an effective KS single-particle potential, $\boldsymbol{V_{eff}(r)}$.

Therefore, the auxiliary Hamiltonian is expressed as the sum of the kinetic energy and the energy of the effective potential,

$$\boldsymbol{\hat{H}_{aux} = -\frac{\hbar^2}{2m}\nabla^2 + V_{eff}(r)} \qquad (\mathbf{II.54})$$

In the subsequent discussions, and for the sake of simplification we will employ atomic units where, $\boldsymbol{\hbar = m_e = e = 4\pi\epsilon_0 = 1}$.

To obtain the energy of the ground state for a system composed of N independent electrons, it is necessary to solve the following N one-electron Schrödinger equations:

$$\hat{H}_{aux}\psi_i = \left[-\frac{1}{2}\nabla^2 + V_{eff}(r)\right]\psi_i = \varepsilon_i\psi_i \qquad (\mathbf{II.55})$$

Each of the N orbitals, $\psi_i(r)$, contains one electron with the lowest eigenvalues ε_i. These orbitals are used to construct the density of the auxiliary system,

$$n(r) = \sum_{i=1}^{N} |\psi_i(r)|^2 \qquad (\mathbf{II.56})$$

The kinetic energy, $T_{KS}[n(r)]$, of the system composed of non-interacting independent particles is given by:

$$T_{KS}[n(r)] = -\frac{1}{2}\sum_{i=1}^{N}\langle\psi_i^*|\nabla^2|\psi_i\rangle \qquad (\mathbf{II.57})$$

So, the universal functional $F[n(r)]$ of Hohenberg-Kohn can be formulated as:

$$F_{HK}[\mathrm{n}] = T_{KS}[n(r)] + E_{Hartree}[n(r)] + E_{xc}[n(r)] \qquad (\mathbf{II.58})$$

The term $E_{Hartree}[n(r)]$ represents the classical Coulomb interaction where the electronic density $n(r)$ interacts with itself. It is defined by the Hartree energy:

$$E_H[n(r)] = \frac{1}{2}\int \frac{n(\vec{r})n(\vec{r}')}{|\vec{r}-\vec{r}'|}drdr' \qquad (\mathbf{II.59})$$

and the term $E_{xc}[n(r)]$ represents the exchange-correlation (XC) energy. It comprises the difference between the kinetic energies of the real interacting system and the fictitious non-interacting system. Additionally, it includes the non-classical contribution to electron interactions, a component of which is the exchange energy.

Since for a given N-electron system, the energy of the ground state can be ascertained by minimizing the energy functional, $E[n(r)] = \int V_{ext}n(r)dr + F[n(r)]$, while the process must uphold the conservation the number of electrons N, as dictated through the constraint $\int n(r)dr = N$, Eq. II. 54 can then be rewritten as follows:

$$\frac{\delta T_{KS}[n(r)]}{\delta n(r)dr} + V_{eff}(r) = \frac{\delta F[n(r)]}{\delta n(r)dr} + V_{ext}(r) = \mu \qquad (\mathbf{II.60})$$

with $V_{eff}(r)$ is the effective KS single-particle potential,

$$V_{eff}(r) = V_{ext}(r) + V_H(r) + V_{XC}(r) = V_{ext}(r) + \frac{\delta E_H[n(r)]}{\delta n(r)dr} + \frac{\delta E_{XC}[n(r)]}{\delta n(r)dr} \qquad (\mathbf{II.61})$$

and the Hartree potential $V_H(r)$ is,

$$V_H(r) = \frac{\delta E_H[n(r)]}{\delta n(r)dr} = \int \frac{n(r')}{|r-r'|}dr' \qquad (\mathbf{II.62})$$

and the XC potential $\boldsymbol{V_{XC}(r)}$ is,

$$\boldsymbol{V_{XC}(r) = \frac{\delta E_{XC}[n(r)]}{\delta n(r) dr}} \qquad (\mathbf{II.63})$$

Eqs. II.55, II.56, and II.61, are widely recognized as the KS equations, and which necessitate a self-consistent solution approach to be solved. This is because the $\boldsymbol{V_{eff}(r)}$ is related to the density via the XC potential.

While the KS theory is exact in principle, it is approximate in practice due to the unknown nature of the XC energy functional $\boldsymbol{E_{XC}[n(r)]}$. The term $\boldsymbol{E_{XC}[n(r)]}$ can be defined implicitly as follows:

$$\boldsymbol{E_{XC}[\mathrm{n(r)}] = T[n(r)] - T_{KS}[n(r)] + E_{e-e}[n(r)] - E_H[n(r)]} \qquad (\mathbf{II.64})$$

where $\boldsymbol{T[n(r)]}$ and $\boldsymbol{E_{e-e}[n(r)]}$ denotes, respectively, the true kinetic energy and the energy of interaction between electrons of the real interacting system.

Finally, the ground state energy in the KS formalism can be expressed as follows:

$$\boldsymbol{E = \sum_{i=1}^{N} \varepsilon_i + E_{xc}[n(r)] - \int V_{ext}(r) n(r) dr - V_H[n(r)] + V_{nucl-nucl}} \qquad (\mathbf{II.65})$$

Here the term $\boldsymbol{V_{nucl-nucl}}$ is added to derive the correct total energy of the Hamiltonian (Eq. II.33). The sum over the single-particle energies ($\boldsymbol{\sum_{i=1}^{N} \varepsilon_i}$) is commonly termed as the band structure energy. However, it is important to note that the "single-particle energies" $\boldsymbol{\varepsilon_i}$ (also referred as the KS energy eigenvalues) enter the formalism just as Lagrange multipliers ($\boldsymbol{\equiv \mu}$) to guarantee the normalization of the wave functions (KS orbitals). These KS energy eigenvalues do not apply to the real many-body system and lack a distinct physical interpretation, except for the highest occupied state in a finite system, which represents the energy of ionization.

In conclusion, the KS formalism has several key points worth mentioning. First, it provides a clear algorithm for calculating the energy of the ground state and the density of an interacting many-body system. Second, it is completely accurate if the true XC potential is known. In addition, it solves the N-electron interacting problem using non-interacting electrons in an external potential, which is highly beneficial. Furthermore, one of the greatest benefices of the KS formalism is that the effective potential is locally constructed. The KS formalism ensures that the potential is identical for all orbitals, similar to the Hartree approximation. This is in opposition to the HF approach, where the potential is dependent on the orbital due to the non-local exchange term. As a result, the KS equations are much easier to solve than the HF equations, which is of great practical significance. Solving for Kohn-Sham orbitals (a Slater determinant of N orbitals) is relatively simple, even for large systems with several hundred electrons. Like the Hartree method, the solutions to the KS equations must be determined in a self-consistent way. The only distinction is the addition of the XC potential term.

II.4.3.3. Exchange-correlation functionals in DFT

The KS formalism effectively maps the real many-body system of interacting particles into a set of independent single-particle equations, simplifying the issue. Nevertheless, without knowing the precise formula of the XC energy functional $\boldsymbol{E_{xc}[n(r)]}$, solving the KS equations becomes unfeasible. Despite the complexity of the exact XC energy functional $\boldsymbol{E_{xc}[n(r)]}$, there have been successful and simple approximations developed that accurately predict a variety of properties across numerous systems while also significantly reducing computational expenses. As a results, DFT has become widely used for electronic structure calculations due to the creation of successful and straightforward approximations. The most commonly employed approximations are the local density approximation (LDA) and the generalized gradient approximation (GGA).

The local density approximation (LDA)

The local density approximation (LDA)[247] is a simple approximation of the XC energy that renders the KS DFT both effective and applicable. Within this method, it is postulated that the true XC energy of a system with multi-electron electrons can be locally approximated by the XC energy of a uniform electron gas (UEG) that has the same density. The total XC energy $\boldsymbol{E_{xc}^{LDA}}$ can be then determined by summing the contributions of each point in space according to the following form:

$$\boldsymbol{E_{xc}^{LDA} = \int n(r)\epsilon_{xc}^{LDA}(n(r))dr = \int n(r)\,[\epsilon_x(n(r)) + \epsilon_c(n(r))]dr = E_x^{LDA}[n(r)] + E_c^{LDA}\,[n(r)]} \quad \textbf{(II.66)}$$

Here, $\boldsymbol{\epsilon_{xc}(n(r))}$ is the XC energy per electron for a UEG for which the electronic density is constant throughout the space. An analytical expression for the UEG is available for the exchange component of the $\boldsymbol{\epsilon_{xc}(n(r))}$,[248] which is known as:

$$\boldsymbol{E_x^{LDA}[n(r)] = \int n(r)\epsilon_x(n(r))\,\mathbf{dr} = -\frac{3}{4}\left(\frac{3}{\pi}\right)^{1/3}\int n(r)^{4/3}dr} \quad \textbf{(II.67)}$$

where

$$\boldsymbol{\epsilon_x(n(r)) = -\frac{3}{4}\left(\frac{3}{\pi}\right)^{1/3} n(r)^{1/3}} \quad \textbf{(II.68)}$$

For the correlation part of the XC energy, however, there is no analytical expression. High level quantum Monte Carlo calculations can provide the numerical value of the correlation energy in a very precise manner[249]. The numerically calculated correlation is fitted to an analytical form and the analytical expression for $\boldsymbol{\epsilon_{xc}(n(r))}$ is obtained[250]. Different local density approximations have been proposed based on the analytic forms utilized for $\boldsymbol{\epsilon_c(n(r))}$. These include Perdew-Wang (PW),[251] Perdew-Zunger (PZ)[250], and Vosko-Wilk-Nusair (VWN)[252].

Although the LDA approximation has been successful, it does have its limitations. It performs well when the density of a system varies slowly and we can obtain very accurate and reproducible chemical properties. Nonetheless, the LDA proves to be imprecise for systems with strong correlation where an

approach based on independent particles falls short. Additionally, the LDA provides poor approximations for energetic details such as overestimating binding energies while underestimating atomic ground state energies and ionization energies. The LDA approximation fails to accurately predict the energy gaps of certain semiconductors (SCs). The shortcomings of the LDA approximation have led to the development of XC energy functional approximations that go beyond LDA. These approximations incorporate longer-range gradient effects by adding gradient corrections.

The generalized gradient approximation (GGA)

As previously motioned, LDA approximates the XC energy functional by considering an electron gas of uniform density. However, in reality, systems do not have uniformly homogeneous density, which is why the LDA does not always accurately model systems. This prompted the creation of several generalized-gradient approximations (GGAs)[253,254] that incorporate density gradient corrections and higher spatial derivatives of electron density, providing improved outcomes in comparison with the LDA approach in many cases. The XC energy functional can be expressed, following the GGA approach, as a function of local density and its gradient $\boldsymbol{\nabla(n(r)}$:

$$\boldsymbol{E_{xc}^{GGA} = \int n(r)\epsilon_{xc}^{GGA}(n(r), |\nabla(n(r)|)dr} \qquad (\mathbf{II.69})$$

In practice, the general form of GGA is expressed as an extension of the LDA with the addition of an enhancement factor $\boldsymbol{F_{XC}(s)}$ that directly modifies the energy within the LDA:

$$\boldsymbol{E_{xc}^{GGA} = \int n(r)\epsilon_{xc}^{LDA}(n(r))F_{xc}(s)dr} \qquad (\mathbf{II.70})$$

The enhancement factor, $\boldsymbol{F_{XC}(s)}$, can be linearly divided into two components: the exchange contribution $\boldsymbol{F_x(s)}$ and correlation contribution $\boldsymbol{F_c(s)}$, Thus, it can be expressed as $\boldsymbol{F_{xc}(s) = F_x(s) + F_c(s)}$. The value of the variable $\boldsymbol{s}$ relies on both the electron density and the gradient of the electron density:

$$\boldsymbol{s = \frac{|\nabla(n(r)|}{2k_F n(r)}} \qquad (\mathbf{II.71})$$

with $\boldsymbol{k_F}$ is the Fermi-wave-vector, $\boldsymbol{k_F = (3\pi^2 n(r))^{1/3}}$

Several GGA functionals have been introduced over the last years. The most widely employed functionals are those proposed by Becke (B88),[254] Perdew and Wang (PW91),[255] and Perdew, Burke and Enzerhof (PBE),[256] which have gained significant attention from the physicists and chemists communities.

The GGA functionals improved the estimations of many physical and chemical properties such as structural parameters, binding energies, activation energies, electronic structure and electronic densities, in particular systems with larger spatial variation in the density. However, like the LDA functionals the

GGA functionals drastically fails to predict electronic properties for strongly correlated systems, in particular, systems with d and f electrons.

II.4.3.4. Limitations of DFT functionals: Band gap underestimation

DFT with the approximated XC functionals such as LDA and GGA is an effective and convenient numerical tool for predicting the properties of various materials. These approximate functionals perform well in optimizing structures, calculating total energy, and determining the electronic properties of simple materials. However, standard DFT significantly underestimates the band gap of SC materials, which is one of the crucial properties of materials, and that is not surprising since the DFT is not designed to calculate excited states.[257] In fact, the underestimation of band gaps within a single KS-DFT calculation commonly reaches up to 40% when compared to the quasi-particle band structure (also known as the fundamental energy gap).[258] This mainly attributed to the inherent limitations of the non-interacting one-electron KS scheme. The KS energies do not represented the difference between the largest energy added and the smallest energy removed of an electron (i.e. the electron affinity, $\boldsymbol{A = E_{tot}(N) - E_{tot}(N+1)}$, and the ionization potential, $\boldsymbol{I = E_{tot}(N-1) - E_{tot}(N)}$), which defines the true band gaps as:

$$\boldsymbol{E_g = I - A = [\,E_{tot}(N-1) - E_{tot}(N)] - [E_{tot}(N) - E_{tot}(N+1)]} \qquad \textbf{(II.72)}$$

According to Janak's theorem[259] both the potential of ionization and the affinity of electrons can be obtained from the ground-state DFT. The potential of ionization is determined by the highest occupied KS eigenvalue, $\boldsymbol{\varepsilon_N(N)}$, for the N-electron system, and the affinity of electrons corresponds to the equivalent eigenvalue, $\boldsymbol{\varepsilon_{N+1}(N+1)}$, for the N+1-electron system. Therefore, the band gap can be formulated as follows:

$$\boldsymbol{E_g = \varepsilon_{N+1}(N+1) - \varepsilon_N(N)} \qquad \textbf{(II.73)}$$

The right-hand side of the aforementioned equation encompasses the highest occupied KS eigenvalues from two different systems: one with N electrons and another with N+1 electrons. Nonetheless, deriving the band gap using this definition would be unfeasible for a solid with 10^{23} electrons.

Conversely, a calculation using KS-DFT provides the KS gap, denoted as $\boldsymbol{E_g^{KS}}$. This corresponds to the difference between the energies of the highest occupied and lowest unoccupied KS orbitals within the same N-particle system:[258,260–262]

$$\boldsymbol{E_g^{KS} = \varepsilon_{N+1}(N) - \varepsilon_N(N)} \qquad \textbf{(II.74)}$$

In standard KS DFT electronic band structure computations, the band gap is typically represented by the aforementioned quantity, and it's straightforward to notice the discrepancy between the real band gap and the KS band gap as:

$$\boldsymbol{E_g - E_g^{KS} = \varepsilon_{n+1}(N+1) - \varepsilon_{n+1}(N) = \Delta_{xc}} \qquad \textbf{(II.75)}$$

The quantity Δ_{xc} is related to the derivative discontinuity or the non-analytic behavior, of the real XC potential when the number of electrons N varies.[258,260,262] This is in opposition to the GGA and LDA approaches, where the XC energy is a continuous function with respect to the number of electrons.

An additional factor contributing to the failure of KS-DFT in calculating the band gaps is attributed to its inability to properly treat the localization behavior of strongly correlated electrons. Unlike s and p orbitals, which are more delocalized and where electrons spend very little time around atomic sites, d and f orbitals are highly localized. Electrons in these orbitals tend to spend more time around a given atomic site within a crystal lattice and are more likely to be localized around a specific atom due to their high spatial confinement. Consequently, the available XC functionals within KS-DFT have a tendency to over-delocalize the valence electrons of strongly correlated systems. This is because they are incapable to completely cancel out the unphysical self-interaction error that derives from the utilization of the classical Coulomb term (Eq. II.59), which refers to the repulsion between electrons in the non-interacting electron system.

In an ideal situation, a KS-DFT calculation would produce exact results only if the unknown exact XC functional were used. Certain conditions are met by the exact XC functional, but these conditions are not satisfied by approximate XC functionals based on LDA and GGA. These exact conditions can often only be defined for certain limiting model systems. The hydrogen atom is an example of a one-electron system where the single electron cannot interact with itself through Coulomb interaction. For a such system, the total energy should have zero contribution from Coulomb interaction, $\boldsymbol{E_{e-e}[n(r)] = 0}$. However, if the Coulomb interaction in a one-electron system is not zero, it will result in an unphysical electron self-interaction.

Within the HF approximation, the erroneous self-interaction contribution in the Hartree term is completely nullified by the corresponding exchange energy term, given that the wave function is set in a Slater determinant. However, as mentioned in earlier sections, the HF theory does not incorporate at all the electronic correlation.

In contrast, within the framework of KS-DFT, the interaction between electrons is defined as a combination of the classical Coulomb contribution and the XC contribution:

$$\boldsymbol{E_{e-e}[n(r)] = E_H[n(r)] + E_{XC}[n(r)]} \qquad (\mathbf{II.76})$$

For a single electron density, Eq. (II.52) yields:

$$\boldsymbol{E_H[n(r)] + E_{XC}[n(r)] = 0} \qquad (\mathbf{II.77})$$

In a single-electron system , the correlation contribution is zero. Therefore, the self-exchange term should cancel out the self-Coulomb energy. However, because the exchange term in standard DFT is approximated , the self-Coulomb energy is not completely removed. Therefore, several techniques are

used to cure the self-interaction error (SIE) and the band gaps problem. The prominent among them are hybrid functionals and DFT+U methods.

II.4.3.5. Hybrid DFT functionals

The hybrid functionals are mixing of HF exact exchange $\boldsymbol{V_x^{HF}(r)}$ calculated using KS orbitals with the semi-local GGA exchange $\boldsymbol{F_x(s)}$. This hybrid approach to construct DFT approximations was first introduced by Becke[263] (1993). The proportion of HF exact exchange in a hybrid functional can be adjusted to address the specific physical and chemical properties of the material being studied. One of the commonly employed hybrid functionals is B3LYP[263,264] (3-parameter, Lee-Yang-Parr), and its XC functional is written as:

$$\boldsymbol{E_{xc}^{B3LYP} = (1-a)E_x^{LDA} + aE_x^{HF} + bE_x^{B88} + (1-c)E_c^{LDA} + cE_c^{LYB}} \qquad \textbf{(II.78)}$$

with values set as $\boldsymbol{a = 0.20}$, $\boldsymbol{b = 0.72}$ and $\boldsymbol{c = 0.81}$. $\boldsymbol{E_x^{B88}}$ represents the gradient correction of the Becke[254] exchange functional and $\boldsymbol{E_c^{LYB}}$ refers to the correlation functional as defined by Lee, Yang and Parr.[264]

Another hybrid functional is PBE0,[265] which combines the exchange energy of Perdew-Burke-Ernzerhof (PBE) and the exchange energy of HF in a fixed ratio of 3:1, in addition to incorporating the full PBE correlation energy:

$$\boldsymbol{E_{xc}^{PBE0} = \frac{3}{4}E_x^{PBE} + \frac{1}{4}E_x^{HF} + E_c^{PBE}} \qquad \textbf{(II.79)}$$

Hybrid functionals can still be improved by separating the range of exact exchange and semi-local exchange. This allows the semi-local exchange to dominate at short range and the non-local HF exchange to dominate at long range.[266] The range separation parameter and the proportion of exact exchange can be adjusted to minimize the SIE.[267]

The Heyd-Scuseria-Ernzerhof (HSE)[268] XC functional is a popular range-separated hybrid functional particularly used in solid-state physics that employs an error-function-screened Coulomb potential to derive the energy's exchange component:

$$\boldsymbol{E_{xc}^{HSE} = \frac{3}{4}E_x^{SR,PBE}(\omega) + \frac{1}{4}E_x^{SR,HF}(\omega) + E_x^{LR,PBE}(\omega) + E_c^{PBE}} \qquad \textbf{(II.80)}$$

where $\boldsymbol{E_x^{SR,PBE}(\omega)}$ and $\boldsymbol{E_x^{LR,PBE}(\omega)}$ represent the short- and long-range terms of the PBE exchange functional, respectively. $\boldsymbol{E_x^{SR,HF}(\omega)}$ is the short-range HF exact exchange functional. The parameter, denoted by **ω,** is adjustable and controls the extent of short-range interaction.

However, the use of such mixing of exchange comes at significantly higher computational cost. The computational complexity of hybrid DFT is given by $O(N^3)$ where N is the number of atoms. As a result, much research has been devoted to developing more accurate functionals or applying corrections to the existing LDA and GGA functionals to better explain the electronic structure, particularly the band gap

problem in strongly correlated system. One such corrective approach applied to currently used DFT formulation is the DFT+U. This method introduces an additional Hubbard like Coulombic interaction term U to the localized d and f valence orbitals to accurately represent the localization behavior of the strongly correlated electrons. Compared to hybrid DFT, the DFT+U method is more suitable for large and complex systems and is less computationally demanding. Consequently, this is was the approach applied in this thesis.

II.4.3.6. DFT + Hubbard U correction

Standard DFT approximations often struggle to accurately represent strongly correlated systems, which typically consist of transition metal or rare earth metal ions that have partially filled d or f shells. The reason for this difficulty is due to the orbital-independent potentials present in LDA and GGA functionals. Therefore, to consider the strong correlations between d electrons or f electrons, an adjustment must to be applied to these electrons. Considering the fact that the over-delocalization of electrons is equivalent to a lack of an on-site Coulomb repulsion, the Hubbard model[269,270] was used as inspiration to add an on-site Hubbard-type Coulomb repulsion term to the DFT Hamiltonian to correct this. The Hubbard model is defined as follows:

$$\boldsymbol{H} = -\mathbf{t}\sum_{\boldsymbol{I}}\sum_{\boldsymbol{\sigma}=\uparrow,\downarrow} \boldsymbol{c}^{\dagger}_{\boldsymbol{I},\boldsymbol{\sigma}}\boldsymbol{c}_{\boldsymbol{I},\boldsymbol{\sigma}} + \boldsymbol{U}\sum_{\boldsymbol{I}} \boldsymbol{n}_{\boldsymbol{I}\uparrow}\boldsymbol{n}_{\boldsymbol{I}\downarrow} \qquad (\mathbf{II.81})$$

where the first expression in the right hand side denotes the electrons movement between different lattice sites I with a hopping strength t, while the second expression represents the on-site Coulomb repulsion electrons situated at the same lattice site. $\boldsymbol{c}^{\dagger}_{\boldsymbol{I},\boldsymbol{\sigma}}$ and $\boldsymbol{c}_{\boldsymbol{I},\boldsymbol{\sigma}}$ terms refer to the fermionic creation and annihilation operators that add/remove an electron of spin, denoted by $\boldsymbol{\sigma}$, to/from an electronic orbital at the i^{th} lattice site.

As mentioned in previous sections, LDA or GGA based functionals are not sufficient for describing localized electrons. To address this issue, Anisimov and his colleagues[271] proposed adding a correction term to standard local and semi-local DFT based on the above described Hubbard model Hamiltonian, which can accounts for the on-site repulsion of localized electrons. This means that the strongly correlated valence electronic states, such as d- or f-orbitals, will be described using the Hubbard model. The rest of the valence states will continue to be described using standard DFT. While the Hubbard correction can be applied to any state in theory, it is typically used for localized d- or f-electrons where on-site Coulomb repulsion is strong. Less localized electrons, such as those with p character, are often not subject to the Hubbard correction.

When the Hubbard correction term U is included in the DFT description, the following DFT+U energy functional is obtained:[271–273]

$$\boldsymbol{E^{DFT+U}}[\boldsymbol{n}(\boldsymbol{r})] = \boldsymbol{E^{DFT}}[\boldsymbol{n}(\boldsymbol{r})] + \boldsymbol{E^{U}}[\boldsymbol{n}_{\boldsymbol{I}}^{\boldsymbol{\sigma}}] - \boldsymbol{E}_{\boldsymbol{dc}}[\boldsymbol{n}_{\boldsymbol{I}}^{\boldsymbol{\sigma}}] \qquad (\mathbf{II.82})$$

where $\boldsymbol{E^U}$ express the interaction energy correction within DFT+U, which comes from the Hubbard model and depends on the occupation number matrix, denoted as $\boldsymbol{n_I^\sigma}$, of a correlated state that is linked to a particular atom at location I. This occupation matrix has a relation with the electron density. $\boldsymbol{E_{dc}}$ is the double-counting term which eliminates the portion of $\boldsymbol{E^U}$ that is already accounted for in the DFT total energy as a mean field interaction of correlated d- or f-electrons.

The Coulomb and exchange energy, $\boldsymbol{E^U[n_i^\sigma]}$, of the localized states coming from the Hubbard model is given in terms of the atomic HF interaction energy:

$$\boldsymbol{E^U[n_i^\sigma] = \frac{1}{2}\sum_{i,\{m\},\sigma}\{\langle m, m''|V_{e-e}|m', m'''\rangle\, n^\sigma_{Imm'} n^{-\sigma}_{Im''m'''} + (\langle m, m''|V_{e-e}|m', m'''\rangle - \langle m, m''|V_{e-e}|m', m'''\rangle)\, n^\sigma_{Imm'} n^\sigma_{Im''m'''}\}} \quad \textbf{(II.83)}$$

Here the term $\boldsymbol{n^\sigma_{Imm'}}$ represents the DFT+U occupation matrix, which has elements that depend on the orbital occupation numbers. The term $\boldsymbol{|m\rangle}$ represents the localized orbitals at a specific atomic site I with a magnetic quantum number m for a certain angular momentum l. The potential of the screened Coulomb interactions among the electrons of d- or f-orbitals is represented by $\boldsymbol{V_{e-e}}$.

The above equation can be simplified by using the rotationally invariant form DFT+U proposed by Liechtenstein and his co-workers[274] and later made simpler by Dudarev and his colleagues.[275] This approach ignores the non-sphericity of electronic interactions and the differences between the interactions in same-spin and different-spin channels. With these proposition, the adjustment to the energy functional can be expressed as follows:

$$\boldsymbol{E^U[n_i^\sigma] = \frac{1}{2}U\sum_{m,m',\sigma} n_{m,\sigma} n_{m',-\sigma} + \frac{1}{2}(U-J)\sum_{m,m',\sigma} n_{m,\sigma} n_{m',\sigma}} \quad \textbf{(II.84)}$$

Here, the sum is over the magnetic quantum number, m, m' and spin quantum number, σ. $\boldsymbol{n_{m,\sigma}}$ and $\boldsymbol{n_{m',-\sigma}}$ are the orbital occupancies. U and J are the effective on-site Coulombic and exchange parameters, respectively, which describe the on-site Hubbard-like interactions.

On the other hand, the double counting term, $\boldsymbol{E_{dc}[n_I^\sigma]}$, in Eq. (II.82) is a somewhat arbitrary part of the derivation of the DFT+U method. There are several approximations for this term, however, one of the most common used approximation in literature, which was originally used by Anisimov and co-workers[271], is the fully-localized limit (FLL) formulation. Within this approximation, it's postulated that the occupation numbers are strictly 0 or 1. This implies that the electrons are either entirely represented by a subspace orbital or not represented at all. Additionally, it is assumed that when the occupation numbers are integer the SIE in standard DFT using LDA or GGA approximations should be small, indicating that standard DFT alone should be sufficient to describe the system. The FLL is inclined towards the integer occupation of localized electrons, and thus it can be considered to be a suitable correction for systems with highly localized electrons.

The energy for the double-counting within the FLL is given by:

$$E_{dc}^{FLL}[n_I^\sigma] = \frac{1}{2}U\sum_\sigma N_\sigma N_{-\sigma} + \frac{1}{2}(U-J)\sum_\sigma N_\sigma(N_\sigma - 1) \qquad (\mathbf{II.85})$$

where N_σ is the total charge in spin channel σ defined as, $N^\sigma = \sum_m n_{m,\sigma}$.

Therefore, the total DFT+U correction term using the Dudarev approach in the FLL approximation, can be described as:

$$\begin{aligned} E^{DFT+U}[n(r)] &= E^{DFT}[n(r)] + E^U[n_i^\sigma] - E_{dc}[n_i^\sigma] \\ &= E^{DFT}[n(r)] + \frac{1}{2}(U-J)\sum_{i\neq j} n_{m,\sigma}(1 - n_{m,\sigma}) \end{aligned} \qquad (\mathbf{II.86})$$

where the terms U and J represents, respectively, the onsite Coulomb and the exchange parameters. The difference between these two parameters can be replaced by a single on-site effective Coulomb repulsion parameter, $U_{eff} = U - J$. In the above motioned Dudarev approach, the additional Hubbard correction to the standard DFT enforces the integer occupation of electrons (i.e., forces the on-site occupancy density matrix, $n_{m,\sigma}$, either to fully occupied or unoccupied) within the localized states.

It's worth mentioning that Mosey et al.[276,277] proposed an *ab-initio* method to calculate the Coulomb and exchange parameters from an HF calculation. Alternately, these parameters can be approximated through constrained DFT calculations, which account for screening and relaxation effects.[278–280] However, in this PhD dissertation, the *U* and *J* terms are used as empirical parameters in our DFT+U calculations to fit observable quantities, such as the experimental band gaps.

II.4.4. Applying DFT calculation in solid material: Introducing periodicity

The KS DFT provides a general understanding of the many-electron systems. It can effectively model simple systems with many electrons in a confined space, such as molecular systems. However, for solids, the results are not as successful. When dealing with expanded solids, two challenges arise: calculating a wavefunction for every electron in a system, which could be infinite number, and expanding each electronic wavefunction throughout the full extent of the solid using a basis set. Therefore, to overcome these challenges, the periodicity of the solid system must be considered. This will ensure that a small section of the solid is sufficient for a reliable DFT calculation. Additionally, a finite representative basis set must be used to describe the infinite large-scale space as a composition of numerous repeated periodic cells in the 3-dimensional space.

II.4.4.1. Bloch's theorem

A crystalline solid system (pure crystal or defect-free surface) can be described as a repetitive sequence of the unit cell. Such a unit cell, being the smallest possible structural component required to reconstruct

the entire solid through translational symmetry operations defined by lattice vectors $\vec{t}$, is in real space characterized by three vectors $\vec{a}_i$. This periodicity property implies that the probability of locating an electron at a point $\vec{r}$ belonging to the unit cell must be identical to the probability at a position $(\vec{r} + \vec{t})$ outside this unit cell. As a result, the total electronic Hamiltonian and all physical quantities that depict the periodic system are defined by the network's translational invariance. This to the degree that the Hamiltonian operator commutes with the operators responsible for generating translations along the network points. In solid state chemistry it is more convenient to project the unit cell into the reciprocal space using a Fourier series, which then results in the so-called first Brillouin zone being expressed via three vectors $\vec{b}_i$ that are orthonormal to the vectors $\vec{a}_i$ in real space. Therefore, any singular functions can be expressed as the multiplication of a function $u_{\vec{g}}(\vec{r})$, that possesses the network periodicity, by a phase factor $e^{i\vec{g}\vec{r}}$ with $\vec{g}$ any vector in the reciprocal space.

$$\boldsymbol{f_{\vec{g}}(\vec{r}) = u_{\vec{g}}(\vec{r})e^{i\vec{g}\vec{r}}} \qquad (\mathbf{II.87})$$

This property of invariance by translational symmetry is more advantageously described in the Bloch theorem which asserts that any single electron wavefunction $\psi_{\vec{k}}(\vec{r})$ in a crystal lattice can be defined as the product of a phase factor $e^{i\vec{k}\vec{r}}$ and a function that shares the same periodicity as the periodic potential $u_{\vec{k}}(\vec{r})$:

$$\boldsymbol{\psi_{\vec{k}}(\vec{r}) = u_{\vec{k}}(\vec{r})e^{i\vec{k}\vec{r}}} \qquad (\mathbf{II.88})$$

$$\boldsymbol{u_{\vec{k}}(\vec{r}) = u_{\vec{k}}(\vec{r} + \vec{t})} \qquad (\mathbf{II.89})$$

Here $\vec{k}$ denotes the wave vector (Bloch vector) of the first Brillouin zone of the reciprocal lattice.

According to Bloch's theorem the problem of infinite number of single-electron wavefunctions can be transformed into a problem of infinite number of k-points within the first Brillouin zone due to the symmetry. Hence, characterizing the properties of the system amounts to an integration over the entire first Brillouin zone, which is a large volume for a small unit cell in real space and vice versa. However, since the wavefunctions of neighboring $\vec{k}$-points yield nearly identical results, this integration over the entire space can be sampled by examining a finite discrete set of $\vec{k}$-points distributed over a grid or, when it comes to very large systems, even to a single $\vec{k}$-point located at the center of the Brillouin zone (Γ-point). By considering the symmetry of the system, the numbers of $\vec{k}$-point can be reduced by limiting them to the irreducible Brillouin zone. The $\vec{k}$-points numbers needed for a precise representation of a system depends on the type, size, and the property being studied of this system. For instance, in isolators, a limited number of $\vec{k}$-points are sufficient as all bands are occupied, whereas in metals, a greater number of $\vec{k}$-points are required for bands crossing the Fermi level. Therefore, it's crucial to check the convergence of calculation with respect to the $\vec{k}$-point grid. Several schemes have been developed to

sample the Brillouin zone with a set of $\vec{k}$-points that provide the best estimate of the full integral. The most commonly used scheme is the one proposed by Monkhorst and Pack.[281]

II.4.4.2. Basis set

In DFT, there are several types of basis sets, but the two mostly commonly used are atomic orbitals and plane waves.[282] The plane wave basis set is the most straightforward extension of Bloch theorem with periodic boundary conditions.[283] Therefore, the periodicity property in Eq. (II.89) can be used to represent the wavefunction employing a discrete basis set of orthogonal plane waves, where the wave vector $\vec{G}$ is part of the reciprocal lattice:

$$\boldsymbol{u_{\vec{k}}(\vec{r}) = \sum_{\vec{G}} c_{i,\vec{k}}(\vec{G}) e^{i\vec{G}\vec{r}}} \qquad (\mathbf{II.90})$$

with $c_{i,\vec{k}}(\vec{G})$ are the coefficients of the plane-waves.

Hence, the electron wavefunctions can also be represented as a linear combination of plane-waves:

$$\boldsymbol{\psi_{\vec{k}}(\vec{r}) = \sum_{\vec{G}} c_{i,\vec{k}}(\vec{G}) e^{i(\vec{k}+\vec{G})\vec{r}}} \qquad (\mathbf{II.91})$$

While theoretically, an infinite basis set is needed to represent electron wave functions, a finite set of plane waves can adequately depict the relatively smooth wave functions of valence electrons. Knowing that these valence electrons are the primarily responsible for the bonding and chemical behavior of solids. By limiting the expansion to only valence electrons using plane waves, it's possible to truncated the basis set to only include plane waves with kinetic energies less than a specific energy cutoff, denoted as E_{cut}:

$$\boldsymbol{|k+G|^2 \frac{\hbar^2}{2m_e} \leq E_{cut}} \qquad (\mathbf{II.92})$$

However, it is important to test systems for convergence to confirm that the truncation effects do not influence the results of the calculation.

Employing plane waves as basis sets for valence electrons offers the benefit of systematically improving the precision of calculations by raising the energy cutoff, which in turn increases the number of plane waves in the basis set. However, it's important to mention that plane waves fall short in accurately representing wave functions that exhibit significant curvature, like those observed in the atomic core regions around nuclei where there are tightly bound states and strong oscillations due to nodal planes. To accurately represent such regions of space, a large number of plane waves is necessary. One way to overcome this limitation is by using pseudopotentials.

II.4.4.3. Pseudopotentials

The consideration of all of the electrons in many-electron systems will increase the computational time. A method to tackle this issue involves the subdivision of the total electron cloud into a core region (inner shell) and valence region (outer shell). This separation relies on the assumption that since the core electrons exhibit more inert behavior than the valence electrons, the latter will be of primary relevance for describing the chemistry of the considered periodic system. Thus, a pseudopotential is employed to approximate the interaction between the core electrons and the valence electrons.[284] This pseudopotential approximation, replaces the core electrons by an effective pseudopotential created by both the electrons of the core and the nuclei and replace rapidly oscillating valence electrons in the core region with pseudo-wavefunctions.[284] An example of a pseudo wavefunction and pseudopotential compared to the all-electron counterparts is illustrated in Fig. II.12. Within this approximation, for valence electrons, a weaker pseudopotential $\boldsymbol{V_{ion}^{PS}}(\vec{\boldsymbol{r}})$ is used in place of the strong ionic potential $\boldsymbol{V_{ion}}(\vec{\boldsymbol{r}})$ in the core shell. This way, the valence wave functions will not have rapid variations in the core shell. Beyond this core region, the pseudopotential and the true all-electron potential are identical and are defined by a cutoff radius $\boldsymbol{r_c}$. Outside this cutoff radius $\boldsymbol{r_c}$, both the pseudo-wavefunction $\boldsymbol{\psi^{PS}}(\vec{\boldsymbol{r}})$, and the all-electron wavefunction $\boldsymbol{\psi^{AE}}(\vec{\boldsymbol{r}})$, for the electrons of valence shell are also the same. The pseudopotential is constructed to ensure that pseudo-wave functions do not have the nodal structure that is responsible for the oscillations inside the cutoff radius. This implies that the pseudo wave functions can be represented using an appropriate number of plane waves. Thus, by considering an equivalent smoother electron density for electrons in the core region (we consider them as frozen electrons), pseudopotentials lower the number of plane waves necessary to represent all electron wavefunctions. This results in a substantial diminution in the computational cost of DFT simulations.

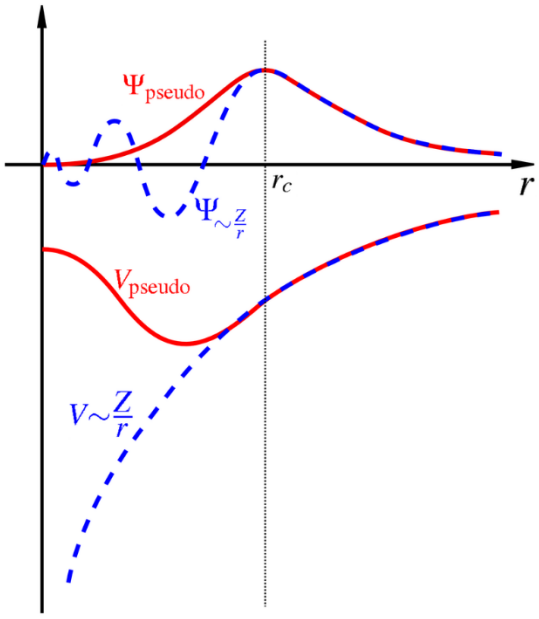

Figure II. 12. Comparison of the wavefunction in the nucleus's Coulomb potential (blue) with the wavefunction in the pseudopotential (red). The real-wavefunction and pseudo-wavefunction and potentials match in the graph a given cutoff radius r_c.[284]

The usefulness of a pseudopotential is determined by two conflicting criteria: (i) It should be a "soft" pseudopotential where only a few plane waves are required to describe the electronic pseudo-wave function, resulting in less computational effort; (ii) It has to be a "transferable" pseudopotential across different chemical environments, meaning that it has to accurately calculate the energy at the ground-state of valence electrons for various systems. To meet the first condition, a large cutoff radius must be used, while a small cutoff energy is required to meet the second condition. Therefore, a practical equilibrium must be established in each instance, and the choice for a particular pseudopotential should be determined by balancing the computational demands and the need for chemical precision. There are several different pseudopotentials existing, such as: norm-conserving pseudopotential (NCPP),[285,286] ultra-soft pseudopotential (USPP),[285,287] and projected augmented waves (PAW)[288] method. Relatively small numbers of plane waves are required to reach the convergence in the PAW scheme. Therefore, in this PhD dissertation, the PAW method was adopted as it is implemented into the Vienna Ab initio Simulation Package (VASP) software. This technique, which was proposed by Bloch as a generalization of ultra-soft pseudopotential and liner-augmented plane wave approaches,[288,289] enables to conserve the nodal characteristics of the wavefunction in proximity to the nucleus, and hence the orthogonality constraint between valence and frozen core orbitals but without the need of describing all functions with plane waves. In addition, the PAW method is capable of providing an optimal mixes between transferable accuracy and speed in DFT calculations.

II.4.5. VASP code and computational procedure

The Vienna Ab-initio Simulation Package, or VASP for short, is a software program that performs atomic-scale materials modelling. It can carry out electronic structure calculations (using DFT or HF) and quantum-mechanical molecular dynamics based on first principles.[290] VASP can compute an approximate solution to the many-body Schrödinger equation within the framework of DFT by solving the KS equations. This program is among the most commonly used computational tools for studying infinite systems like solid states and condensed matter. The software uses a plane wave basis set to represent valence electrons. Meanwhile, the interactions between ions and non-valence electrons can be represented using NCPP, USPP, or the PAW method to reduce the size of the basis set. VASP determine the electronic ground state, by using efficient iterative matrix diagonalization techniques and various algorithms meet the required electronic convergence and force tolerance criteria. In the software, both the self-consistency cycles and numerical techniques applied to find the electronic KS ground state are effective and reliable. To handle an infinite number of atoms, periodic boundary conditions are implemented, and the Monkhorst Pack is included also in the package for Brillouin zone sampling.[281] These features make VASP well-suited for computing extended large systems. Additionally, VASP makes use of parallel machines, splitting the calculation into many tasks, that communicate with each other using Message Passing Interface (MPI). In parallel computing, using more processors should theoretically result in faster calculations. However, in the case of computer clusters, there exists an important number of CPUs, which varies based on the processor type, beyond which the increase in computational speed is no longer linear with the number of CPUs utilized. For instance, while using four nodes may double the speed compared to using two nodes, using eight nodes may not necessarily quadruple the efficiency. Thus, to find the optimal parallelization setup of a VASP calculation, it is necessary to run tests for each system, algorithm and computer architecture. A standard calculation using VASP necessitates at least four basic input files, (1) INCAR, contains the parameters of the calculation and therefore defines the type of simulation; (2) POTCAR, contains the pseudopotentials used, (3) POSCAR, contains the initial structure, the Bravais lattice and atomic positions; and (4) KPOINTS, contains the k-point grid used to integrate the first Brillouin zone of the reciprocal space. On the other hand, there are three important output files: (1) CHGCAR, contains the calculated charge densities (2) CONTCAR, contains the final atomic positions; and (3) WAVECAR, contains the final wavefunctions.

Fig. II.13 illustrates the general flow of a typical VASP run solving KS equations via self-consistency field (SCF) method. To start the process, we use an initial trial for the electron density, $\boldsymbol{n^{in}(r)}$, usually based on the atomic electron densities. Then we compute the trial effective potential of KS, $\boldsymbol{V_{eff}(r)}$, and solve the KS equation to get the single-particle wavefunctions, $\boldsymbol{\psi_i}$, and eigenvalues, $\boldsymbol{\varepsilon_i}$. From the wavefunctions, we obtain the new electron density, $\boldsymbol{n^{out}(r)}$. Next, we verify the self-consistent condition, which can depend on the change in the electron density or the variance in the total energy compared with the last iteration, the total force acting on atoms being smaller than a certain value, or a

mix of these factors. If the self-consistency condition isn't reached, the computed electron density is merged with the electron density from prior iterations to form a new electron density. This new electron density is then reused to starts a new iteration. This procedure is repeated until a state of self-consistency is achieved. Upon reaching self-consistency, many parameters can be obtained, such as total energy, eigenvalues, stress, forces, band structure, electron density of states, and more.

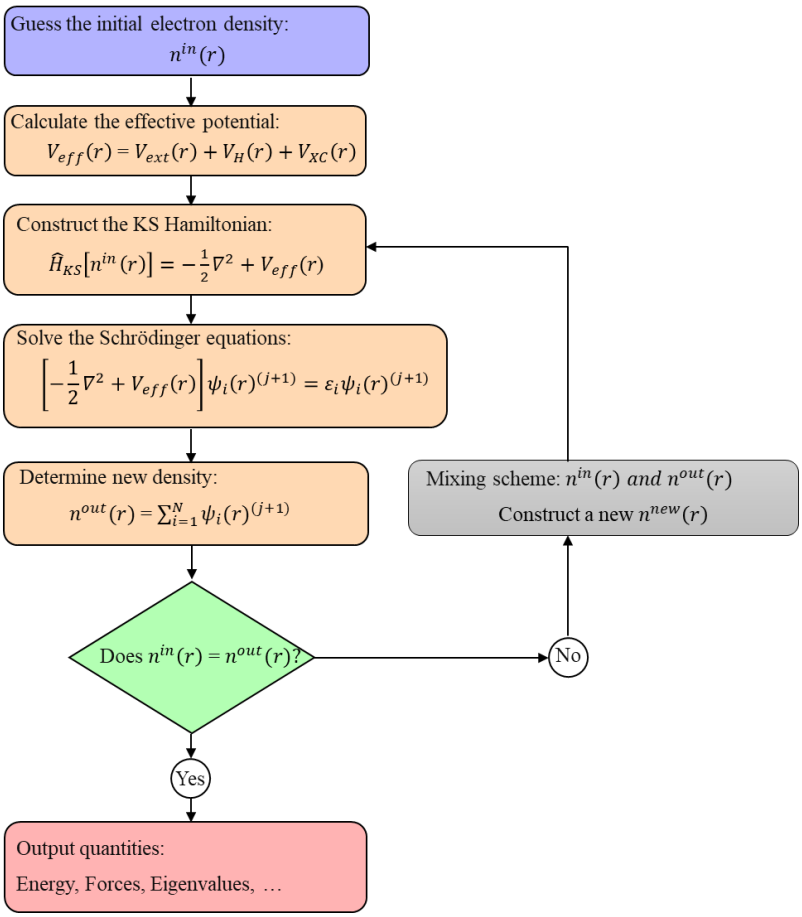

Figure II. 13. Flow-chart diagram of a self-consistent scheme to solve the KS equations.

Computational procedure of our DFT calculation

The electronic structure of the $AgTi_2(PO_4)_3$ system was investigated within density functional theory using VASP code.[290–292] The XC functional was treated using the generalized gradient approximation (GGA) in the Perdew-Bruke-Ernzerhof (PBE) scheme.[255,256] The interaction between the ionic core and valence electrons was represented by the projector augmented wave (PAW) pseudopotentials,[288] which considered Ag (5s4d), Ti (4s3d), P (3s3p) and O (2s2p) as valence states. An energy cutoff of 520 eV for plane wave and the Monkhorst-Pack k-point grids of 4×4×4 and 21×21×21 were employed for the geometry relaxation and electronic structure calculations, respectively. The generalized gradient approximation functional is known to significantly underestimate the band gaps of strongly correlated systems due to its inability to accurately capture the strong correlation interaction of d-orbitals.[293–295] As a result, we used the GGA+U method proposed by Dudarev et al.[275] in which the underestimated

electron-electron interaction of Ti 3d orbitals is corrected by a Hubbard term U, with a value ranging from 2 to 8 eV.

II.5. Catalytic activity and kinetic modelling

II.5.1. Model organic pollutants

Methylene blue (MB), methyl orange (MO), Rhodamine B (RhB) and, 4-nitrophenol (4-NP) were selected as model pollutants so that to explore the catalytic performance of the prepared Ag-based NASICON materials, as they meet certain requirements such as being water-soluble, stable in the presence of a reductant, and under ultraviolet and visible illumination (no photolysis), and easily detectable by UV-Vis spectroscopy. Table II.3 lists the molecular formula and general proprieties of the target organic molecules.

Table II. 3. Chemical and physical properties of model organic pollutants.

Chemical names	Methylene blue	Methyl orange	Rhodamine B	4-nitrophenol
Chemical formula	$C_{16}H_{18}ClN_3S$	$C_{14}H_{14}N_3NaO_3S$	$C_{28}H_{31}ClN_2O_3$	$C_6H_5NO_3$
Chemical structure	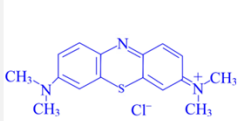	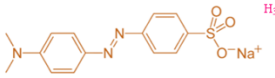	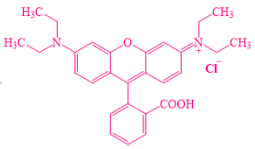	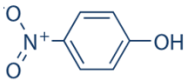
Chemical class	Thiazine dye	Azo dye	Xanthene dye	Nitrophenolic compound
Molecular weight, g/mol	319.85	327.33	479.02	139.11
Colour	Blue	Red at pH = 3.0 Yellow at pH = 4.4	Reddish-violet	Light-yellow
Melting point, °C	180-190	> 300	210-211	110-115
Density, g/cm^3	1.0	0.98	1.28	1.48
Adsorption, λ_{max}(nm)	664, 613, 292, 246	464, 270	554	400
Water solubility, g/L	43.6 at 25 °C	5 at 20 °C	8-15 at 20 °C	16 at 25 °C

II.5.2. Catalytic reduction of organic pollutants

Reduction of MB and MO over Ag NPs/$AgTi_2(PO_4)_3$

The catalytic reduction experiments were performed in a 50 mL beaker that was placed in an ultrasonic bath at ambient temperature. The production of Ag NPs on the $AgTi_2(PO_4)_3$ surface and the catalytic reduction process were conducted at the same time in one reaction mixture. The catalytic reaction was carried out by first dispersing 2 mg of $AgTi_2(PO_4)_3$ uniformly in 35 mL of DDW. Then, 10 mL of an aqueous solution of $NaBH_4$ (87.5 mM) was added. The mixture was sonicated for 10 minutes, resulting in a color change from white (the color of the $AgTi_2(PO_4)_3$ suspension) to yellow-green, indicating the formation of Ag NPs. Next, 5 mL of either MB dye (3.5 mM) or MO dye (3.5 mM) aqueous solution was added to the mixture. This resulted in final concentrations of 0.35 mM for the organic dyes and 17.5 mM for $NaBH_4$. Finally, we monitored the progress of dyes conversion by taking measurements of the

mixture's absorption spectra over time using a UV-Vis spectrometer in the 200-800 nm wavelength range.

Recyclability and regeneration tests: To test the catalyst's reusability, 0.1 g of $AgTi_2(PO_4)_3$ was homogeneously mixed with 900 mL of a $NaBH_4$ solution (19.45 mM) for 10 min. Next, 100 mL of either MB or MO solution (3.5 mM) was added to the suspension. The reaction time was recorded when the solution become completely colourless and transparent. The used Ag NPs/$AgTi_2(PO_4)_3$ catalyst was then filtered and thoroughly washed with DDW before being calcined at 700 °C for 3 h, and characterized by XRD, SEM, and EDX analyses to further evaluate its stability. Afterwards, the regenerated sample was reused for the next catalytic conversion under identical conditions. The amount of silver that had leaked into the solution was measured using inductively coupled plasma atomic emission spectroscopy (ICP-AES). Before performing the ICP-AES analysis, the solution was acidified with 3% HNO_3.

Reduction of 4-NP over Ag NPs/$AgZr_2(PO_4)_3$

The effectiveness of Ag NPs/$AgZr_2(PO_4)_3$ as a catalyst was evaluated by measuring its ability to reduce 4-nitrophenol (4-NP) into 4-aminophenol (4-AP) using an excess of $NaBH_4$. The procedure was carried out in a 50 mL beaker, which was positioned inside an ultrasonic bath at ambient temperature. In a typical process, $AgZr_2(PO_4)_3$ (2 mg) was dispersed in 35 mL of DDW using an ultrasonic bath for 5 min. Afterward, 10 mL of freshly prepared $NaBH_4$ solution (87.5 mM) was added to the $AgZr_2(PO_4)_3$ suspension. Shortly after mixing, the solution changed from white (the color of the $AgZr_2(PO_4)_3$ suspension) to a light-yellow, indicating that Ag NPs had formed. Next, 5 mL of a 4-NP solution (3.5 mM) was added to the mixture containing Ag NPs/$AgZr_2(PO_4)_3$ and $NaBH_4$. In these conditions, the molar ratio between $NaBH_4$ and 4-NP was 50:1. To monitor the progress of the reduction reaction, 1 mL of the reaction mixture was periodically taken out using a micropipette, transferred to a quartz cuvette, and diluted to 3 ml with cooled DDW to slow down the reaction. The UV-Vis absorption spectra were subsequently recorded in the 200-500 nm wavelength scanning range.

Recyclability and regeneration tests: The ability of Ag NPs/$AgZr_2(PO_4)_3$ to be reused was assessed by performing 10 consecutive cycles of 4-NP conversion using the same reaction procedure. Then, after completing the 10 reusability tests, the used $AgZr_2(PO_4)_3$ catalyst was regenerated by adding an excess of sodium chloride (NaCl) to the mixture containing Ag NPs/$AgZr_2(PO_4)_3$, $NaBH_4$, and 4-AP. This process allowed for the recovery of Ag NPs as Ag aggregates. The recovered product (Ag aggregates/$AgZr_2(PO_4)_3$) was then treated with a nitric acid (HNO_3) solution for 1 h at 70 °C. During this stage, only the metallic Ag was oxidized, while the NASICON material remained unaffected owing to its stability and resistance to dissolution in HNO_3. The resulting product was filtered, repeatedly washed with DDW, and dried overnight at 80 °C. It was then analyzed using XRD, SEM, and EDX techniques. In addition, the corresponding filtrate solution was also examined using the ICP-AES

technique. Subsequently, the catalytic reduction of 4-NP was performed again for 10 additional cycles to test the reusability of the regenerated $AgZr_2(PO_4)_3$ catalyst. This recycling process was carried out three times.

II.5.3. Visible light photocatalytic oxidation of organic pollutants

Oxidation of RhB over $AgTi_2(PO_4)_3$

Catalytic tests of $AgTi_2(PO_4)_3$ material for the photodegradation of rhodamine B (RhB) dye conducted at ambient temperature in a sealed 200 ml glass Pyrex photoreactor placed inside a wooden box. A tungsten halogen lamp (125 W) placed along the central axis of the photocatalytic reactor on top was used as the source of visible light. The distance between the lamp and the fluid level inside the reactor was set at 100 mm. The temperature of the photoreactor was maintained at approximately 25 °C using a water jacket that circulated around it. Three openings necks were used for taking samples, purging air, and measuring the temperature. The inside of the box that contained the reactor was covered with aluminium foil to block any unwanted light from entering the reactor from the surrounding environment. For the photodegradation study, 100 mg of the as-synthesized $AgTi_2(PO_4)_3$ sample was mixed with water containing a 5 mg L^{-1} RhB dye initial concentration with pH = 7.

The photocatalytic experiment consisted of two consecutive steps: first adsorption, followed by oxidation.

Adsorption step: 100 mL of DDW containing a specific concentration of the organic dye model was added to the photoreactor. Then, a predetermined amount of the photocatalytic material was introduced. The solution was stirred using a magnetic stirrer inside the box, in the dark and without any light exposure at 25°C for 60 min. This allowed the dye molecules to reach an equilibrium between adsorption and desorption on the surface of the catalyst. During the adsorption process, a sample was taken immediately and additional samples were collected at regular intervals for analysis using UV-Visible spectrophotometry.

Oxidation step: Once the adsorption process was finished, the photodegradation process was initiated by switching on the visible light lamp. An air stream was also introduced to increase agitation and mass transfer, and to provide sufficient oxygen for the reaction to occur. During the oxidation step, samples were collected at regular intervals and analyzed using UV-Visible spectrophotometry.

Recyclability tests: For the recycling experiments, $AgTi_2(PO_4)_3$ sample (200 mg) was mixed with 200 mL of RhB solution (10 ppm) and stirred at ambient temperature in the dark for 60 min to allow maximum absorption of the dye by the catalyst. The beaker was positioned inside the photoreactor, which was set at a temperature of 25 °C, and exposed to visible light. Once the reaction was finished, the photocatalyst was separated by filtration, washed, and then used again in another photocatalytic

cycle under the same conditions. After conducting several experiments, the sample was analyzed using XPS to assess its stability.

Radicals-trapping experiments: To gain an in-depth understanding of the photocatalytic process, trapping tests were performed to discover the active species responsible of the photo-oxidation of RhB. Isopropyl alcohol (IPA), ethylenedinitrilotetraacetic acid disodium salt dihydrate (Na_2-EDTA) and ascorbic acid (As-Ac) were employed as scavengers to neutralize hydroxyl species (•OH), the holes (h^+) and the superoxide species ($•O_2^-$), respectively. Prior to the photocatalytic experiment, 5 mL of 20 mM scavengers were added to 95 mL of the reaction mixture. The rest of the experiment was performed under similar conditions as mentioned above.

Oxidation of MO over Ag_2O NPs/$AgZr_2(PO_4)_3$

The process for degrading methyl orange (MO) dye using visible light photocatalysis was conducted as described previously in section II.5.4. A 200 mL glass Pyrex beaker was used as the photocatalytic reactor, and a tungsten halogen lamp (125 W) was employed as the source of visible light. The lamp was positioned approximately 100 mm above the liquid surface. A circulating water jacket was utilized to keep the temperature of the reaction at around 25 °C. In a typical photocatalysis experiment, 100 mg of the $Ag_2O/AgZr_2(PO_4)_3$ composite was added into 100 mL of a MO solution (5 mg L^{-1}). Prior to exposing the solution to light, it was stirred for 40 min in the dark using a magnetic stirrer to achieve an adsorption-desorption equilibrium between the $Ag_2O/AgZr_2(PO_4)_3$ catalyst and the dye molecule. Afterward, an air purging tube was inserted and the lamp was switched on. During the photodegradation process, aliquots of the reaction mixture (about 3 mL) was periodically withdrawn at a regular time period from the photoreactor. The samples were passed through a 0.45 µm membrane filter using a syringe to remove any particles, and then analyzed using UV-Vis spectrophotometry.

Recyclability tests: To examine the sample's reusability and stability, 200 mg of the $Ag_2O/AgZr_2(PO_4)_3$ sample was introduced into 200 mL of a MO solution (10 mg L^{-1}), followed by stirring for 40 min in darkness at ambient temperature, to promote the adsorption/desorption equilibrium. Then, the mixture was illuminated with visible light under stirring. Once the photocatalytic degradation was completed, the composite material was separated from the reaction mixture, washed several times before being used again in another photocatalytic run under similar conditions. Finally, after repeated experiments, the spent photocatalyst was analyzed by X-ray diffraction (XRD) to evaluate its stability.

Radicals-trapping experiments: In order to elucidate the photocatalytic process, radicals-trapping tests were performed to shed light on the dominant reactive species contributing in the degradation of MO dye. Ascorbic acid (As-Ac), ethylenedinitrilotetraacetic acid disodium salt dihydrate (Na_2-EDTA) and isopropyl alcohol (IPA) were employed as scavengers for quenching the superoxide species ($•O_2^-$), the holes (h^+), and the hydroxyl species (•OH) respectively. Before the photocatalytic reaction, 5 mL of

scavengers (20 mM) were separately added to 95 ml of MO solutions (5 mg L^{-1}). Subsequently, the photocatalytic tests were executed under the identical conditions as described above.

Regeneration procedure of catalyst: To check the regeneration property, the spent $Ag_2O/AgZr_2(PO_4)_3$ photocatalyst was dispersed in 10 mL of distilled water and sonicated for 5 min. Subsequently, 15 mL of hydrogen peroxide H_2O_2 solution (30%) was added slowly to the above dispersion while stirring at 35 °C. After continuous stirring for 3 h, the sample was recovered by filtration and dried at 80 °C for 6 h. Finally, the product was characterized by XRD and SEM-EDS analyses.

II.5.4. Kinetic studies

To assess the practicality of the catalytic systems, it's crucial to conduct in-depth kinetic studies of the reactions. The data obtained from these studies will allows us to establish a connection between the microscopic realm of reacting molecules with the macroscopic realm of industrial reaction engineering. The quantification of the kinetics of the catalytic systems involves both determining the reaction order and developing a kinetic model. This helps to comprehend the reaction mechanism and allows for effective categorization of specific chemical reaction. Since most catalytic reactions occur on particles surface, the kinetics of model reactions can be analyzed using either the Eley-Rideal or Langmuir-Hinshelwood mechanisms.[296]

In the Eley-Rideal kinetic model, only one of the reactants, for example reactant A (the organic pollutant), is adsorbed onto the catalyst's surface. Reactant B (either the reducing agent BH_4^-, or the hydroxyl radical •OH) remains in the surrounding medium (the aqueous phase). When the chemisorbed and unbound species collide, they react to form product C (harmless molecules). This second reaction is the step that dictates the kinetic rate. Finally, the product C desorbs from the catalyst's surface.

$$\mathbf{A_{aq} + * \rightarrow A_{ads}} \qquad (\mathbf{II.93})$$

$$\mathbf{A_{ads} + B_{aq} \rightarrow C_{ads}} \qquad (\mathbf{II.94})$$

$$\mathbf{C_{ads} \rightarrow C_{aq}(Intermediate\ or\ final\ product) + *} \qquad (\mathbf{II.95})$$

where * is the vacant adsorption site on the catalyst's surface.

Unlike the kinetic model based on the Eley-Rideal mechanism, the Langmuir-Hinshelwood model assumes that all species can be adsorbed and can reach thermal equilibrium on the catalyst's surface prior to participating in any reaction. As a result, species undergo reactions while they are in the chemisorbed state on the catalyst's surface. The steps of the reaction are as follows:

$$\mathbf{A_{aq} + * \rightarrow A_{ads}} \qquad (\mathbf{II.96})$$

$$\mathbf{B_{aq} + * \rightarrow B_{ads}} \qquad (\mathbf{II.97})$$

$$\mathbf{A_{ads} + B_{ads} \rightarrow C_{ads}} \qquad (\mathbf{II.98})$$

$$\mathbf{C_{ads} \rightarrow C_{aq}(Intermediate\ or\ final\ product) + *} \qquad (\mathbf{II.99})$$

The step that governs the rate of the reaction is the one that occurs on the surface of the catalyst (as illustrated in Eq. II. 98). All reactants compete for the available active sites. Therefore, if a reactant has a stronger affinity to the catalyst surface, an augmentation in its concentration will lead to a augmentation in the rate of reaction. Conversely, if the concentration of this reactant decreases, the reaction rate may increase if the ratio of all reactants is not optimal. At the end, the product desorbs from the catalyst surface. The Langmuir-Hinshelwood (L-H) kinetics is the most commonly employed mechanism for the description of heterogeneous catalytic processes.[97] As a results, it was applied in this project to quantitatively approximate the catalytic reactions.

The L-H kinetic model can be determined using the formula below:

$$\boldsymbol{r = -\frac{d[C]}{dt} = \frac{k_r K_{ads} C}{1 + K_{ads} C}} \qquad (\mathbf{II.100})$$

where r refers to the decomposition rate of the organic pollutant (mM s^{-1}), C represents the concentration of the pollutant (mM) in the aqueous medium at any time, t is the time of the reaction (s), k_r represents the rate constant of the reaction (mM s^{-1}), and K_{ads} is the Langmuir adsorption equilibrium constant (mM^{-1}).

It has been suggested that at very dilute concentrations of the pollutant (i.e., C_0[pollutants] << C_0[reductant/oxidant]), the expression $K_{ads}C$ becomes << 1, and the L-H kinetic is reduced to an apparent pseudo first-order equation:

$$\mathbf{\ln\left(\frac{C_t}{C_0}\right) = -k_r K_{ads} t = -k_{app} t} \qquad (\mathbf{II.101})$$

Where k_{app} represents the rate constant following the pseudo-first order. A graph of $\ln(C_t/C_0)$ vs. the catalytic degradation time gives a straight line with a slope corresponding to the pseudo-first order constant, and is utilized as a criterion for the comparison of catalysts activities.

To assess the performance of catalysts, we also determine the activity factor, denoted as k', using the following equation:

$$\mathbf{k' = \frac{k_{app}}{m}} \qquad (\mathbf{II.102})$$

where m (g) refers to the mass of the catalyst involved in the reaction.

Chapter III: Catalytic reduction of organic dye pollutants over Ag NPs/$AgTi_2(PO_4)_3$

This chapter is based on the work published as:

A. Moussadik, F. S. Brigiano, F. Tielens, M. Halim, M. Kacimi, A. El Hamidi, Self-supported Ag nanoparticles on $AgTi_2(PO_4)_3$ for hazardous dyes reduction in industrial wastewater. Journal of Environmental Chemical Engineering, 2022, vol. 10, no 1, p. 106939.

III.1 Introduction

Water pollution by organic compounds, especially organic dyes, remains one of the major environmental and public problems. Various industries, such as textiles, cosmetics, leather tanning, paint, pulp and paper, printing, pharmaceuticals, plastics, and food, simultaneously consume large amounts of water and discharge great amounts of organic dye substances into aquatic ecosystems.[297–299] Azo dyes, among all, like methylene blue (MB) and methyl orange (MO) are the major sources of water pollution because they are extensively used in countless industrial activities.[300] The occurrence of these azo dyes in water, even very small quantities, is easily noticeable and the public perception of water quality is greatly influenced by color. The discharge of azo dyes into water bodies is a major ecological concern, which amplified considering that the majority of these chemicals, due to their electrophilicities (i.e., azo bond (–N=N–)), are not so easily degradable by standard wastewater treatment techniques.[300] Furthermore, in recent decades, there have been concerns about the possible harmful effects of synthetic azo dyes, which pose a serious risk to humans, animals, and aquatic living organisms.[300] Therefore, it is crucial to eliminate or convert these dangerous chemicals into eco-friendly compounds for the well-being of both people and the aquatic environment.

Several methods have been developed for the treatment of these organic contaminants, including biodegradation,[301] physical adsorption,[302] membrane separation,[303] electrochemical degradation,[304] photocatalytic degradation,[305] etc. However, as pointed out in the previous chapters, due to their low efficiency, expensive installation, and high energy demands, the above-mentioned methods lack practicality. In contrast, the chemical reduction of organic dyes using catalysts and borohydride ($NaBH_4$) as a reducing agent has benefits over other methods, such as being easy to implement, cost-effective, and highly efficient.[306–308] In addition, $NaBH_4$ is relatively eco-friendly due to the low toxicity of borates. During a chemical reduction process, the catalyst serves as an electron transfer system between BH_4^- ions and organic dyes, accelerating the rate at which dyes are reduced.[309,310] Traditionally, the utilized catalysts are often noble metal nanoparticles (e.g., Au, Ag, Pt, and Pd) due to their abundant active sites, large specific surface area, high adsorption capacity, rapid electron transfer capabilities, and superior reactivities.[311,312]

Among different noble metallic nanoparticles, Ag NPs are of great interest by virtue of their unique features such as catalytic activity, low toxicity, antimicrobial activity, low prices and ease of

accessibility. However, free Ag NPs with high surface energy have a tendency to rapidly aggregate and/or agglomerate, reducing the number of active sites accessible for reactant adsorption and thus decreasing catalytic efficiency.[19] Another challenge is the difficulty in recovering small-sized Ag particles, which hinders their ability to be recycled. To address these issues, support materials are often used to stabilize Ag NPs, prevent aggregation and agglomeration, and enhance their recyclability. In recent times, numerous support materials have been introduced to stabilize Ag NPs. These comprise polymer matrices,[313] carbon-based materials,[314] porous silica,[315] metal oxide,[316] and metal-organic frameworks,[317] and others. Nevertheless, despite these developments, there remain significant challenges that must be addressed in the present context. For example, the deactivation and loss of the catalytic performance of supported Ag NPs during recycling experiments, which mainly results from the poisoning of Ag NPs by intermediate products and/or inorganic ions adhering to their surface more strongly than the reactants themselves, which hinder their practical application. As a results, it is very crucial to create a simultaneously effective and simple strategy for the regeneration of the deactivated Ag NPs catalysts.

This chapter describes the preparation of self-grown Ag NPs on the surface of $AgTi_2(PO_4)_3$ NASICON phosphates to be applied as a nanocomposite catalyst in the decomposition of dye contaminants in wastewater. The chapter also aim to explore the regeneration of deactivated surface Ag NPs at the end of the catalytic process through their reinsertion into the original $AgTi_2(PO_4)_3$ material via a simple re-calcination process. This chapter builds on the previous work of our group,[24–26,211,212] which demonstrated that NASICON phosphates with the chemical formula $A_xM_2(PO_4)_3$, where A represents Ag or Cu ions, and M polyvalent elements such as Zr, Hf, or Th, and so on, are promising precursors, supports, and hosts for the creation, immobilization, and regeneration of highly active silver and copper catalysts. Our group's research has shown that the Ag^+ (or Cu^+) cations within the 3-dimensional framework of the NASICON structure are highly mobile and can undergo partial reduction when exposed to a high-temperature reductive atmosphere (e.g., hydrogen gas). This process results in the formation of nano-sized Ag NPs (or Cu NPs), while simultaneously exchanging with protons (H^+), without causing the NASICON skeleton to collapse. The metallic NPs formed *in situ* can serve as effective catalysts for a variety of reactions. Additionally, these self-supported nanoparticles can be re-oxidized through heat treatment and reversibly incorporated back into the NASICON structure, restoring the original composition of the material.

The objectives of this chapter are three new perspectives. First, we prepare self-grown Ag NPs on the $AgTi_2(PO_4)_3$ surface by wet chemical reduction at ambient temperature using $NaBH_4$. Then, we analyze the crystalline structures, morphological features, and phase composition of the prepared products using various characterization techniques. Second, we evaluate the catalytic ability of *in situ* self-supported Ag NPs on $AgTi_2(PO_4)_3$ for the reductive conversion of MB and MO as reference organic contaminants.

Third, we perform a simple catalyst regeneration strategy, via a simple re-calcination route, to show that the spent Ag NPs/$AgTi_2(PO_4)_3$ catalyst can achieve self-regeneration to the initial $AgTi_2(PO_4)_3$ material. For convenience, the term "AgTiP" will be used to refer to $AgTi_2(PO_4)_3$ in the following sections.

III.2 Results and discussions

III.2.1. XRD characterization

Fig. III.1 displays the XRD diffractograms of the as-synthesized AgTiP material and the Ag NPs/AgTiP composite. As depicted in Fig. III.1(a), all the diffraction lines of AgTiP could be completely indexed in terms of the rhombohedral $NaTi_2(PO_4)_3$ NASICON-type material (as per ICDD card No. 33-1296) without any impurity phases, which is consistent with the previous report.[210] The distinct and clear diffraction lines suggest a high level of long-range periodicity. After being reduced by $NaBH_4$, the XRD diffractogram of Ag NPs/AgTiP reveals that the product retains its rhombohedral structure, as exhibited in Fig. III.1(b). However, the newly detected line at 38.10° 2θ can be ascribed to the (111) plane of face-centered cubic Ag (according to ICDD card No. 04–0783), proving the existence of metallic silver on the AgTiP surface. On the other hand, the peak at 20.12° 2θ can be attributed to the (104) plane of the $NaTi_2(PO_4)_3$ (NaTiP) phase (as per ICDD card No. 33-1296). These findings demonstrate that reducing AgTiP with $NaBH_4$ simultaneously leads to the production of Ag^0 and a new NASICON phase, $Ag_{1-x}Na_xTi_2(PO_4)_3$ (AgNaTiP). The average dimension of the supported Ag particles was calculated utilizing the Scherrer's equation[216] (Eq. II.2) and the full-width at half-maximum of the Ag (111) plane. The average crystalline dimension of the Ag NPs was found to be around 16 nm.

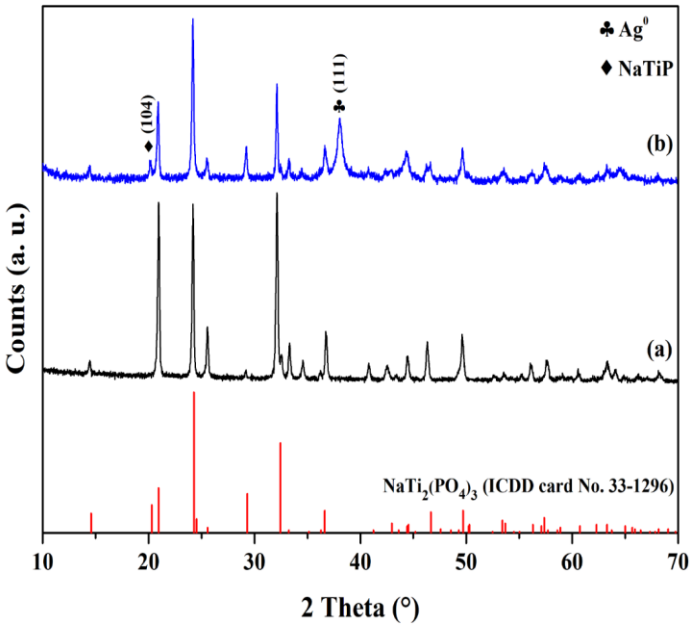

Figure III. 1. XRD diffractograms of (a) AgTiP and (b) Ag NPs/AgNaTiP.

III.2.2. Rietveld analysis

The XRD diffractograms were further analyzed by the Rietveld method[217] employing the FullProf program[222] to obtain the structural composition of the newly formed NASICON matrix after reduction with $NaBH_4$ and to estimate the weight percentage of Ag NPs on its surface. Fig. III.2(a) and (b) display the Rietveld plots comparing the experimental and calculated XRD diffractograms of AgTiP material and the Ag NPs/AgNaTiP nanocomposite, respectively. The experimentally observed diffractograms and theoretical show very little difference (close to the intensity scale's zero point), as indicated by the residual plots (blue curves). Refined crystallographic parameters and site occupancies of the studied Ag-based samples are listed in Table III.1. The good quality of the structural refinement was confirmed, as indicated in Table III.1, by the small deviations in the reliability parameters (χ^2, R_p, and R_{wp}). The Rietveld refinement results prove that the AgTiP sample has grown as a monophase with rhombohedral symmetry in the $\boldsymbol{R\bar{3}c}$ space group, as shown in Fig. III.2(c). In the AgTiP crystal structure, the atoms are arranged as follows: Ag is located at *6b* (0, 0, 0), Ti at *12c* (0, 0, z), P at *18e* (x, 0, z) and O occupies two different sites at *36f* (x, y, z). After reduction, the Rietveld analysis plot reveals the presence of both a cubic Ag phase ($\boldsymbol{Fm\bar{3}m}$) and a rhombohedral AgNaTiP phase ($\boldsymbol{R\bar{3}c}$) as illustrated in Fig. III.2(c). In the AgNaTiP crystal structure, Ag^+ cations were partially replaced by Na^+ cations at the *6b* (0, 0, 0) position, as anticipated. The Ag and Na contents at this site were determined to be 28% and 72%, respectively. Finally, the weight fractions of each identified phase (w_i) were calculated using the FullProf software from the refined scale factors of the respective calculated intensities, as previously described by Hill and Howard[221] (Eq. II.15). Based on this quantitative approach, the weight percentage the Ag NPs supported on AgNaTiP surface was found to be 16.16% versus 22.08% of the total theoretical Ag content.

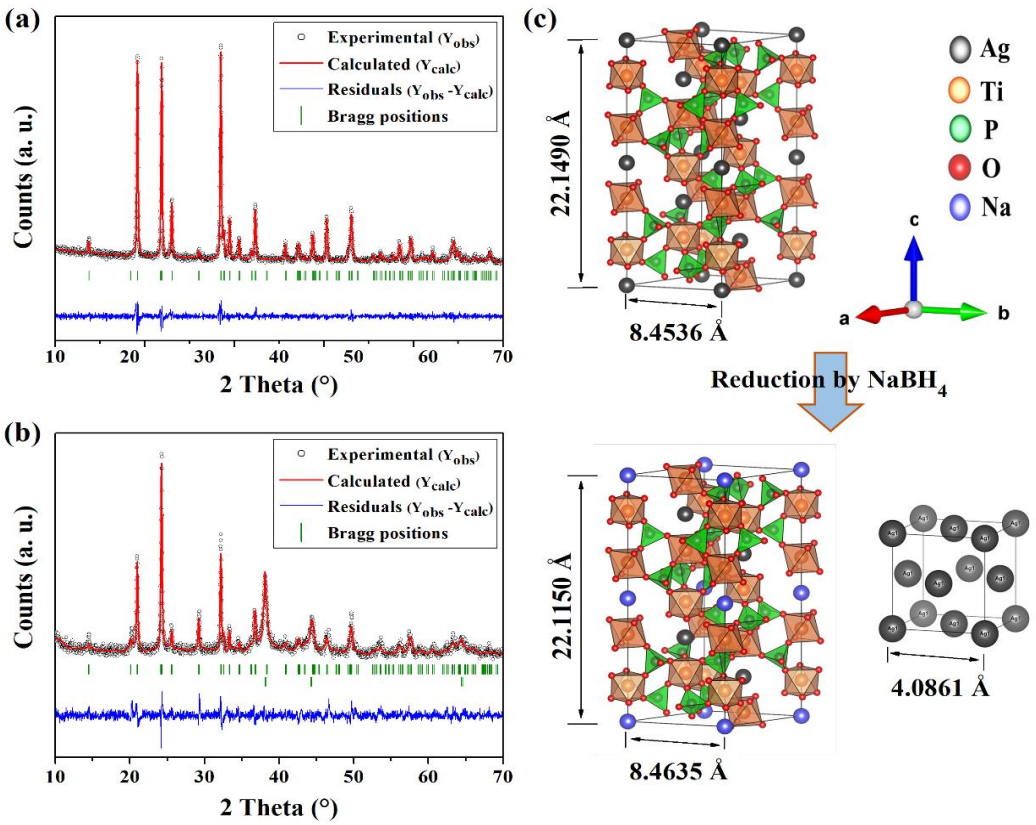

Figure III. 2. Rietveld refinement of (a) AgTiP, (b) Ag NPs/AgNaTiP and (c) the rhombohedral crystal structures of AgTiP and AgNaTiP, and the face-centered cubic structure of Ag.

Table III. 1. The different parameters acquired from the Rietveld refinement of AgTiP before and after reduction with $NaBH_4$.

Parameter		$AgTi_2(PO_4)_3$	$Ag_{1-x}Na_xTi_2(PO_4)_3$
a (b) Å		8.4536(6)	8.4635(18)
c Å		22.1490(15)	22.115(4)
V Å^3		1370.77(16)	1371.9(5)
O1 (*36f*)	x	0.1678(16)	0.162(3)
	y	-0.019(2)	-0.051(3)
	z	0.1961(6)	0.2002(13)
	Occ.	1.0000	1.0000
O2 (*36f*)	x	0.1999(16)	0.194(3)
	y	0.1755(13)	0.174(2)
	z	0.0913(5)	0.0942(11)
	Occ.	1.0000	1.0000
Ag (*6b*)	x	0	0
	y	0	0
	z	0	0
	Occ.	0.16667	0.04833
Na (*6b*)	x	-	0
	y	-	0
	z	-	0
	Occ.	-	0.12059

Ti (*12c*)	x	0	0
	y	0	0
	z	0.1464(2)	0.1448(6)
	Occ.	0.33333	0.33333
P (*18e*)	x	0.2840(10)	0.2843(20)
	y	0	0
	z	0.25	0.25
	Occ.	0.50000	0.50000
Reliability factors	χ^2	1.99	2.37
	R_p	7.98	9.15
	R_{wp}	10.01	11.6

III.2.3. ATR-FTIR characterization

Fig. III.3(a) and (b) display the ATR-FTIR spectra of the materials that were synthesized. The spectrum of AgTiP, depicted in Fig. III.3(a), reveals the vibrational bands of tetrahedral PO_4^{3-} unit with point group symmetry Td.[318,319] The pair of peaks found at 500 and 600 cm^{-1} are ascribed to the antisymmetric bending modes (ν_4) of the O-P-O unit. The broad peak located between 900 and 1040 cm^{-1}, along with the shoulder at 1060 cm^{-1}, are ascribed to the symmetric and antisymmetric stretching modes (ν_1 and ν_3) of the PO_4 group, respectively. The peak found at 1280 cm^{-1} is associated with the symmetric stretching vibrations (ν_3) of the P-O unit. This high frequency absorption band is mainly affected by the electronic density of the highly charged Ti^{4+} ions.[319] After the reductive reaction, the Ag NPs/AgNaTiP spectrum remains unchanged and the primary absorption bands are preserved, as depicted in Fig. III.3(b). These findings matche the XRD results and verify the structural stability of the rhombohedral NASICON skeleton.

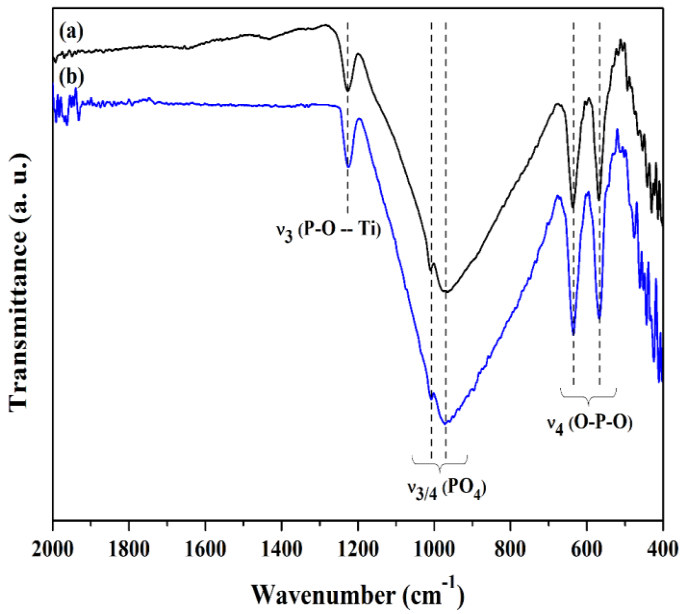

Figure III. 3. ATR-FTIR spectra of (a) AgTiP and (b) Ag NPs/AgNaTiP.

III.2.4. SEM-EDX analysis

SEM technique was performed to analyze the shape and morphology of the prepared Ag-based materials. Fig. III.4(a) shows that the AgTiP material consists of numerous interconnected particles that are micrometric in size. The SEM images of Ag NPs/AgNaTiP after reduction by $NaBH_4$ (Fig. III.4(b) to (d)) clearly show that the surfaces of the AgNaTiP sample are randomly decorate with Ag NPs. The average dimensions of Ag NPs was calculated to be between 20-35 nm, which is greater than the sizes of the Ag crystallites determined from the XRD pattern employing Scherrer's formula.[216] This is agreement with prior research that has demonstrated that crystallites are often equal to or smaller in size than their corresponding nanoparticles.[320] On the other hand, after the reductive reaction, there are no visible changes to the overall appearance of AgTiP.

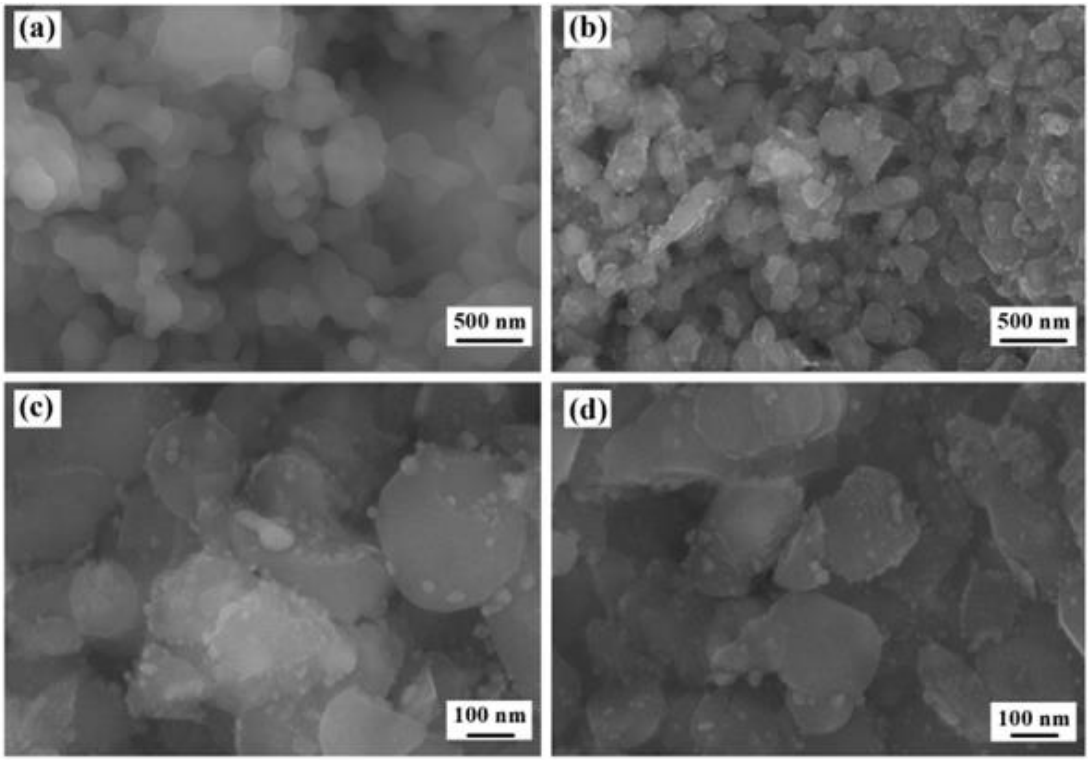

Figure III. 4. SEM micrographs of (a) AgTiP and (b, c, d) Ag NPs/AgNaTiP.

In addition, an EDX system was coupled to the SEM technique, enabling a semi-quantitative chemical analysis of the individual elements. Fig. III.5(a) and (b) show the EDX spectra of the synthesized products. The EDX spectrum of AgTiP (Fig. III.5(a)) verifies the existence of Ag, Ti, O, and P atoms in the obtained material. The weight percent for silver is 5.85%, for titanium is 11.34%, and for phosphorus is 17.72%, which closely matches the theoretical molar ratio of 1:2:3 in the chemical formula of $AgTi_2(PO_4)_3$. Additionally to the peaks of Ag, Ti, O, and P, the EDX spectrum of the Ag NPs/AgNaTiP nanocomposite (Fig. III.5(b)) also displays an extra peak at 1 keV that is attributed to sodium cations (Na^+). This confirms that after the reduction process of AgTiP by $NaBH_4$, Ag^+ ions were replaced by Na^+ ions in the NASICON crystal framework.

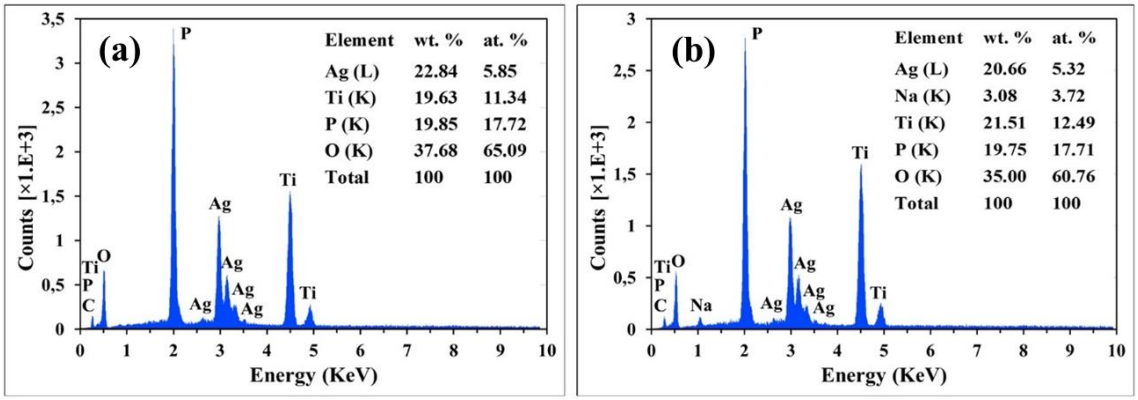

Figure III. 5. EDX analysis of (a) AgTiP and (b) Ag NPs/AgNaTiP.

The reduction mechanism of AgTiP by aqueous $NaBH_4$ can proceed through two processes, as indicated by the combined data from XRD, ATR-FTIR and SEM-EDX that was presented above. The first process takes place when the Ag^+ ions within AgTiP are reduced by BH_4^- ions through the reaction that follows[123,126] (Eq. III.1):

$$\mathbf{AgTi_2(PO_4)_3 + (Na^+, BH_4^-) + 4H_2O}$$
$$\downarrow \qquad (\mathbf{III.1})$$
$$\mathbf{xAg^0@Ag_{1-x}\square_xTi_2(PO_4)_3 + B(OH)_4^- + 3.5H_2 + xH^+ + Na^+}$$

The second process occurs immediately when Ag^+ vacancies are replaced by Na^+ ions to balance the negatively charged framework, as shown in the following reaction (Eq. III.2):

$$\mathbf{xAg^0@Ag_{1-x}\ \ _xTi_2(PO_4)_3 + Na^+ \rightarrow xAg^0@Ag_{1-x}Na_xTi_2(PO_4)_3} \qquad (\mathbf{III.2})$$

III.2.5. LSPR analysis

The synthesized Ag NPs on AgTiP surface were also characterized during real-time *in situ* formation by UV-Vis spectroscopy. The reduction AgTiP with respect to time was observed from 2 to 120 min. Fig. III.6(a) shows the development of the Ag NPs' distinctive localized surface plasmon resonance (LSPR) band over time. The figure illustrates that the formation of Ag NPs on AgTiP began as soon as the borohydride ions were added. The existence of a single LSPR peak implies that the Ag NPs formed are either spherical or nearly spherical in shape.[321] As the reaction continued, the absorption band of Ag NPs moved towards the red region from 385 to 396 nm owing to the size growth of the silver nanoparticles. This was accompanied by an augmentation in absorbance intensity, indicating the ongoing formation of Ag NPs. However, as illustrated in Fig. III.6(b), the highest LSPR intensity was achieved at 10 minutes, suggesting that the maximum amount of Ag ions in AgTiP had been reduced.

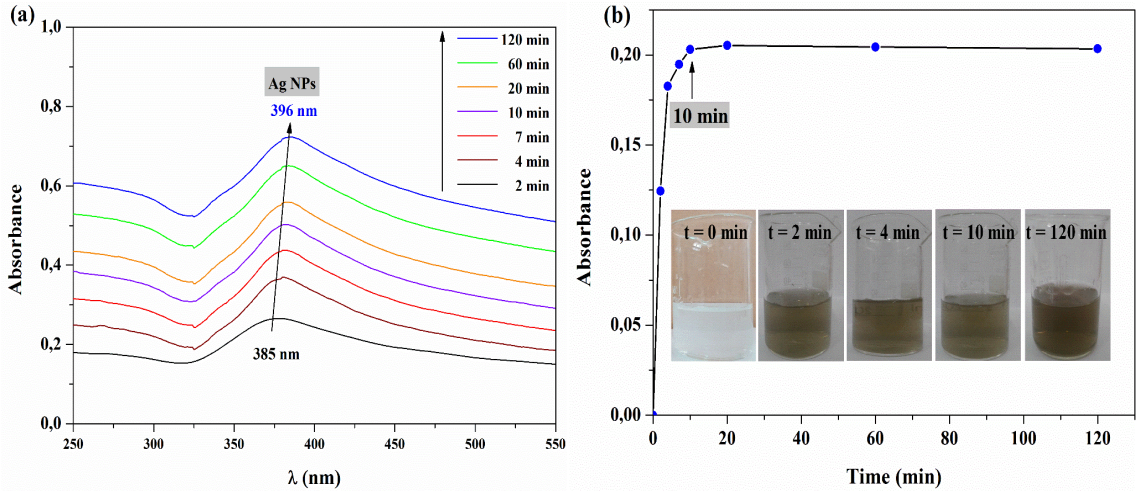

Figure III. 6. (a) Changes over time of the UV-Vis spectra of Ag NPs formation, (b) Absorbance versus time plot of Ag NPs formation at λ_{max} = 385 to 396 nm, inset pictures show the color change over time during the reduction of AgTiP.

III.2.6. Reduction of methylene blue and methyl orange dye pollutants

The catalytic performance of Ag NPs/AgNaTiP was examined through the reductive conversion of MB and MO as reference organic dye pollutants using $NaBH_4$ as a reducing agent. Although these two reduction reactions are thermodynamically feasible processes, they are kinetically restricted without a catalyst, because the kinetic barrier between MB (or MO) and BH_4^- is very high.[149] Fig. III.7(a) and (b) display the change over time of the characteristic absorption bands of MB and MO dyes when only $NaBH_4$ is present. Without the catalyst, the band intensities did not surpass 6% even after 4 h, indicating a very slow reduction rate. On the other hand, when $NaBH_4$ and Ag NPs/AgNaTiP are present, the intensities of the absorption peaks of MB and MO decrease rapidly with respect to reaction time and vanish after 320 s for the MB and 270 s for the MO, as depicted in Fig. III.7(c) and (d). The reductive conversion started when both BH_4^- ions and MB (or MO) dyes were adsorbed on the catalyst surface, where electrons transferred from donor BH_4^- to acceptor dye molecules. Thus, Ag NPs/AgNaTiP serve as an electronic transfer system and facilitate the conversion of MB and MO.[322] At the same time, new bands emerged at 259 nm for the MB and 252 nm for the MO. The appearance of these absorption band, along with the fading of the dye solutions, indicates the creation of new aromatic compounds that have no chromophoric groups. As stated in the literature,[18,323,324] the resulting colorless and low-toxicity molecules are leuco-methylene blue from MB and sulfanilic acid and dimethyl-4-phenylenediamine from MO. Further, the catalytic activity can be judged from the reduction efficiency using the equation given below (Eq. III.3):

$$\textbf{Reduction efficiency}\ (\%) = \left(\frac{C_0 - C_t}{C_0}\right) \times 100 \qquad (\textbf{III.3})$$

where C_0 denotes the starting concentration, and C_t is the concentration at a specific time t.

Accordingly, the efficiency of MB and MO dye reduction at the end of reactions was approximately 96.30% and 94.60%, respectively. This indicates that the Ag NPs/AgNaTiP nanocomposite exhibits excellent catalytic performance.

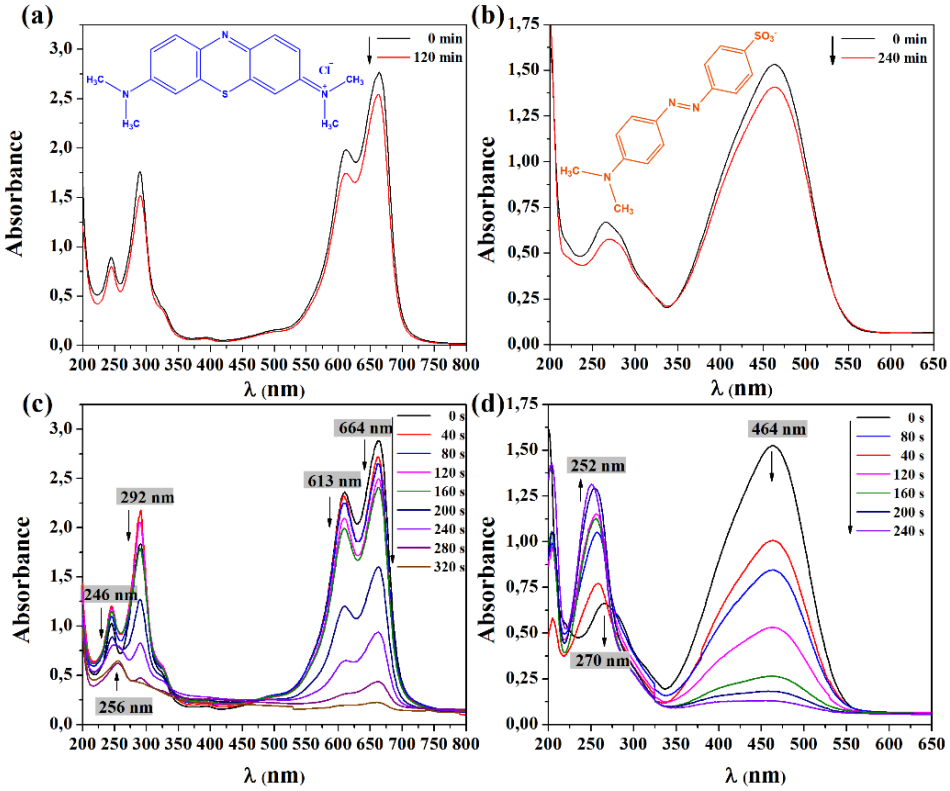

Figure III. 7. UV-Vis absorbance spectra of (a) MB and (b) MO, in the presence of $NaBH_4$ and Ag NPs/AgNaTiP.

III.2.7. Kinetic studies

The Langmuir–Hinshelwood kinetic scheme is commonly the most suggested model for describing the kinetics of catalytic reactions involving aqueous organic compounds.[325,326] According to this model, there is one rate determining all the steps mechanism for catalytic reaction of substrates, including adsorption, surface reaction, and desorption. In this study, since $NaBH_4$ was used in a much larger quantity than the organic dyes ($[BH_4^-]$/[MB or MO] = 50), the pseudo-first-order model can be employed to analyze the kinetic data. Fig. III.8(a) and (b) display the graph of ln (C_t/C_0) versus the conversion time (t), as determined by analyzing the absorption peak intensities at 664 nm for the MB and 464 nm for the MO. For the conversion of MB, as appreciated in Fig. III.8(a), it was observed that Ag NPs/AgNaTiP requires an induction time (IT) of 160 s, during which the reaction rate is nearly zero. Such an IT of metal nanocatalysts was previously reported in similar reduction conversions using $NaBH_4$.[327,328] After the end of the IT, the MB concentration decreases linearly relative to the reduction time, confirming the appropriateness of the chosen kinetic model. For the conversion MO, as shown Fig. III.8(b), the reduction began immediately and no IT was required. The plot ln (C_t/C_0) vs. time shows

a good linear correlation, consistent with the pseudo-first-order model. The observed rate constants k_{obs} for both MB and MO reductions were determined by analyzing the slope of the plots as per Eq. II.101. As a result, the calculated rate constants were 0.0196 s^{-1} for MB and 0.0125 s^{-1} for MO. However, To compare the catalytic performance of our catalyst with others mentioned in literature, it is better to use their activity parameter *k'* (Eq. II.102). Here, the calculated k' values were 61.25 s^{-1} g^{-1} for the MB and 39.06 s^{-1} g^{-1} for the MO. Table III.2 lists the catalytic performance of various Ag nanocatalysts mentioned in the literature in comparison with our Ag-based catalyst. As we can see, the Ag NPs/AgNaTiP nanocomposite shows greater performance compared to other catalysts previously reported under similar experimental conditions.

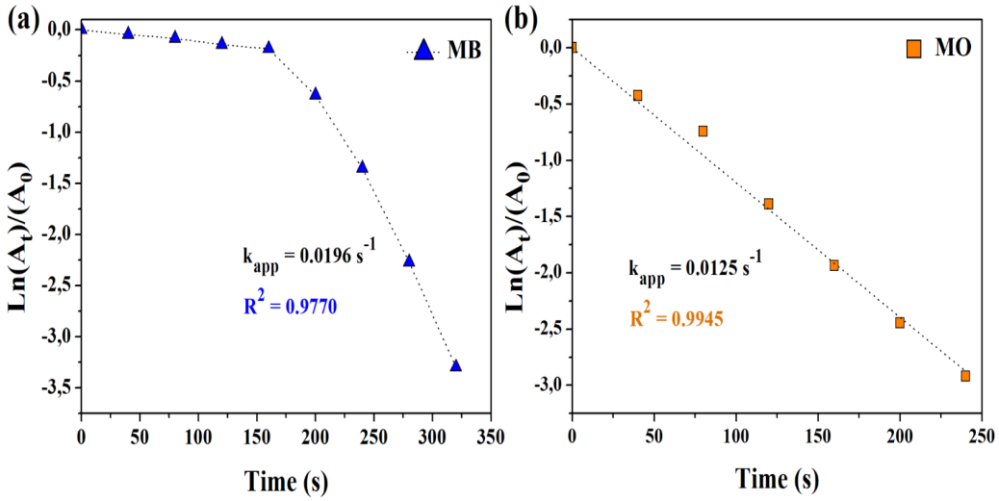

Figure III. 8. Pseudo first order graphs for the reduction of (a) MB and (b) MO.

Table III. 2. Comparison of the performance of our catalyst with others mentioned in literature.

Catalyst	Pollutant	Catalyst weight[a] (mg)	Catalyst weight[b] (mg)	k' (s^{-1} g^{-1})	Time (min)	Ref.
3D-Graphene/Ag		5	2	2.10	15	[329]
Cotton@Ag NPs		50	1.79	4.45	8	[330]
Ag@SMt	MB	9	1.37	11.92	15	[331]
Ag NPs@Mt		2	0.4	23.3	7	[327]
Ag NPs/AgTiP		2	0.32	61.25	5.34	This study
Ag/TP		10	5.94	0.68	7	[332]
Ag/ZnO		100	6	2.38	6	[333]
Ag-M	MO	4	-	7.4	2	[334]
Fe_2O_3@SiO-Ag		2	-	32	1	[335]
Ag NPs/AgNaTiP		2	0.32	39.06	4.5	This study

a. The total mass used of the catalyst.

b. The quantity of supported Ag NPs on the catalyst.

III.2.8. Mechanism of reduction

Since the present catalytic reductions are bimolecular reactions, depending on whether one or both reactants are adsorbed onto the Ag NPs/AgNaTiP surface, either the Eley-Rideal model or the Langmuir-Hinshelwood model could be applied.[296] However, the most suggested mechanism for this reaction is the Langmuir–Hinshelwood mechanism, which involves the simultaneous adsorption of both BH_4^- and organic dyes onto the solid surface before their reaction. The conversions of the MB into leuco-methylene blue and the MO into sulfanilic acid and dimethyl-4-phenylenediamine are illustrated in Fig. III.9(a) and (b). Ag NPs/AgNaTiP serves as an electron transfer bridge between the organic molecules and BH_4^-, accelerating the reaction process. The reduction of MB requires the transfer of two electrons, while the reductive cleavage of MO necessitates the transfer of eight electrons. The reaction may take place in four stages: (i) the reactant species adsorb onto the surface of Ag NPs; (ii) BH_4^- undergoes hydrolysis, followed by the diffusion of hydrogen anion (H^-) and organic dyes (MB or MO) to the active catalytic site and formation of a surface complex; (iii) the adsorbed organic dyes react with surface hydrogen anion to form an adsorbed product; and finally, (iv) the resulting products detach from the Ag NPs active site, allowing new reactive substrates to bind.

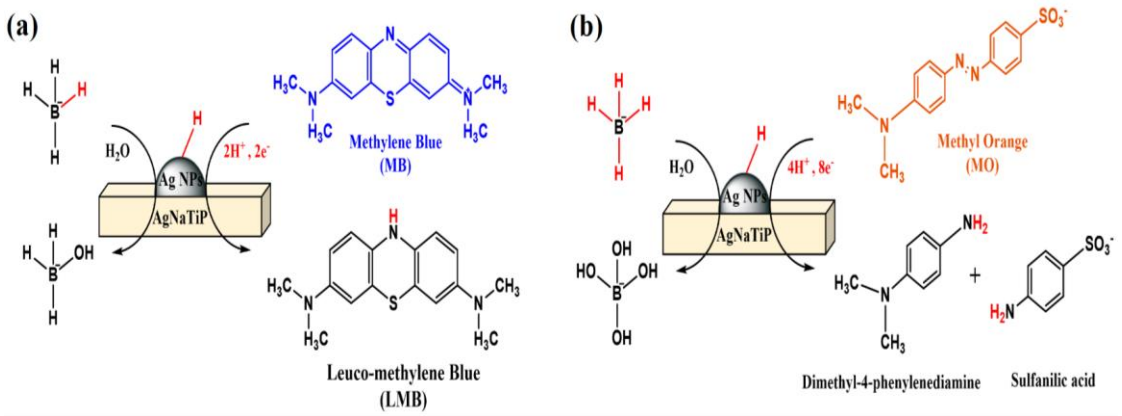

Figure III. 9. Proposed reductions of (a) MB and (b) MO with $NaBH_4$ via Ag NPs/AgNaTiP.

III.2.9. Regeneration and recyclability of catalyst

Regeneration and recyclability of catalysts are very important conditions for their future practical applications. Thus, the regeneration and recyclability of Ag NPs/AgNaTiP catalyst were examined by performing multiple cycles of organic dye reduction. After each reaction cycle, the used Ag NPs/AgNaTiP nanocomposite was collected, washed, and dried in the oven. Then, after being finely ground in an agate mortar, the powdered sample was subjected to a temperature of 700 °C for 3 h. Fig. III.10(a) to (d) show the XRD diffractogram, SEM micrograph, and EDX spectrum of regenerated AgTiP material, along with the conversion efficiency of MB and MO obtained at each cycle. After treatment at high temperature, the XRD pattern of the used Ag NPs/AgNaTiP sample (Fig. III.10(a)) revealed that the diffraction lines associated with the (111) plane of metallic Ag and the (012) plane of

the NaTiP structure had completely disappeared. However, despite the calcination process, the parent compound maintained its NASICON structure quite well. In addition, the SEM image (Fig. III.10(b)) showed almost no Ag nanoparticles present on the NASICON crystal's surface, which maintained its original morphology. Furthermore, the sodium (Na^+) peak at 1 keV that was visible in the EDX spectrum for the Ag NPs/AgNaTiP (Fig. III.5(b)) was not detected in the sample spectrum after calcination (Fig. III.10(c)). These findings indicate that after calcination, the supported Ag NPs on the surface of the AgNaTiP were reinserted into the Na^+ sites, restoring the original AgTiP phase. This provides evidence that the Ag-NASICON material can be regenerated through this process. Subsequently, the regenerated sample was employed again in the catalytic conversion of MB and MO to test its ability to be recycled. As can be appreciated in Fig. III.10(d), the catalyst's performance remained nearly unchanged after five cycles of use, with reduction efficiencies of approximately 96% for MB and 94% for MO. Moreover, the amount of Ag that had leaked into the solution after five cycles of catalysis was measured using ICP-AES analysis. As shown in Table III.3, only about 2.5% of the Ag NPs supported on AgNaTiP were found to be leached into the solution. These results indicate that AgTiP acts as a precursor, support, and host for the creation, immobilization, and regeneration of Ag NPs catalysts that are effective in reducing toxic organic dyes in wastewater.

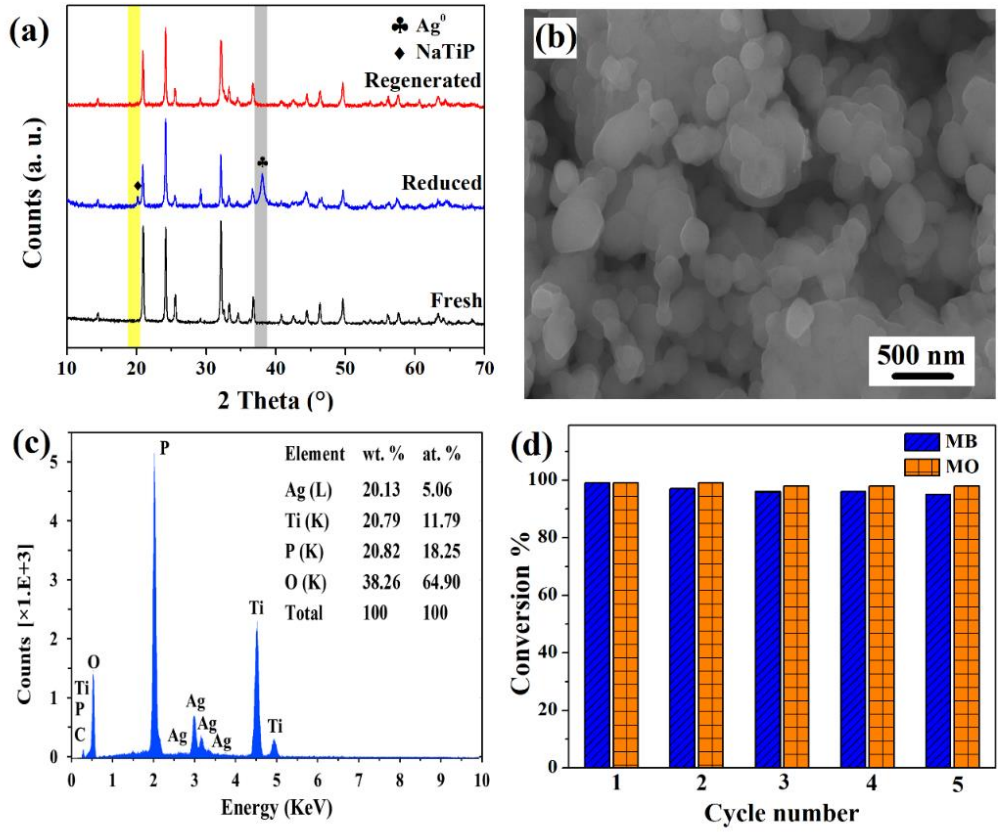

Figure III. 10. (a) XRD diffractograms of AgTiP before and after regeneration, (b) SEM micrograph of AgTiP after regeneration, (c) EDX spectrum AgTiP after regeneration and (d) Repeated reduction of MB and MO over Ag NPs/AgTiP using $NaBH_4$.

Table III. 3. Amount of silver leaked into the solution

	Ag conc. (ppm)	**$Ag_{leached}/Ag_{Supported}$ (wt.%)**
Reduction of MB	0.3323	2.46
Reduction of MO	0.2945	2.18

III.3 Conclusion

In this study, we synthesized Ag NPs on an Ag-based NASICON-type material employing a chemical reduction procedure at ambient temperature. $NaBH_4$ was used as both a reductant (BH_4^-) and a source of compensating cations (Na^+). The samples were analyzed before and after the reduction process using methods like XRD, ATR-FTIR, SEM, and EDX. The findings indicate that the Ag^+ ions within the NASICON structure can be reduced by BH_4^- to form Ag NPs ranging in size from 20 to 35 nm. These nanoparticles were uniformly dispersed on the surface and were concomitantly replaced by Na^+ ions, resulting in the generation of $Ag_{1-x}Na_xTi_2(PO_4)_3$. The NASICON crystal can thus be considered as a unique precursor and support for the *in situ* generated active species. The prepared Ag nanocomposite has been shown to be an exceptionally efficient catalyst for reducing harmful dyes. Furthermore, the original AgTiP composition can be regenerated through a straightforward calcination process and can be reused up to five times with no notable decrease in catalytic performance. This novel approach for synthesizing metallic NPs on NASICON phosphates-based transition metals highlights the potential of these materials as effective, regenerable, and reusable catalysts for removing harmful pollutants from wastewater.

Chapter IV: Catalytic reduction of nitrophenolic pollutant over Ag NPs/$AgZr_2(PO_4)_3$

This chapter is based on the article published as:

A. Moussadik, M. Halim, S. Arsalane, F. Tielens, M. Kacimi, A. El Hamidi, In situ synthesis of self-supported Ag NPs on $AgZr_2(PO_4)_3$ NASICON type phosphate: Application in catalytic reduction of 4-nitrophenol, Materials Research Bulletin, 2022, 111764.

IV.1. Introduction

Water is a vital natural resource indispensable for all life forms on Earth. Humans depend on water not just for their nutritional needs and health, but also for their economic development and social well-being.[336] Water is required in all sectors of society, including households, agriculture, energy, and industry.[3] In addition, water is fundamental to ensuring the integrity and sustainability of ecosystems. However, anthropogenic activities have caused great damage to the quality of global water sources. Water pollution by toxic contaminants has emerged one of the most urgent issues that threatens our modern society. Over the last few decades, it has been recognized that the existence of many pollutants in the aquatic environment can be correlated with the discharge of inadequately treated or untreated wastewater effluents, mainly from the industrial sector.[5] Indeed, Industrial wastewater typically contains a significant number of chemicals that are hazardous for all living organisms and strongly affect ecosystems. Among these chemicals, organic pollutants have been recognized as a major threat to the general public health and aquatic life as they are mostly resistant to environmental degradation, have a tendency for long-range transport, are capable of bioaccumulation in fish and animal tissue, and biomagnification in food webs.[42]

Among various organic pollutants, nitrophenolic compounds (NPCs) constitute one of the largest and prevalent groups of highly toxic, non-degradable and persistent contaminants in industrial wastewater and natural water bodies.[12] In particular 2-nitrophenol, 4-nitrophenol, 2,4-dinitrotoluene, 2,6-dinitrotoluene, and nitrobenzene are considered by the United States Environmental Protection Agency (EPA) as pollutants of priority concern, and are on the list of 129 dangerous substances.[65] 4-Nitrophenol (4-NP), especially, poses an apparent health risk since it is toxic to mammals and aquatic microorganisms. Because of its regular and substantial use in the manufacturing of pesticides, herbicides, insecticides, explosives, synthetic dyes, and pharmaceutical drugs, 4-NP can often be found in high levels in industrial wastewater streams.[13,62,66] The toxicity of 4-NP is attributed to its nitro group ($-NO_2$) being easily reduced under anaerobic conditions to nitroso and hydroxylamine compounds.[63] These by-products are responsible for the potential cytotoxic, mutagenic, and carcinogenic properties of nitro compounds. Acute 4-NP exposure may also result in blood disorders, the formation of methemoglobin, damage of liver and kidney, lung disease, irritation to the skin and eyes, and respiratory

issues.[64] Therefore, these pollutants need to be removed from contaminated water to prevent their detrimental impacts on humans and the environment.

There are several treatment processes for the elimination of these harmful contaminants from wastewater.[67] Yet, despite their potential, the effectiveness of removing NPCs is not satisfactory due to limitations such as a slow rate of elimination, the production of secondary pollution, or high operating expenses. In order to address these issues, chemical reduction of NPCs to their corresponding amino-aromatic compounds using metal NPs has been reported among the most advantageous treatment techniques for such hazardous compounds compared to other techniques. Pal and his co-workers[106] were the pioneers in documenting the reduction of 4-NP over various nanocatalytic systems, utilizing sodium borohydride ($NaBH_4$) as reductant to obtain environmentally friendly 4-aminophenol. This latter is considered to be an industrially useful intermediate for the producing analgesic and antipyretic medications like phenacetin, paracetamol, and acetanilide.[337] It also finds extensive use as a corrosion inhibitor, anti-corrosion lubricant, a hair-dyeing colorant, and a photographic developer.[337] The most popular applied catalysts for the 4-NP reduction were noble metal NPs like Au, Ag, Pt, and Pd, maintained on different supports.[97] It's worth mentioning that many studies centered on the conversion of 4-NP to 4-aminophenol (4-AP) use this transformation as a benchmark reduction to test the effectiveness of the synthesized metal NPs catalysts.[338–340]

This chapter falls within this framework and focuses on the reductive transformation of 4-NP, a model NPCs, to produce 4-AP. In the current research, we describe the preparation of low-cost self-supported Ag NPs on the surface of $AgZr_2(PO_4)_3$ NASICON phosphate and their efficiencies in the conversion of 4-NP to form 4-AP using $NaBH_4$ as a reductant. The Ag NPs catalysts were self-grown *in situ* on $AgZr_2(PO_4)_3$ surfaces prior to the reduction of the organic pollutant. An in-depth analysis of the kinetics and transformation mechanism of 4-NP have been conducted, considering the experimental conditions and the structural properties of the nanocomposite catalyst. Characterization methods like the XRD, ATR-FTIR, SEM, and EDX were used. The conversion rates of 4-NP to 4-AP were measured using UV-vis spectrophotometry. Moreover, the durability, stability, and regeneration ability of the catalyst have been investigated for long-term use. Hereafter, we have used the acronym AgZrP for $AgZr_2(PO_4)_3$ in the next sections.

IV.2. Results and discussions

IV.2.1. XRD characterization

Fig. IV.1 displays the XRD diffractograms of the obtained sample and its resulting products after undergoing reduction processes at room temperature. As manifested in Fig. IV.1(a), a pure AgZrP NASICON phase was achieved. The indexing of all the diffractions lines matched the rhombohedral system ($R\bar{3}c$). After being reduced by various concentrations of $NaBH_4$, the NASICON structure

remained unchanged and all the main reflections peaks of AgZrP were preserved, as can be appreciated in Fig. IV.1(b) to (f). However, three additional peaks were detected at 38.10° 2θ, 44.26° 2θ, and 64.50° 2θ. These lines are attributed to the (111), (200), and (220) planes of metallic silver (Ag^0) with face-centered cubic crystal structure, as indicated by ICDD card No. 04-0783. These reflections become more pronounced as the concentration of $NaBH_4$ increases, indicating that more Ag^0 is formed. Additionally, another peak was observed at 13.92° 2θ during the reduction process. This peak corresponds to the (012) plane of the $NaZr_2(PO_4)_3$ (NaZrP) NASICON structure, as indicated by ICDD card No. 33-1312. These findings indicate that when AgZrP is reduced by aqueous $NaBH_4$, it results in the simultaneous production of Ag^0 particles and the creation of NaZrP phase. The average diameters of the produced Ag particles were calculated using Scherrer's equation (Eq. II.2) applied to the Ag (111) plane and are enumerated in Table IV.1. As shown in the table, the Ag particles' mean sizes are within the nanoscale and exhibit a slight augmentation with the rise in the $NaBH_4$ concentration. This size augmentation is a result of the excess production of metallic Ag NPs, which leads to aggregation.

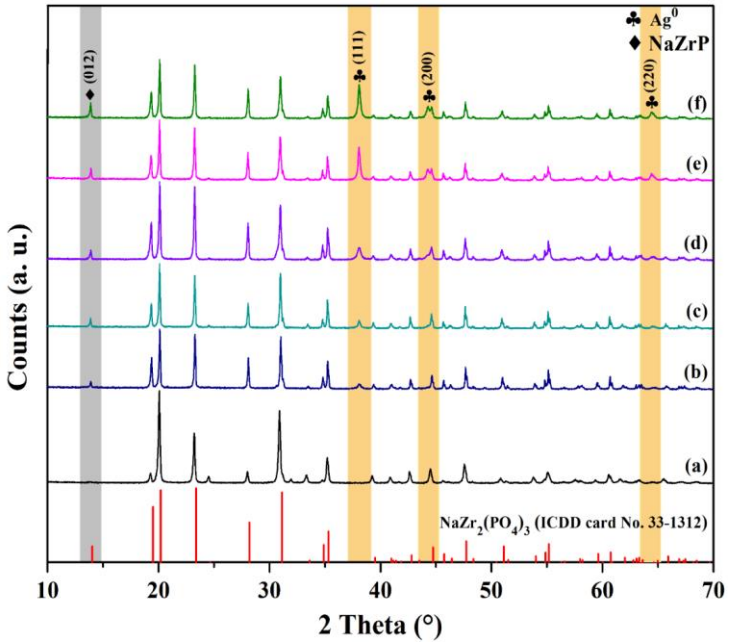

Figure IV. 1. XRD diffractograms of AgZrP (a) as-synthesized, and after reduction by $NaBH_4$ at the molar ratio (b) = 0.4, (c) $\frac{[BH_4^-]}{[AgZrP]}$ = 0.7, (d) $\frac{[BH_4^-]}{[AgZrP]}$ = 1, (e) $\frac{[BH_4^-]}{[AgZrP]}$ = 1.5 and (f) $\frac{[BH_4^-]}{[AgZrP]}$ = 5.

Table IV. 1. Average sizes of Ag NPs vs. the molar ratio $[BH_4^-]/[AgZrP]$

$[BH_4^-]/[AgZrP]$	0.4	0.7	1	1.5	5
size (nm)	22	32	35	38	42

IV.2.2. Rietveld analysis

The quantity of self-supported Ag NPs on the NASICON matrix was calculated from XRD measurements by employing the Rietveld technique[217] via the FullProf program.[222] On the opposite

side, the amount of Ag NPs that were not supported and had leaked into the solution was measured using ICP-AES analysis. As a result, the total quantity of Ag NPs produced through the chemical reduction at varying concentrations of $NaBH_4$ is calculated by adding the self-supported Ag on the NASICON surface to the leaked Ag in the solution. Fig. IV.2 displays the percentage of produced Ag NPs as a function of the ratio $\frac{[BH_4^-]}{[AgZrP]}$. As depicted in the figure, the amount of metallic silver generated increases gradually as the concentration of $NaBH_4$ rises, and reaches a maximum of ~84% at $\frac{[BH_4^-]}{[AgZrP]}$ = 1.5. These findings suggest that the utilization of $NaBH_4$ for the chemical reduction enables the control of metallic silver production from AgZrP.

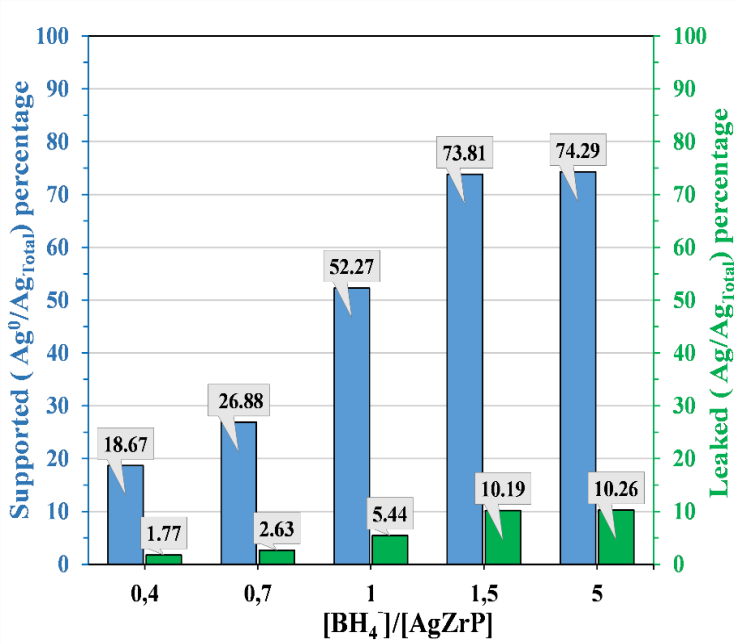

Figure IV. 2. Amount of formed Ag from AgZrP vs. $NaBH_4$ concentration, evaluated using Rietveld method and ICP-AES analysis.

IV.2.3. ATR-FTIR characterization

Fig. IV.3 displays the ATR-FTIR spectra of AgZrP as-prepared and after reduction at a molar ratio of $\frac{[BH_4^-]}{[AgZrP]}$ = 1.5. The infrared spectrum of AgZrP (Fig. IV.3(a)) show a signature that is similar to the NaZrP NASICON-type structure reported in previous studies.[341,342] The vibrational spectrum include three absorption peaks at 553, 572, and 636 cm^{-1}, which are attributed to the asymmetric bending vibration modes (ν_4) of the O-P-O units. A wide band centered between 900-1040 cm^{-1} and a small peak at 1060 cm^{-1} are associated with the symmetric and asymmetric stretching vibrations (ν_1 and ν_3) of the phosphate units. A band at 1280 cm^{-1}, , which is not typical for the PO_4^{3-} ions, has been ascribed to the asymmetric stretching vibrations (ν_3). According to prior studies, this band can be explained by the influence of the electron density of the highly charged Zr^{4+} cation on the P-O bond.[319,343] After the

reduction process (Fig. IV.3(b)), the spectral profile of AgZrP exhibited no changes and the main absorption bands remained unaltered. These observation is consistent with the stability of the NASICON structure.

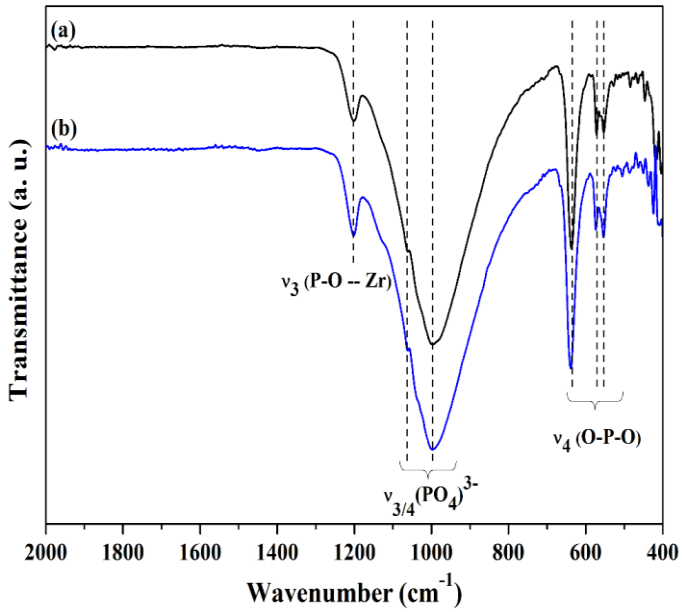

Figure IV. 3. ATR-FTIR spectra of AgZrP. (a) as-prepared and (b) after reduction by aqueous $NaBH_4$ at the molar ratio $\frac{[BH_4^-]}{[AgZrP]}$ = 1.5.

IV.2.4. SEM-EDX analysis

SEM-EDX method was conducted to examine alterations in the morphology and composition of AgZrP before and after reduction, and to determine the shape and size of the formed Ag NPs. The SEM micrograph of AgZrP (Fig. IV.4(a)) exhibits a well-crystallized and heterogeneous grain size. After reducing AgZrP at the molar ratio $\frac{[BH_4^-]}{[AgZrP]}$ = 1.5, the SEM micrographs (Fig. IV.4(b) to (d)) showed the presence of nearly spherical Ag NPs distributed across the sample surface. As documented in prior researches, metallic NPs produced through chemical reduction at ambient temperature employing $NaBH_4$, as a reductant, typically exhibit a spherical shape.[134,344] The Ag NPs were observed to have an average dimensions ranging from 30-90 nm, which matches the values obtained from the XRD data listed in Table IV.1. The variation in size of the Ag NPs synthesized from AgZrP could be due to the difficulties in achieving uniform growth of the Ag NPs during the reduction process when only $NaBH_4$ is present.

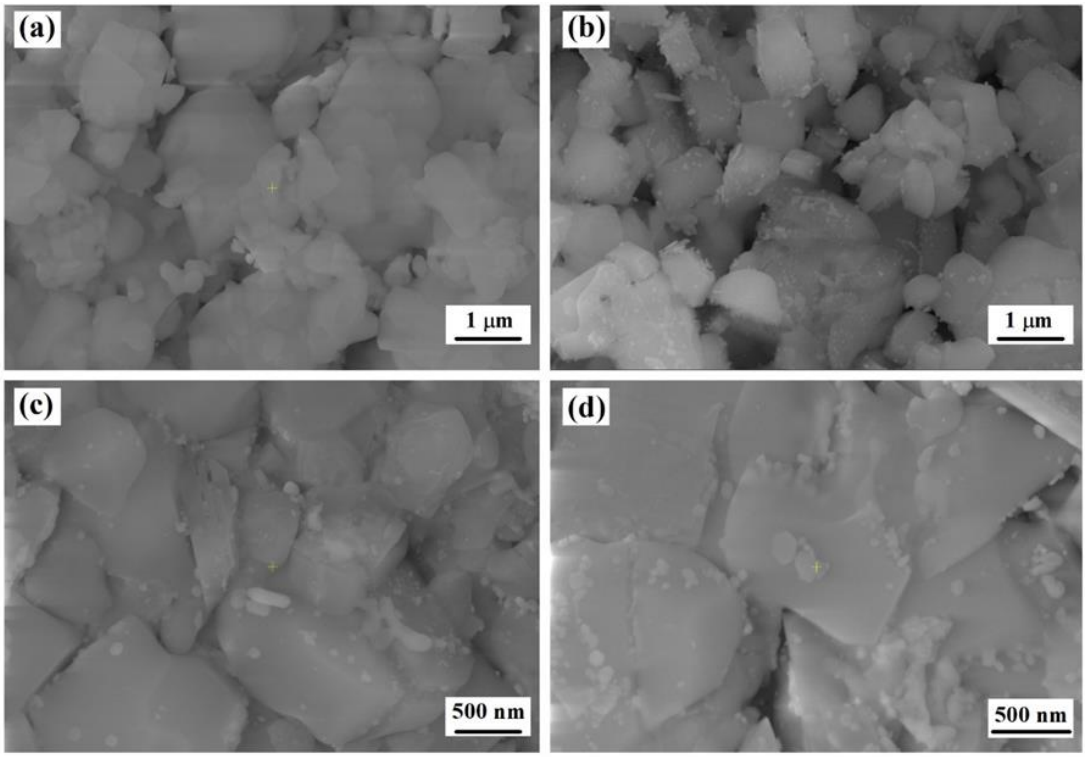

Figure IV. 4. SEM micrographs of AgZrP (a) as-synthesized and (b, c, d) after reduction by $NaBH_4$.

The EDX analysis of AgZrP is depicted in Fig. IV.5(a). The elemental composition of AgZrP was determined to be 5.35% for silver, 11.42% for zirconium and 17.09% for phosphorus, which corresponds to the theoretical stoichiometric values in the chemical formula $AgZr_2(PO_4)_3$. The EDX analysis of AgZrP after the reduction process is presented in Fig. IV.5(b). As shown in the figure, additionally to the presence of Ag, Zr, P, and O elements, an extra peak of sodium (Na) was detected at 1 keV. The amount of Na element was determined to be 4.77%. This provides strong evidence for the substitution of Ag^+ ions with Na^+ ions within the NASICON structure after reaction using $NaBH_4$. However, a decrease in the Ag contents was noted, which is due to the leakage of Ag into the solution.

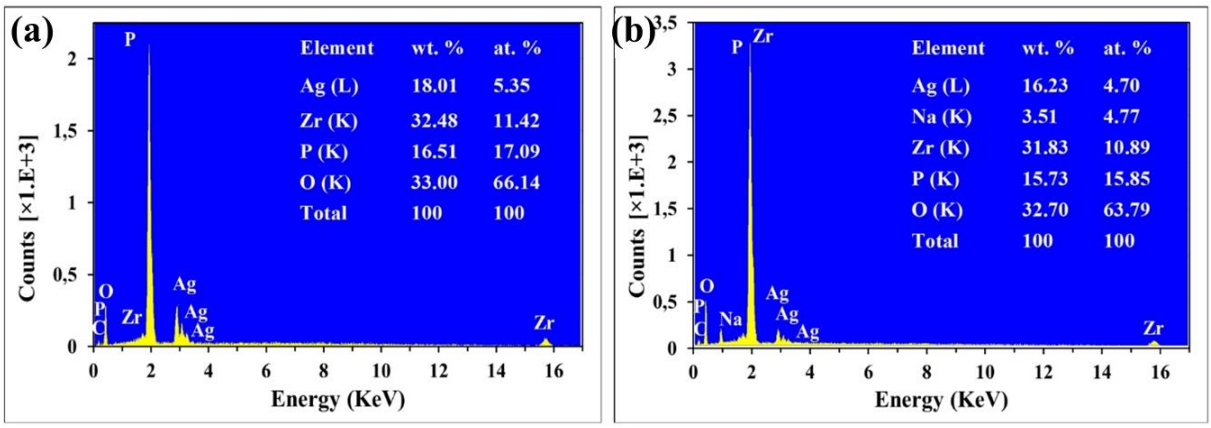

Figure IV. 5. EDX analysis of AgZrP (a) as-synthesized and (b) after reduction by $NaBH_4$.

Based on the combined results from XRD, ATR-FTIR and SEM-EDX analysis, as with AgTiP in the previous chapter, the overall reduction reaction of AgZrP by aqueous $NaBH_4$ can be represented as follows (Eq. IV.1):

$$\mathbf{AgZr_2(PO_4)_3 + (Na^+, BH_4^-) + 4H_2O}$$

$$\downarrow \qquad \textbf{(IV.1)}$$

$$\mathbf{x_1 Ag^0@Ag_{1-x}Na_xZr_2(PO_4)_3 + x_2 Ag^0 + B(OH)_4^- + 3.5H_2 + xH^+ + Na^+}$$

Where x = $x_1 + x_2$ increases as the concentration of $NaBH_4$ increases.

IV.2.5. LSPR analysis

The reduction of AgZrP over time was tracked *in situ* from 2 to 120 minutes using UV-Vis spectroscopy. Fig. IV.6(a) displays how the distinctive LSPR band of Ag NPs changes and grows over time in relation to the production of Ag NPs. The figure demonstrates that the formation of Ag NPs from AgZrP began right after borohydride was added. The presence of a single LSPR band signifies that spherical or nearly spherical Ag NPs have formed.[321] As the reaction progresses, the absorption band of Ag NPs moved towards the red region from 380 to 390 nm due to the growth in size of Ag NPs. Simultaneously, there was a continuous increase in absorbance intensity, indicating the still formation of Ag NPs. As can be seen in Fig. IV.6(b), the LSPR intensity reached its maximum at 10 minutes, suggesting that the maximum amount of Ag^+ ions in AgZrP had been reduced.

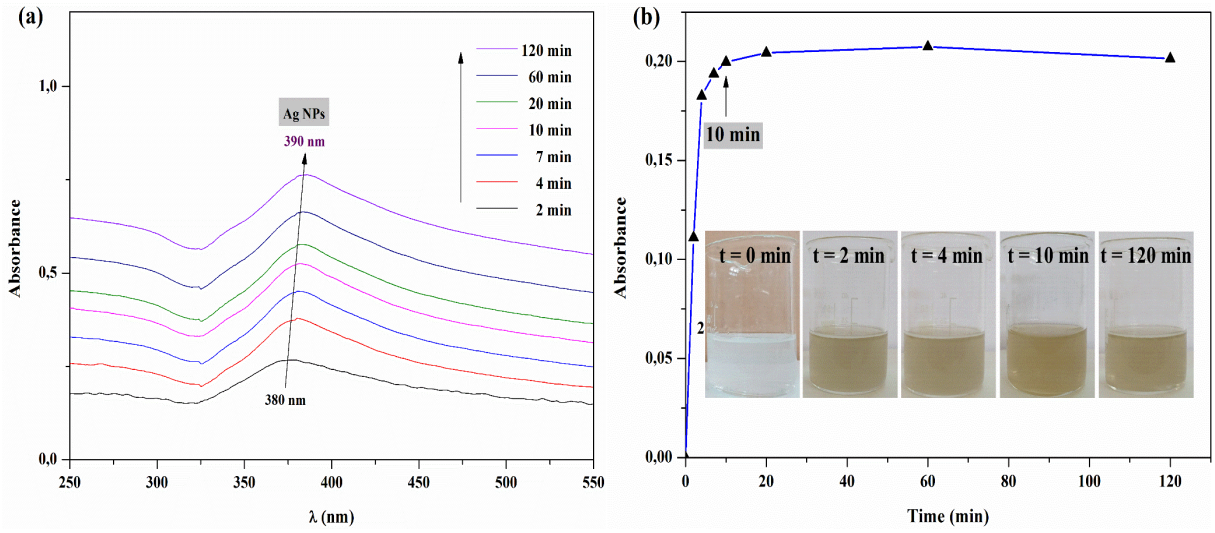

Figure IV. 6. (a) UV-Vis spectra of AgZrP reduction using $NaBH_4$ with respect to time, (b) absorbance vs. time plot of AgZrP reduction at λ_{max} = 380 to 390 nm, inset pictures show the change of colors for the AgZrP reduction with respect to time.

IV.2.6. Reduction of 4-nitrophenol pollutant

In this chapter, we have selected the reductive conversion of 4-NP as a reference NPC pollutant to assess the catalytic performance of the Ag NPs produced from AgZrP. The reduction produces 4-AP, which is 500-fold less toxic than 4-NP.[345] This reduction process of 4-NP in the presence $NaBH_4$ is thermodynamically favorable reaction, with standard electrode potentials of E^0 for 4-NP/4-AP = −0.76 eV and $B(OH)_3/BH_4^-$ = −1.33 eV vs the normal hydrogen electrode (NHE). However, in the absence of a catalyst, the reaction is kinetically restricted. It's important to note that a solution of 4-NP has a maximum peak at λ_{max} = 318 nm owing to $\pi \rightarrow \pi*$ transition, but when $NaBH_4$ solution is added, the band shifts to the red region at 400 nm because of the dark-yellow color of 4-nitrophenolate molecules in the alkaline environment of $NaBH_4$. Fig. IV.7(a) shows the reaction progress between the 4-nitrophenolate and $NaBH_4$, in the absence of the catalyst. As we can see, under the chosen experimental conditions with only $NaBH_4$ present, the intensity of the absorption band at 400 nm slowly reduced, but it did not exceed 5% even after 4 h. This finding confirms that without a catalyst, the catalytic conversion of 4-NP does not take place. Conversely, with Ag NPs/AgNaZrP acting as a catalyst and an excess of $NaBH_4$, the characteristic band of 4-NP at 400 nm gradually diminished over time and completely disappeared after 420 s, as illustrated in Fig. IV.7(b), attesting the catalytic elimination of 4-NP. In this case, Ag NPs/AgNaZrP catalyst mediated the electron transfer from BH_4^-, serving as the donor, to the aforementioned 4-nitrophenolate, the acceptor molecule. Besides, two new absorption bands emerged at 230 and 298 nm. These peaks are characteristic of the colorless 4-AP,[346] whereas the existence of isosbestic points at 280 and 310 nm confirms that 4-AP is the only formed molecule after the reduction process.[347] Furthermore, it was observed that under the applied conditions ([AgZrP] = 0.04 g L^{-1}, $[BH_4^-]$ = 17.5 mM, [4-NP] = 0.35 mM), the elimination yield of 4-NP was approximately 99% after 420 s of reaction time.

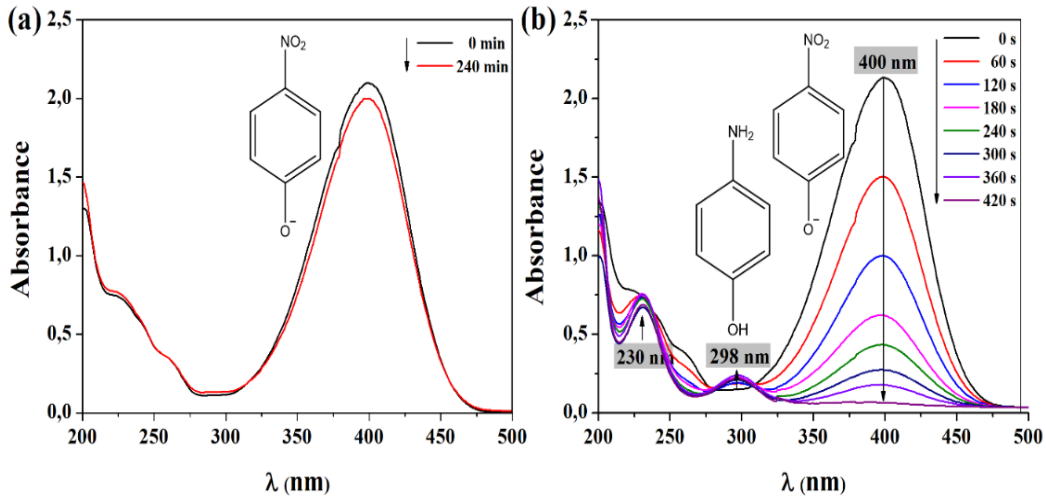

Figure IV. 7. UV-Vis spectra of 4-NP elimination over Ag NPs/AgNaZrP using $NaBH_4$.

IV.2.7. Kinetic studies

The rate of 4-NP reduction was presumed to be not dependent of $NaBH_4$ concentration since this latter was employed in a much large excess relative to the organic molecule. As a result, the apparent rate constant (k_{app}) was determined using the pseudo-first-order model (Eq. II.101). The catalytic reaction's ln (A_t/A_0) vs. time profile, generated at λ_{max} = 400 nm, is shown in Fig. IV.8. As manifested in the figure, the values of ln (A_t/A_0) vary linearly with time, indicating that the pseudo-first-order model considered for the conversion of 4-NP over Ag NPs/AgNaZrP is appropriate. Based on the slope obtained, the apparent rate constant k_{app} for the reductive transformation of 4-NP was determined to be 0.0080 s^{-1}. The larger the value k_{app}, the faster the rate of catalytic reduction. To further assess the performance of Ag NPs/AgNaZrP, the activity factor k' was calculated using Eq. II.102. The calculated activity factor for the Ag NPs/AgNaZrP catalyst was found to be 25.4620 s^{-1} g^{-1}. The performances of different Ag NPs catalysts documented in the literature are enumerated in Table IV.2 for comparison purposes. It is noticeable that the Ag NPs/AgNaZrP exhibits superior catalytic activity in the conversion 4-NP to 4-AP, relative to other previously reported catalysts.

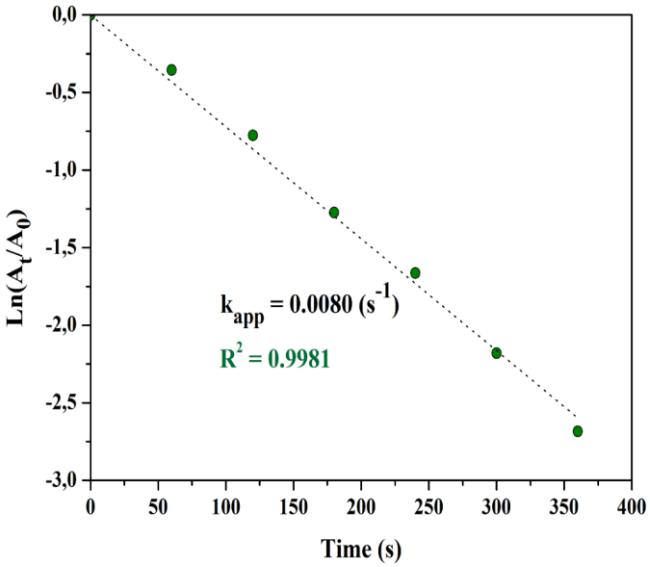

Figure IV. 8. First-order kinetic plot for the 4-NP conversion.

Table IV. 2. Comparison of various Ag-catalysts in the conversion of 4-NP to 4-AP using $NaBH_4$.

Catalyst	k' (s^{-1} g^{-1})	Time (min)	Conditions				Ref.
			$NaBH_4$ (mM)	4-NP (mM)	Catalyst mass[a] (mg)	Catalyst mass[b] (mg)	
Fe_3O_4@Tween20@Ag	0.6	12	64.5	0.16	3	-	[348]
TAC-Ag-1.0	1.3	6.9	0.1	0.01	4	4	[349]
Ag/cotton	1.75	2	300	1	20	20	[350]
Ag/C composite	2.66	12	5.90	0.061	1000	2	[351]
Ag/TiO_2	6.5	3	100	0.053	3	-	[352]

Fe_3O_4@SiO_2-Ag	7.67	8	5.90	0.061	1000	1	[353]
10%Ag/Fe_2O_3	14	1.5	18.18	0.09	3	0.3	[354]
Ag/ZrGP (S2)	19.31	10	83.3	0.083	10	0.151	[355]
Ag NPs/AgNaZrP	25.46	7	17.5	0.35	2	0.375 (0.315)[c]	This study

a. The total mass used of the catalyst.

b. The quantity of Ag NPs supported on the catalyst.

c. The quantity of Ag NPs generated from AgZrP material.

IV.2.8. Mechanism of reduction

The schematic representation of the conversion of 4-nitrophenolate to 4-AP is shown in Fig. IV.9. In our case, it is believed that the reduction occurs solely on the Ag NPs/AgNaZrP catalyst surface following the Langmuir-Hinshelwood model[356] through the outlined steps: (i) The competitive adsorption of 4-nitrophenolate and BH_4^- onto the surface of Ag NPs/AgNaZrP composite, followed by the formation of surface hydrogen anion (H^-) species due to the BH_4^- hydrolysis on the surface of NPs; (ii) the H^- anion and 4-NP molecules diffuse to the active catalytic site and form a surface complex; (iii) the reaction between the adsorbed nitro compound and surface hydrogen species produces 4-AP; and finally (iv) the 4-AP produced is desorbed from the surface of Ag NPs/AgNaZrP, which can then host fresh reactive molecules.

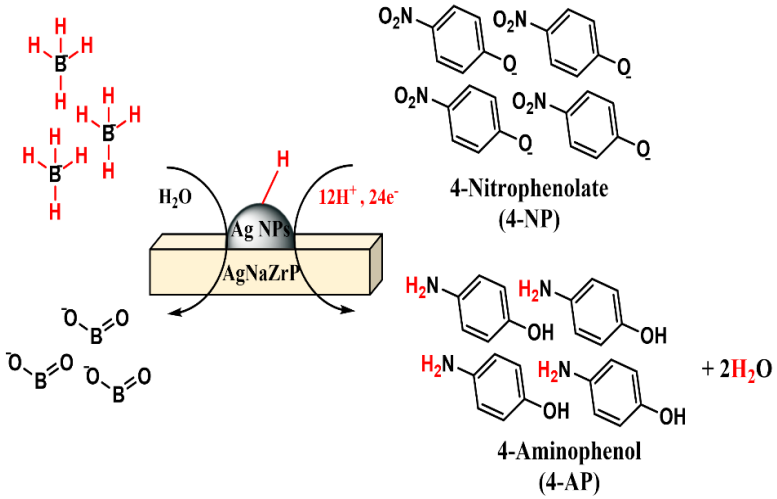

Figure IV. 9. Mechanism of 4-nitrophenolate reduction into 4-AP using $NaBH_4$ via Ag NPs/AgNaZrP.

IV.2.9. Regeneration and recyclability of catalyst

The durability and recyclability of supported metal NPs catalysts are crucial factors for large scale application in wastewater treatment. Hence, the long-term stability of the self-supported Ag NPs on the AgNaZrP sample has been investigated through repeated catalytic experiments. After each catalytic reduction cycle was completed, a new solution of 4-NP was repeatedly added to the reaction batch while

maintaining the started concentration of 4-NP at 3.5 mM. The reusability results depicted in Fig. IV.10(a) show that the performance of Ag NPs/AgNaZrP was maintained with no decline in catalytic efficiency over 10 consecutive reduction cycles. The reduction of 4-NP to 4-AP reached approximately 99% within 420 s for all 10 cycles. Then, an excess of sodium chloride (NaCl) solution was introduced to the mixture to transform the Ag NPs into Ag aggregates, thus simulating a true aggregation and agglomeration process, which is a normal tendency for metal NPs in aqueous solution. Afterward, the resulting Ag aggregates/AgNaZrP was separated from the reaction media, washed, dried in the oven, and treated with a nitric acid (HNO_3, 65%) solution at 70 °C for 1 h, to see if the sample could release regeneration. Fig. IV.10(b) to (d) depict the XRD diffractogram, SEM micrograph, and EDX spectrum of the treated Ag NPs/AgNaZrP material. As observed in the XRD diffractogram (Fig. IV.10(b)), the diffraction peaks corresponding to the (111), (200), and (220) zero-valent metallic Ag and the (012) plane of the NaZrP phase completely disappeared in the regenerated sample. In addition, the concentration of Ag that leaked into the solution during the regeneration process was determined using ICP-AES analysis, and the results showed that only 0.25% (0.2956 ppm) of the total Ag content in AgZrP was leached into the solution. This indicates that when the Ag aggregates/AgNaZrP sample was treated with HNO_3 as an oxidizing agent, the supported metallic Ag was oxidized and reinserted into the NASICON crystal structure, restoring the initial AgZrP composition through a reversible ion exchange between the Ag^+ ions present in the aqueous medium and the Na^+ cations within the NASICON farmwork. Additionally, the process of regeneration did not have an impact on the basic structure of the AgZrP skeleton, as can be seen in Fig. IV.10(b). The SEM micrograph of AgZrP after regeneration is illustrated in Fig. IV.10(c). We notice from the image that the supported Ag NPs have disappeared from the Ag-NASICON matrix surface, which matches the XRD findings. Aside from this, no notable changes detected in the morphology of the parent compound. Furthermore, the EDX spectrum of the regenerated AgZrP (Fig. IV.10(d)) does not display the Na^+ peak at 1 keV, further confirming that Ag^+ were successfully reinserted back into Na^+ sites in the NASICON farmwork. These results indicate that the spent Ag NPs/AgNaZrP catalyst can release regeneration to the initial AgZrP phase in aqueous solution by a simple treatment with an oxidant agent.

Based on these findings, we assumed that the regeneration process take place in two stages. The first one is exothermic and occurs as shown below (Eq. IV.2):

$$\mathbf{x Ag^0@Ag_{1-x}Na_xZr_2(PO_4)_3 + 2x(H^+, NO_3^-)}$$

$$\downarrow \qquad \textbf{(IV.2)}$$

$$\mathbf{Ag_{1-x}Na_xZr_2(PO_4)_3 + x(Ag^+, NO_3^-) + xNO_2 + xH_2O}$$

The second stage involves a reversible ion exchange between Ag^+ cations present in the solution and Na^+ cations within the NASICON material as demonstrated in the reaction below (Eq. IV.3):

$$Ag_{1-x}Na_xZr_2(PO_4)_3 + xAg^+ \rightarrow AgZr_2(PO_4)_3 + xNa^+ \qquad (IV.3)$$

The regenerated sample was then employed again in the catalytic conversion of 4-NP to test its effectiveness and reusability. The results presented in Fig. IV.10(a) indicates that the recycled Ag NPs/AgNaZrP catalyst experienced a minor and insignificant decrease in activity from approximately 99% in the first 10 cycles to around 96% in the next 10 cycles and finally to about 90% in the third set of 10 cycles. The negligible reduction in the efficiency of the catalytic conversion is attributed to the contraction of the NASICON framework because of the repeated reduction and regeneration processes. According to previous reports,[201] the mobility of the monovalent cations inside the NASICON crystal depends essentially on the dimensions of the NASICON 3D interconnected tunnels, which constitute the migration routes during the ion exchange process. Thus, the repeated reduction and regeneration processes result in a shrinkage of the 3D framework accompanied by a diminution in ionic mobility and therefore the diffusion of Ag^+ from the NASICON framework towards its interface to be reduced will become relatively difficult, implying a diminution in the percentage of the produced silver in 2nd and 3rd recycling cycles.

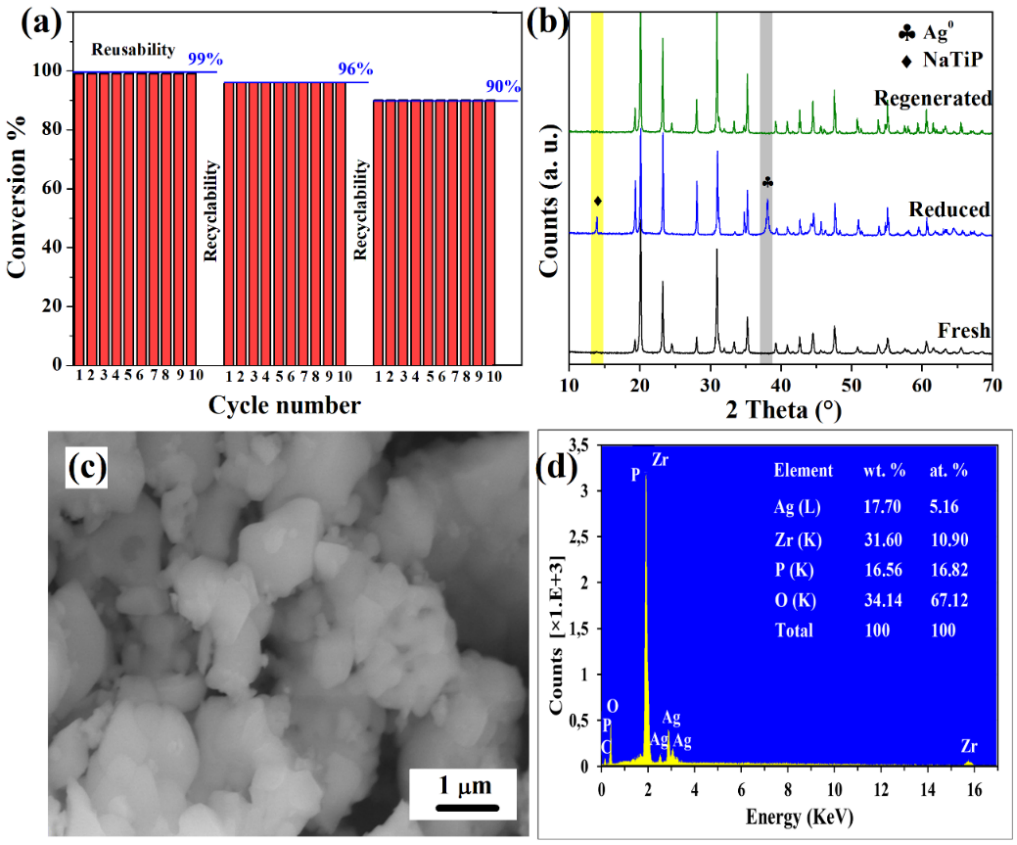

Figure IV. 10. (a) Repeated conversion of 4-NP using $NaBH_4$ in the presence of Ag NPs/AgNaZrP within 420 s, (b) XRD diffractogram of regenerated AgZrP, (b) SEM image of regenerated AgZrP, and (c) EDX spectrum of regenerated AgZrP.

IV.3. Conclusion

In this study, Ag NPs were successfully grown on the AgZrP NASICON sample surface through a straightforward reduction process at ambient temperature utilizing $NaBH_4$ as thr reducing agent. The structural characteristics, composition changes, surface morphology, and reduction mechanisms of AgZrP before and after the reduction process, along with the size and shape of the formed Ag NPs, were analyzed using various physicochemical methods. The findings showed that the Ag^+ ions inside the NASICON crystal can be reduced by BH_4^- ions, resulting in the formation of Ag NPs with dimensions varying from 30 to 90 nm and a nearly spherical shape. These Ag NPs are then replaced by Na^+ ions of appropriate size to form the $Ag_{1-x}Na_xZr_2(PO_4)_3$ phase. The catalytic behavior of the self-supported Ag NPs/AgNaZrP has then been examined in the reduction of 4-NP, which serves as a model harmful nitro-organic contaminant. The Ag NPs/AgNaZrP nanocomposite demonstrated effective catalytic performance in reducing 4-NP to 4-AP and exhibited long-term stability throughout its usage. Moreover, the Ag NPs supported on the AgNaZrP surface can reversibly return back to the NASICON structure, restoring the starting AgZrP composition through a simple regeneration process, and the catalytic efficiency of the regenerated sample can almost reach the original level of the initial prepared sample.

Chapter V: Photocatalytic degradation of dye pollutant over $AgTi_2(PO_4)_3$

This chapter is based on the paper published as:

A. Moussadik, N. Lazar, D. Mazkad, F. S. Brigiano, K. Baert, T. Hauffman, A. Benzaouak, Y. Abrouki, M. Kacimi, F. Tielens, M. Halim, A. El Hamidi, Investigation of electronic and photocatalytic properties of $AgTi_2(PO_4)_3$ NASICON-type phosphate: combining experimental data and DFT calculations, Journal of Photochemistry and Photobiology A: Chemistry, 2023, 114289.

V.1. Introduction

Clean water is vital for the survival of all life forms on Earth. Yet, the issue of water pollution has escalated to a worldwide concern due to factors such as population growth, rapid urbanization, and industrialization expansion.[4–6] Nowadays, humans are generating and discharging more wastewater than at any other time. As per the UN World Water Development report,[7] more than 80% of wastewater is disposed into the aquatic environment without undergoing any prior treatment, contaminating rivers, lakes, groundwater, soil, and the oceans. Traditionally, the industrial sector is the major source of direct and often continuous input of hazardous pollutants, while wastewater from households is usually relatively free of hazardous substances.[8] Industrial effluents are frequently contaminated by various toxic compounds that can have long-term impacts not only on the environment but on biodiversity resources, even when present in small amounts. Among the contaminants, organic dyes are common water pollutants arising from numerous industries like textiles, plastic, paper, paint, etc.[9] It is reported that, among the 0.7 million metric tons of dyes generated globally each year, approximately 10 to 15% are directly released into the waterways.[10] This massive influx of untreated effluent not only introduces aesthetic concerns, but far more, it compromises sunlight infiltration and decreases oxygen exchange of aquatic organisms, which adversely affects the photosynthesis process. In addition, a large number of these hazardous substances are toxic and potentially cancer-causing, which pose a grave risk to human and animal health.[11] Therefore, the treatment of industrial wastewater from such harmful substances is imperative before its dissemination. Wastewater so treated may also be considered an additional water resource and can be reused for lower grade purposes than drinking, including the industrial sector, recreational activities, and, in some cases, agriculture for irrigation.

In this regard, there has been substantial advancement in the past few years to develop effective techniques for treating wastewater, and up to now, the currently available technologies are biological treatment,[301,357] adsorption,[358,359] membrane filtration,[303,360] and chemical oxidation.[69,71,72] However, in most of these techniques, polluting organic dyes are not completely removed or destroyed, and the operational costs are too high. Recently, semiconductor heterogeneous photocatalysis, a simple, efficient, renewable, and ecologically safe method, which is a part of advanced oxidation processes (AOPs), has received widespread interest for its potential use in environmental treatment.[155] In

semiconductor heterogeneous photocatalysis, the semiconductor material is activated by UV, visible or near infrared light based on its energy band gap, then react with water and/or dissolved oxygen to form highly reactive oxygen species such as $\bullet O_2^-$ H_2O_2, •OH, etc., which have a strong oxidizing ability and can rapidly degrade organic dyes into harmless intermediates or further mineralize the pollutants into CO_2 and H_2O molecules. However, the large scale use of traditional semiconductors like titanium oxide (TiO_2) and zinc oxide (ZnO) is limited by their poor absorption of visible light owing to their wide band gaps.[361,362] Although these photocatalysts can be activated by UV light, UV only makes up about 4% of the total sunlight spectrum. Nowadays, it is important to create new visible light-active semiconductor photocatalysts with narrow band gaps to address water pollution. This is because visible light makes up about 43% of the total solar spectrum and is also the primary component of indoor artificial lighting.

In recent years, a range of Ag-based compounds, including Ag_3PO_4,[363,364] Ag_2O,[365,366] Ag_3VO_4,[29,367] Ag_2CrO_4,[31,368] AgX (X= Cl, Br, I)[32,176] etc., have demonstrated excellent photocatalytic activity when exposed to visible light or sunlight. For example, Yi et al.[369] demonstrated the strong photo-oxidative ability of Ag_3PO_4 in the decomposition of methylene blue, while being exposed to visible light. Wang et al.[191] studied the stability and visible light photocatalytic performance of Ag_2O in decomposing methyl orange dye. They found that Ag_2O remains stable upon illumination with visible light due to the formation of a small quantity of Ag nanoparticles (NPs) on its surface during the catalytic decomposition. They suggested that these Ag NPs can prevent the fast recombination of the charge carriers in Ag_2O, thereby improving the photocatalytic activity. Xu et al.[370] conducted a study to understand the correlation between the structural, optical, and electronic properties of Ag_2MO_4 (M = Cr, Mo, W) materials and their photocatalytic activities. They found that the ability to absorb light, photocatalytic behavior, and stability are closely linked to the electronic structure.

Motivated by such importance of Ag-containing compounds, we investigated the visible-light photocatalytic behavior of NASICON-type $AgTi_2(PO_4)_3$ both experimentally and theoretically in this chapter. The optical band gap of the synthesized sample was evaluated by UV-Visible DRS. Concurrently, the electronic band structure was studied using density functional theory (DFT) using the generalized gradient approximation (GGA). To remedy the miscalculation of the band gap energy by the GGA functional, we have explored the effects of incorporating a Hubbard-like correction U. This addition aims to more accurately represent the intense on-site Coulomb interactions of localized d electrons in $AgTi_2(PO_4)_3$. Then, the photocatalytic properties were examined in the decomposition of RhB as a model organic contaminant, under visible light illumination. Finally, by combining experimental findings with first-principles calculations, we were capable to explain the origin of the photocatalytic performance and the mechanism behind the degradation of RhB. Henceforth, we will refer to $AgTi_2(PO_4)_3$ as AgTiP in the following sections.

V.2. Results and discussions

V.2.1. Raman characterization

The AgTiP NASICON-type material's crystalline structure, phase composition, and surface morphology were detailed earlier in Chapter III. To further investigate the functional groups of as-synthesized AgTiP, Raman spectroscopy was carried out. Fig. III.1 demonstrates the Raman scattering spectrum of AgTiP between 100 and 1700 cm^{-1}. The frequency lines at 1096 and 992 cm^{-1} are associated with the anti-symmetric stretching vibrations (ν_3) of the PO_4^{3-} tetrahedron. The peak located at a frequency of 976 cm^{-1} is caused by the symmetric stretching vibrations (ν_1) of the PO_4^{3-} ions. The weak peaks observed at frequencies of 595 and 540 cm^{-1} are due to the anti-symmetric bending vibrations (ν_4) of the PO_4^{3-} group. The bands at frequencies of 440 and 426 cm^{-1} originate from the symmetric bending vibrations (ν_2) of the phosphate group. Frequency lines that fall under 400 cm^{-1} are attributed to external vibration modes of the PO_4^{3-} unit. This is due to the influence of the electron density from the highly charged Ti cations on the P–O bond. All these observed Raman bands for AgTiP sample are consistent with those reported for similar NASICON-type materials in the literature.[371,372] However, some vibrational bands were not observed in the AgTiP spectrum because of overlapping and/or low intensity peaks. The Raman results confirm that AgTiP has short-range structural order.

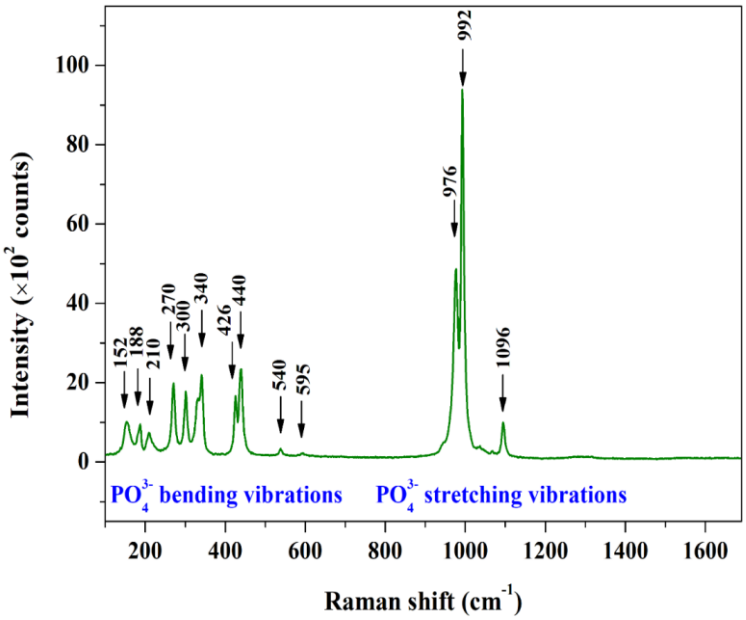

Figure V. 1. Raman-active modes of AgTiP.

V.2.2. XPS analysis

X-ray photoelectron spectroscopy was performed to examine the purity and element compositions of the as-synthetized AgTiP material. The XPS survey scan in Fig. V.2(a) shows that, aside from the C 1s element, which can be assigned to adventitious hydrocarbons from the XPS measurement, the sample contains only silver, titanium, phosphorus, and oxygen elements, indicating that the material prepared

is of high purity. The electronic core levels of the P 2p, Ag 3d, Ti 2p, and O 1s elements in AgTiP were investigated by high resolution XPS, with the findings presented in Fig. V.2(b). In the P 2p core-level spectrum, the symmetric peak situated at 133.64 eV is ascribed to the P 2p3/2 binding energy of the PO_4^{3-} group. For the Ag 3d spectrum, the doublet peaks situated at 368.0 eV as well as 374.0 eV are respectively attributed to the Ag 3d5/2 and Ag 3d3/2, which implies that Ag species exist in the form of Ag^+ ions. With regard to the Ti 2p spectrum, the two signature lines centered at 459.9 eV and 465.6 eV correspond, respectively, to Ti 2p3/2 and Ti 2p1/2. This spin-orbit doublet indicates that Ti species exist in the form of Ti^{4+} chemical state and are distributed over the octahedral sites in the NASICON lattice. The asymmetric peak in the high-resolution spectrum of O 1s has been separated into two Gaussian XPS lines through deconvolution. The lines located at the binding energy of 530.9 eV indicates the existence of lattice oxygen in the AgTiP structure, while the O 1s line centered at a higher binding energy of 532.8 eV is associated with chemisorbed oxygen species on the AgTiP surface, appearing as oxygen (O_2^-) and/or hydroxyl (HO^-) ions.[193,373,374] However, since photocatalysis takes place on semiconductor surfaces, absorbed oxygen can easily be captured by photogenerated electrons to produce reactive species, leading to enhanced photocatalytic properties.

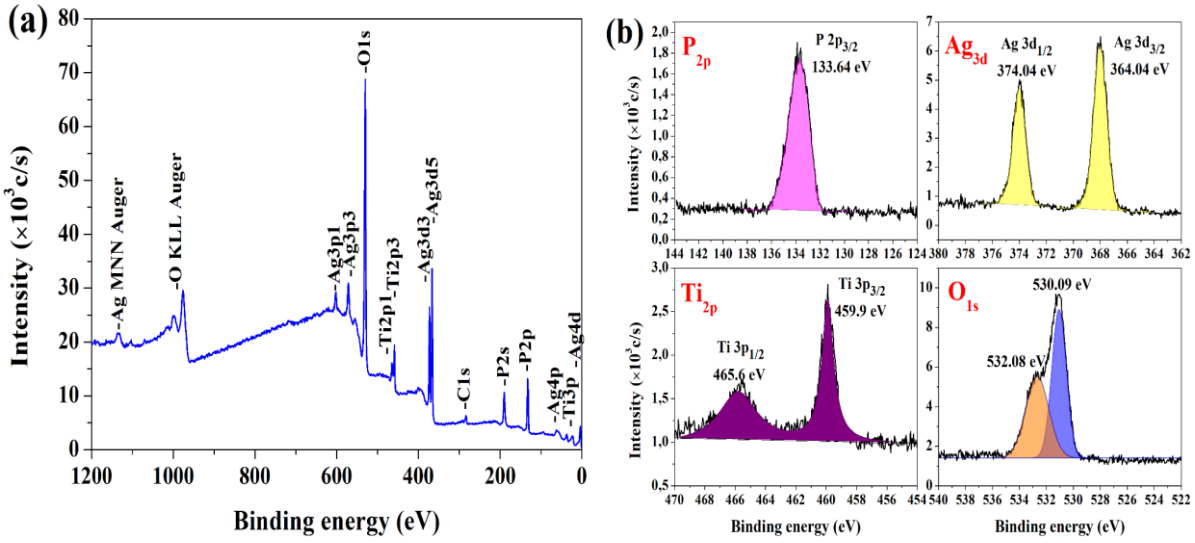

Figure V. 2. (a) XPS survey scan of AgTiP material, (b) high-resolution XPS analysis of P 2p, Ag 3d, Ti 2p and O 1s.

V.2.3. UV-Vis DRS characterization

The optical property of pure AgTiP was investigated by measuring its UV-Vis absorption spectrum. As can be seen in Fig. V.3(a), the sample has a band centered around 250-325 nm. This band is due to electron transfers between oxygen and titanium $O^{2-} \rightarrow Ti^{4+}$, which has been previously observed in similar NASICON-type materials.[24,26] The broadening of the bottom of this charge transfer band at high energy (between 210 and 230 nm) is attributed to the electronic transitions $4d^{10} \rightarrow 4d^9 5s^1$ of Ag^+ ions, which commonly appear for silver-based compounds around 220 nm. In order to gain a comprehensive

understanding of the optical properties of the synthesized material, the band gap (Eg) is calculated via fitting the relevant absorption results into the Wood-Tauc formula (Eq. II.18):[232,375,376]

$$\alpha h\nu = A\left(h\nu - E_g\right)^{n/2} \qquad (V.3)$$

Here, α represents the coefficient of absorption, h is the Plank constant, ν is the frequency of the incident light, and A is a constant. The value of the index n relies on the characteristics of the semiconductor: if the electronic transition between the valence band (VB) and conduction band (CB) is direct, the n value is 1; if the transition is indirect, the n value is 4. According to the electronic structure analysis presented in the later text (section V.2.2), AgTiP has an optical absorption spectrum that is governed by an indirect transition, with an n value equal to 4. Hence, the estimated energy gap can be determined by linearly extrapolating the $(\alpha h\nu)^{1/2}$ vs. hν plot as illustrated in Fig. V.3(b). Consequently, the energy gap of the prepared material was determined to be 2.6 eV.

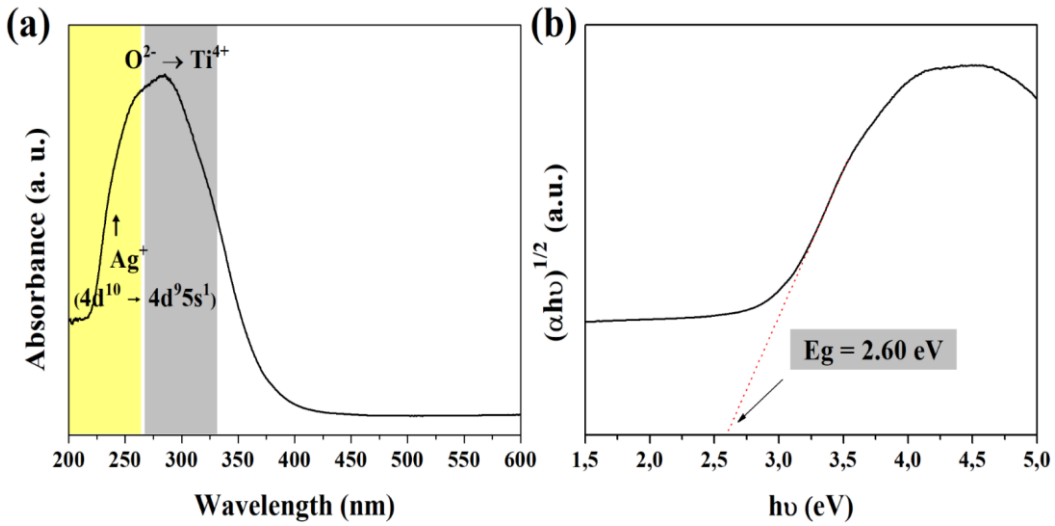

Figure V. 3. UV-Vis analysis of AgTiP; the inset depicts the Tauc plot estimating the energy gap.

V.2.4. Electronic structure analysis

V.2.4.1. Density of state (DOS)

The electronic structure's composition can be examined by looking at the density of state (DOS) of AgTiP, which was obtained via the Generalized Gradient Approximation (GGA) of Perdew-Burke-Ernzerhof (PBE), as depicted in Fig. V.4(a). Generally, the DOS provides insight into the availability of states across different energy levels. A high number of states at a specific energy level, indicated by a high DOS, implies a large number of available states for electrons occupation. Conversely, if the DOS is zero, it signifies the absence of available states for electrons at that particular energy level to occupy. However, to interpret the electronic structure of a semiconductor, it can be helpful to know which states are significant near specific atoms. A frequently used approach to accomplish this involves the use of the partial density of states (PDOS). The PDOS corresponding to the elements Ag, Ti, P, and O are

illustrated in the inset of Fig. V.4(a). The calculated DOS and PDOS of AgTiP material reveal that the electronic states in the low-energy zone ranging from -10 and -5 eV, consist of a mixture of O 2s, P 3s, and P 3p orbitals. The states from -5 to 0 eV are predominantly occupied by O 2p and Ag 4d orbitals, with a smaller input from the Ti orbitals and almost no presence of P orbitals. This suggests that the O 2p and Ag 4d states are dominant at upper boundary of the VB. On the other hand, the lower boundary of the CB, above the Fermi level (E_F), is predominantly constituted of Ti 3d states with a small contribution from O 2p and P 3p orbitals. The band gap computed using the GGA method is approximately equal to 1.88 eV. This value is lower in comparison with the UV-Vis measured band gap of 2.6 eV. According to the literature, this discrepancy in band gap is related to the exchange correlation energy functional of the semi-local GGA approach, which fails significantly in predicting the band gaps of strongly correlated systems whose ground state is characterized by a more pronounced localization of electrons, especially when transition metal 3d and rare earth 4f-orbitals are present. The inaccurate description of these systems given by standard DFT functionals can be remedied, at least partially, by Hubbard U corrections, which increases the total energy preventing the unwanted delocalization of the too shallow d- and f-electrons. In our case, we have applied the GGA + U method proposed by Dudarev et al.[275,377] according to the following equation (Eq. V.2):

$$\mathbf{E_{GGA+U} = E_{GGA} + \frac{U-J}{2}\sum_{\sigma}(n_{m,\sigma} - n_{m,\sigma}^2)} \qquad (\mathbf{V.2})$$

where U and J denote the on-site Coulomb repulsion and the exchange interaction, respectively, n represents the occupation matrix of the on-site 3d-states, which is derived by projecting the wave function onto 3d atomic-like states, m refers to the momentum of the orbital, and σ denotes the spin index. Note that we can incorporate the exchange interaction with the Coulomb term, so we can define the effective Hubbard U_{eff}, represented as $U_{eff} = U - J$.

However, no systematic studies of the U term have been conducted across all elements with all possible oxidation states. Therefore, we have fitted the U value to the 3d-orbiats of the Ti element from the range of 2 to 8 eV, while the Hubbard term J was set to zero for all calculations. As shown in Table V.1, the band gap improved with an augmentation in the U parameter. Calculations indicate that using GGA + U with a Hubbard term of 7 eV yielded a more accurate result, with the estimated electronic band gap of the sample being closer to the experimental data. Fig. V.4(b) displays the DOS and PDOS of the material calculated using the GGA + U (7 eV) method. By applying the U value, the conduction levels of AgTiP were shifted to a higher energy region. This caused an adjustment in the hybridized Ti 3d and O 2p states, aligning them with the measured band gap value.

Table V. 1. The band gap with U adjustment applied to Ti d orbitals in the range of 0 to 8 eV.

Hubbard U (eV)	0	2	3	4	5	6	7	8
Calculated band gap (eV)	1.88	2.07	2.13	2.23	2.33	2.46	2.57	2.65

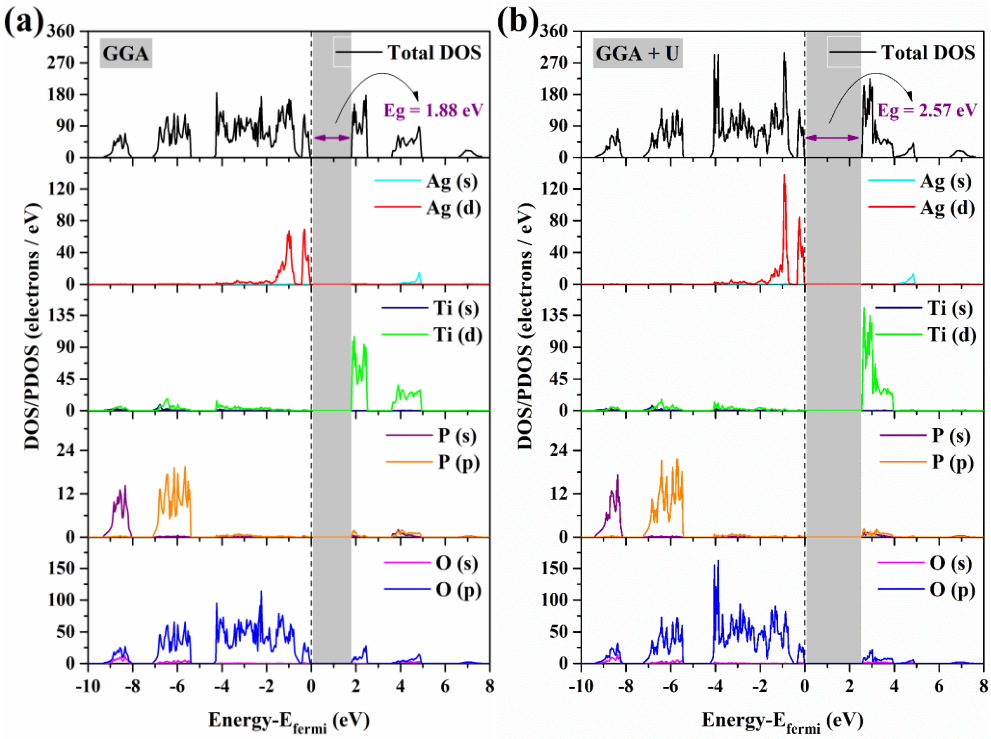

Figure V. 4. DOS and PDOS of AgTiP obtained within (a) GGA and (b) GGA + U (7 eV).

V.2.4.2. Band structure

Now, let's discuss the features of the electronic band structure of AgTiP. The band structure serves as a valuable tool in identifying the direct band gaps and indirect band gaps, which is crucial in characterizing the electrical properties of solid materials. It is convenient when discussing bands energy to work in k-space, where the energy of crystal orbitals is calculated relative to a wavevector, k. Fig. V.5(a) depicts the k-points and high-symmetry directions within the rhombohedral Brillouin zone (BZ) generated via the algorithms of SeeK-path.[378] The filled black points denote one symbol of each unique k-vectors in the reciprocal space of the BZ with the highest symmetry. The green lines, on the other hand, point out sections of the auto-generated band path, which follows the pattern Γ-T-H_2|H_0-L-Γ-S_0|S_2-F-Γ. Fig. V.5(b) shows the calculated band structure with a zoomed view of the valence band and conduction band edges of the AgTiP sample along the high symmetry directions of the BZ, obtained using the GGA + U (7 eV) method. As observed, the maximum of the VB (red dot) is situated at the Γ point, while the minimum of the CB (blue dot) is positioned between the Γ and T symmetry points of the BZ, which means that AgTiP is an indirect-gap semiconductor. It's widely recognized that materials, in which the CB minimum and the VB maximum are not vertically aligned, can exhibit enhanced photocatalytic performance because the recombination of the generated charge carriers (e^-/h^+) under light illumination is relatively difficult.

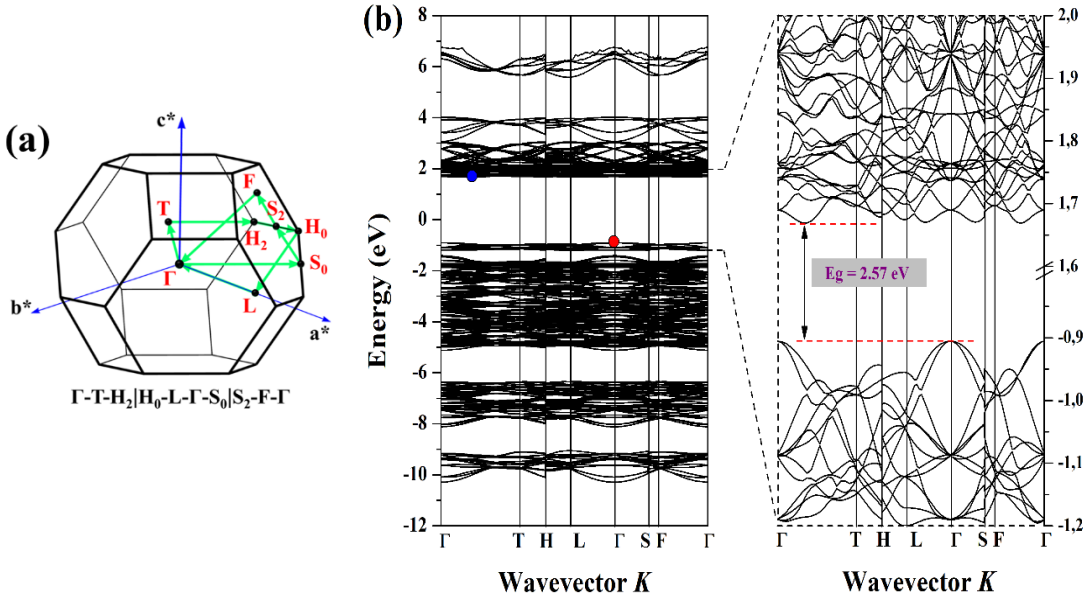

Figure V. 5. (a) The special k-point of the rhombohedral BZ and generated band path for AgTiP, (b) the obtained band structure of AgTiP with U correction (7 eV); The inset is a zoomed view of the band structure near the Fermi level.

V.2.5. Visible-light photocatalytic decomposition of Rhodamine B dye pollutant

Considerable water pollution is caused by dyes as the major effluents arising from different industrial sectors. Non-biodegradable, persistent in the environment, and often toxic are the characteristics of many of these dyes. The as-prepared AgTiP photocatalyst was used to degrade RhB, a model industrial dye pollutant in water, under visible light. RhB absorbs light between 200-600 nm with the stronger absorption peak occurring at 554 nm. The absorption spectrum of RhB was recorded every 20 min while being exposed to light in the presence of AgTiP, as illustrated in Fig. V.6(a). The characteristic absorption peaks of the organic molecule gradually decrease in intensity over time and disappear after 120 min of irradiation. This indicates that AgTiP is an effective visible light photocatalyst. Furthermore, during the decomposition reaction of RhB, no shifts in its absorption band at λ_{max}= 554 nm were observed for its intermediates such as N,N,N′-tri-ethylated Rh at λ_{max}= 539 nm, N,N′-di-ethylated Rh at λ_{max}= 522 nm, N-ethylated Rh at λ_{max}= 510 nm, and Rh at λ_{max}= 498 nm.[379] Therefore, it was suggested that the photodecomposition of RhB over the synthesized catalyst occurs through the cleavage process of the whole conjugated chromophore. Fig. V.6(b) displays the photodecomposition profile of RhB with respect to illumination time. The dye molecule's stability was confirmed by conducting a blank experiment (photolysis) in which only a minimal quantity of dye was degraded under visible light without the presence of the photocatalyst. Furthermore, before the light exposure, the RhB's adsorption on the catalyst was tested for 60 min and it was observed that only about 5% of the starting dye concentration was adsorbed onto the sample surface. After the introduction of AgTiP, the RhB concentration decreases gradually with respect to irradiation time, and the rate of decomposition reaches

88% in 60 min. Then the rate slowed down, as expected for an exponential decay kinetic. The photocatalytic decomposition efficiency for RhB over AgTiP was 97.2% in 120 min of irradiation.

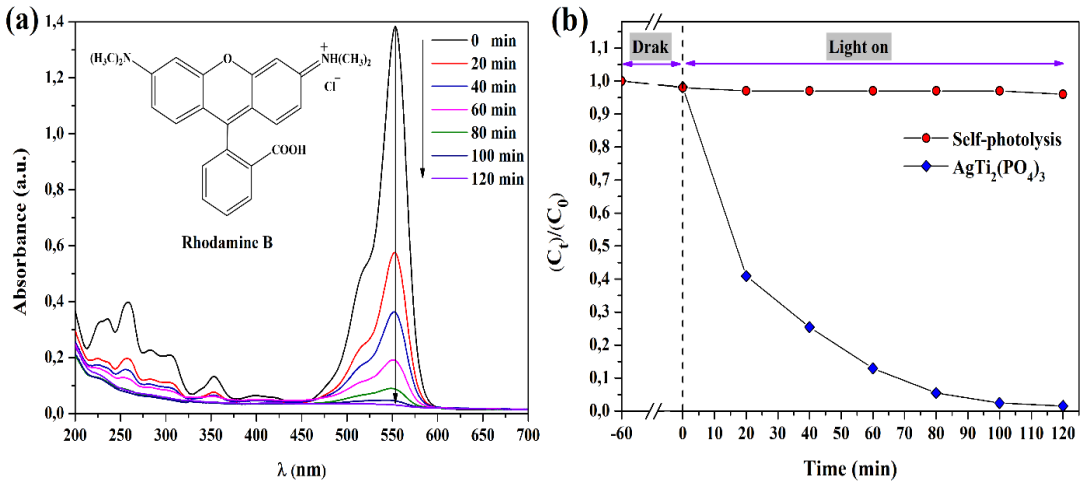

Figure V. 6. (a) UV-Vis absorption spectra of RhB under light irradiation in the presence of AgTiP, (b) C_t/C_0 plot of RhB with respect to the illumination time.

V.2.6. kinetics studies

The kinetics model for the photodecomposition of RhB can be described by the pseudo-first-order rate from the Langmuir–Hinshelwood expression (Eq. II.101). Fig. V.7 displays the plot of $\ln(C_t/C_0)$ vs. oxidation time obtained by analyzing the absorption band at 554 nm. A very good linear correlation of $\ln(C_t/C_0)$ vs. irradiation time, up to 99% was observed, indicating that the pseudo-first-order is the suitable kinetic model. According to the slope of the $\ln(C_t/C_0)$ versus time plot, the kinetic constant k was determined to be about 0.0352 min^{-1}. Table V.2 compares the performance of AgTiP with other catalysts reported in the literature. AgTiP shows high catalytic efficiency in decomposing RhB dye compared to the other catalysts.

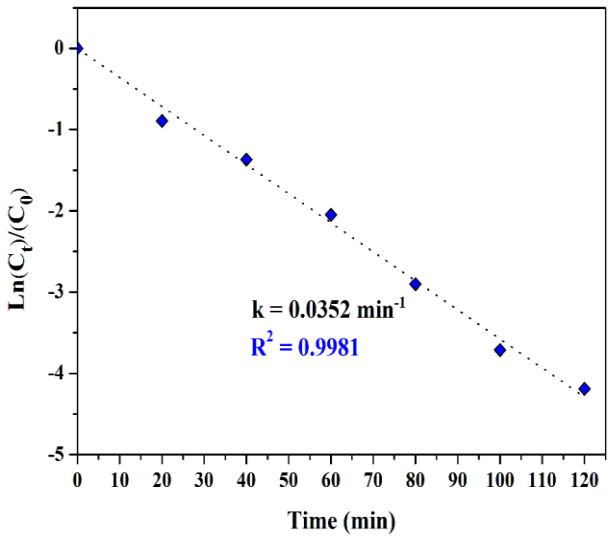

Figure V. 7. First-order kinetic plot for the decomposition of RhB

Table V. 2. Comparison of different catalysts in the photodecomposition of RhB

Catalyst	Decomposition time (min)	RhB concentration (ppm)	Efficiency (%)	Reference
β-$AgVO_3$	180	10	56.00	[380]
10wt%Ag@STO@10wt%CNT	105	5	73.00	[381]
$Bi_2WO_6/TiO_2/Ag_{2.0}$	180	5	88.18	[382]
$NiFe_2O_4$-g-C_3N_4	225	10	90.00	[383]
$[BW_{12}O_{40}]^{5-}/Ag^+$	150	10	91.71	[384]
$CuWO_4$/g-C_3N_4	150	-	93.00	[385]
10%Ag/Bi_2WO_6	210	4.79	94.21	[386]
$AgTi_2(PO_4)_3$	120	5	97.20	This work

V.2.7. Recyclability of photocatalyst

The stability of catalyst at long-term is crucial for its practical usage. Therefore, recycling experiments were conducted to evaluate the decomposition of RhB using AgTiP under visible light illumination, as can be seen in Fig. V.8(a). The photocatalytic performance remained stable and the degradation efficiency of RhB was still above 90% within 120 minutes after four consecutive runs. The slight decrease in performance after repeated runs is mainly due to the loss of photocatalyst during the recycling process . These results suggest that the as-synthesized AgTiP material exhibits good stability and could be reused as a photocatalyst with significant activity. To further support this finding, the composition AgTiP surface was analyzed using XPS before and after the four cycles of photocatalytic tests. Fig. V.8(b) and (c) show the XPS survey scan and high-resolution spectra of AgTiP before and after recycling tests, respectively. The survey scan spectrum of the used sample (Fig. V.8(b)) reveals that all of the main XPS peaks of AgTiP are still present, indicating a very high level of structural stability. However, a distinguishable increase in the intensities of Ag 3d and Ag (MNN) Auger peaks was noticed in the spent catalyst, as illustrated in Fig. V.8(c). This increase is attributed to the *in-situ* generated metallic Ag^0 on the AgTiP surface in the course of the photocatalytic reaction due to prolonged light irradiation. However, the Ag 3d photoelectron peaks did not exhibit any noticeable shifts in position. This suggests that only a small quantity of metallic Ag^0 was present on the sample surfaces. According to previous researchers[178,191] moderate formation of metallic silver from Ag-containing photocatalysts during the course of reaction could potentially enhances the catalytic performance in the visible light region and could also inhibit further photo-corrosion and realize the photochemical self-stability of Ag-based semiconductors.

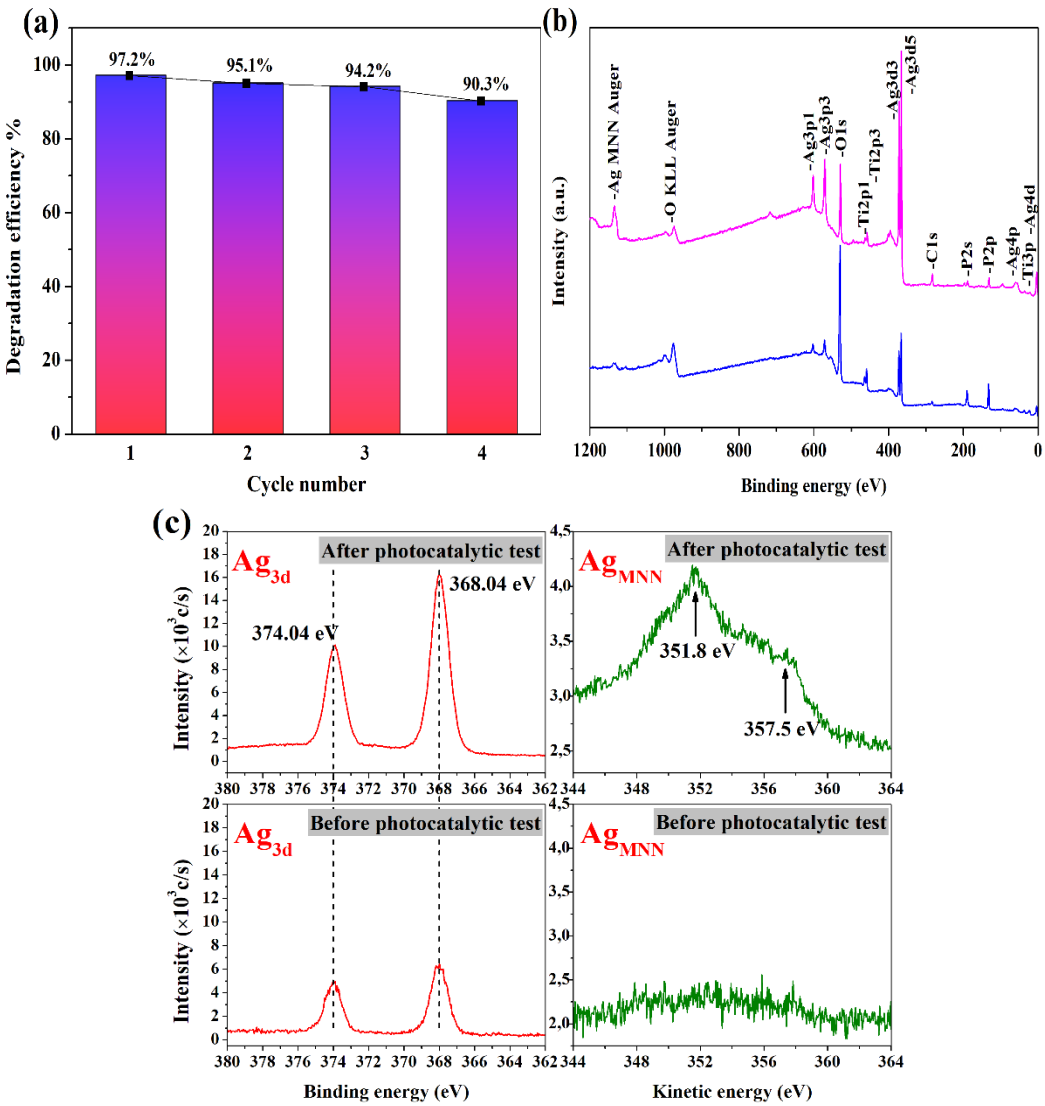

Figure V. 8. (a) 4-cycles of RhB degradation over AgTiP, (b) XPS spectrum of AgTiP before and after photocatalysis, (c) XPS high-resolution spectra of Ag 3d and Ag (MNN) before and after recycling tests.

V.2.8. Photodegradation mechanism

To reveal the reaction mechanism, it's essential to examine the dominating reactive species in the photodecomposition of RhB over AgTiP. Typically, the reactive substances include superoxide radicals ($\bullet O_2^-$), holes (h^+) and hydroxyl species (•OH), which are the key players in the photocatalytic process. In order to evaluate the contribution of these oxidizing species, we used as hydroxyl radicals (•OH) trap the isopropyl alcohol (IPA), as holes (h^+) trap the Na_2-EDTA, and as superoxide radicals ($\bullet O_2^-$) trap the ascorbic acid (As-Ac).[387] Table V.3 displays the rate of RhB photo-oxidation in the presence of AgTiP and different scavengers, after being irradiated by visible light for a period of 120 min. When the hydroxyl radical scavenger IPA was added, the rate of decomposition of RhB reached 67.0% after 120 min of irradiation. This suggests that •OH species are present in the reaction equilibrium. After the

addition of Na_2-EDTA as holes capturer, the percentage of RhB degradation was 64.8%. This shows that some h^+ species also participate in the elimination of RhB along with the other oxidative agents. However, it was noticed that the addition of As-Ac as a scavenger of superoxide radicals considerably reduced the photodecomposition process from 97.2% to 44.7%. The findings indicate that the three reactive species •OH, h^+, and $•O_2^-$ have a synergistic effect. But, the existence of $•O_2^-$ plays a pivotal role in the photocatalytic performance as well as in the decomposition rate.

Table V. 3. Percentage of RhB photodecomposition, without and with different scavengers.

Sample	No scavenger	IPA	Na_2-EDTA	As-Ac
$AgTi_2(PO_4)_3$	97.2%	67.0%	64.8%	44.7%

Prior to exploring the mechanism of photocatalysis, it's essential to identify the locations of the minimum of the conduction band and the maximum of the valence band in AgTiP. The positions of the band edges were calculated using the absolute electronegativity and the experimentally determined band gap value using the empirical equations (Eq. V.3) and (Eq. V.4):[388]

$$\mathbf{E_{CB} = \chi - E_e - \frac{1}{2} E_g} \quad (\mathbf{V.3})$$

$$\mathbf{E_{VB} = E_{CB} + E_g} \quad (\mathbf{V.4})$$

Here, E_{CB} and E_{VB} denotes respectively the conduction band (CB) and the valence band (VB) potentials, χ represents the absolute electronegativity, E_e refers to the energy of free electrons on the hydrogen scale (~4.5 eV), and Eg denotes the band gap energy. The value of χ for the AgTiP material was determined to be around 6.39 eV. Consequently, the positions of the CB and VB edges for AgTiP were respectively located at about 0.59 eV and 3.19 eV.

A potential mechanism is suggested based on the experimental data and theoretical findings mentioned above, as illustrated in Figure V.9. A photocatalytic process typically involves three steps: (i) absorption of photons with energy (hν) that is equal to or surpasses the band gap of the semiconductor; (ii) the separation, migration or recombination of photo-induced charge carriers (e^-/h^+); and finally (iii) redox reactions occur the surface of the semiconductor involving the adsorbate (reactive species and dyes). In this study, the exposure of AgTiP to visible light illumination leads to the formation of e^-/h^+ pairs on its surface. Because the CB potential of AgTiP (0.59 eV vs NHE) is lower than that of $O_2/•O_2^-$ (-0.33 eV vs. NHE), the generated e^- due to photon excitation are unable to reduce the adsorbed O_2 to $•O_2^-$. Still, the e^- injected into the CB can easily reduce Ag^+ *in situ* to produce Ag NPs, as confirmed by XPS analysis (Fig. V.8(b) and (c)). Simultaneously, the h^+ in AgTiP's VB initiate the decomposition of RhB dyes. In addition, the Ag NPs generated *in situ* can serve as an electron pool preventing the recombination of AgTiP's e^-/h^+ pairs, resulting in the accumulation of photoinduced e^- on the surface of Ag NPs, which then reduces O_2 to $•O_2^-$.[389,390] Subsequently, through further reactions, $•O_2^-$ species will transform into

hydrogen peroxide (H_2O_2), and then into •OH radicals.[193] It's also crucial to highlight that the Ag NPs formed can prevent further photoreduction of AgTiP by creating a protective shell around the photocatalyst material. Similar findings of this self-stabilizing mechanism in Ag-containing semiconductors have been reported in previous studies.[191,370] Ultimately, the photogenerated species, $•O_2^-$, •OH and h^+, will degrade the RhB pollutants into H_2O, CO_2, and inorganic salts.[391]

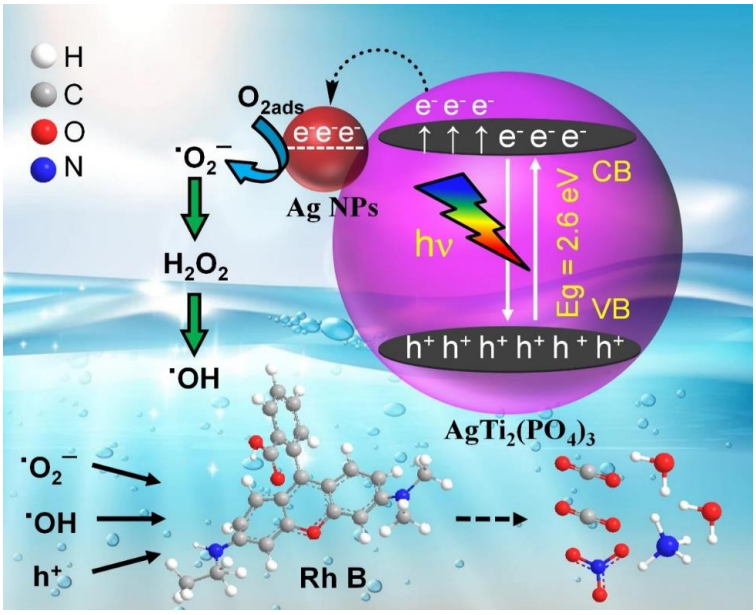

Figure V. 9. Schematic of the electron-hole transfer mechanism in AgTiP under light illumination and the photocatalytic decomposition of RhB.

V.3. Conclusion

In this research, $AgTi_2(PO_4)_3$ NASICON-type phosphate was reported for the first time as a visible-light active catalyst for the decomposition of persistent organic dye. The material was obtained using a simple coprecipitation-calcination method and analyzed by different characterization techniques. Raman spectroscopy showed that almost all of the sample's vibrational modes are characteristic of the PO_4^{3-} group. XPS observations confirmed the stoichiometric composition and high purity of $AgTi_2(PO_4)_3$. The Tauc plot, derived from the UV-Vis DRS data, revealed a band gap of 2.6 eV. A comprehensive insight into the electronic properties was provided by the first-principle DFT computations, adjusted with a Hubbard U correction. The calculated band gap using DFT-GGA plus Hubbard U of 7 eV for Ti 3d accurately reproduced the measured optical gap energy. The E-k diagram, which represents the calculated band structure, indicated that the prepared sample have indirect permitted transitions between the valence band and the conduction band. The ability of $AgTi_2(PO_4)_3$ to decompose RhB dye when exposed to visible light was associated with the *in situ* generation of a small quantity of Ag NPs on the sample surface during the reaction. This was confirmed through XPS analysis. Finally, radicals and holes trapping experiments showed that the primary reactive species involved in the decomposition of RhB were $•O_2^-$. The research illuminated the potential of Ag-based NASICON phosphate for the

decomposition of organic dyes in wastewater when exposed to visible light, which could be useful for other NASICON-structured materials for visible-light active photocatalysis.

Chapiter VI: Photocatalytic degradation of dye pollutant over Ag_2O NPs/$AgZr_2(PO_4)_3$

This chapter is based on a submitted paper:

A. Moussadik, D. Mazkad, N. Lazar, A. Benzaouak, Y. Abrouki, M. Halim, F. Tielens, A. El Hamidi, Self-grown Ag_2O nanoparticles on Ag-NASICON material for visible-light degradation of dyes in wastewater.

VI.1. Introduction

Environmental issues have become a main challenge and concern for researchers all over the world in the past several years, especially involving water pollution. Industrial growth, along with the unprecedented rise in the population, amplified by rapid urbanization, has led to high demand for the Earth's limited freshwater resources.[38,336,392,393] Simultaneously, the discharge of hazardous materials and wastes into the aquatic environment has posed a risk to natural ecosystems and human health.[4,8] The significant part of this issue refers to the pollution caused by the discharge of industrial wastewater, which typically contains many toxic contaminant compounds.[394–396] Most of these pollutants in industrial effluent are resistant to conventional wastewater treatment techniques. As a result, they have become widespread and have been detected in water bodies such as rivers, lakes, and oceans.

Among different kinds of recalcitrant compounds, organic dyes like rhodamine B, Congo red, crystal violet, methylene blue, methyl red, methyl orange, and many other colorants have been recognized as the most common pollutants in wastewater released from various industries such as textiles, cosmetics, leather tanning, pulp and paper, printing, pharmaceuticals, and food.[60,297–299,397–399] Scientific reports revealed that 10 to 15% of the total dyes generated globally ends up in wastewater during manufacturing processes.[400,401] The presence of these pollutants in water is highly visible and undesirable, while the public perception of water quality is generally influenced by color. Apart from the aesthetic deterioration, dyes can absorb and reflect sunlight entering the water bodies and reduce dissolved oxygen, which slows down the photosynthesis of aqueous flora and consequently affects aquatic life.[402,403] Furthermore, many of these organic dyes have relatively high toxicity, carcinogenicity, and potentially mutagenic properties.[59,404,405] Therefore, such pollutants need to be eliminated at the source sites before discharging, to prevent their detrimental impact on humans and the environment.

Different types of technologies have been documented for the remediation of wastewater containing organic dyes and can be categorized according to biological, physical, and chemical principles. These include biological degradation,[301,357] microbiological treatments,[406,407] adsorption,[358,359] membrane filtration,[408,409] ion-exchange resins,[410,411] chemical oxidation,[412,413] electrochemical oxidation,[414,415] electrocoagulation,[416,417] etc. However, because of the low efficiency, disposal problems, high costs, and technical constraints, numerous techniques for treating dye effluents have not been successfully implemented at the industrial scale. Therefore, there is a demand for innovative wastewater treatment solutions that are efficient, eco-friendly, less expensive, and acceptable for industrial use.

Recently, considerable attention has been given to semiconductor-based heterogeneous photocatalysis. This technology is green and effective and falls under the category of advanced oxidation processes (AOPs).[417–419] It is seen as a promising solution to environmental pollution issues. In a typical photocatalytic process, a semiconductor material absorbs irradiation energy from a light source equal or superior to its band gap energy, leading to the promotion of electrons (e^-) into the conduction band and generating an equivalent number of holes (h^+) in the valence band. Then e^-/h^+ pairs can migrate the photocatalyst's surface and interact with adsorbed water and dissolved oxygen to form highly reactive oxygen radicals, e.g. superoxide ($\bullet O_2^-$) and hydroxyl ($\bullet$OH) radicals, which have a strong oxidizing ability and can non-selectively degrade all organic pollutants in wastewater, eventually converting them to CO_2 and H_2O.[420–422] However, industrial exploitation of this technology is constrained due to the limitations inherent in conventional photocatalysts such as TiO_2 or ZnO can only be active under UV light,[423,424] which comprises ~4% of the total sunlight spectrum, whereas visible light represents about 43% and is the principal component of indoor artificial illumination.[425,426] As a result, a more efficient utilization of this portion is worthy of further research.

At present, some Ag-based semiconductors, like Ag_3PO_4,[27,427] Ag_3VO_4,[428,429] $AgSbO_3$,[30,430] Ag_2CrO_4,[368,431] AgX (X= Cl, Br, I),[176,432] and so on, have generated huge interest owing to their characteristics of easy visible-light excitation and low toxicity. Among these Ag-containing compounds, the silver oxide (Ag_2O) p-type semiconductor, which possesses a small band gap of approximately 1.3 eV, can be considered as one of the most prospective substitutes to traditional photocatalysts due to its excellent visible light absorption capacity and very high photo-oxidative properties for organic dye pollutants.[191,433,434] Nevertheless, despite the progress achieved, there are still obstacles that warrant attention. A key concern is the stability of Ag^+ in Ag_2O. This problem has been a subject of investigation for researchers over a long time, because Ag^+ tends to reduce into metallic Ag^0 when exposed to prolonged light illumination, which results in severe deactivation of the photocatalyst during recycling experiments.[28,435] To overcome this drawback, a new strategy must be developed simultaneously to regenerate the catalytic performance from time to time in order to make the catalyst recyclable and less cost-effective.

In this chapter, we have self-supported Ag_2O nanoparticles on the surface of $AgZr_2(PO_4)_3$ NASICON-type material via an easy-handling co-precipitation/calcination route, followed by a simple precipitation route using sodium hydroxide at room temperature. The fabricated nanocomposite was fully characterized using various methods. The photocatalytic properties of the sample were subsequently investigated in depth for the decomposition of methyl orange, which served as a reference toxic dye contaminant, under visible-light illumination. The stability of the synthetized material was also studied, and the possible photocatalytic reaction mechanism was examined systematically. Finally, we show that H_2O_2 can be utilized as a chemical oxidant to almost regenerate the initial phase of the spent

photocatalyst by converting the surface-deactivated silver back into $AgZr_2(PO_4)_3$. Henceforth, we will use the abbreviation AgZrP for $AgZr_2(PO_4)_3$ in the coming sections.

VI.2. Results and discussions

VI.2.1. XRD characterization

The XRD was employed to characterize the crystalline structures of the synthesized AgZrP material and the Ag_2O/AgZrP composite. As presented in Fig. VI.1(a), all the diffraction lines of AgZrP could be completely indexed in terms of the rhombohedral structure of $NaZr_2(PO_4)_3$ (ICDD card No. 33-1312), with no impurity phases present. The intense and sharp diffraction lines clearly imply that AgZrP has a high level of structural order and crystallinity over the long range. After treatment by aqueous NaOH (Fig. VI.1(b)), the diffractogram of AgZrP undergoes no obvious change, suggesting that the material maintains a rhombohedral symmetry. Meanwhile, two supplementary peaks were observed at 32.82° and 38.09° 2θ. These two diffraction peaks are identified as the (111) and (200) planes of cubic Ag_2O (ICDD card No. 41-1104), indicating the self-growth of Ag_2O particles on the surfaces of AgZrP. The broadening of these diffraction lines suggests that the produced Ag_2O particles are nanosized. The size of the crystallites within these nanoparticles can be obtained from the XRD peak appearing at 32.82° 2θ by Scherrer's expression (Eq. II.2),[216] the average size of the self-supported Ag_2O nanoparticles on the surfaces of AgZrP was estimated to be approximately 30-32 nm.

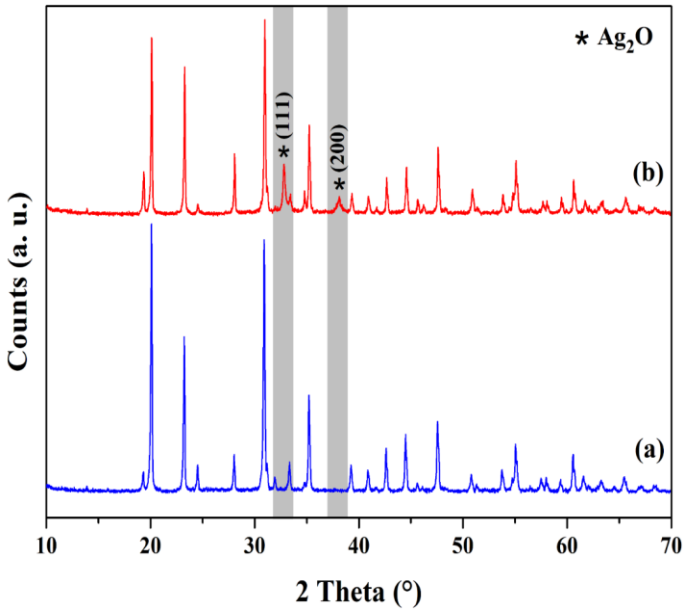

Figure VI. 1. XRD diffractograms of (a) AgZrP and (b) Ag_2O/AgZrP nanocomposite.

VI.2.2. Rietveld analysis

The Rietveld method[217] was utilized in this research to quantify the crystalline phases. Fig. VI.2 shows the Rietveld plots for the measured XRD profile versus the simulated profile of the Ag_2O/AgZrP nanocomposite. Refined crystallographic parameters of the studied sample with corresponding

reliability factors are presented in Table VI.1. The refinement's quality was validated through a visual assessment of the plotted difference between the experimental and simulated patterns. In particular, the fitting parameters χ^2, R_p, and R_{wp},[220] suggest good matches between the refined and measured XRD diffractograms. Rietveld analyses confirm the co-existence of a rhombohedral AgZrP structure within an $R\bar{3}c$ space group, and a cubic Ag_2O phase belonging to the space group $Pn\bar{3}m$. The relative weight fractions of each phase were estimated directly from the refined scale factors of the respective calculated intensities according to Eq. II.15.[221] Therefore, the weight percentage of the formed Ag_2O phase on the surfaces of AgZrP was found to be 9.8 wt.% in our experimental conditions.

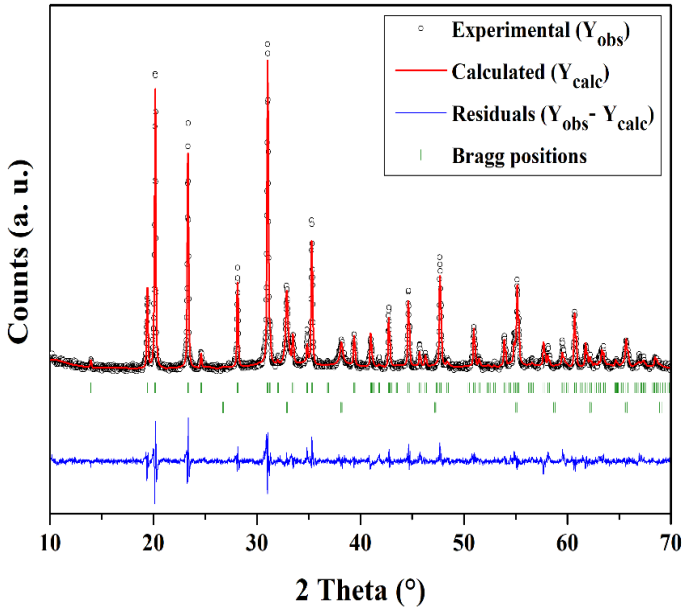

Figure VI. 2. Rietveld refinement of Ag_2O/AgZrP based on the powder XRD.

Table VI. 1. Results of the Rietveld refinement of Ag_2O/AgZrP.

Chemical formula	$AgZr_2(PO_4)_3$	Ag_2O
Crystal structure	Rhombohedral	Cubic
Space group	$R\bar{3}c$	$Pn\bar{3}m$
Lattice parameters (in Å)		
a	8.804 (38)	4.715 (47)
b	8.804 (38)	4.715 (47)
c	22.858 (106)	4.715 (47)
V, $Å^3$	1534.503 (117)	104.87 (18)
Z	6	2
Weight fractions	90.20%	9.80%
Reliability factors	$\chi^2 = 2.74$, $R_p = 10.3\%$, $R_{wp} = 13.1\%$	

VI.2.3. SEM-EDX analysis

The morphological information of the as-prepared materials was examined using SEM technology. As illustrated in Fig. VI.3(a), the as-prepared AgZrP is composed of many irregular-shaped micrometric

particles that are well connected to one another. After the treatment by aqueous NaOH (Fig. VI.3(b), (c) and (d)), it is observable that multiple Ag_2O nanoparticles are randomly dispersed on the AgZrP surface, resulting in a roughened surface for the obtained Ag_2O/AgZrP. The Ag_2O nanoparticles exhibited an average size in the range of 35-45 nm. This SEM deduced size was higher than that estimated from the XRD diffractogram using Scherrer's equation,[216] which is to be expected since it is well established that crystallites are always smaller than or equal to nanoparticles in size.[320] Besides, there was no noticeable change in the form of the original compound.

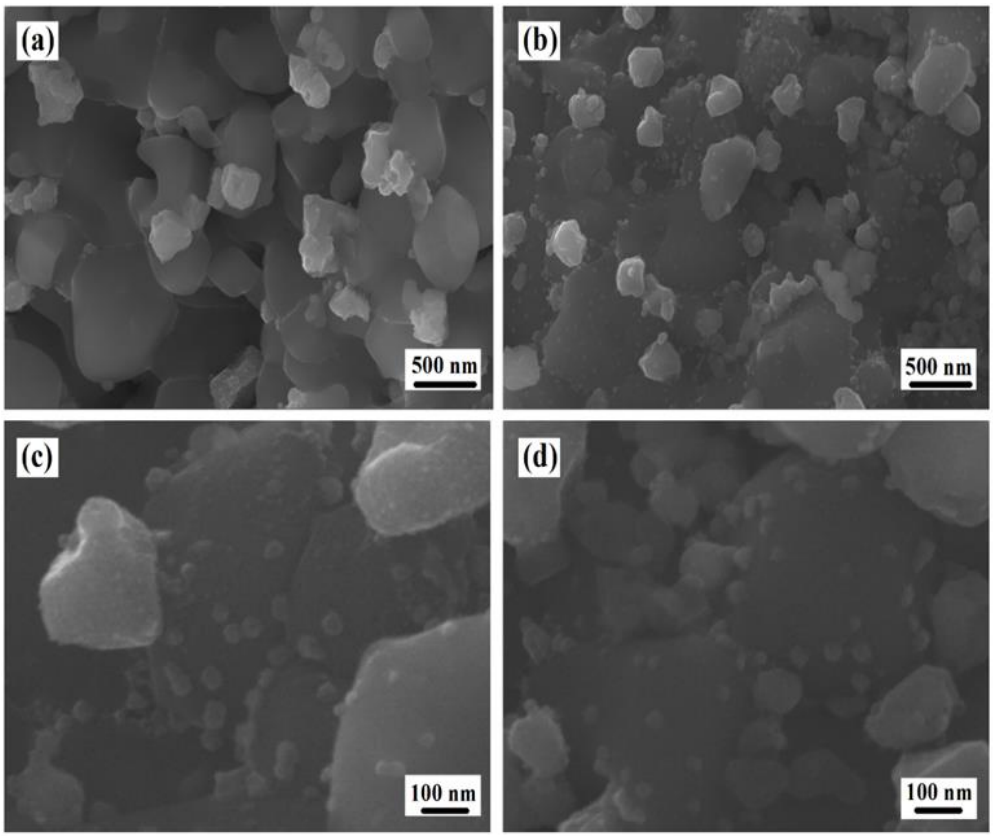

Figure VI. 3. SEM micrographs of (a) AgZrP and (b, c and d) of Ag_2O/AgZrP.

In addition, an EDX system was coupled to the SEM technique, enabling a semi-quantitative analysis of the individual elements. The EDX spectra of AgZrP and Ag_2O/AgZrP are depicted in Fig. VI.4(a) and (b), respectively. For AgZrP, the spectrum indicates that the sample only contains elements of Ag, Zr, P, and O. The atomic weight percent is 5.43% for silver, 11.38% for zirconium, 17.01% for phosphorus, and 66.18% for oxygen, which matches the theoretical stoichiometric value in the chemical formula of $AgZr_2(PO_4)_3$. On the other side, after the treatment of AgZrP by aqueous NaOH, the patterns show that the sample is composed of Ag, Na, Zr, P, and O. The percentage of elements is 5.76% for silver, 2.38% for sodium, 11.48% for zirconium, 16.08% for phosphorus, and 64.30% for oxygen.

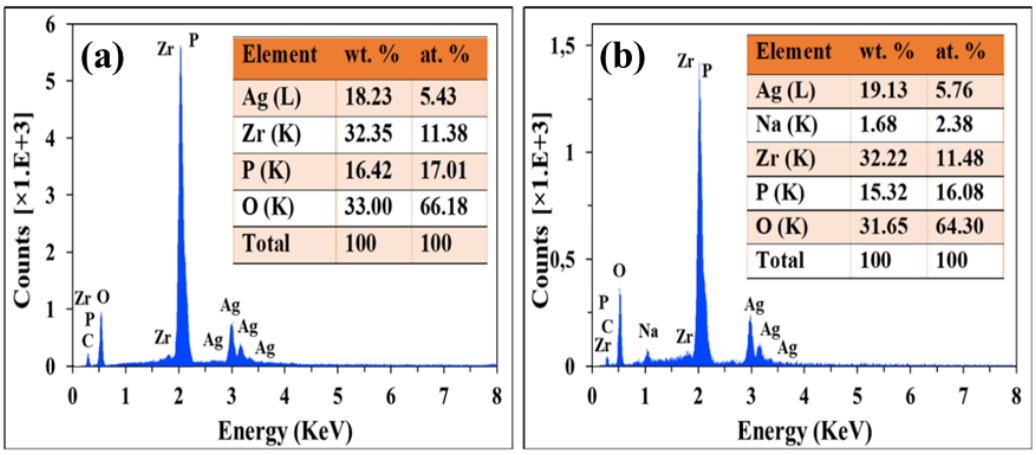

Figure VI. 4. EDX spectra of (a) AgZrP and (b) Ag_2O/AgZrP

These findings suggest that the migration of Ag^+ ions from the matrix to the sample surface, as well as the growth of Ag_2O in the presence of NaOH, is concomitantly associated with the insertion of Na^+ inside the NASICON structure to balance the negatively charged framework, resulting in the formation of $Ag_{1-x}Na_xZr_2(PO_4)_3$ material. The total reaction can be described as follow (Eq. VI.2):

$$\mathbf{AgZr_2(PO_4)_3 + x(Na^+ + OH^-) \rightarrow \frac{x}{2}Ag_2O + Ag_{1-x}Na_xZr_2(PO_4)_3 + \frac{x}{2}H_2O} \qquad \mathbf{(VI.2)}$$

VI.2.4. UV-Vis DRS characterization

To examine the optical absorption response, we have conducted measurements of the UV-Vis diffuse reflectance spectra of AgZrP and Ag_2O/AgZrP. As exhibited in Fig. VI.5(a), the pure AgZrP has an absorption band centered around 250-325 nm assigned to electron transfer $O^{2-} \rightarrow Zr^{4+}$. The broadening of the bottom of this charge transfer band at high energy (210-230 nm) could be ascribed to the electronic transitions of Ag^+ cations occurring between $4d^{10}$ and $4d^95s^1$ states, which has been already observed in similar Ag-based NASICON-type phosphates.[26] Besides, no absorption was evidenced in the visible region, implying that the sample can only be stimulated by UV light. On the other hand, after the self-growth of Ag_2O nanoparticles on the AgZrP surface (Fig. VI.5(b)), an intense absorption over the entire visible domain was noticed, along with a partial absorption in the near infrared range. This obvious shift towards the red region and pronounced enhancement in the whole visible-light area is assigned to the narrow band gap of the Ag_2O phase. In order to gain a deeper comprehension of the optical response of the obtained samples, their energy band gaps (Eg) were estimated by fitting the absorption data to the Wood-Tauc formula (Eq. II.18).[232,375] Based on the graphs depicted in Fig. VI.5(c) and (d), the Eg of AgZrP and Ag_2O/AgZrP are separately calculated to be 3.48 and 2.10 eV.

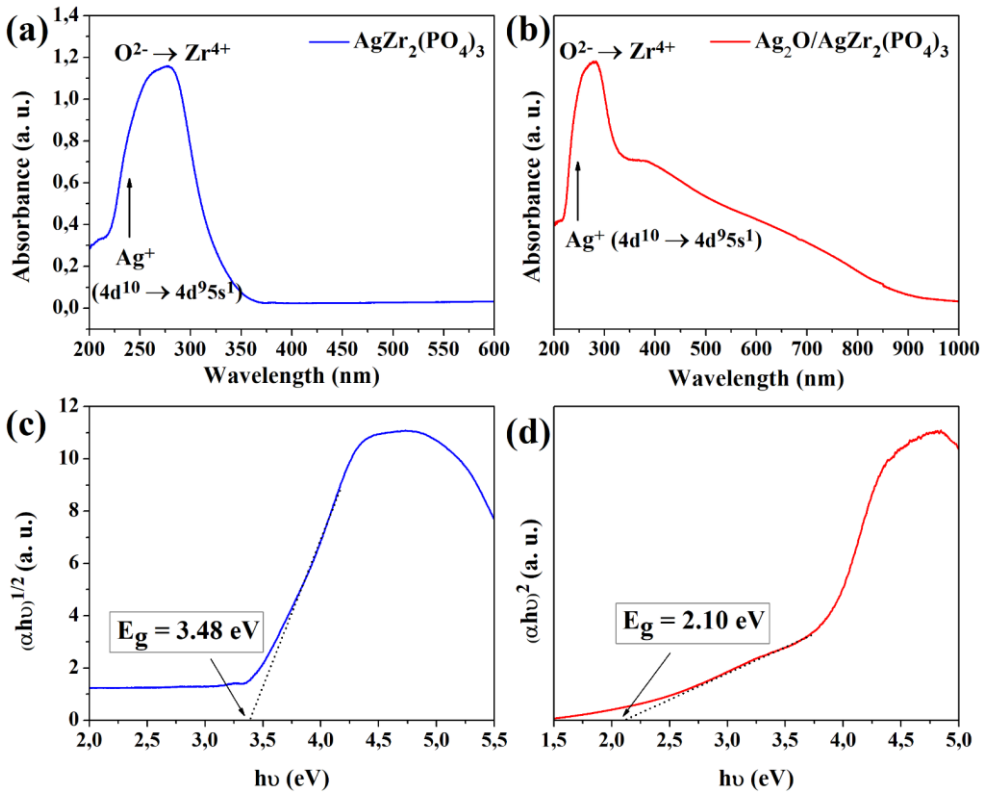

Figure VI. 5. UV-Vis absorption spectra of (a) AgZrP and (b) Ag_2O/AgZrP; The Tauc plot estimating the energy gaps of (c) AgZrP and (d) Ag_2O/AgZrP

VI.2.5. Visible-light photocatalytic degradation of methyl orange dye pollutant

The decomposition of MO as a model dye pollutant was employed to evaluate the oxidation capacity of the Ag_2O/AgZrP system upon the application of visible light. Fig. VI.6(a) shows the photo-degradation graph of MO over time in the presence of Ag_2O/AgZrP. Before exposing the system to light, the adsorption of MO on the catalyst was checked for 60 min. The results revealed that only ~8% of the initial dye concentration had been adsorbed onto the nanocomposite surfaces. After the introduction of Ag_2O/AgZrP, the characteristic absorption band of MO at 464 nm has been noticed to decrease as a function of irradiation time, and the solution finally became colorless, indicating nearly complete removal of the toxic molecule. The direct photolysis of the dye without the photocatalyst, or over only AgZrP were also investigated. The relative concentration variations of MO aqueous solutions with respect to time for each experiment are illustrated in Fig. VI.6(b). As we can see, the self-photolysis was negligible under visible light illumination, which reveals that the dye pollutant has good stability. The pure AgZrP exhibits poor photocatalytic performance with a MO decomposition rate of ~2 % following a duration of 60 min, which is attributed to its large band gap energy (3.48 eV). On the other hand, the Ag_2O/AgZrP shows greatly improved photocatalytic activity compared with the parent compound. The nanocomposite degrades the dye very quickly, and the rate reaches 95.08 % in just 60 min.

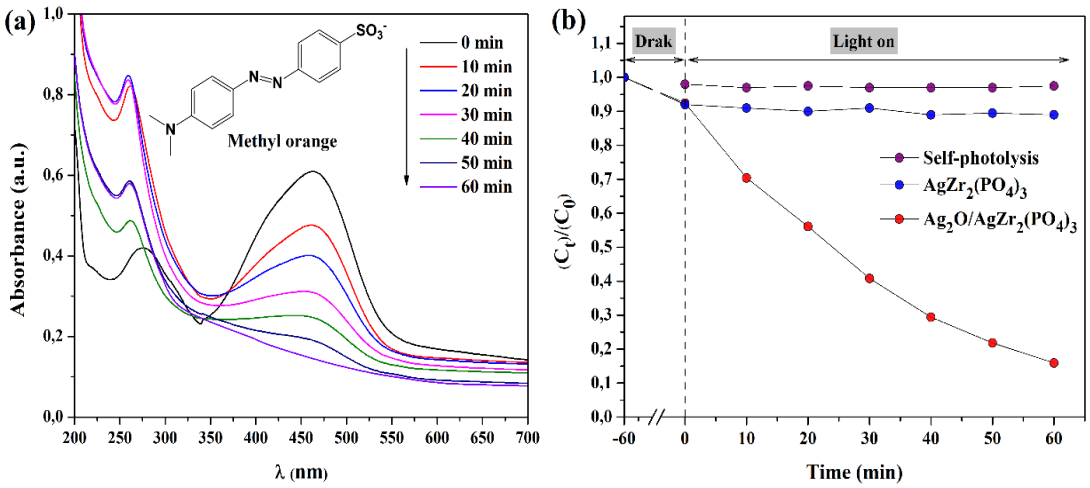

Figure VI. 6. (a) Absorbance spectra of MO degradation over Ag_2O/AgZrP, (b) time dependence of relative concentration (C/C_0).

VI.2.6. Kinetic studies

The process of photocatalytic discoloration can be described by the pseudo-first-order kinetic rate as per the Langmuir-Hinshelwood expression in Eq II.101. Fig. VI.7(c) shows the graph of $\ln(C_t/C_0)$ vs. the time of visible light exposure (t). A good correlation to the pseudo-first-order was observed, indicating the suitability of the model adopted. The photodegradation rate k of MO over the photocatalyst calculated by the corresponding linear fit was estimated to be 0.0303 min^{-1}. Table VI.2 presents a comparative analysis of MO's photodegradation using Ag_2O/Ag-NASICON and various catalysts documented in the literature. According to the results in Table VI.2, the current catalyst exhibits very good catalytic activity compared to other catalysts in similar experimental conditions.

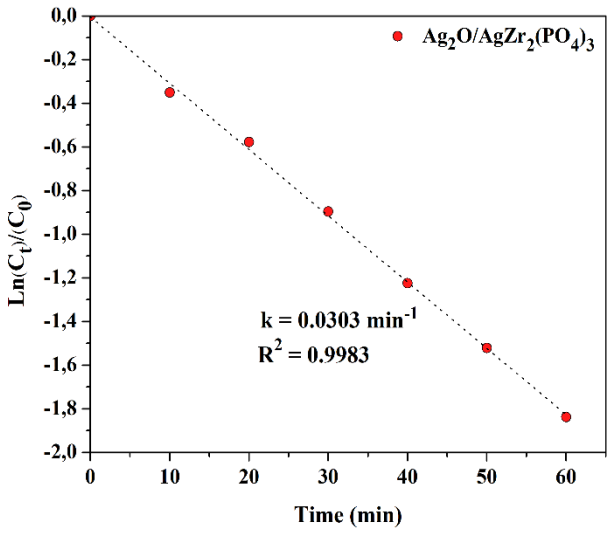

Figure VI. 7. First-order plot for the photocatalytic discoloration of MO.

Table VI. 2. Comparison of various catalysts in the photodegradation of dye contaminants.

Photocatalyst	Photocatalyst mass	Initial dye concentration	Experimental conditions	Dye degradation rate	Reference
Ag doped ZrO_2	100 mg	5 mg L^{-1}	Visible lamp (125 W)	After 105 min of irradiation: 75.00%	[436]
AgI/g-C_3N_4	50 mg	5 mg L^{-1}	Osram lamp (125 W)	After 120 min of irradiation: 80.00%	[437]
Ag_2O NPs	20 mg	5 mg L^{-1}	Visible lamp (300 W)	After 240 min of irradiation: 83.63%	[438]
Pristine-Ag_3PO_4 MSs	50 mg	5 mg L^{-1}	Metal halide lamp (150 W)	After 120 min of irradiation: 85.91%	[439]
Ag_2O/Bi_2MoO_6	30 mg	5.75 mg L^{-1}	Xenon lamp (300 W)	After 180 min of irradiation: 90.00%	[440]
Mn,Zr-Ag_2O	200 mg	4.79 mg L^{-1}	Xenon arc lamp (300 W)	After 150 min of irradiation: 93.58%	[441]
Ag-doped ZnO	100 mg	10 mg L^{-1}	Halogen lamp (100 W)	After 210 min of irradiation: 94.40%	[442]
Ag_2O/AgZrP	100 mg	5 mg L^{-1}	Halogen lamp (125 W)	After 60 min of irradiation: 95.08%	This work

VI.2.7. Recyclability of photocatalyst

The durability of the prepared sample has been examined via multiple photocatalytic tests. As displayed in Fig. VI.8(a), no significant loss of photocatalytic performance was observed for Ag_2O/AgZrP after four cycles, demonstrating the robust stability and recyclability of the fabricated catalyst. However, at the 5^{th} cycle, the photocatalytic activity slightly decreased to 87.36%, which originates from the photo-corrosion of the Ag_2O active phase. It's widely understood that under the influence of visible light, certain amounts of Ag nanoparticles may be formed on the surface of Ag-containing photocatalysts. These Ag nanoparticles act as electron trapping centers, serving to prevent additional photo-corrosion of the materials and inhibit the recombination of photo-induced e^-/h^+ pairs. Nonetheless, prolonged irradiation time can lead to a decrease in photocatalytic performance due to the shielding properties of Ag layers that are deposited on the material surface. Similar finding of this inevitable photo-corrosion phenomenon of Ag-based photocatalysts have been revealed in previous works.[193,443] Further analysis of the XRD diffractograms of the Ag_2O/AgZrP following repeated tests is presented in Fig. VI.8(b). The diffractograms reveal that the distinctive diffraction lines of the photocatalyst still conserved, suggesting a high level of photochemical stability. Remarkably, two new diffraction lines located at 44.26◦ 2θ, and 64.50◦ 2θ, which correspond to the respective (200) and (220) planes of zero-valent silver (Ag^0) (as per ICDD card No. 04–0783), are noticeable, while the Ag_2O lines are slightly less intense after the photocatalytic runs. This confirms that a small amount of Ag_2O was converted to metallic Ag when exposed to visible light.

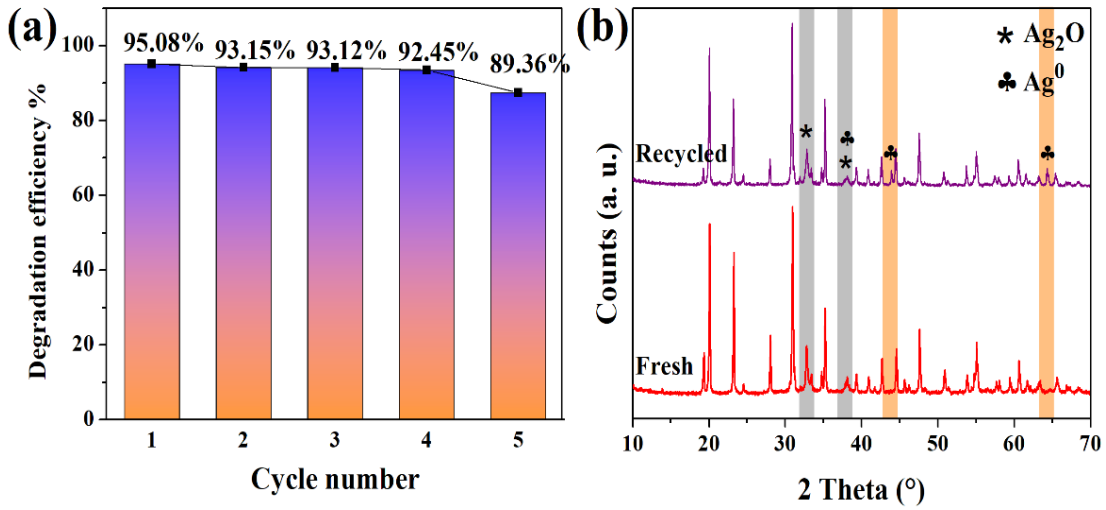

Figure VI. 8. (a) Repetitive decomposition of MO in the presence of Ag_2O/AgZrP, and (b) the XRD diffractograms of Ag_2O/AgZrP before and after 5-cycle photocatalytic tests.

VI.2.8. Photodegradation mechanism

The possible photocatalytic mechanism can be viewed from the following three aspects: (i) the main reactive species; (ii) the location of the valence band (VB) and conduction band (CB) edges of the nanocomposite; and (iii) the possible photocatalytic reactions. In general, the reactive substances include superoxide radicals ($\bullet O_2^-$), holes (h^+) and hydroxyl radicals (•OH), which play major roles in the photocatalytic process.[420] A range of photocatalytic tests were designed, involving the addition of different scavengers to the reaction mixtures to unveil the active entities that are responsible for the oxidation of MO. The radical scavengers of ascorbic acid (As-Ac), Na_2-EDTA, and isopropyl alcohol (IPA) were employed to trap superoxide radicals ($\bullet O_2^-$), holes (h^+), and hydroxyl radicals (•OH), respectively.[387] Table II.3 shows the decomposition rate of MO after 60 min of exposure to visible light, with respect to the scavengers action. After the introduction of the As Ac to the reaction system, the photodegradation efficiency of MO was reduced from 95.08% to 23.87%. When the Na_2-EDTA or IPA were added, the photodegradation of MO reached 39.79% and 46.12%, respectively. These results suggest that the three reactive entities, namely $\bullet O_2^-$, h^+, and •OH, have a synergistic effect. However, $\bullet O_2^-$ is the primary agent in the photo-oxidation of MO.

Table VI. 3. The decomposition rate of MO in the absence and presence of various scavengers.

Sample	No scavenger	As-Ac	Na_2-EDTA	IPA
Ag_2O/AgZrP	95.08%	23.87%	39.79%	46.12%

To describe the enhanced photocatalytic reactivity of the Ag_2O/AgZrP nanocomposite, it is necessary to ascertain the respective optical band gaps of AgZrP and Ag_2O semiconductors. The band edge positions of the VB and CB were determined by the Mulliken electronegativity approach according to Eq. V.3 and Eq. V.4.[388] The values of χ for AgZrP and Ag_2O are 6.40 and 5.29. The estimated VB and

CB positions of AgZrP were 0.16 eV and 3.64 eV, respectively. While for Ag_2O, the VB and CB positions were found at -0.25 eV and 1.85 eV, respectively.

Based on the aforementioned experimental findings, a potential mechanism for the photocatalytic decomposition of MO dye over Ag_2O/AgZrP is proposed, as shown in Fig. VI.9. When exposed to visible light illumination, only Ag_2O can be excited to generate electrons (e^-) and holes (h^+). While the AgZrP acts as a support for the highly photo-sensitive silver oxide. However, the CB level of Ag_2O (-0.25 eV) is less negative than that of $O_2/{\bullet}O_2^-$ (-0.33 eV), and reducing the adsorbed O_2 to give rise to ${\bullet}O_2^-$ via direct electron transfer routes ($O_2 + e^- \rightarrow {\bullet}O_2^-$) is thermodynamically unfavorable. So, the generated photoelectrons, on the other side, can migrate to the Ag_2O surface and reduce Ag^+ to zero-valent Ag, as demonstrated by the XRD analysis (Fig VI.8(b)). The *in situ* generated metallic Ag can form a Schottky potential barrier on the interface of Ag_2O,[181,192,444] which will be helpful in limiting the recombination of the photogenerated e^-/h^+ pair. Consequently, the photo-excited holes in the VB of Ag_2O can initiate the decomposition of MO pollutants. Then, it's possible that Ag nanoparticles transfer the injected and accumulated electrons to O_2 resulting in the formation of ${\bullet}O_2^-$ and H_2O_2 molecules (O_2/H_2O_2; +0.682 eV). Following this, the formed H_2O_2 molecules may interact with electrons to generate active ${\bullet}OH$ radicals ($H_2O_2 + e^- \rightarrow {\bullet}OH + HO^-$). Thus, the reactive species of ${\bullet}O_2^-$, h^+, and ${\bullet}OH$ are responsible for the decomposition of MO into H_2O, CO_2, and harmless minerals.

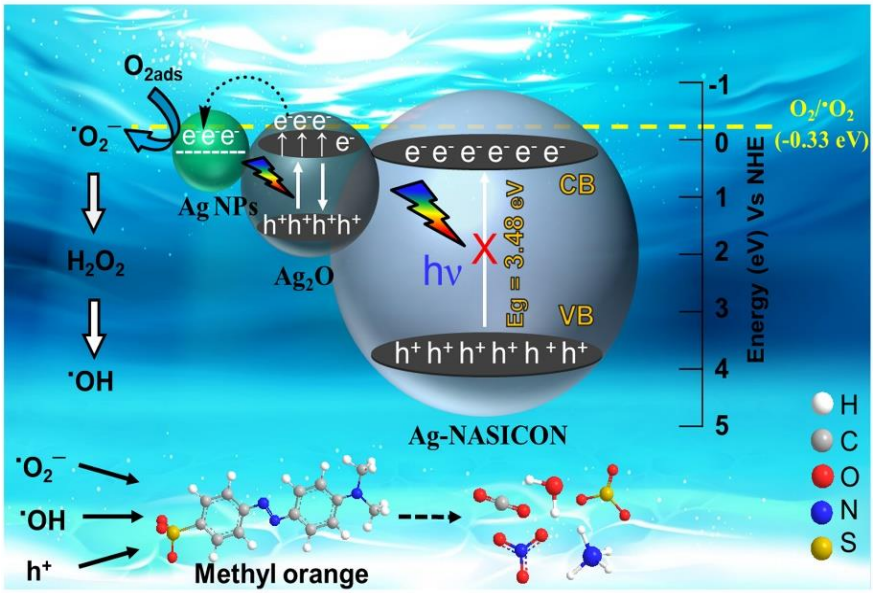

Figure VI. 9. Schematic illustration of the photodecomposition of MO over Ag_2O/AgZrP.

VI.2.9. Regeneration of photocatalyst

Once a catalyst reaches its lifetime, there are two options: either replace it or regenerate it. Since replacement is not economically desirable, the potential for regenerating the initial AgZrP phase has been explored. After multiple cycles of photocatalytic reactions, the spent Ag_2O/AgZrP nanocomposite

was collected, washed, and dried in the oven. Then, after thorough grinding in an agate mortar, the powdered sample was added into a solution of H_2O_2 and stirred for 3 h at 35 °C. Fig. VI.10(a) and (b) display the XRD and SEM-EDS analyses of the treated photocatalyst. The X-ray diffraction patterns (Fig. VI.10(a)) show a total disappearance of the diffraction lines ascribed to the (111) and (200) planes of cubic Ag_2O as well as the (200) and (220) planes of metallic silver. Moreover, after the treatment process over H_2O_2, AgZrP maintained its crystal structure quite well. In addition , the SEM image and the EDX spectrum (Fig. VI.10(b)) show that the surface Ag_2O nanoparticles vanish, while the Ag weight percentage remains almost the same in the treated sample. In contrast, the content of sodium has significantly decreased compared to its content in Ag_2O/AgZrP (Fig. VI.4(b)). This indicates that after oxidation by H_2O_2, the Ag^+ ions are reinserted back into the NASICON framework via exchange with Na^+ ions. These results constitute evidence that the AgZrP material realizes regeneration.

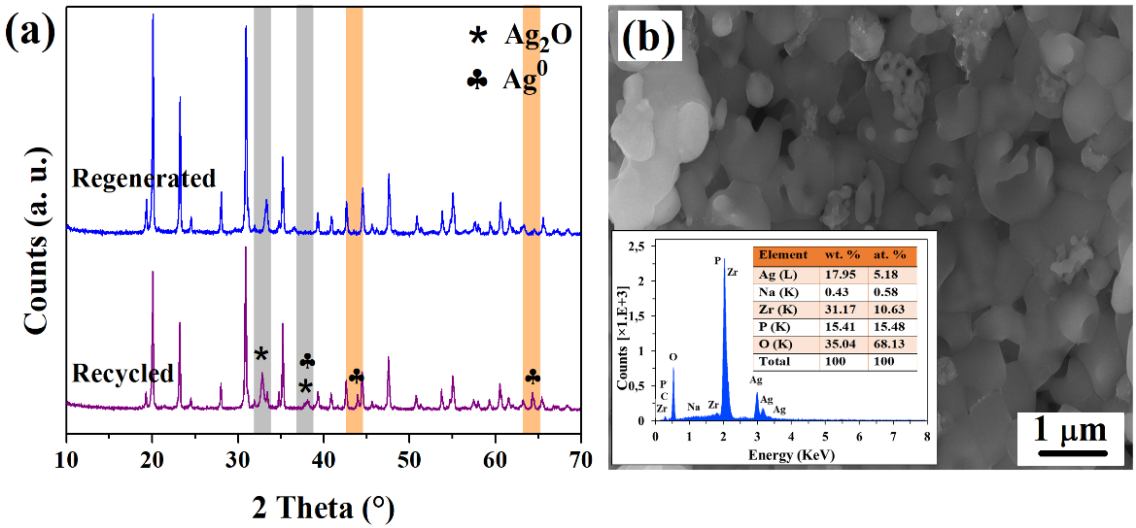

Figure VI. 10. (a) XRD pattern of regenerated AgZrP and (b) SEM image and EDX spectrum of regenerated AgZrP

VI.3. Conclusion

In summary, a novel $Ag_2O/Ag_{1-x}Na_xZr_2(PO_4)_3$ nanocomposite photocatalyst with visible-light response has been produced using an easy-handling co-precipitation/calcination route, followed by a sodium hydroxide-assisted precipitation at room temperature. From the XRD and SEM results, we concluded that Ag_2O nanoparticles were successfully self-supported on the $AgZr_2(PO_4)_3$ surfaces, while the EDX analysis suggested the substitution of Ag by Na atoms into the NASICON crystal lattice. The absorption edge of Ag_2O/AgZrP in the UV-Vis absorbance spectrum showed a pronounced red shift compared to the AgZrP material. The nanocomposite exhibited excellent performance towards dye degradation under visible-light illumination with 95.08% efficiency in 60 min. The enhancement in photocatalytic performance was credited to the in-situ formed metallic Ag from photo-reduction of Ag_2O during the course of reaction and the cooperative effect between Ag^0 and Ag_2O, which boosts the separation

efficiency of the charge carriers of the latter, transfer the electrons to react with O_2 to form $\bullet O_2^-$ and H_2O_2, and also protect the Ag_2O cores from further photo-corrosion. Additionally, the radical trapping experiments reveal that $\bullet O_2^-$, h^+, and •OH are crucial in the decomposition of MO dye under visible light exposure, while $\bullet O_2^-$ being the primary reactive species. More importantly, the used sample can realize regeneration to the initial AgZrP phase by a simple treatment with H_2O_2 used as an oxidation agent. This study provides a new perspective for the creation of attractive Ag-based photocatalysts that respond to visible-light.

General Conclusion

Wastewater pollution, especially organic pollution, is rising at an alarming rate and has posed a severe threat to human health, animals and aquatic life. The primary focus of current research is how to reduce this pollution level as fast as we can and as soon as possible. In this PhD dissertation, we reported the preparation, characterization, and catalytic capability of $AgM_2(PO_4)_3$ (M = Ti or Zr) NASICON-type materials for the remediation of toxic organic pollutants through two emerging wastewater treatment technologies, namely nanotechnology and photocatalysis. Silver (Ag) has been chosen as the core metal of this researcher work given its fascinating advantages, including unique physiochemical properties, high catalytic activity, good stability, easy preparation, relatively low price, and less toxicity. We believe that the presented research clearly demonstrates the importance of Ag-containing catalysts for environmental pollution mitigation. The main conclusions of this thesis are summarized below.

i) Self-Supported Ag NPs on $AgM_2(PO_4)_3$ for Hazardous Dyes and Nitrophenol Reductions

In the first parts of this thesis, self-supported Ag NPs were obtained at the surface of $AgM_2(PO_4)_3$ NASICON-type phosphates through an *in situ* chemical reduction approach at room temperature using sodium borohydride ($NaBH_4$) serving dual roles, as a reductant (BH_4^-) and a source of compensator ions (Na^+). The crystalline structure, surface morphology and composition of the synthesized Ag nanocomposites were probed utilizing different complementary characterization methods including XRD, ATR-FTIR, SEM and EDX analyses. The synthesized Ag NPs were also characterized during real-time *in situ* formation by UV-Vis spectroscopy. Generally, each technique gave us useful insights and by combining them, we were able to get a comprehensive understanding of our systems. In the course of the synthesis process, the UV-Vis analysis indicated the formation of small sized and monodispersed Ag particles by recording the characteristic localized surface plasmon resonance (LSPR) optical band of Ag NPs with respect to time. The XRD findings confirmed the successful growth and self-adhesion of nanosized Ag particles, i.e., 15 to 45 nm, on the surface of $AgM_2(PO_4)_3$ material, without the detection of any deleterious phases. It was remarked that the production of metallic Ag from silver-rich materials like $AgM_2(PO_4)_3$ can be rigorously controlled depending on the concentration of BH_4^- species. In addition, the XRD results proved an *in situ* compensation of Ag^+ by Na^+ ions within the vacancies inside the crystal lattice, without any alteration in the NASICON framework. By applying the Rietveld method, we were able to determine the nominal mass fraction of Ag NPs self-loading with high immobilization and confinement with the support. The purity of the as-prepared samples was further validated by ATR-FTIR spectroscopy. The SEM results showed that the adopted wet chemical reduction method successfully achieved the synthesis of ultrasmall Ag particles with a narrow size range. These nanoparticles were evenly dispersed and affixed to the NASICON support. The SEM findings were consistent with the UV-Vis and XRD analyses. Finally, the EDX spectroscopy

corroborated the XRD results by proving the replacement of Ag^+ by Na^+ ions in the NASICON crystal framework.

Next, the catalytic efficiency of the produced Ag nanocomposites was assessed in the process of reducing methylene blue (MB) and methyl orange (MO), with $NaBH_4$ serving as the reductant. The self-supported Ag NPs demonstrated high activity and effective catalytic performance in a very short time of reaction. The reactions mechanisms follow the Langmuir-Hinshelwood model. As a result, both reactants (MB/MO and BH_4^-) are adsorbed onto the catalyst's surface. The step determining the kinetic rate is the surface reaction between the two reactants. After the reaction is complete, the low-toxicity products that are formed, including leuco-methylene blue from MB and sulfanilic acid and dimethyl-4-phenylenediamine from MO, desorb from the surface and a free active site is available. Applying the pseudo-first-order using the Langmuir-Hinshelwood kinetics to the UV-Vis absorption data reveals the apparent rate constants (k_{obs}) and the activity factors (k') for both reactants. Additionally, the supported Ag NPs-based catalysts showed a long-term stability throughout reuse for multiple consecutive cycles with no appreciable loss of catalytic activity. The regeneration of used catalysts through calcination was also studied. The optimal temperature and duration were determined to be 700 °C and 180 min, which is lower than the conditions needed for preparing fresh catalysts. The regenerated catalysts were used again in a second cycle of the process. In conclusion, calcination was proven to be an energy-efficient method for regenerating spent catalysts.

The performance of supported Ag NPs was further evaluated in the process of reducing 4-nitrophenol (4-NP) to 4-aminophenol (4-AP) by $NaBH_4$. It has been reported from previous studies that 4-AP, which involves an $–NH_2$ group in its structure, is 500-fold less toxic than its corresponding 4-NP. The supported Ag NPs showed efficient catalytic conversion of 4-NP to 4-AP using $NaBH_4$, because Ag NPs function as an electron transfer center, alternating between accepting and donating electrons. Efficient electron transfer is possible when the redox potential of the Ag NPs is between that of the electron donor (BH_4^-) and the electron acceptor system (organic molecules). The kinetics and the catalytic mechanism for the conversion of 4-NP by means of the nanocomposite were analyzed. The reduction followed pseudo-first-order kinetics. Moreover, the spent catalyst can also be regenerated by nitric acid treatment at 70 °C for 60 min, which is much more energy-efficient than preparing a fresh catalyst at 900 °C for 48 h. Following the regeneration process, it was noticed that the catalytic reactivity of the newly generated Ag NPs on the NASICON matrix was nearly identical to that of the fresh catalyst.

ii) Electronic and Photocatalytic Properties of $AgM_2(PO_4)_3$ NASICON-type Materials

Instead of combining nanotechnology with chemical reduction to enhance the treatment of aqueous organic pollutants in wastewater, another alternative is the application of photocatalysis with organics-degrading capabilities. In the second parts of this dissertation, we examined the photocatalytic performance of original $AgM_2(PO_4)_3$ NASICON material in the treatment of organic dyes in water

under the exposure of visible light irradiation. Combining experimental findings with density functional theory (DFT) studies, a thorough investigation of the optical and electronic properties of the Ag-based photocatalysts has been conducted. Using UV-Vis DRS, the optical band gap energies of the as-prepared $AgM_2(PO_4)_3$ materials were calculated. We discovered that the nature of the M^{4+} element play the major role in the band structure configuration. The DFT simulation were performed, using the GGA-PBE exchange-correlation functional. Theoretical results showed that the DFT severely underestimates the band gap of $AgM_2(PO_4)_3$, which is not surprising since the standard DFT method is not designed to access excited states. The band gap underestimation reaches up 27% when compared with the experimental energy gap. Therefore, in order to remediate **t**he inaccurate description of our systems given by standard DFT functionals we applied the DFT+U correction approach. As a result, the band gap value has improved and we were able to reproduce the experimentally measured value by means of UV-Vis DRS.

Besides, we have modified the $AgM_2(PO_4)_3$ material by silver oxide (Ag_2O) NPs via a sodium hydroxide-assisted precipitation at room temperature. From the XRD and SEM results, it was observed that Ag_2O NPs were successfully self-grown on the $AgM_2(PO_4)_3$ surfaces, while the XRD and EDX analyses confirmed the purity of the synthesized Ag nanocomposites. In addition, from the SEM studies, it was observed that nano-sized Ag_2O particles of about 35-45 nm were evenly dispersed on the NASICON matrix surface.

Finally, the photocatalytic activities of original $AgM_2(PO_4)_3$ and Ag_2O NPs/$AgM_2(PO_4)_3$ samples toward the decomposition of Rhodamine B (RhB) and MO model dyes have been examined. It was noticed that all synthesized Ag-based photocatalysts could effectively degrade dyes in water-based solutions when exposed to visible light illumination. The effect of self-grown Ag_2O NPs on the photoactivity was explored. Moreover, it has been demonstrated that an *in situ* generation of Ag NPs during reaction processes enhances the visible light response of these materials. The photocatalytic reaction mechanisms were then proposed, and the dominant reactive species among •OH, $\bullet O_2^-$ and h^+, that play a significant role in the degradation of organic pollutants, were identified through radical scavenger experiments. At last, a simple catalyst regeneration strategy based on hydrogen peroxide (H_2O_2) was adopted, revealing that the spent photocatalyst can achieve nearly total self-regeneration thanks to the NASICON-type materials structural properties.

In summary, during this PhD thesis, we investigated two emerging technological practices in terms of removing organic pollutants from wastewater: nanotechnology and photocatalysis. In the field of nanotechnology, Ag NPs, owing to their small size and high specific surface area, can catalyze the reductive conversion of toxic organic pollutants in aqueous media into harmless and eco-friendly products. On the other side, within the field of photocatalysis, Ag-based NASICON photocatalysts demonstrated promising activities in organics degradation under visible light illumination. We tested

three different regeneration methods: thermal air calcination, acid aqueous treatment, and hydrogen peroxide treatment, to regenerate the spent Ag-based catalysts and reexamine their activity for the removal of toxic compounds. Along with catalyst performance, regeneration is of utmost importance, it is useful for restoring activity that has been lost over time due to a decrease in the dispersion of the active metal. The choice of regeneration method is often determined by the need to achieve specific process run lengths for economic or practical reasons. When deciding whether to regenerate or replace a catalyst, it is important to consider the life-cycle operating strategies. Regeneration treatments can prolong the lifespan of catalysts.

References

[1] P.O. Ukaogo, U. Ewuzie, C. IV. Onwuka, Environmental pollution: causes, effects, and the remedies, Microorganisms for Sustainable Environment and Health. (**2020**) 419–429.

[2] H. Qadri, R. Bhat, M. Mehmood, G. Dar, Fresh water pollution dynamics and remediation, (**2020**).

[3] A. Boretti, L. Rosa, Reassessing the projections of the World Water Development Report, Npj Clean Water 2019 2:1. 2 (**2019**) 1–6.

[4] A. Müller, H. Österlund, J. Marsalek, M. Viklander, The pollution conveyed by urban runoff: A review of sources, Science of The Total Environment. 709 (**2020**) 136125.

[5] J. Ahmed, A. Thakur, A. Goyal, Industrial Wastewater and Its Toxic Effects, Biological Treatment of Industrial Wastewater. (**2021**) 1–14.

[6] B. Moss, Water pollution by agriculture, Philosophical Transactions of the Royal Society B: Biological Sciences. 363 (**2007**) 659–666.

[7] The United Nations world water development report, 2017: Wastewater: the untapped resource, J Chem Inf Model. 53 (**2017**) 1689–1699.

[8] B.S. Rathi, P.S. Kumar, D.V.N. Vo, Critical review on hazardous pollutants in water environment: Occurrence, monitoring, fate, removal technologies and risk assessment, Science of The Total Environment. 797 (**2021**) 149134.

[9] A. Tkaczyk, K. Mitrowska, A. Posyniak, Synthetic organic dyes as contaminants of the aquatic environment and their implications for ecosystems: A review, Science of The Total Environment. 717 (**2020**) 137222.

[10] K. Maheshwari, M. Agrawal, A.B. Gupta, Dye Pollution in Water and Wastewater, (**2021**) 1–25.

[11] R. Al-Tohamy, S.S. Ali, F. Li, K.M. Okasha, Y.A.G. Mahmoud, T. Elsamahy, H. Jiao, Y. Fu, J. Sun, A critical review on the treatment of dye-containing wastewater: Ecotoxicological and health concerns of textile dyes and possible remediation approaches for environmental safety, Ecotoxicol Environ Saf. 231 (**2022**) 113160.

[12] M. Bilal, A.R. Bagheri, P. Bhatt, S. Chen, Environmental occurrence, toxicity concerns, and remediation of recalcitrant nitroaromatic compounds, J Environ Manage. 291 (**2021**) 112685.

[13] Z. Xiong, H. Zhang, W. Zhang, B. Lai, G. Yao, Removal of nitrophenols and their derivatives by chemical redox: A review, Chemical Engineering Journal. 359 (**2019**) 13–31.

[14] F.M.M. Tchieno, I.K. Tonle, P-Nitrophenol determination and remediation: An overview, Rev Anal Chem. 37 (**2018**).

[15] G. Crini, E. Lichtfouse, Advantages and disadvantages of techniques used for wastewater treatment, Environ Chem Lett. 17 (**2019**) 145–155.

[16] N. Dasgupta, S. Ranjan, E. Lichtfouse, eds., Environmental Nanotechnology Volume 4, 32 (**2020**).

[17] S. Sikiru, O.J.A. Abiodun, Y.K. Sanusi, Y.A. Sikiru, H. Soleimani, N. Yekeen, A.B.A. Haslija, A comprehensive review on nanotechnology application in wastewater treatment a case study of metal-based using green synthesis, J Environ Chem Eng. 10 (**2022**) 108065.

[18] S.M. Albukhari, M. Ismail, K. Akhtar, E.Y. Danish, Catalytic reduction of nitrophenols and dyes using silver nanoparticles @ cellulose polymer paper for the resolution of waste water treatment challenges, Colloids Surf A Physicochem Eng Asp. 577 (**2019**) 548–561.

[19] G. Liao, Y. Gong, L. Zhong, J. Fang, L. Zhang, Z. Xu, H. Gao, B. Fang, Unlocking the door to highly efficient Ag-based nanoparticles catalysts for NaBH4-assisted nitrophenol reduction, Nano Res. 12 (**2019**) 2407–2436.

[20] Y. Wang, J. Niu, Z. Zhang, X. Long, Photocatalytic Degradation of Organic Pollutants in Water, Progress in Chemistry. 20 (**2013**) 1621–1627.

[21] N. Serpone, Relative photonic efficiencies and quantum yields in heterogeneous photocatalysis, J Photochem Photobiol A Chem. 104 (**1997**) 1–12.

[22] D. Zhu, Q. Zhou, Action and mechanism of semiconductor photocatalysis on degradation of organic pollutants in water treatment: A review, Environ Nanotechnol Monit Manag. 12 (**2019**) 100255.

[23] M. Nemiwal, T.C. Zhang, D. Kumar, Recent progress in g-C3N4, TiO2 and ZnO based photocatalysts for dye degradation: Strategies to improve photocatalytic activity, Science of The Total Environment. 767 (**2021**) 144896.

[24] S. Arsalane, M. Ziyad, G. Coudurier, J.C. Védrine, Silver-Cluster Formation on AgZr2(PO4)3and Catalytic Decomposition of Butan-2-ol, J Catal. 159 (**1996**) 162–169.

[25] M. Ziyad, S. Arsalane, M. Kacimi, G. Coudurier, J.M. Millet, J.C. Védrine, Behavior of silver-thorium phosphate AgTh2(PO4)3 in butan-2-ol conversion, Appl Catal A Gen. 147 (**1996**) 363–373.

[26] Y. Brik, M. Kacimi, F. Bozon-Verduraz, M. Ziyad, Characterization of active sites on AgHf2(PO4)3 in butan-2-ol conversion, Microporous and Mesoporous Materials. 43 (**2001**) 103–112.

[27] C. Yu, X. Chen, N. Li, Y. Zhang, S. Li, J. Chen, L. Yao, K. Lin, Y. Lai, X. Deng, Ag3PO4-based photocatalysts and their application in organic-polluted wastewater treatment, Environmental Science and Pollution Research. 29 (**2022**) 18423–18439.

[28] H. Xu, J. Xie, W. Jia, G. Wu, Y. Cao, The formation of visible light-driven Ag/Ag2O photocatalyst with excellent property of photocatalytic activity and photocorrosion inhibition, J Colloid Interface Sci. 516 (**2018**) 511–521.

[29] H. Sun, P. Qin, Z. Wu, C. Liao, J. Guo, S. Luo, Y. Chai, Visible light-driven photocatalytic degradation of organic pollutants by a novel Ag3VO4/Ag2CO3 p–n heterojunction photocatalyst: Mechanistic insight and degradation pathways, J Alloys Compd. 834 (**2020**) 155211.

[30] J. Singh, S. Uma, Efficient photocatalytic degradation of organic compounds by ilmenite agSbO3under visible and UV light irradiation, Journal of Physical Chemistry C. 113 (**2009**) 12483–12488.

[31] N. Rajalakshmi, D. Barathi, S. Meyvel, P. Sathya, S-scheme Ag2CrO4/g-C3N4 photocatalyst for effective degradation of organic pollutants under visible light, Inorg Chem Commun. 132 (**2021**) 108849.

[32] X. Zou, Y. Dong, S. Li, J. Ke, Y. Cui, Facile anion exchange to construct uniform AgX (X = Cl, Br, I)/Ag2CrO4 NR hybrids for efficient visible light driven photocatalytic activity, Solar Energy. 169 (**2018**) 392–400.

[33] G. Meran, M. Siehlow, C. von Hirschhausen, Water Availability: A Hydrological View, Springer Water. (**2021**) 9–21.

[34] L. Petersen, M. Heynen, F. Pellicciotti, Freshwater Resources: Past, Present, Future, International Encyclopedia of Geography: People, the Earth, Environment and Technology. (**2017**) 1–11.

[35] Ajit, N.K. Gupta, Progresses in Solar Still Technology with Phase Change Material, IOP Conf Ser Mater Sci Eng. 1116 (**2021**) 012055.

[36] N. Mancosu, R.L. Snyder, G. Kyriakakis, D. Spano, Water Scarcity and Future Challenges for Food Production, Water 2015, Vol. 7, Pages 975-992. 7 (**2015**) 975–992.

[37] The United Nations world water development report 2018: nature-based solutions for water, UN Water Report. (**2018**) 154.

[38] R.S. Kookana, P. Drechsel, P. Jamwal, J. Vanderzalm, Urbanisation and emerging economies: Issues and potential solutions for water and food security, Science of The Total Environment. 732 (**2020**) 139057.

[39] G.W. Leeson, The Growth, Ageing and Urbanisation of our World, Journal of Population Ageing 2018 11:2. 11 (**2018**) 107–115.

[40] AR4 Climate Change 2007: Impacts, Adaptation, and Vulnerability — IPCC, (n.d.).

[41] N. Akhtar, M.I. Syakir Ishak, S.A. Bhawani, K. Umar, Various Natural and Anthropogenic Factors Responsible for Water Quality Degradation: A Review, Water 2021, Vol. 13, Page 2660. 13 (**2021**) 2660.

[42] L. Schweitzer, J. Noblet, Water Contamination and Pollution, Green Chemistry: An Inclusive Approach. (**2018**) 261–290.

[43] J. Lunn, R. Foxen, How much water do we really need?, Nutr Bull. 33 (**2008**) 336–342.

[44] B.J. Cisneros, Safe Sanitation in Low Economic Development Areas, Treatise on Water Science. 4 (**2011**) 147–200.

[45] P. Xie, Q. Yan, J. Xiong, H. Li, X. Ma, J. You, Point or non-point source: Toxicity evaluation using m-POCIS and zebrafish embryos in municipal sewage treatment plants and urban waterways, Environmental Pollution. 292 (**2022**) 118307.

[46] O. Thomas, M.F. Thomas, Industrial wastewater, UV-Visible Spectrophotometry of Waters and Soils. (**2022**) 385–416.

[47] T. Shahady, Agricultural water pollution, Water and Climate Change: Sustainable Development, Environmental and Policy Issues. (**2022**) 365–382.

[48] G. Crini, E. Lichtfouse, Wastewater Treatment: An Overview, (**2018**) 1–21.

[49] J.C.G. Sousa, A.R. Ribeiro, M.O. Barbosa, M.F.R. Pereira, A.M.T. Silva, A review on environmental monitoring of water organic pollutants identified by EU guidelines, J Hazard Mater. 344 (**2018**) 146–162.

[50] P.C. Lindholm-Lehto, J.S. Knuutinen, H.S.J. Ahkola, S.H. Herve, Refractory organic pollutants and toxicity in pulp and paper mill wastewaters, Environmental Science and Pollution Research. 22 (**2015**) 6473–6499.

[51] F. Lu, D. Astruc, Nanocatalysts and other nanomaterials for water remediation from organic pollutants, Coord Chem Rev. 408 (**2020**) 213180.

[52] G. Nagendrappa, Sir William Henry Perkin: The man and his "Mauve," Resonance. 15 (**2010**) 779–793.

[53] S. Benkhaya, S. M' rabet, A. El Harfi, A review on classifications, recent synthesis and applications of textile dyes, Inorg Chem Commun. 115 (**2020**) 107891.

[54] W. Zhang, L. Zhang, H. Zhao, B. Li, H. Ma, A two-dimensional cationic covalent organic framework membrane for selective molecular sieving, J Mater Chem A Mater. 6 (**2018**) 13331–13339.

[55] S. Mani, R.N. Bharagava, Textile Industry Wastewater : Environmental and Health Hazards and Treatment Approaches, Recent Advances in Environmental Management. (**2018**) 47–69.

[56] T.G. Choudhury, S. Gita, Impact of Textile Dyes Waste on Aquatic Environments and its Treatment, (**2017**).

[57] O. Sahu, N. Singh, Significance of bioadsorption process on textile industry wastewater, The Impact and Prospects of Green Chemistry for Textile Technology. (**2019**) 367–416.

[58] The Impact of Chemical Dyes on Our Waterways – Sustain by Kat, (n.d.).

[59] B. Lellis, C.Z. Fávaro-Polonio, J.A. Pamphile, J.C. Polonio, Effects of textile dyes on health and the environment and bioremediation potential of living organisms, Biotechnology Research and Innovation. 3 (**2019**) 275–290.

[60] M. Farhan Hanafi, N. Sapawe, A review on the water problem associate with organic pollutants derived from phenol, methyl orange, and remazol brilliant blue dyes, Mater Today Proc. 31 (**2020**) A141–A150.

[61] P.O. Oladoye, T.O. Ajiboye, E.O. Omotola, O.J. Oyewola, Methylene blue dye: Toxicity and potential elimination technology from wastewater, Results in Engineering. 16 (**2022**) 100678.

[62] X. Zhang, Y. man Lin, X. quan Shan, Z. liang Chen, Degradation of 2,4,6-trinitrotoluene (TNT) from explosive wastewater using nanoscale zero-valent iron, Chemical Engineering Journal. 158 (**2010**) 566–570.

[63] J. Tiwari, P. Tarale, S. Sivanesan, A. Bafana, Environmental persistence, hazard, and mitigation challenges of nitroaromatic compounds, Environ Sci Pollut Res Int. 26 (**2019**) 28650–28667.

[64] A. Balakrishnan, G.J. Gaware, M. Chinthala, Heterojunction photocatalysts for the removal of nitrophenol: A systematic review, Chemosphere. 310 (**2023**) 136853.

[65] R. Fatima, M.N. Afridi, IV. Kumar, J. Lee, I. Ali, K.H. Kim, J.O. Kim, Photocatalytic degradation performance of various types of modified TiO2 against nitrophenols in aqueous systems, J Clean Prod. 231 (**2019**) 899–912.

[66] R. Loos, B.M. Gawlik, G. Locoro, E. Rimaviciute, S. Contini, G. Bidoglio, EU-wide survey of polar organic persistent pollutants in European river waters, Environmental Pollution. 157 (**2009**) 561–568.

[67] M.F. Hanafi, N. Sapawe, A review on the current techniques and technologies of organic pollutants removal from water/wastewater, Mater Today Proc. 31 (**2020**) A158–A165.

[68] Y.H. Teow, K.C. Ho, S.R. Wickramasinghe, M.G. Jebur, Z.H. Chang, Integrated process technology for recycling and re-use of industrial and municipal wastewater: A review, Integrated Environmental Technologies for Wastewater Treatment and Sustainable Development. (**2022**) 49–80.

[69] V.K. Gupta, I. Ali, T.A. Saleh, A. Nayak, S. Agarwal, Chemical treatment technologies for waste-water recycling—an overview, RSC Adv. 2 (**2012**) 6380–6388.

[70] S. Roy, A. Garg, S. Garg, T.A. Tran, eds., Advanced Industrial Wastewater Treatment and Reclamation of Water, (**2022**).

[71] Uses of KMnO4, H2O2 and ClO2 in Wastewater Applications, (**2021**) 222–238.

[72] M. Wagner, D. Brumelis, R. Gehr, Disinfection of Wastewater by Hydrogen Peroxide or Peracetic Acid: Development of Procedures for Measurement of Residual Disinfectant and Application to a Physicochemically Treated Municipal Effluent, Water Environment Research. 74 (**2002**) 33–50.

[73] S. Ullah, M. Noman, K.S. Ali, M. Siddique, K. Sahak, S.K. Hashmi, H. Emiliya, F. Khan, Treatment of Industrial Wastewater (IWW) and Reuse through Advanced Oxidation Processes (AOPs): A Comprehensive Overview, 15 (**2021**) 4–14.

[74] Y. di Chen, X. Duan, X. Zhou, R. Wang, S. Wang, N. qi Ren, S.H. Ho, Advanced oxidation processes for water disinfection: Features, mechanisms and prospects, Chemical Engineering Journal. 409 (**2021**) 128207.

[75] Mu. Naushad, S. Rajendran, F. Gracia, eds., Advanced Nanostructured Materials for Environmental Remediation, 25 (**2019**).

[76] X. Qu, P.J.J. Alvarez, Q. Li, Applications of nanotechnology in water and wastewater treatment, Water Res. 47 (**2013**) 3931–3946.

[77] J. Theron, J.A. Walker, T.E. Cloete, Nanotechnology and Water Treatment: Applications and Emerging Opportunities, 34 (**2008**) 43–69.

[78] T.A. Saleh, Nanomaterials: Classification, properties, and environmental toxicities, Environ Technol Innov. 20 (**2020**) 101067.

[79] E. Roduner, Size matters: why nanomaterials are different, Chem Soc Rev. 35 (**2006**) 583–592.

[80] P.N. Sudha, K. Sangeetha, K. Vijayalakshmi, A. Barhoum, Nanomaterials history, classification, unique properties, production and market, Emerging Applications of Nanoparticles and Architectural Nanostructures: Current Prospects and Future Trends. (**2018**) 341–384.

[81] Z. Wang, T. Hu, R. Liang, M. Wei, Application of Zero-Dimensional Nanomaterials in Biosensing, Front Chem. 8 (**2020**) 320.

[82] M. Samykano, Progress in one-dimensional nanostructures, Mater Charact. 179 (**2021**) 111373.

[83] C. Tan, X. Cao, X.J. Wu, Q. He, J. Yang, X. Zhang, J. Chen, W. Zhao, S. Han, G.H. Nam, M. Sindoro, H. Zhang, Recent Advances in Ultrathin Two-Dimensional Nanomaterials, Chem Rev. 117 (**2017**) 6225–6331.

[84] J.N. Tiwari, R.N. Tiwari, K.S. Kim, Zero-dimensional, one-dimensional, two-dimensional and three-dimensional nanostructured materials for advanced electrochemical energy devices, Prog Mater Sci. 57 (**2012**) 724–803.

[85] High Resolution Imaging of Quantum Dots By Jared Fialkoff, (n.d.).

[86] S. Jadoun, R. Arif, N.K. Jangid, R.K. Meena, Green synthesis of nanoparticles using plant extracts: a review, Environ Chem Lett. 19 (**2021**) 355–374.

[87] X.H. Yang, H.T. Fu, K. Wong, X.C. Jiang, A.B. Yu, Hybrid Ag@TiO2 core-shell nanostructures with highly enhanced photocatalytic performance, Nanotechnology. 24 (**2013**).

[88] S. Wang, W. Xi, F. Cai, X. Zhao, Z. Xu, J. Qian, S. He, Three-Photon Luminescence of Gold Nanorods and Its Applications for High Contrast Tissue and Deep In Vivo Brain Imaging, Theranostics. 5 (**2015**) 251.

[89] A.J. Hassiba, M.E. El Zowalaty, T.J. Webster, A.M. Abdullah, G.K. Nasrallah, K.A. Khalil, A.S. Luyt, A.A. Elzatahry, Synthesis, characterization, and antimicrobial properties of novel double layer nanocomposite electrospun fibers for wound dressing applications, Int J Nanomedicine. 12 (**2017**) 2205–2213.

[90] A. Dobrzańska-Danikiewicz, D. Łukowiec, D. Cichocki, W. Wolany, Carbon nanotubes manufacturing using the CVD equipment against the background of other methods, Archives of Materials Science and Engineering. (**2013**).

[91] A. Shahzad, J. Chung, T.J. Lee, Y.H. Kim, S.H. Bhang, W.S. Kim, T. Yu, A Facile Room Temperature Synthesis of Large Silver Nanoplates with Low Cytotoxicity, ChemistrySelect. 3 (**2018**) 1801–1808.

[92] H.J. Cho, H. Kondo, K. Ishikawa, M. Sekine, M. Hiramatsu, M. Hori, Density control of carbon nanowalls grown by CH4/H2 plasma and their electrical properties, Carbon N Y. 68 (**2014**) 380–388.

[93] M. Wang, L. Fan, X. Wu, D. Tian, J. Cheng, Y. Qiu, H. Wu, B. Guan, N. Zhang, K. Sun, Y. Wang, Hierarchical mesoporous SnO2 nanosheets on carbon cloth toward enhancing the polysulfides redox for lithium–sulfur batteries, J Mater Chem A Mater. 5 (**2017**) 19613–19618.

[94] P.Y. Chang, K. Bindumadhavan, R.A. Doong, Size Effect of Ordered Mesoporous Carbon Nanospheres for Anodes in Li-Ion Battery, Nanomaterials 2015, Vol. 5, Pages 2348-2358. 5 (**2015**) 2348–2358.

[95] J. Zhao, M. Sun, Z. Liu, B. Quan, C. Gu, J. Li, Three Dimensional Hybrids of Vertical Graphene-nanosheet Sandwiched by Ag-nanoparticles for Enhanced Surface Selectively Catalytic Reactions, Scientific Reports 2015 5:1. 5 (**2015**) 1–11.

[96] H.I. Abdulgafour, Z. Hassan, N. Al-Hardan, F.K. Yam, Growth of zinc oxide nanoflowers by thermal evaporation method, Physica B Condens Matter. 405 (**2010**) 2570–2572.

[97] M.J. Ndolomingo, N. Bingwa, R. Meijboom, Review of supported metal nanoparticles: synthesis methodologies, advantages and application as catalysts, Journal of Materials Science 2020 55:15. 55 (**2020**) 6195–6241.

[98] T. Pradeep, Anshup, Noble metal nanoparticles for water purification: A critical review, Thin Solid Films. 517 (**2009**) 6441–6478.

[99] M. Naz, A. Rafiq, M. Ikram, A. Haider, S.O.A. Ahmad, J. Haider, S. Naz, Elimination of dyes by catalytic reduction in the absence of light: A review, Journal of Materials Science 2021 56:28. 56 (**2021**) 15572–15608.

[100] S. Sankar Sana, R. Haldhar, J. Parameswaranpillai, M. Chavali, S.C. Kim, Silver nanoparticles-based composite for dye removal: A comprehensive review, Cleaner Materials. 6 (**2022**) 100161.

[101] A. Syafiuddin, Salmiati, M.R. Salim, A. Beng Hong Kueh, T. Hadibarata, H. Nur, A Review of Silver Nanoparticles: Research Trends, Global Consumption, Synthesis, Properties, and Future Challenges, Journal of the Chinese Chemical Society. 64 (**2017**) 732–756.

[102] O. Pryshchepa, P. Pomastowski, B. Buszewski, Silver nanoparticles: Synthesis, investigation techniques, and properties, Adv Colloid Interface Sci. 284 (**2020**) 102246.

[103] H. Wang, J. Lu, A Review on Particle Size Effect in Metal-Catalyzed Heterogeneous Reactions, Chin J Chem. 38 (**2020**) 1422–1444.

[104] K.K. Harish, IV. Nagasamy, B. Himangshu, K. Anuttam, Metallic Nanoparticle: A Review, Biomed J Sci &Tech Res. 4 (**2018**).

[105] F.T. Rabouw, C. de Mello Donega, Excited-State Dynamics in Colloidal Semiconductor Nanocrystals, Topics in Current Chemistry 2016 374:5. 374 (**2016**) 1–30.

[106] N. Pradhan, A. Pal, T. Pal, Silver nanoparticle catalyzed reduction of aromatic nitro compounds, Colloids Surf A Physicochem Eng Asp. 196 (**2002**) 247–257.

[107] G. Mie, Beiträge zur Optik trüber Medien, speziell kolloidaler Metallösungen, Ann Phys. 330 (**1908**) 377–445.

[108] M.R. Jones, K.D. Osberg, R.J. MacFarlane, M.R. Langille, C.A. Mirkin, Templated techniques for the synthesis and assembly of plasmonic nanostructures, Chem Rev. 111 (**2011**) 3736–3827.

[109] K.L. Kelly, E. Coronado, L.L. Zhao, G.C. Schatz, The optical properties of metal nanoparticles: The influence of size, shape, and dielectric environment, Journal of Physical Chemistry B. 107 (**2003**) 668–677.

[110] S. Linic, P. Christopher, D.B. Ingram, Plasmonic-metal nanostructures for efficient conversion of solar to chemical energy, Nat Mater. 10 (**2011**) 911–921.

[111] S. Peiris, J. McMurtrie, H.Y. Zhu, Metal nanoparticle photocatalysts: Emerging processes for green organic synthesis, Catal Sci Technol. 6 (**2016**) 320–338.

[112] J.C. Scaiano, K.G. Stamplecoskie, G.L. Hallett-Tapley, Photochemical Norrish type I reaction as a tool for metal nanoparticle synthesis: importance of proton coupled electron transfer, Chemical Communications. 48 (**2012**) 4798–4808.

[113] P.G. Jamkhande, N.W. Ghule, A.H. Bamer, M.G. Kalaskar, Metal nanoparticles synthesis: An overview on methods of preparation, advantages and disadvantages, and applications, J Drug Deliv Sci Technol. 53 (**2019**) 101174.

[114] H. Lu, S.Y. Tang, G. Yun, H. Li, Y. Zhang, R. Qiao, W. Li, Modular and Integrated Systems for Nanoparticle and Microparticle Synthesis—A Review, Biosensors (Basel). 10 (**2020**).

[115] K.M.M. Abou El-Nour, A. Eftaiha, A. Al-Warthan, R.A.A. Ammar, Synthesis and applications of silver nanoparticles, Arabian Journal of Chemistry. 3 (**2010**) 135–140.

[116] A.A. Yaqoob, K. Umar, M.N.M. Ibrahim, Silver nanoparticles: various methods of synthesis, size affecting factors and their potential applications–a review, Applied Nanoscience (Switzerland). 10 (**2020**) 1369–1378.

[117] A. Van Hoonacker, P. Englebienne, Revisiting Silver Nanoparticle Chemical Synthesis and Stability by Optical Spectroscopy, Curr Nanosci. 2 (**2006**) 359–371.

[118] T. Bai, P. Lu, Z. Guo, L. Xiang, L. Liu, A simple approach towards citrate-stabilized Ag nanoparticles with widely tunable sizes, Colloids Surf A Physicochem Eng Asp. 540 (**2018**) 143–149.

[119] A. Zielińska, E. Skwarek, A. Zaleska, M. Gazda, J. Hupka, Preparation of silver nanoparticles with controlled particle size, Procedia Chem. 1 (**2009**) 1560–1566.

[120] J.P. Oliveira, A.R. Prado, W.J. Keijok, M.R.N. Ribeiro, M.J. Pontes, B. IV. Nogueira, M.C.C. Guimarães, A helpful method for controlled synthesis of monodisperse gold nanoparticles through response surface modeling, Arabian Journal of Chemistry. 13 (**2020**) 216–226.

[121] P.C. Lee, D. Meisel, Adsorption and surface-enhanced Raman of dyes on silver and gold sols, Journal of Physical Chemistry. 86 (**1982**) 3391–3395.

[122] J. Turkevich, P.C. Stevenson, J. Hillier, A study of the nucleation and growth processes in the synthesis of colloidal gold, Discuss Faraday Soc. 11 (**1951**) 55–75.

[123] N.L. Pacioni, C.D. Borsarelli, IV. Rey, A. IV. Veglia, Synthetic Routes for the Preparation of Silver Nanoparticles: A Mechanistic Perspective, Engineering Materials. (**2015**) 13–46.

[124] Z.S. Pillai, P. IV. Kamat, What Factors Control the Size and Shape of Silver Nanoparticles in the Citrate Ion Reduction Method?, Journal of Physical Chemistry B. 108 (**2003**) 945–951.

[125] Y. Qin, X. Ji, J. Jing, H. Liu, H. Wu, W. Yang, Size control over spherical silver nanoparticles by ascorbic acid reduction, Colloids Surf A Physicochem Eng Asp. 372 (**2010**) 172–176.

[126] K.C. Song, S.M. Lee, T.S. Park, B.S. Lee, Preparation of colloidal silver nanoparticles by chemical reduction method, Korean Journal of Chemical Engineering. 26 (**2009**) 153–155.

[127] K.J. Hartlieb, M. Saunders, R.J.J. Jachuck, C.L. Raston, Continuous flow synthesis of small silver nanoparticles involving hydrogen as the reducing agent, Green Chemistry. 12 (**2010**) 1012–1017.

[128] M.A. Pérez, R. Moiraghi, E.A. Coronado, IV.A. Macagno, Hydroquinone synthesis of silver nanoparticles: A simple model reaction to understand the factors that determine their nucleation and growth, Cryst Growth Des. 8 (**2008**) 1377–1383.

[129] V. Gurusamy, R. Krishnamoorthy, B. Gopal, IV. Veeraravagan, Periyasamy, Systematic investigation on hydrazine hydrate assisted reduction of silver nanoparticles and its antibacterial properties, 47 (**2016**) 761–767.

[130] I. Pastoriza-Santos, L.M. Liz-Marzán, Synthesis of Silver Nanoprisms in DMF, Nano Lett. 2 (**2002**) 903–905.

[131] Y. Sun, Y. Xia, Shape-Controlled Synthesis of Gold and Silver Nanoparticles, Science (1979). 298 (**2002**) 2176–2179.

[132] J.O. Edwards, G.C. Morrison, IV.F. Ross, J.W. Schultz, The Structure of the Aqueous Borate Ion, J Am Chem Soc. 77 (**1955**) 266–268.

[133] S. Agnihotri, S. Mukherji, S. Mukherji, Size-controlled silver nanoparticles synthesized over the range 5–100 nm using the same protocol and their antibacterial efficacy, RSC Adv. 4 (**2013**) 3974–3983.

[134] J. Polte, X. Tuaev, M. Wuithschick, A. Fischer, A.F. Thuenemann, K. Rademann, R. Kraehnert, F. Emmerling, Formation mechanism of colloidal silver nanoparticles: Analogies and differences to the growth of gold nanoparticles, ACS Nano. 6 (**2012**) 5791–5802.

[135] S.D. Solomon, M. Bahadory, A. IV. Jeyarajasingam, S.A. Rutkowsky, C. Boritz, L. Mulfinger, Synthesis and Study of Silver Nanoparticles, J Chem Educ. 84 (**2007**) 322–325.

[136] S.A. Khan, M. Jain, A. Pandey, K.K. Pant, Z.M. Ziora, M.A.T. Blaskovich, N.P. Shetti, T.M. Aminabhavi, Leveraging the potential of silver nanoparticles-based materials towards sustainable water treatment, J Environ Manage. 319 (**2022**) 115675.

[137] H.L. Cao, H.B. Huang, Z. Chen, B. Karadeniz, J. Lü, R. Cao, Ultrafine Silver Nanoparticles Supported on a Conjugated Microporous Polymer as High-Performance Nanocatalysts for Nitrophenol Reduction, ACS Appl Mater Interfaces. 9 (**2017**) 5231–5236.

[138] P. Sudhakar, H. Soni, Catalytic reduction of Nitrophenols using silver nanoparticles-supported activated carbon derived from agro-waste, J Environ Chem Eng. 6 (**2018**) 28–36.

[139] S. Liu, Y. Guo, S. Yi, S. Yan, C. Ouyang, F. Deng, C. Li, G. Liao, Q. Li, Facile synthesis of pure silicon zeolite-confined silver nanoparticles and their catalytic activity for the reduction of 4-nitrophenol and methylene blue, Sep Purif Technol. 307 (**2023**) 122727.

[140] M. Zienkiewicz-Strzałka, S. Pasieczna-Patkowska, M. Kozak, S. Pikus, Silver nanoparticles incorporated onto ordered mesoporous silica from Tollen's reagent, Appl Surf Sci. 266 (**2013**) 337–343.

[141] A.P. Osonio, M.R. Vasquez, Plasma-assisted reduction of silver ions impregnated into a natural zeolite framework, Appl Surf Sci. 432 (**2018**) 156–162.

[142] P.H. Keijzer, B. Donoeva, K.P. de Jong, P.E. de Jongh, Supported silver catalysts prepared via melt infiltration: Synthesis, characterization and performance in selective hydrogenation, Catal Today. 375 (**2021**) 393–400.

[143] M.A. Behnajady, H. Eskandarloo, Silver and copper co-impregnated onto TiO2-P25 nanoparticles and its photocatalytic activity, Chemical Engineering Journal. 228 (**2013**) 1207–1213.

[144] P.M. More, D.L. Nguyen, P. Granger, C. Dujardin, M.K. Dongare, S.B. Umbarkar, Activation by pretreatment of Ag–Au/Al2O3 bimetallic catalyst to improve low temperature HC-SCR of NOx for lean burn engine exhaust, Appl Catal B. 174–175 (**2015**) 145–156.

[145] H. Hofmeister, P.-T. Miclea, M. Steen, W. Mörke, H. Drevs, Structural characteristics of oxide nanosphere supported metal nanoparticles, Topics in Catalysis 2007 46:1. 46 (**2007**) 11–21.

[146] D.S. Ahmed, M.R. Mohammed, M.K.A. Mohammed, Synthesis of Multi-walled Carbon Nanotubes Decorated with ZnO/Ag Nanoparticles by Co-precipitation Method, Nanoscience & Nanotechnology-Asia. 10 (**2020**) 127–133.

[147] Z. Guerra-Que, G. Torres-Torres, H. Pérez-Vidal, I. Cuauhtémoc-López, A. Espinosa de Los Monteros, J.N. Beltramini, D.M. Frías-Márquez, Silver nanoparticles supported on zirconia–ceria for the catalytic wet air oxidation of methyl tert -butyl ether, RSC Adv. 7 (**2017**) 3599–3610.

[148] B. Baruah, G.J. Gabriel, M.J. Akbashev, M.E. Booher, Facile synthesis of silver nanoparticles stabilized by cationic polynorbornenes and their catalytic activity in 4-nitrophenol reduction, Langmuir. 29 (**2013**) 4225–4234.

[149] X. Du, L. Shi, J. Pang, H. Zheng, J. Shi, M. Zhang, Fabrication of superwetting and antimicrobial wood-based mesoporous composite decorated with silver nanoparticles for purifying the polluted-water with oils, dyes and bacteria, J Environ Chem Eng. 10 (**2022**) 107152.

[150] M. Hu, X. Yan, X. Hu, R. Feng, M. Zhou, Synthesis of silver decorated silica nanoparticles with rough surfaces as adsorbent and catalyst for methylene blue removal, J Solgel Sci Technol. 89 (**2019**) 754–763.

[151] A. Taratayko, Y. Larichev, IV. Zaikovskii, N. Mikheeva, G. Mamontov, Ag–CeO2/SBA-15 composite prepared from Pluronic P123@SBA-15 hybrid as catalyst for room-temperature reduction of 4-nitrophenol, Catal Today. 375 (**2021**) 576–584.

[152] N.M. Dat, P.N.B. Long, D.C.U. Nhi, N.N. Minh, L.M. Duy, L.N. Quan, H.M. Nam, M.T. Phong, N.H. Hieu, Synthesis of silver/reduced graphene oxide for antibacterial activity and catalytic reduction of organic dyes, Synth Met. 260 (**2020**) 116260.

[153] M. Amir, S. Güner, A. Yıldız, A. Baykal, Magneto-optical and catalytic properties of Fe3O4@HA@Ag magnetic nanocomposite, J Magn Magn Mater. 421 (**2017**) 462–471.

[154] S.A. Rasaki, C. Zhao, R. Wang, J. Wang, H. Jiang, M. Yang, Facile synthesis approach for preparation of robust and recyclable Ag/ZnO nanorods with high catalytic activity for 4-nitrophenol reduction, Mater Res Bull. 119 (**2019**) 110536.

[155] H. Wang, X. Li, X. Zhao, C. Li, X. Song, P. Zhang, P. Huo, A review on heterogeneous photocatalysis for environmental remediation: From semiconductors to modification strategies, Chinese Journal of Catalysis. 43 (**2022**) 178–214.

[156] J. Hong, K.H. Cho, IV. Presser, X. Su, Recent advances in wastewater treatment using semiconductor photocatalysts, Curr Opin Green Sustain Chem. 36 (**2022**) 100644.

[157] C. Song, Z. Wang, Z. Yin, D. Xiao, D. Ma, Principles and applications of photothermal catalysis, Chem Catalysis. 2 (**2022**) 52–83.

[158] A. Fujishima, K. Honda, Electrochemical Photolysis of Water at a Semiconductor Electrode, Nature 1972 238:5358. 238 (**1972**) 37–38.

[159] J.H. Carey, J. Lawrence, H.M. Tosine, Photodechlorination of PCB's in the presence of titanium dioxide in aqueous suspensions, Bull Environ Contam Toxicol. 16 (**1976**) 697–701.

[160] F.F. Wang, Q. Li, D.S. Xu, Recent Progress in Semiconductor-Based Nanocomposite Photocatalysts for Solar-to-Chemical Energy Conversion, Adv Energy Mater. 7 (**2017**) 1700529.

[161] K. Nakata, A. Fujishima, TiO2 photocatalysis: Design and applications, Journal of Photochemistry and Photobiology C: Photochemistry Reviews. 13 (**2012**) 169–189.

[162] S. Chakrabarti, B.K. Dutta, Photocatalytic degradation of model textile dyes in wastewater using ZnO as semiconductor catalyst, J Hazard Mater. 112 (**2004**) 269–278.

[163] D. Ayodhya, G. Veerabhadram, A review on recent advances in photodegradation of dyes using doped and heterojunction based semiconductor metal sulfide nanostructures for environmental protection, Mater Today Energy. 9 (**2018**) 83–113.

[164] G. Li, C. Yang, Q. He, J. Liu, Ag-based photocatalytic heterostructures: Construction and photocatalytic energy conversion application, J Environ Chem Eng. 10 (**2022**) 107374.

[165] K. Wetchakun, N. Wetchakun, S. Sakulsermsuk, An overview of solar/visible light-driven heterogeneous photocatalysis for water purification: TiO2- and ZnO-based photocatalysts used in suspension photoreactors, Journal of Industrial and Engineering Chemistry. 71 (**2019**) 19–49.

[166] S. Rehman, R. Ullah, A.M. Butt, N.D. Gohar, Strategies of making TiO2 and ZnO visible light active, J Hazard Mater. 170 (**2009**) 560–569.

[167] S.G. Kumar, K.S.R.K. Rao, Comparison of modification strategies towards enhanced charge carrier separation and photocatalytic degradation activity of metal oxide semiconductors (TiO2, WO3 and ZnO), Appl Surf Sci. 391 (**2017**) 124–148.

[168] N. Serpone, A. IV. Emeline, Semiconductor photocatalysis - Past, present, and future outlook, Journal of Physical Chemistry Letters. 3 (**2012**) 673–677.

[169] S. Dong, J. Feng, M. Fan, Y. Pi, L. Hu, X. Han, M. Liu, J. Sun, J. Sun, Recent developments in heterogeneous photocatalytic water treatment using visible light-responsive photocatalysts: a review, RSC Adv. 5 (**2015**) 14610–14630.

[170] J. Li, W. Fang, C. Yu, W. Zhou, L. Zhu, Y. Xie, Ag-based semiconductor photocatalysts in environmental purification, Appl Surf Sci. 358 (**2015**) 46–56.

[171] G. Li, Y. Wang, L. Mao, Recent progress in highly efficient Ag-based visible-light photocatalysts, RSC Adv. 4 (**2014**) 53649–53661.

[172] Y. Zhang, J. Liu, Y.S. Kang, X.L. Zhang, Silver based photocatalysts in emerging applications, Nanoscale. 14 (**2022**) 11909–11922.

[173] M.E. Khan, M.H. Cho, Surface Plasmon-Based Nanomaterials as Photocatalyst, (**2019**) 173–187.

[174] H. Dong, J. Sun, G. Chen, C. Li, Y. Hu, C. Lv, An advanced Ag-based photocatalyst Ag2Ta4O11 with outstanding activity, durability and universality for removing organic dyes, Physical Chemistry Chemical Physics. 16 (**2014**) 23915–23921.

[175] H. Dong, G. Chen, J. Sun, Y. Feng, C. Li, C. Lv, Stability, durability and regeneration ability of a novel Ag-based photocatalyst, Ag2Nb4O11, Chemical Communications. 50 (**2014**) 6596–6599.

[176] C. An, S. Wang, Y. Sun, Q. Zhang, J. Zhang, C. Wang, J. Fang, Plasmonic silver incorporated silver halides for efficient photocatalysis, J Mater Chem A Mater. 4 (**2016**) 4336–4352.

[177] P. Wang, B. Huang, X. Qin, X. Zhang, Y. Dai, J. Wei, M.-H. Whangbo, P. Wang, B. Huang, X. Qin, X. Zhang, J. Wei, Y. Dai, M. Whangbo, Ag@AgCl: A Highly Efficient and Stable Photocatalyst Active under Visible Light**, Angew. Chem. Int. Ed. 47 (**2008**) 1–4.

[178] N. Kakuta, N. Goto, H. Ohkita, T. Mizushima, Silver Bromide as a Photocatalyst for Hydrogen Generation from CH3OH/H2O Solution, Journal of Physical Chemistry B. 103 (**1999**) 5917–5919.

[179] Q. Xiao, E. Jaatinen, H. Zhu, Direct Photocatalysis for Organic Synthesis by Using Plasmonic-Metal Nanoparticles Irradiated with Visible Light, Chem Asian J. 9 (**2014**) 3046–3064.

[180] M. Rehan, A. Barhoum, T.A. Khattab, L. Gätjen, R. Wilken, Colored, photocatalytic, antimicrobial and UV-protected viscose fibers decorated with Ag/Ag2CO3 and Ag/Ag3PO4 nanoparticles, Cellulose. 26 (**2019**) 5437–5453.

[181] M.R. Khan, T.W. Chuan, A. Yousuf, M.N.K. Chowdhury, C.K. Cheng, Schottky barrier and surface plasmonic resonance phenomena towards the photocatalytic reaction: Study of their mechanisms to enhance photocatalytic activity, Catal Sci Technol. 5 (**2015**) 2522–2531.

[182] T.G.U. Ghobadi, A. Ghobadi, E. Ozbay, F. Karadas, Strategies for Plasmonic Hot-Electron-Driven Photoelectrochemical Water Splitting, ChemPhotoChem. 2 (**2018**) 161–182.

[183] W. Hou, Z. Liu, P. Pavaskar, W.H. Hung, S.B. Cronin, Plasmonic enhancement of photocatalytic decomposition of methyl orange under visible light, J Catal. 277 (**2011**) 149–153.

[184] P. Christopher, D.B. Ingram, S. Linic, Enhancing photochemical activity of semiconductor nanoparticles with optically active Ag nanostructures: Photochemistry mediated by Ag surface plasmons, Journal of Physical Chemistry C. 114 (**2010**) 9173–9177.

[185] J.B. Lee, S. Choi, J. Kim, Y.S. Nam, Plasmonically-assisted nanoarchitectures for solar water splitting: Obstacles and breakthroughs, Nano Today. 16 (**2017**) 61–81.

[186] P.K. Jain, X. Huang, I.H. El-Sayed, M.A. El-Sayed, Noble metals on the nanoscale: Optical and photothermal properties and some applications in imaging, sensing, biology, and medicine, Acc Chem Res. 41 (**2008**) 1578–1586.

[187] A. Kahn, Fermi level, work function and vacuum level, Mater Horiz. 3 (**2015**) 7–10.

[188] K.C. Kao, Charge Carrier Injection from Electrical Contacts, Dielectric Phenomena in Solids. (**2004**) 327–380.

[189] M.J. Fakharian-Qomi, A. Sadeghzadeh-Attar, Template Based Synthesis of Plasmonic Ag-modified TiO2/SnO2 Nanotubes with Enhanced Photostability for Efficient Visible-Light Photocatalytic H2 Evolution and RhB Degradation, ChemistrySelect. 5 (**2020**) 6001–6010.

[190] Z. Zhang, J.T. Yates, Band bending in semiconductors: Chemical and physical consequences at surfaces and interfaces, Chem Rev. 112 (**2012**) 5520–5551.

[191] X. Wang, S. Li, H. Yu, J. Yu, S. Liu, Ag2O as a New Visible-Light Photocatalyst: Self-Stability and High Photocatalytic Activity, Chemistry – A European Journal. 17 (**2011**) 7777–7780.

[192] S. Liang, D. Zhang, X. Pu, X. Yao, R. Han, J. Yin, X. Ren, A novel Ag2O/g-C3N4 p-n heterojunction photocatalysts with enhanced visible and near-infrared light activity, Sep Purif Technol. 210 (**2019**) 786–797.

[193] J. Li, F. Liu, Y. Li, Fabrication of an Ag/Ag2MoO4 plasmonic photocatalyst with enhanced photocatalytic performance for the degradation of ciprofloxacin, New Journal of Chemistry. 42 (**2018**) 12054–12061.

[194] L. Kuai, B. Geng, X. Chen, Y. Zhao, Y. Luo, Facile subsequently light-induced route to highly efficient and stable sunlight-driven Ag-AgBr plasmonic photocatalyst, Langmuir. 26 (**2010**) 18723–18727.

[195] Y. Bi, H. Hu, S. Ouyang, Z. Jiao, G. Lu, J. Ye, Selective growth of metallic Ag nanocrystals on Ag3PO4 submicro-cubes for photocatalytic applications, Chemistry. 18 (**2012**) 14272–14275.

[196] J. Hu, H. Xu, S. Wang, W. Jia, Y. Cao, In-situ solid-state synthesis and regulation of Ag2O/Ag2CO3 heterojunctions with promoted visible-light driven photocatalytic decomposition for organic pollutant, Sep Purif Technol. 226 (**2019**) 95–108.

[197] M. Šljukić, B. Matković, B. Prodić, S. Ščavnićar, Preparation and Crystallographic Data of Phosphates with Common Formula M1M~v (P04)3 (M 1 = Li, Na, K, Rb, Cs; M 1v= Zr, Hf), Croatica Chemica Acta. 39 (**1967**) 145–148.

[198] L.-O. Hagman, P. Kierkegaard, P. Karvonen, A.I. Virtanen, J. Paasivirta, The Crystal Structure of NaM2IV(PO4)3; MeIV = Ge, Ti, Zr., Acta Chem Scand. 22 (**1968**) 1822–1832.

[199] J.B. Goodenough, H.Y.P. Hong, J.A. Kafalas, Fast Na+-ion transport in skeleton structures, Mater Res Bull. 11 (**1976**) 203–220.

[200] N. Anantharamulu, K. Koteswara Rao, G. Rambabu, B. Vijaya Kumar, IV. Radha, M. Vithal, A wide-ranging review on Nasicon type materials, Journal of Materials Science 2011 46:9. 46 (**2011**) 2821–2837.

[201] M. Avdeev, Crystal Chemistry of NaSICONs: Ideal Framework, Distortion, and Connection to Properties, Chemistry of Materials. 33 (**2021**) 7620–7632.

[202] H. Yang, N. Wu, Ionic conductivity and ion transport mechanisms of solid-state lithium-ion battery electrolytes: A review, Energy Sci Eng. 10 (**2022**) 1643–1671.

[203] R. Rajagopalan, Z. Zhang, Y. Tang, C. Jia, X. Ji, H. Wang, Understanding crystal structures, ion diffusion mechanisms and sodium storage behaviors of NASICON materials, Energy Storage Mater. 34 (**2021**) 171–193.

[204] M. Chen, W. Hua, J. Xiao, D. Cortie, W. Chen, E. Wang, Z. Hu, Q. Gu, X. Wang, S. Indris, S.L. Chou, S.X. Dou, NASICON-type air-stable and all-climate cathode for sodium-ion batteries with low cost and high-power density, Nat Commun. 10 (**2019**).

[205] L. Zhang, Y. Liu, Y. You, A. Vinu, L. Mai, C. Ya You, NASICONs-type solid-state electrolytes: The history, physicochemical properties, and challenges, Interdisciplinary Materials. 2 (**2023**) 91–110.

[206] Y.B. Rao, K.K. Bharathi, L.N. Patro, Review on the synthesis and doping strategies in enhancing the Na ion conductivity of Na3Zr2Si2PO12 (NASICON) based solid electrolytes, Solid State Ion. 366–367 (**2021**) 115671.

[207] S.K. Pal, R. Saha, G. Vijay Kumar, S. Omar, Designing High Ionic Conducting NASICON-type Na Solid-Electrolytes for Na-Ion Batteries, J. Phys. Chem. C. 124 (**2020**) 0.

[208] C. Li, R. Li, K. Liu, R. Si, Z. Zhang, Y.-S. Hu, NaSICON: A promising solid electrolyte for solid-state sodium batteries, Interdisciplinary Materials. 1 (**2022**) 396–416.

[209] N. IV. Dorofeeva, O. IV. Vodyankina, O.S. Pavlova, G. IV. Mamontov, Synthesis of mixed zirconium-silver phosphates and formation of active catalyst surface for the ethylene glycol oxidation process, Stud Surf Sci Catal. 175 (**2010**) 759–762.

[210] Z. Wei, Z. Zhang, N. Chen, G. Chen, C. Wang, F. Du, In Situ Electrochemical Coating Mechanism of NASICON-Structured AgTi2(PO4)3 for Sodium-Ion Batteries, ACS Appl Mater Interfaces. 12 (**2020**) 5932–5938.

[211] A. Serghini, R. Brochu, M. Ziyad, M. Loukah, J.C. Védrine, Behaviour of copper–zirconium nasicon-type phosphate, CuIZr2(PO4)3, in the decomposition of isopropyl alcohol, Journal of the Chemical Society, Faraday Transactions. 87 (**1991**) 2487–2491.

[212] S. Arsalane, M. Kacimi, M. Ziyad, G. Coudurier, J.C. Védrine, Behaviour of copper-thorium phosphate CuTh2(PO4)3 in butan-2-ol conversion, Appl Catal A Gen. 114 (**1994**) 243–256.

[213] I.Y. Pinus, T.O. Bok, A.B. Yaroslavtsev, Synthesis and properties of AgTi 2(PO 4) 3-based NASICON-type phosphates doped with Nb 5+, Zr 4+, and Ga 3+, Inorganic Materials. 46 (**2010**) 412–417.

[214] N.W. Gregory, Elements of X-Ray Diffraction, J Am Chem Soc. 79 (**1957**) 1773–1774.

[215] P. Atkins, T. Overton, Shriver and Atkins' inorganic chemistry, (**2010**).

[216] A.L. Patterson, The Scherrer Formula for X-Ray Particle Size Determination, Physical Review. 56 (**1939**) 978.

[217] H.M. Rietveld, IUCr, A profile refinement method for nuclear and magnetic structures, Urn:Issn:0021-8898. 2 (**1969**) 65–71.

[218] G. Will, Powder diffraction: The rietveld method and the two stage method to determine and refine crystal structures from powder diffraction data, Powder Diffraction: The Rietveld Method and the Two Stage Method to Determine and Refine Crystal Structures from Powder Diffraction Data. (**2006**) 1–224.

[219] P. Paufler, R. A. Young (ed.). The Rietveld Method. International Union of Crystallography. Oxford University Press, (1993) 298 p. ISBN 0–19–855577–6, Crystal Research and Technology. 30 (**1995**) 494–494.

[220] B.H. Toby, R factors in Rietveld analysis: How good is good enough?, Powder Diffr. 21 (**2006**) 67–70.

[221] R.J. Hill, C.J. Howard, Quantitative phase analysis from neutron powder diffraction data using the Rietveld method, Urn:Issn:0021-8898. 20 (**1987**) 467–474.

[222] J. Rodríguez-Carvajal, An introduction to the program FullProf (2001), (n.d.).

[223] A.A. Ismail, F.R. van de Voort, J. Sedman, Chapter 4 Fourier transform infrared spectroscopy: Principles and applications, Techniques and Instrumentation in Analytical Chemistry. 18 (**1997**) 93–139.

[224] A. Subramanian, L. Rodriguez-Saona, Fourier Transform Infrared (FTIR) Spectroscopy, Infrared Spectroscopy for Food Quality Analysis and Control. (**2009**) 145–178.

[225] J.R. Ferraro, K. Nakamoto, C.W. Brown, Introductory Raman Spectroscopy: Second Edition, Introductory Raman Spectroscopy: Second Edition. (**2003**) 1–434.

[226] T. Rochow, P. Tucker, Introduction to microscopy by means of light, electrons, X rays, or acoustics, (**1994**).

[227] A. Ul-Hamid, A Beginners' Guide to Scanning Electron Microscopy, A Beginners' Guide to Scanning Electron Microscopy. (**2018**).

[228] P. Van der Heide, X-ray photoelectron spectroscopy: an introduction to principles and practices, (**2011**).

[229] J. Lynch, Physico-chemical analysis of industrial catalysts: a practical guide to characterisation, (**2003**).

[230] J.R. Rumble, D.M. Bickham, C.J. Powell, The NIST x-ray photoelectron spectroscopy database, Surface and Interface Analysis. 19 (**1992**) 241–246.

[231] P. Makuła, M. Pacia, W. Macyk, How To Correctly Determine the Band Gap Energy of Modified Semiconductor Photocatalysts Based on UV-Vis Spectra, Journal of Physical Chemistry Letters. 9 (**2018**) 6814–6817.

[232] J. Tauc, R. Grigorovici, A. Vancu, Optical Properties and Electronic Structure of Amorphous Germanium, Physica Status Solidi (b). 15 (**1966**) 627–637.

[233] E.A. Davis, N.F. Mott, Conduction in non-crystalline systems IV. Conductivity, optical absorption and photoconductivity in amorphous semiconductors, 22 (**2006**) 903–922.

[234] D.F. Swineharf, E. The, B.-L. Law, The Beer-Lambert law, J Chem Educ. 39 (**1962**) 333–335.

[235] P. Atkins, J. De Paula, J. Keeler, Atkins' physical chemistry, (**2014**).

[236] M.O. Steinhauser, S. Hiermaier, A Review of Computational Methods in Materials Science: Examples from Shock-Wave and Polymer Physics, Int J Mol Sci. 10 (**2009**) 5135.

[237] E. Schrödinger, An Undulatory Theory of the Mechanics of Atoms and Molecules, Physical Review. 28 (**1926**) 1049.

[238] M. Born, R. Oppenheimer, Zur Quantentheorie der Molekeln, Ann Phys. 389 (**1927**) 457–484.

[239] D.R. Hartree, The Wave Mechanics of an Atom with a Non-Coulomb Central Field. Part I. Theory and Methods, Mathematical Proceedings of the Cambridge Philosophical Society. 24 (**1928**) 89–110.

[240] D.R. Hartree, The Wave Mechanics of an Atom with a Non-Coulomb Central Field. Part I. Some Results and Discussion, Mathematical Proceedings of the Cambridge Philosophical Society. 24 (**1928**) 111–132.

[241] D.R. Hartree, The Wave Mechanics of an Atom with a non-Coulomb Central Field. Part II. Term Values and Intensities in Series in Optical Spectra, Mathematical Proceedings of the Cambridge Philosophical Society. 24 (**1928**) 426–437.

[242] D.R. Hartree, The Wave Mechanics of an Atom with a Non-Coulomb Central Field. Part III. Further Results relating to Terms of the Optical Spectrum, Mathematical Proceedings of the Cambridge Philosophical Society. 25 (**1929**) 310–314.

[243] W. Pauli, Über den Zusammenhang des Abschlusses der Elektronengruppen im Atom mit der Komplexstruktur der Spektren, Zeitschrift Für Physik. 31 (**1925**) 765–783.

[244] V. Fock, Näherungsmethode zur Lösung des quantenmechanischen Mehrkörperproblems, Zeitschrift Für Physik. 61 (**1930**) 126–148.

[245] J.C. Slater, The Normal State of Helium, Physical Review. 32 (**1928**) 349.

[246] P. Hohenberg, W. Kohn, Inhomogeneous electron gas, Physical Review. 136 (**1964**) B864.

[247] W. Kohn, L.J. Sham, Self-consistent equations including exchange and correlation effects, Physical Review. 140 (**1965**) A1133.

[248] P.A.M. Dirac, Note on Exchange Phenomena in the Thomas Atom, Mathematical Proceedings of the Cambridge Philosophical Society. 26 (**1930**) 376–385.

[249] D.M. Ceperley, B.J. Alder, Ground State of the Electron Gas by a Stochastic Method, Phys Rev Lett. 45 (**1980**) 566.

[250] J.P. Perdew, A. Zunger, Self-interaction correction to density-functional approximations for many-electron systems, Phys Rev B. 23 (**1981**) 5048.

[251] J.P. Perdew, Y. Wang, Accurate and simple analytic representation of the electron-gas correlation energy, Phys Rev B. 45 (**1992**) 13244.

[252] S.H. Vosko, L. Wilk, M. Nusair, Accurate spin-dependent electron liquid correlation energies for local spin density calculations: a critical analysis, Can J Phys. 58 (**1980**) 1200–1211.

[253] D.C. Langreth, M.J. Mehl, Beyond the local-density approximation in calculations of ground-state electronic properties, Phys Rev B. 28 (**1983**) 1809.

[254] A.D. Becke, Density-functional exchange-energy approximation with correct asymptotic behavior, Phys Rev A (Coll Park). 38 (**1988**) 3098.

[255] J.P. Perdew, J.A. Chevary, S.H. Vosko, K.A. Jackson, M.R. Pederson, D.J. Singh, C. Fiolhais, Atoms, molecules, solids, and surfaces: Applications of the generalized gradient approximation for exchange and correlation, Phys Rev B. 46 (**1992**) 6671.

[256] J.P. Perdew, K. Burke, M. Ernzerhof, Generalized Gradient Approximation Made Simple, Phys Rev Lett. 77 (**1996**) 3865.

[257] E.J. Baerends, O. IV. Gritsenko, R. Van Meer, The Kohn–Sham gap, the fundamental gap and the optical gap: the physical meaning of occupied and virtual Kohn–Sham orbital energies, Physical Chemistry Chemical Physics. 15 (**2013**) 16408–16425.

[258] J.P. Perdew, M. Levy, Physical Content of the Exact Kohn-Sham Orbital Energies: Band Gaps and Derivative Discontinuities, Phys Rev Lett. 51 (**1983**) 1884.

[259] J.F. Janak, Proof that $\partial E \partial n_i = \varepsilon$ in density-functional theory, Phys Rev B. 18 (**1978**) 7165–7168.

[260] J.P. Perdew, R.G. Parr, M. Levy, J.L. Balduz, Density-Functional Theory for Fractional Particle Number: Derivative Discontinuities of the Energy, Phys Rev Lett. 49 (**1982**) 1691.

[261] M. Levy, J.P. Perdew, IV. Sahni, Exact differential equation for the density and ionization energy of a many-particle system, Phys Rev A (Coll Park). 30 (**1984**) 2745.

[262] J.P. Perdew, M. Levy, Comment on "Significance of the highest occupied Kohn-Sham eigenvalue," Phys Rev B. 56 (**1997**) 16021.

[263] A.D. Becke, Density-functional thermochemistry. II. The role of exact exchange, J Chem Phys. 98 (**1998**) 5648.

[264] C. Lee, W. Yang, R.G. Parr, Development of the Colle-Salvetti correlation-energy formula into a functional of the electron density, Phys Rev B. 37 (**1988**) 785.

[265] J.P. Perdew, M. Ernzerhof, K. Burke, Rationale for mixing exact exchange with density functional approximations, J Chem Phys. 105 (**1998**) 9982.

[266] J. Toulouse, F. Colonna, A. Savin, Long-range - Short-range separation of the electron-electron interaction in density-functional theory, Phys Rev A. 70 (**2004**) 062505.

[267] S. Refaely-Abramson, R. Baer, L. Kronik, Fundamental and excitation gaps in molecules of relevance for organic photovoltaics from an optimally tuned range-separated hybrid functional, Phys Rev B Condens Matter Mater Phys. 84 (**2011**) 075144.

[268] J. Heyd, G.E. Scuseria, M. Ernzerhof, Hybrid functionals based on a screened Coulomb potential, J Chem Phys. 118 (**2003**) 8207.

[269] Electron correlations in narrow energy bands II. An improved solution, Proc R Soc Lond A Math Phys Sci. 281 (**1964**) 401–419.

[270] Electron correlations in narrow energy bands. I. The degenerate band case, Proc R Soc Lond A Math Phys Sci. 277 (**1964**) 237–259.

[271] V.I. Anisimov, J. Zaanen, O.K. Andersen, Band theory and Mott insulators: Hubbard U instead of Stoner I, Phys Rev B. 44 (**1991**) 943–954.

[272] V.I. Anisimov, I. IV. Solovyev, M.A. Korotin, M.T. Czyyk, G.A. Sawatzky, Density-functional theory and NiO photoemission spectra, Phys Rev B. 48 (**1993**) 16929.

[273] I. IV. Solovyev, P.H. Dederichs, IV.I. Anisimov, Corrected atomic limit in the local-density approximation and the electronic structure of *d* impurities in Rb, Phys Rev B. 50 (**1994**) 16861.

[274] A.I. Liechtenstein, IV.I. Anisimov, J. Zaanen, Density-functional theory and strong interactions: Orbital ordering in Mott-Hubbard insulators, Phys Rev B. 52 (**1995**) R5467.

[275] S.L. Dudarev, G.A. Botton, S.Y. Savrasov, C.J. Humphreys, A.P. Sutton, Electron-energy-loss spectra and the structural stability of nickel oxide: An LSDA+U study, Phys Rev B. 57 (**1998**) 1505.

[276] N.J. Mosey, E.A. Carter, Ab initio evaluation of Coulomb and exchange parameters for DFT+U calculations, Phys Rev B Condens Matter Mater Phys. 76 (**2007**) 155123.

[277] N.J. Mosey, P. Liao, E.A. Carter, Rotationally invariant ab initio evaluation of Coulomb and exchange parameters for DFT+U calculations, J Chem Phys. 129 (**2008**) 014103.

[278] V.I. Anisimov, O. Gunnarsson, Density-functional calculation of effective Coulomb interactions in metals, Phys Rev B. 43 (**1991**) 7570.

[279] M. Cococcioni, S. De Gironcoli, Linear response approach to the calculation of the effective interaction parameters in the LDA+U method, Phys Rev B Condens Matter Mater Phys. 71 (**2005**) 035105.

[280] H.J. Kulik, M. Cococcioni, D.A. Scherlis, N. Marzari, Density functional theory in transition-metal chemistry: A self-consistent hubbard U approach, Phys Rev Lett. 97 (**2006**) 103001.

[281] H.J. Monkhorst, J.D. Pack, Special points for Brillouin-zone integrations, Phys Rev B. 13 (**1976**) 5188.

[282] W. Koch, M.C. Holthausen, A Chemist's Guide to Density Functional Theory, A Chemist's Guide to Density Functional Theory. (**2001**).

[283] Ashcroft, N.W. and Mermin, N.D. (1976) Solid State Physics. Saunders College, Philadelphia, 116, 217. - References - Scientific Research Publishing, (n.d.).

[284] M.C. Payne, M.P. Teter, D.C. Allan, T.A. Arias, J.D. Joannopoulos, Iterative minimization techniques for ab initio total-energy calculations: Molecular dynamics and conjugate gradients, Rev Mod Phys. 64 (**1992**) 1045–1097.

[285] G. Kresse, J. Hafner, Norm-conserving and ultrasoft pseudopotentials for first-row and transition elements, Journal of Physics: Condensed Matter. 6 (**1994**) 8245.

[286] N. Troullier, J.L. Martins, Efficient pseudopotentials for plane-wave calculations, Phys Rev B. 43 (**1991**) 1993.

[287] D. Vanderbilt, Soft self-consistent pseudopotentials in a generalized eigenvalue formalism, Phys Rev B. 41 (**1990**) 7892.

[288] P.E. Blöchl, Projector augmented-wave method, Phys Rev B. 50 (**1994**) 17953.

[289] D. Singh, L. Nordstrom, Planewaves, Pseudopotentials, and the LAPW method, (**2006**).

[290] G. Kresse, J.F.-P. review B, undefined 1996, Efficient iterative schemes for ab initio total-energy calculations using a plane-wave basis set, APS. 54 (**1996**) 11169–11186.

[291] G. Kresse, J. Hafner, *Ab initio* molecular dynamics for liquid metals, Phys Rev B. 47 (**1993**) 558.

[292] J. Hafner, Ab-initio simulations of materials using VASP: Density-functional theory and beyond, J Comput Chem. 29 (**2008**) 2044–2078.

[293] L.J. Sham, M. Schl̈ter, Density-Functional Theory of the Energy Gap, Phys Rev Lett. 51 (**1983**) 1888.

[294] R.W. Godby, M. Schlüter, L.J. Sham, Accurate Exchange-Correlation Potential for Silicon and Its Discontinuity on Addition of an Electron, Phys Rev Lett. 56 (**1986**) 2415.

[295] L.J. Sham, M. Schlüter, Density-functional theory of the band gap, Phys Rev B. 32 (**1985**) 3883.

[296] M.A. Vannice, Kinetics of catalytic reactions, Kinetics of Catalytic Reactions. (**2005**) 1–240.

[297] D.A. Yaseen, M. Scholz, Textile dye wastewater characteristics and constituents of synthetic effluents: a critical review, International Journal of Environmental Science and Technology. 16 (**2019**) 1193–1226.

[298] S. Samsami, M. Mohamadi, M.H. Sarrafzadeh, E.R. Rene, M. Firoozbahr, Recent advances in the treatment of dye-containing wastewater from textile industries: Overview and perspectives, Process Safety and Environmental Protection. 143 (**2020**) 138–163.

[299] K.G. Pavithra, S.K. P., IV. Jaikumar, S.R. P., Removal of colorants from wastewater: A review on sources and treatment strategies, Journal of Industrial and Engineering Chemistry. 75 (**2019**) 1–19.

[300] S.H. Hashemi, M. Kaykhaii, Azo dyes: Sources, occurrence, toxicity, sampling, analysis, and their removal methods, Emerging Freshwater Pollutants: Analysis, Fate and Regulations. (**2022**) 267–287.

[301] D. Bhatia, N.R. Sharma, J. Singh, R.S. Kanwar, Biological methods for textile dye removal from wastewater: A review, 47 (**2017**) 1836–1876.

[302] N.H. Othman, N.H. Alias, M.Z. Shahruddin, N.F. Abu Bakar, N.R. Nik Him, W.J. Lau, Adsorption kinetics of methylene blue dyes onto magnetic graphene oxide, J Environ Chem Eng. 6 (**2018**) 2803–2811.

[303] Y. Tan, Z. Sun, H. Meng, Y. Han, J. Wu, J. Xu, Y. Xu, X. Zhang, A new MOFs/polymer hybrid membrane: MIL-68(Al)/PVDF, fabrication and application in high-efficient removal of p-nitrophenol and methylene blue, Sep Purif Technol. 215 (**2019**) 217–226.

[304] M.R. Samarghandi, A. Dargahi, A. Shabanloo, H.Z. Nasab, Y. Vaziri, A. Ansari, Electrochemical degradation of methylene blue dye using a graphite doped PbO2 anode: Optimization of operational parameters, degradation pathway and improving the biodegradability of textile wastewater, Arabian Journal of Chemistry. 13 (**2020**) 6847–6864.

[305] F. Ouanji, I. Ellouzi, M. Kacimi, M. Ziyad, Ca-hydroxyzincate: Synthesis and Enhanced Photocatalytic Activity for the Degradation of Methylene Blue Under UV-Light Irradiation, Chemistry Africa. 2 (**2019**) 395–400.

[306] N. Benhadria, M. Hachemaoui, F. Zaoui, A. Mokhtar, S. Boukreris, T. Attar, L. Belarbi, B. Boukoussa, Catalytic Reduction of Methylene Blue Dye by Copper Oxide Nanoparticles, J Clust Sci. 33 (**2022**) 249–260.

[307] A. Lajevardi, M. Tavakkoli Yaraki, A. Masjedi, A. Nouri, M. Hossaini Sadr, Green synthesis of MOF@Ag nanocomposites for catalytic reduction of methylene blue, J Mol Liq. 276 (**2019**) 371–378.

[308] S.A. Sallam, G.M. El-Subruiti, A.S. Eltaweil, Facile Synthesis of Ag–γ-Fe2O3 Superior Nanocomposite for Catalytic Reduction of Nitroaromatic Compounds and Catalytic Degradation of Methyl Orange, Catal Letters. 148 (**2018**) 3701–3714.

[309] K. Zhang, J.M. Suh, J.W. Choi, H.W. Jang, M. Shokouhimehr, R.S. Varma, Recent Advances in the Nanocatalyst-Assisted NaBH4 Reduction of Nitroaromatics in Water, ACS Omega. 4 (**2019**) 483–495.

[310] M. Li, G. Chen, Revisiting catalytic model reaction p -nitrophenol/NaBH 4 using metallic nanoparticles coated on polymeric spheres, Nanoscale. 5 (**2013**) 11919–11927.

[311] L. Liu, A. Corma, Metal Catalysts for Heterogeneous Catalysis: From Single Atoms to Nanoclusters and Nanoparticles, Chem Rev. 118 (**2018**) 4981–5079.

[312] T.K. Sau, A.L. Rogach, F. Jäckel, T.A. Klar, J. Feldmann, Properties and Applications of Colloidal Nonspherical Noble Metal Nanoparticles, Advanced Materials. 22 (**2010**) 1805–1825.

[313] M.U. Gürbüz, G. Elmacı, A.S. Ertürk, In situ deposition of silver nanoparticles on polydopamine-coated manganese ferrite nanoparticles: Synthesis, characterization, and application to the degradation of organic dye pollutants as an efficient magnetically recyclable nanocatalyst, Appl Organomet Chem. 35 (**2021**) e6284.

[314] T.N.J.I. Edison, R. Atchudan, N. Karthik, J. Balaji, D. Xiong, Y.R. Lee, Catalytic degradation of organic dyes using green synthesized N-doped carbon supported silver nanoparticles, Fuel. 280 (**2020**) 118682.

[315] A. Mohan, L. Rout, A.M. Thomas, S. Nagappan, S. Parambadath, S.S. Park, C.S. Ha, Silver nanoparticles impregnated pH-responsive nanohybrid system for the catalytic reduction of dyes, Microporous and Mesoporous Materials. 303 (**2020**) 110260.

[316] M.U. Gürbüz, M. Koca, G. Elmacı, A.S. Ertürk, In situ green synthesis of MnFe2O4@EP@Ag nanocomposites using Epilobium parviflorum green tea extract: An efficient magnetically recyclable catalyst for the reduction of hazardous organic dyes, Appl Organomet Chem. 35 (**2021**) e6230.

[317] C. Duan, J. Meng, X. Wang, X. Meng, X. Sun, Y. Xu, W. Zhao, Y. Ni, Synthesis of novel cellulose- based antibacterial composites of Ag nanoparticles@ metal-organic frameworks@ carboxymethylated fibers, Carbohydr Polym. 193 (**2018**) 82–88.

[318] H. Güler, F. Kurtuluş, A rapid synthesis of sodium titanium phosphate, NaTi2(PO4)3 by using microwave energy, Mater Chem Phys. 99 (**2006**) 394–397.

[319] P. Tarte, A. Rulmont, C. Merckaert-Ansay, Vibrational spectrum of nasicon-like, rhombohedral orthophosphates MIMIV2(PO4)3, Spectrochim Acta A. 42 (**1986**) 1009–1016.

[320] B. Akbari, M.P. Tavandashti, M. Zandrahimi, PARTICLE SIZE CHARACTERIZATION OF NANOPARTICLES–A PRACTICALAPPROACH, Iranian Journal of Materials Science and Engineering. (**2011**).

[321] X. Dong, X. Ji, H. Wu, L. Zhao, J. Li, W. Yang, Shape control of silver nanoparticles by stepwise citrate reduction, Journal of Physical Chemistry C. 113 (**2009**) 6573–6576.

[322] Y. Zheng, A. Wang, Ag nanoparticle-entrapped hydrogel as promising material for catalytic reduction of organic dyes, J Mater Chem. 22 (**2012**) 16552–16559.

[323] N. Cyril, J.B. George, L. Joseph, IV.P. Sylas, Catalytic Degradation of Methyl Orange and Selective Sensing of Mercury Ion in Aqueous Solutions Using Green Synthesized Silver Nanoparticles from the Seeds of Derris trifoliata, J Clust Sci. 30 (**2019**) 459–468.

[324] V.K. Vidhu, D. Philip, Catalytic degradation of organic dyes using biosynthesized silver nanoparticles, Micron. 56 (**2014**) 54–62.

[325] P. Ncube, N. Bingwa, H. Baloyi, R. Meijboom, Catalytic activity of palladium and gold dendrimer-encapsulated nanoparticles for methylene blue reduction: A kinetic analysis, Appl Catal A Gen. 495 (**2015**) 63–71.

[326] R. Grzeschik, D. Schäfer, T. Holtum, S. Küpper, A. Hoffmann, S. Schlücker, On the Overlooked Critical Role of the pH Value on the Kinetics of the 4-Nitrophenol NaBH4-Reduction Catalyzed by Noble-Metal Nanoparticles (Pt, Pd, and Au), Journal of Physical Chemistry C. 124 (**2020**) 2939–2944.

[327] N. Wang, Y. Hu, Z. Zhang, Sustainable catalytic properties of silver nanoparticles supported montmorillonite for highly efficient recyclable reduction of methylene blue, Appl Clay Sci. 150 (**2017**) 47–55.

[328] S. Joseph, B. Mathew, Microwave-assisted green synthesis of silver nanoparticles and the study on catalytic activity in the degradation of dyes, J Mol Liq. 204 (**2015**) 184–191.

[329] P.K. Sahoo, N. Kumar, S. Thiyagarajan, D. Thakur, H.S. Panda, Freeze-Casting of Multifunctional Cellular 3D-Graphene/Ag Nanocomposites: Synergistically Affect Supercapacitor, Catalytic, and Antibacterial Properties, ACS Sustain Chem Eng. 6 (**2018**) 7475–7487.

[330] L. Qi, K. Zhang, W. Qin, Y. Hu, Highly efficient flow-through catalytic reduction of methylene blue using silver nanoparticles functionalized cotton, Chemical Engineering Journal. 388 (**2020**) 124252.

[331] N. Wang, F. Xiao, J. Zhang, H. Zhou, Y. Qin, D. Pan, Spherical montmorillonite-supported nano-silver as a self-sedimentary catalyst for methylene blue removal, Appl Clay Sci. 174 (**2019**) 146–151.

[332] M. Ismail, M.I. Khan, S.B. Khan, K. Akhtar, M.A. Khan, A.M. Asiri, Catalytic reduction of picric acid, nitrophenols and organic azo dyes via green synthesized plant supported Ag nanoparticles, J Mol Liq. 268 (**2018**) 87–101.

[333] T. Kamal, M.S.J. Khan, S.B. Khan, A.M. Asiri, M.T.S. Chani, M.W. Ullah, Silver Nanoparticles Embedded in Gelatin Biopolymer Hydrogel as Catalyst for Reductive Degradation of Pollutants, Journal of Polymers and the Environment 2019 28:2. 28 (**2019**) 399–410.

[334] D. Das, R. Sarkar, S. Mukherjee, K.K. Chattopadhyay, Sodium borohydride assisted reduction of toxic pollutants by silver coordinated melamine based polymeric material, Mater Today Proc. 44 (**2021**) 444–452.

[335] P. Mohammadi, H. Sheibani, Green synthesis of Fe3O4@SiO2-Ag magnetic nanocatalyst using safflower extract and its application as recoverable catalyst for reduction of dye pollutants in water, Appl Organomet Chem. 32 (**2018**) e4249.

[336] W.J. Cosgrove, D.P. Loucks, Water management: Current and future challenges and research directions, Water Resour Res. 51 (**2015**) 4823–4839.

[337] J. Noh, R. Meijboom, Reduction of 4-Nitrophenol as a Model Reaction for Nanocatalysis, Application of Nanotechnology in Water Research. 9781118496305 (**2014**) 333–405.

[338] T. Aditya, A. Pal, T. Pal, Nitroarene reduction: A trusted model reaction to test nanoparticle catalysts, Chemical Communications. 51 (**2015**) 9410–9431.

[339] P. Hervés, M. Pérez-Lorenzo, L.M. Liz-Marzán, J. Dzubiella, Y. Lub, M. Ballauff, Catalysis by metallic nanoparticles in aqueous solution: Model reactions, Chem Soc Rev. 41 (**2012**) 5577–5587.

[340] P. Zhao, X. Feng, D. Huang, G. Yang, D. Astruc, Basic concepts and recent advances in nitrophenol reduction by gold- and other transition metal nanoparticles, Coord Chem Rev. 287 (**2015**) 114–136.

[341] S. Palla, N.K. Veldurthi, R. Guje, G. Prasad, N.R. Muniratnam, M. Vithal, Synthesis and catalytic performance of Na2HfM(PO4)3 and Ag2-xNaxHfM(PO4)3 (M = Fe and Al and 0.07 ≤ x ≤ 0.13), Synthesis and Reactivity in Inorganic, Metal-Organic and Nano-Metal Chemistry. 45 (**2014**) 730–739.

[342] V.S. Kurazhkovskaya, D.M. Bykov, A.I. Orlova, Infrared spectroscopy and structure of trigonal zirconium orthophosphates with lanthanides and actinides, Journal of Structural Chemistry. 45 (**2004**) 966–973.

[343] D.M. Bykov, R.J.M. Konings, C. Apostolidis, A. Hen, E. Colineau, T. Wiss, P. Raison, Synthesis and investigation of neptunium zirconium phosphate, a member of the NZP family: Crystal structure, thermal behaviour and Mössbauer spectroscopy studies, Dalton Transactions. 46 (**2017**) 11626–11635.

[344] X. Dong, X. Ji, J. Jing, M. Li, J. Li, W. Yang, Synthesis of triangular silver nanoprisms by stepwise reduction of sodium borohydride and trisodium citrate, Journal of Physical Chemistry C. 114 (**2010**) 2070–2074.

[345] B.A. Donlon, E. Razo-Flores, J.A. Field, G. Lettinga, Toxicity of N-substituted aromatics to acetoclastic methanogenic activity in granular sludge, Appl Environ Microbiol. 61 (**1995**) 3889–3893.

[346] S. Sirohi, A. Mittal, R. Nain, N. Jain, R. Singh, S. Dobhal, B. Pani, D. Parida, Effect of nanoparticle shape on the conductivity of Ag nanoparticle poly(vinyl alcohol) composite films, Polym Int. 68 (**2019**) 1961–1967.

[347] H.P. Singh, S. Sharma, S.K. Sharma, R.K. Sharma, Biogenic synthesis of metal nanocatalysts using Mimosa pudica leaves for efficient reduction of aromatic nitrocompounds, RSC Adv. 4 (**2014**) 37816–37825.

[348] U. Kurtan, A. Baykal, Fe3O4@Tween20@Ag Magnetically Recyclable Nanocatalyst for Various Hydrogenation Reactions, J Inorg Organomet Polym Mater. 25 (**2015**) 657–663.

[349] M.H. Rashid, T.K. Mandal, Synthesis and catalytic application of nanostructured silver dendrites, Journal of Physical Chemistry C. 111 (**2007**) 16750–16760.

[350] Z. Li, Z. Jia, T. Ni, S. Li, Green and facile synthesis of fibrous Ag/cotton composites and their catalytic properties for 4-nitrophenol reduction, Appl Surf Sci. 426 (**2017**) 160–168.

[351] Y. Chi, J. Tu, M. Wang, X. Li, Z. Zhao, One-pot synthesis of ordered mesoporous silver nanoparticle/carbon composites for catalytic reduction of 4-nitrophenol, J Colloid Interface Sci. 423 (**2014**) 54–59.

[352] S.P. Deshmukh, R.K. Dhokale, H.M. Yadav, S.N. Achary, S.D. Delekar, Titania-supported silver nanoparticles: An efficient and reusable catalyst for reduction of 4-nitrophenol, Appl Surf Sci. 273 (**2013**) 676–683.

[353] Y. Chi, Q. Yuan, Y. Li, J. Tu, L. Zhao, N. Li, X. Li, Synthesis of Fe 3O 4@SiO 2-Ag magnetic nanocomposite based on small-sized and highly dispersed silver nanoparticles for catalytic reduction of 4-nitrophenol, J Colloid Interface Sci. 383 (**2012**) 96–102.

[354] Z. Jiang, D. Jiang, A.M. Showkot Hossain, K. Qian, J. Xie, In situ synthesis of silver supported nanoporous iron oxide microbox hybrids from metal-organic frameworks and their catalytic application in p-nitrophenol reduction, Physical Chemistry Chemical Physics. 17 (**2015**) 2550–2559.

[355] A. Zhou, J. Li, G. Wang, Q. Xu, Preparation of Ag/ZrGP nanocomposites with enhanced catalytic activity for catalytic reduction of 4-nitrophenol, Appl Surf Sci. 506 (**2020**) 144570.

[356] S. Wunder, F. Polzer, Y. Lu, Y. Mei, M. Ballauff, Kinetic analysis of catalytic reduction of 4-nitrophenol by metallic nanoparticles immobilized in spherical polyelectrolyte brushes, Journal of Physical Chemistry C. 114 (**2010**) 8814–8820.

[357] V. Bharti, K. Vikrant, M. Goswami, H. Tiwari, R.K. Sonwani, J. Lee, D.C.W. Tsang, K.H. Kim, M. Saeed, S. Kumar, B.N. Rai, B.S. Giri, R.S. Singh, Biodegradation of methylene blue dye in a batch and continuous mode using biochar as packing media, Environ Res. 171 (**2019**) 356–364.

[358] S. Velusamy, A. Roy, S. Sundaram, T. Kumar Mallick, A Review on Heavy Metal Ions and Containing Dyes Removal Through Graphene Oxide-Based Adsorption Strategies for Textile Wastewater Treatment, The Chemical Record. 21 (**2021**) 1570–1610.

[359] W. Li, B. Mu, Y. Yang, Feasibility of industrial-scale treatment of dye wastewater via bio-adsorption technology, Bioresour Technol. 277 (**2019**) 157–170.

[360] Y. Ren, T. Li, W. Zhang, S. Wang, M. Shi, C. Shan, W. Zhang, X. Guan, L. Lv, M. Hua, B. Pan, MIL-PVDF blend ultrafiltration membranes with ultrahigh MOF loading for simultaneous adsorption and catalytic oxidation of methylene blue, J Hazard Mater. 365 (**2019**) 312–321.

[361] H. Wang, L. Zhang, Z. Chen, J. Hu, S. Li, Z. Wang, J. Liu, X. Wang, Semiconductor heterojunction photocatalysts: design, construction, and photocatalytic performances, Chem Soc Rev. 43 (**2014**) 5234–5244.

[362] C. Karthikeyan, P. Arunachalam, K. Ramachandran, A.M. Al-Mayouf, S. Karuppuchamy, Recent advances in semiconductor metal oxides with enhanced methods for solar photocatalytic applications, J Alloys Compd. 828 (**2020**) 154281.

[363] A. Tab, B. Bellal, C. Belabed, M. Dahmane, M. Trari, Visible light assisted photocatalytic degradation and mineralization of Rhodamine B in aqueous solution by Ag3PO4, Optik (Stuttg). 214 (**2020**) 164858.

[364] E. Abroshan, S. Farhadi, A. Zabardasti, Novel magnetically separable Ag3PO4/MnFe2O4 nanocomposite and its high photocatalytic degradation performance for organic dyes under solar-light irradiation, Solar Energy Materials and Solar Cells. 178 (**2018**) 154–163.

[365] G. Liu, G. Wang, Z. Hu, Y. Su, L. Zhao, Ag2O nanoparticles decorated TiO2 nanofibers as a p-n heterojunction for enhanced photocatalytic decomposition of RhB under visible light irradiation, Appl Surf Sci. 465 (**2019**) 902–910.

[366] H. Guo, H.Y. Niu, C. Liang, C.G. Niu, D.W. Huang, L. Zhang, N. Tang, Y. Yang, C.Y. Feng, G.M. Zeng, Insight into the energy band alignment of magnetically separable Ag2O/ZnFe2O4 p-n heterostructure with rapid charge transfer assisted visible light photocatalysis, J Catal. 370 (**2019**) 289–303.

[367] L. Liu, T. Hu, K. Dai, J. Zhang, C. Liang, A novel step-scheme BiVO4/Ag3VO4 photocatalyst for enhanced photocatalytic degradation activity under visible light irradiation, Chinese Journal of Catalysis. 42 (**2021**) 46–55.

[368] A. Kumar, G. Sharma, M. Naushad, T. Ahamad, R.C. Veses, F.J. Stadler, Highly visible active Ag2CrO4/Ag/BiFeO3@RGO nano-junction for photoreduction of CO2 and photocatalytic removal of ciprofloxacin and bromate ions: The triggering effect of Ag and RGO, Chemical Engineering Journal. 370 (**2019**) 148–165.

[369] Z. Yi, J. Ye, N. Kikugawa, T. Kako, S. Ouyang, H. Stuart-Williams, H. Yang, J. Cao, W. Luo, Z. Li, Y. Liu, R.L. Withers, An orthophosphate semiconductor with photooxidation properties under visible-light irradiation, Nature Materials 2010 9:7. 9 (**2010**) 559–564.

[370] D. Xu, B. Cheng, J. Zhang, W. Wang, J. Yu, W. Ho, Photocatalytic activity of Ag2MO4 (M = Cr, Mo, W) photocatalysts, J Mater Chem A Mater. 3 (**2015**) 20153–20166.

[371] K.J. Rao, K.C. Sobha, S. Kumar, Infrared and Raman spectroscopic studies of glasses with NASICON-type chemistry, Journal of Chemical Sciences 2001 113:5. 113 (**2001**) 497–514.

[372] C.J. Antony, A. Aatiq, C.Y. Panicker, M.J. Bushiri, H.T. Varghese, T.K. Manojkumar, FT-IR and FT-Raman study of Nasicon type phosphates, ASnFe(PO4)3 [A = Na2, Ca, Cd], Spectrochim Acta A Mol Biomol Spectrosc. 78 (**2011**) 415–419.

[373] H. Gao, F. Wang, S. Wang, X. Wang, Z. Yi, H. Yang, Photocatalytic activity tuning in a novel Ag2S/CQDs/CuBi2O4 composite: Synthesis and photocatalytic mechanism, Mater Res Bull. 115 (**2019**) 140–149.

[374] D. Hou, W. Luo, Y. Huang, J.C. Yu, X. Hu, Synthesis of porous Bi4Ti3O12 nanofibers by electrospinning and their enhanced visible-light-driven photocatalytic properties, Nanoscale. 5 (**2013**) 2028–2035.

[375] D.L. Wood, J. Tauc, Weak absorption tails in amorphous semiconductors, Phys Rev B. 5 (**1972**) 3144–3151.

[376] B.D. Viezbicke, S. Patel, B.E. Davis, D.P. Birnie, Evaluation of the Tauc method for optical absorption edge determination: ZnO thin films as a model system, Physica Status Solidi (b). 252 (**2015**) 1700–1710.

[377] L. Wang, T. Maxisch, G. Ceder, Oxidation energies of transition metal oxides within the GGA+U framework, Phys Rev B Condens Matter Mater Phys. 73 (**2006**) 195107.

[378] Y. Hinuma, G. Pizzi, Y. Kumagai, F. Oba, I. Tanaka, Band structure diagram paths based on crystallography, Comput Mater Sci. 128 (**2017**) 140–184.

[379] Y.H. Chiu, T.F.M. Chang, C.Y. Chen, M. Sone, Y.J. Hsu, Mechanistic Insights into Photodegradation of Organic Dyes Using Heterostructure Photocatalysts, Catalysts 2019, Vol. 9, Page 430. 9 (**2019**) 430.

[380] M. Pudukudy, Q. Jia, H. Wang, S. Shan, R. Rajendran, Influence of synthesis parameters on the crystalline, structural, textural, optical and photocatalytic properties of α and β polymorphs of AgVO3 nanorods, Mater Sci Semicond Process. 107 (**2020**) 104824.

[381] K. Sharifian, IV. Mahdikhah, S. Sheibani, Ternary Ag@SrTiO3@CNT plasmonic nanocomposites for the efficient photodegradation of organic dyes under the visible light irradiation, Ceram Int. 47 (**2021**) 22741–22752.

[382] V. Kavinkumar, A. Verma, K. Uma, S. Moscow, K. Jothivenkatachalam, Y.P. Fu, Plasmonic metallic silver induced Bi2WO6/TiO2 ternary junction towards the photocatalytic, electrochemical OER/HER, antibacterial and sensing applications, Appl Surf Sci. 569 (**2021**) 150918.

[383] B. Palanivel, C. Ayappan, IV. Jayaraman, S. Chidambaram, R. Maheswaran, A. Mani, Inverse spinel NiFe2O4 deposited g-C3N4 nanosheet for enhanced visible light photocatalytic activity, Mater Sci Semicond Process. 100 (**2019**) 87–97.

[384] Q.L. Liang, N.N. Du, L.G. Gong, C.X. Wang, C.M. Wang, K. Yu, B. bin Zhou, A {BW12O40} hybrid decorated by Ag+ for use as a supercapacitor electrode material and photocatalyst, New Journal of Chemistry. 45 (**2021**) 14444–14450.

[385] S. Zhou, Y. Wang, G. Zhao, C. Li, L. Liu, F. Jiao, Enhanced visible light photocatalytic degradation of rhodamine B by Z-scheme CuWO4/g-C3N4 heterojunction, Journal of Materials Science: Materials in Electronics 2021 32:3. 32 (**2021**) 2731–2743.

[386] T. Bunluesak, A. Phuruangrat, S. Thongtem, T. Thongtem, Visible-light-driven heterostructure Ag/Bi2WO6 nanocomposites synthesized by photodeposition method and used for photodegradation of rhodamine B dye, Research on Chemical Intermediates 2021 47:7. 47 (**2021**) 3079–3092.

[387] H. Ait ahsaine, A. El Jaouhari, A. Slassi, M. Ezahri, A. Benlhachemi, B. Bakiz, F. Guinneton, J.R. Gavarri, Electronic band structure and visible-light photocatalytic activity of Bi2WO6: elucidating the effect of lutetium doping, RSC Adv. 6 (**2016**) 101105–101114.

[388] M. Mousavi, A. Habibi-Yangjeh, M. Abitorabi, Fabrication of novel magnetically separable nanocomposites using graphitic carbon nitride, silver phosphate and silver chloride and their applications in photocatalytic removal of different pollutants using visible-light irradiation, J Colloid Interface Sci. 480 (**2016**) 218–231.

[389] J. Chen, H. Che, K. Huang, C. Liu, W. Shi, Fabrication of a ternary plasmonic photocatalyst CQDs/Ag/Ag2O to harness charge flow for photocatalytic elimination of pollutants, Appl Catal B. 192 (**2016**) 134–144.

[390] Y. Huang, X. Zhang, S. Zou, Y. Zeng, Construction and characterization of 3D hollow Ag/AgBr/Bi4Ti3O12 heterojunction photocatalyst: Mechanism investigation of rhodamine B degradation, Mater Lett. 317 (**2022**) 131964.

[391] S. Kokilavani, A. Syed, A.M. Elgorban, A.H. Bahkali, H.A. AL-Shwaiman, R.S. Varma, A. Das, S.S. Khan, Designing Z-scheme AgIO4 nanorod embedded with Bi2S3 nanoflakes for expeditious visible light photodegradation of congo red and rhodamine B, Chemosphere. 294 (**2022**) 133755.

[392] J. Liu, H. Yang, S.N. Gosling, M. Kummu, M. Flörke, S. Pfister, N. Hanasaki, Y. Wada, X. Zhang, C. Zheng, J. Alcamo, T. Oki, Water scarcity assessments in the past, present, and future, Earths Future. 5 (**2017**) 545–559.

[393] A.Y. Hoekstra, The water footprint: The relation between human consumption and water use, The Water We Eat: Combining Virtual Water and Water Footprints. (**2015**) 35–48.

[394] S. Khan, M. Naushad, M. Govarthanan, J. Iqbal, S.M. Alfadul, Emerging contaminants of high concern for the environment: Current trends and future research, Environ Res. 207 (**2022**) 112609.

[395] R.N. Bharagava, G. Saxena, S.I. Mulla, Introduction to Industrial Wastes Containing Organic and Inorganic Pollutants and Bioremediation Approaches for Environmental Management, Bioremediation of Industrial Waste for Environmental Safety. (**2020**) 1–18.

[396] R. Kishor, D. Purchase, G.D. Saratale, R.G. Saratale, L.F.R. Ferreira, M. Bilal, R. Chandra, R.N. Bharagava, Ecotoxicological and health concerns of persistent coloring pollutants of textile industry wastewater and treatment approaches for environmental safety, J Environ Chem Eng. 9 (**2021**) 105012.

[397] C.M. Motta, P. Simoniello, C. Arena, T. Capriello, R. Panzuto, E. Vitale, C. Agnisola, M. Tizzano, B. Avallone, I. Ferrandino, Effects of four food dyes on development of three model species, Cucumis sativus, Artemia salina and Danio rerio: Assessment of potential risk for the environment, Environmental Pollution. 253 (**2019**) 1126–1135.

[398] U. Shanker, M. Rani, IV. Jassal, Degradation of hazardous organic dyes in water by nanomaterials, Environmental Chemistry Letters 2017 15:4. 15 (**2017**) 623–642.

[399] L. Pérez-Ibarbia, T. Majdanski, S. Schubert, N. Windhab, U.S. Schubert, Safety and regulatory review of dyes commonly used as excipients in pharmaceutical and nutraceutical applications, European Journal of Pharmaceutical Sciences. 93 (**2016**) 264–273.

[400] R. Kant, Textile dyeing industry an environmental hazard, Nat Sci (Irvine). 2012 (**2011**) 22–26.

[401] I. Bazin, A. Ibn Hadj Hassine, Y. Haj Hamouda, W. Mnif, A. Bartegi, M. Lopez-Ferber, M. de Waard, C. Gonzalez, Estrogenic and anti-estrogenic activity of 23 commercial textile dyes, Ecotoxicol Environ Saf. 85 (**2012**) 131–136.

[402] E.N. el Qada, S.J. Allen, G.M. Walker, Adsorption of Methylene Blue onto activated carbon produced from steam activated bituminous coal: A study of equilibrium adsorption isotherm, Chemical Engineering Journal. 124 (**2006**) 103–110.

[403] M. Berradi, R. Hsissou, M. Khudhair, M. Assouag, O. Cherkaoui, A. el Bachiri, A. el Harfi, Textile finishing dyes and their impact on aquatic environs, Heliyon. 5 (**2019**) e02711.

[404] K.T. Chung, Azo dyes and human health: A review, 34 (**2016**) 233–261.

[405] B.J. Brüschweiler, C. Merlot, Azo dyes in clothing textiles can be cleaved into a series of mutagenic aromatic amines which are not regulated yet, Regulatory Toxicology and Pharmacology. 88 (**2017**) 214–226.

[406] S. Varjani, P. Rakholiya, H.Y. Ng, S. You, J.A. Teixeira, Microbial degradation of dyes: An overview, Bioresour Technol. 314 (**2020**) 123728.

[407] M. Solís, A. Solís, H.I. Pérez, N. Manjarrez, M. Flores, Microbial decolouration of azo dyes: A review, Process Biochemistry. 47 (**2012**) 1723–1748.

[408] C. Yang, W. Xu, Y. Nan, Y. Wang, Y. Hu, C. Gao, X. Chen, Fabrication and characterization of a high performance polyimide ultrafiltration membrane for dye removal, J Colloid Interface Sci. 562 (**2020**) 589–597.

[409] C. Zhijiang, X. Ping, Z. Cong, Z. Tingting, G. Jie, Z. Kongyin, Preparation and characterization of a bi-layered nano-filtration membrane from a chitosan hydrogel and bacterial cellulose nanofiber for dye removal, Cellulose. 25 (**2018**) 5123–5137.

[410] M.M. Hassan, C.M. Carr, A critical review on recent advancements of the removal of reactive dyes from dyehouse effluent by ion-exchange adsorbents, Chemosphere. 209 (**2018**) 201–219.

[411] Y. Jia, L. Ding, P. Ren, M. Zhong, J. Ma, X. Fan, Performances and Mechanism of Methyl Orange and Congo Red Adsorbed on the Magnetic Ion-Exchange Resin, J Chem Eng Data. 65 (**2020**) 725–736.

[412] C. IV. Rekhate, J.K. Srivastava, Recent advances in ozone-based advanced oxidation processes for treatment of wastewater- A review, Chemical Engineering Journal Advances. 3 (**2020**) 100031.

[413] M. Moradi, A. Elahinia, Y. Vasseghian, E.N. Dragoi, F. Omidi, A. Mousavi Khaneghah, A review on pollutants removal by Sono-photo -Fenton processes, J Environ Chem Eng. 8 (**2020**) 104330.

[414] C.A. Martínez-Huitle, M. Panizza, Electrochemical oxidation of organic pollutants for wastewater treatment, Curr Opin Electrochem. 11 (**2018**) 62–71.

[415] S. Garcia-Segura, J.D. Ocon, M.N. Chong, Electrochemical oxidation remediation of real wastewater effluents — A review, Process Safety and Environmental Protection. 113 (**2018**) 48–67.

[416] Ö. Bulca, B. Palas, S. Atalay, G. Ersöz, Performance investigation of the hybrid methods of adsorption or catalytic wet air oxidation subsequent to electrocoagulation in treatment of real textile wastewater and kinetic modelling, Journal of Water Process Engineering. 40 (**2021**) 101821.

[417] A. Shahedi, A.K. Darban, F. Taghipour, A. Jamshidi-Zanjani, A review on industrial wastewater treatment via electrocoagulation processes, Curr Opin Electrochem. 22 (**2020**) 154–169.

[418] A.R. Ribeiro, O.C. Nunes, M.F.R. Pereira, A.M.T. Silva, An overview on the advanced oxidation processes applied for the treatment of water pollutants defined in the recently launched Directive 2013/39/EU, Environ Int. 75 (**2015**) 33–51.

[419] M. Saeed, M. Muneer, A. ul Haq, N. Akram, Photocatalysis: an effective tool for photodegradation of dyes—a review, Environmental Science and Pollution Research 2021 29:1. 29 (**2021**) 293–311.

[420] Y. Nosaka, A.Y. Nosaka, Generation and Detection of Reactive Oxygen Species in Photocatalysis, Chem Rev. 117 (**2017**) 11302–11336.

[421] G. Liu, J. Zhao, Photocatalytic degradation of dye sulforhodamine B: a comparative study of photocatalysis with photosensitization, New Journal of Chemistry. 24 (**2000**) 411–417.

[422] V.W. Atul, G. Gaikwad, … M.D.-Res.J.C., undefined 2013, Removal of organic pollutant from water by heterogenous photocatalysis: a review, Researchgate.Net. 17 (**2013**).

[423] K.P. Gopinath, N.V. Madhav, A. Krishnan, R. Malolan, G. Rangarajan, Present applications of titanium dioxide for the photocatalytic removal of pollutants from water: A review, J Environ Manage. 270 (**2020**) 110906.

[424] K.M. Lee, C.W. Lai, K.S. Ngai, J.C. Juan, Recent developments of zinc oxide based photocatalyst in water treatment technology: A review, Water Res. 88 (**2016**) 428–448.

[425] W. Zhang, H. He, H. Li, L. Duan, L. Zu, Y. Zhai, W. Li, L. Wang, H. Fu, D. Zhao, Visible-Light Responsive TiO2-Based Materials for Efficient Solar Energy Utilization, Adv Energy Mater. 11 (**2021**) 2003303.

[426] T. Di, Q. Xu, W.K. Ho, H. Tang, Q. Xiang, J. Yu, Review on Metal Sulphide-based Z-scheme Photocatalysts, ChemCatChem. 11 (**2019**) 1394–1411.

[427] M. al Kausor, S. sen Gupta, D. Chakrabortty, Ag3PO4-based nanocomposites and their applications in photodegradation of toxic organic dye contaminated wastewater: Review on material design to performance enhancement, Journal of Saudi Chemical Society. 24 (**2020**) 20–41.

[428] H. Dong, G. Chen, J. Sun, C. Li, Y. Yu, D. Chen, A novel high-efficiency visible-light sensitive Ag2CO3 photocatalyst with universal photodegradation performances: Simple synthesis, reaction mechanism and first-principles study, Appl Catal B. 134–135 (**2013**) 46–54.

[429] E. Nyankson, B. Agyei-Tuffour, E. Annan, A. Yaya, B. Mensah, B. Onwona-Agyeman, R. Amedalor, B. Kwaku-Frimpong, J.K. Efavi, Ag2CO3-halloysite nanotubes composite with enhanced removal efficiency for water soluble dyes, Heliyon. 5 (**2019**) e01969.

[430] Z. Wang, Y. Li, Q. Cheng, X. Wang, J. Wang, G. Zhang, Sb-based photocatalysts for degradation of organic pollutants: A review, J Clean Prod. 367 (**2022**) 133060.

[431] Y. Che, B. Lu, Q. Qi, H. Chang, J. Zhai, K. Wang, Z. Liu, Bio-inspired Z-scheme g-C3N4/Ag2CrO4 for efficient visible-light photocatalytic hydrogen generation, Scientific Reports 2018 8:1. 8 (**2018**) 1–12.

[432] Y. Shi, J. Ma, Y. Chen, Y. Qian, B. Xu, W. Chu, D. An, Recent progress of silver-containing photocatalysts for water disinfection under visible light irradiation: A review, Science of The Total Environment. 804 (**2022**) 150024.

[433] N. Bi, H. Zheng, Y. Zhu, W. Jiang, B. Liang, Visible-light-driven photocatalytic degradation of non-azo dyes over Ag2O and its acceleration by the addition of an azo dye, J Environ Chem Eng. 6 (**2018**) 3150–3160.

[434] W. Jiang, X. Wang, Z. Wu, X. Yue, S. Yuan, H. Lu, B. Liang, Silver oxide as superb and stable photocatalyst under visible and near-infrared light irradiation and its photocatalytic mechanism, Ind Eng Chem Res. 54 (**2015**) 832–841.

[435] X. Hu, X. Liu, J. Tian, Y. Li, H. Cui, Towards full-spectrum (UV, visible, and near-infrared) photocatalysis: achieving an all-solid-state Z-scheme between Ag2O and TiO2 using reduced graphene oxide as the electron mediator, Catal Sci Technol. 7 (**2017**) 4193–4205.

[436] T.M.S. Dawoud, IV. Pavitra, P. Ahmad, A. Syed, G. Nagaraju, Photocatalytic degradation of an organic dye using Ag doped ZrO2 nanoparticles: Milk powder facilitated eco-friendly synthesis, J King Saud Univ Sci. 32 (**2020**) 1872–1878.

[437] Y. Orooji, M. Ghanbari, O. Amiri, M. Salavati-Niasari, Facile fabrication of silver iodide/graphitic carbon nitride nanocomposites by notable photo-catalytic performance through sunlight and antimicrobial activity, J Hazard Mater. 389 (**2020**) 122079.

[438] S.P. Vinay, Udayabhanu, G. Nagaraju, C.P. Chandrappa, N. Chandrasekhar, Novel Gomutra (cow urine) mediated synthesis of silver oxide nanoparticles and their enhanced photocatalytic, photoluminescence and antibacterial studies, Journal of Science: Advanced Materials and Devices. 4 (**2019**) 392–399.

[439] M. Batvandi, A. Haghighatzadeh, · Babak Mazinani, J. Dutta, Visible-light-driven photocatalysis with Z-scheme Ag3PO4@N-GQDs@g-C3N4 nano/hetero-junctions, Applied Physics A 2022 128:10. 128 (**2022**) 1–18.

[440] J. Zhang, H. Liu, Z. Ma, Flower-like Ag2O/Bi2MoO6 p-n heterojunction with enhanced photocatalytic activity under visible light irradiation, J Mol Catal A Chem. 424 (**2016**) 37–44.

[441] A. Subalakshmi, B. Kavitha, A. Karthika, S. Nikhil, N. Srinivasan, M. Rajarajan, A. Suganthi, Design of Mn and Zr incorporated Ag2O nanoparticles and their enhanced photocatalytic activity driven by visible light irradiation for degradation of rose bengal dye, New Journal of Chemistry. 45 (**2021**) 1876–1886.

[442] D. Kwon, J. Kim, Silver-doped ZnO for photocatalytic degradation of methylene blue, Korean Journal of Chemical Engineering 2020 37:7. 37 (**2020**) 1226–1232.

[443] J. Wan, E. Liu, J. Fan, X. Hu, L. Sun, C. Tang, Y. Yin, H. Li, Y. Hu, In-situ synthesis of plasmonic Ag/Ag3PO4 tetrahedron with exposed {111} facets for high visible-light photocatalytic activity and stability, Ceram Int. 41 (**2015**) 6933–6940.

[444] H.T. Ren, J. Han, T.T. Li, F. Sun, J.H. Lin, C.W. Lou, Visible light-induced oxidation of aqueous arsenite using facile Ag2O/TiO2 composites: Performance and mechanism, J Photochem Photobiol A Chem. 377 (**2019**) 260–267.